RUPRECHT-KARLS-UNIVERSITÄT HEIDELBERG

Andreas Werner Jung

Measurement of the $D^{*\pm}$ Meson Cross Section and Extraction of the Charm Contribution, $F_2^c(x, Q^2)$, to the Proton Structure in Deep Inelastic ep Scattering with the H1 Detector at HERA

Dissertation

HD-KIP-09-01

KIRCHHOFF-INSTITUT FÜR PHYSIK

INAUGURAL - DISSERTATION

zur

Erlangung der Doktorwürde

der

Naturwissenschaftlich - Mathematischen

Gesamtfakultät

der Ruprecht - Karls - Universität

Heidelberg

vorgelegt von

Dipl.-Phys. Andreas Werner Jung

aus Dortmund (Nordrhein - Westfalen)

Tag der mündlichen Prüfung: 14. Januar 2009

Measurement of the $D^{*\pm}$ Meson Cross Section

and

Extraction of the Charm Contribution, $F_2^c(x, Q^2)$, to the Proton Structure

in Deep Inelastic ep Scattering with

the H1 Detector at HERA

Gutachter: Prof. Dr. Hans-Christian Schultz-Coulon
Prof. Dr. Norbert Herrmann

Kurzfassung

Die Produktion von D^*-Mesonen in tiefunelastischer Streuung bei HERA wurde mit Daten untersucht, die mit dem H1-Detektor in den Jahren 2004-2007 aufgezeichnet wurden. Diese Daten entsprechen einer integrierten Luminosität von 347 pb^{-1}, welches eine Steigerung der verfügbaren Statistik um den Faktor acht, verglichen mit der vorherigen H1-Publikation, darstellt. Der sichtbare Bereich dieser Messung deckt Photonvirtualitäten von $5 < Q^2 < 100$ GeV^2 und einen erweiterten Inelastizitätsbereich von $0.02 < y < 0.70$ ab. Das D^*-Meson wird dabei im Transversalimpulsbereich ab $p_T(D^*) > 1.5$ GeV in einem Pseudorapiditätsbereich von $|\eta(D^*)| < 1.5$ gemessen. Einfach- und doppeltdifferentielle Verteilungen werden mit perturbativen QCD Vorhersagen in führender und nächstführender Ordnung verglichen. Der systematische Fehler der Messung ist entscheidet verringert worden. Der Beitrag von charm-Quarks zur Protonstruktur, $F_2^c(x, Q^2)$, wird in zwei verschiedenen QCD Evolutionsschemata aus den gemessenen D^*-Meson Wirkungsquerschnitten bestimmt und mit pQCD Vorhersagen in nächst-führender Ordnung verglichen. Dabei wird eine, verglichen mit der letzten H1-Publikation, 18fach höhere Statistik genutzt.
Die vorliegende Arbeit umfaßt ebenfalls ein erfolgreich beendetes Hardwareprojekt: Die Inbetriebnahme und Optimierung der dritten Stufe des schnellen Spurtriggers (FTT) bei H1, die Anfang 2006 erfolgreich abgeschlossen wurde. Der FTT ist in die ersten drei Stufen des zentralen H1-Triggersystems integriert und stellt eine verbesserte Selektivität für die Identifizierung von Ereignissen mit geladenen Teilchen zur Verfügung. Die dritte Stufe des FTT führt innerhalb von 100 μs eine spurbasierte Ereignisrekonstruktion aus und ist als Computerfarm, bestehend aus PowerPC Karten, realisiert. Außerdem wurde die FTT Simulation in die Simulation des H1-Triggersystems integriert.

Abstract

Inclusive production of D^* mesons in deep inelastic scattering at HERA is studied using data taken with the H1 detector in the years 2004 to 2007 corresponding to an integrated luminosity of 347 pb^{-1}. The measurement covers the region $5 < Q^2 < 100$ GeV^2 in photon virtuality and the increased region $0.02 < y < 0.70$ in the inelasticity of the scattering process. The visible range of the D^* meson is restricted in transverse momentum and pseudorapidity to $p_T(D^*) > 1.5$ GeV and $|\eta(D^*)| < 1.5$. The present measurement is based on an eightfold increased statistics compared to the previous H1 publication and provides a significantly reduced systematic error. Single and double-differential cross sections are compared to leading and next-to-leading order perturbative QCD predictions. The charm contribution, $F_2^c(x, Q^2)$, to the proton structure in different QCD evolution schemes is derived from the D^* cross sections and compared to next-to-leading order perturbative QCD predictions. This F_2^c measurement is performed using a factor of 18 more data compared to the previous H1 publication.
The present thesis additionally describes a successfully completed hardware project: The commissioning and optimisation of the third level of the H1 Fast Track Trigger (FTT), which was fully operational from 2006 onwards. The FTT is integrated in the first three levels of the H1 trigger system and provides enhanced selectivity for events with charged particles. The third trigger level of the FTT performs a track-based event reconstruction within a latency of about 100 μs. The third trigger level of the FTT is realised by a farm of PowerPC boards. Furthermore, the FTT simulation is now incorporated into the H1 trigger simulation.

Contents

1. Introduction

The *standard model of particle physics* is a very successful theory, which predicts and explains most of the phenomena observed in elementary particle physics. It consists of three gauge theories for the strong, weak and electromagnetic interaction. In addition there is the gravitational force dominant at very large distances, where up to now a theoretical framework similar to the formulation of the standard model is missing.
In the standard model matter is built from elementary particles out of three so-called families – I., II., and III. –, which incorporate six leptons and six quarks and the charge conjugated (*c.c.*) states. Moreover the families possess very different mass scales from a few MeV for up- and down-quarks to 180 GeV for the top-quark [Y+06]. In that sense a classification of the quarks into light (*uds*) quarks and heavy (*sct*) quarks is obvious and useful for later discussions. The standard model describes the three fundamental forces between the 12 fermions (spin 1/2-particles) via the exchange of gauge bosons (spin 1-particles) for the strong, weak and electromagnetic interactions. These are known as gluons g for the strong force, as W and Z bosons for the weak force and as γ boson for the electromagnetic force.
For the theory of the strong interactions (quantum chromodynamics, QCD) one of the ideal experimental setups is deep inelastic scattering of leptons on nucleons where the photon (γ) is utilised as a probe of the nucleon. Deep inelastic scattering experiments played a major role for the measurement of the nucleon structure, which is dominated by QCD effects. These experiments started as fixed target experiments at low centre-of-mass energies. Due to the fixed-target setup the available centre-of-mass energy increased only slowly for these kind of experiments. HERA[1], where an electron and a proton beam have been collided, allowed the access of much higher energies that would not have been possible with fixed target experiments. For these an electron beam energy of 50 TeV would have been needed to reach the HERA centre-of-mass energy of 320 GeV which is even nowadays far from trivial. Moreover HERA has confirmed many aspects of the standard model and in particular of QCD with a high experimental precision. One of the highlights are the precise structure function data utilised by global analyses for the determination of proton parton density functions (PDF). These structure function data is only indirectly sensitive to the gluon density of the proton. A precise knowledge of the parton density distributions is of great importance for the Large Hadron Collider where two collimated proton beams or basically two highly collimated parton beams are collided at highest centre-of-mass energies of 14 TeV. Many new phenomena are expected at an energy scale of a few TeV because of certain shortcomings of the standard model that concern for instance the very high energy behaviour, the origin of matter, the origin of mass & families. To overcome these problems a variety of extensions to the standard model exist, which are expected to be observable at a scale the LHC[2] is able to reach.

[1] Hadron-Elektron-Ring-Anlage
[2] Large Hadron Collider

1.1. Motivation of the present Measurement

The measurement of heavy flavor or charm production in deep inelastic scattering (DIS) at the electron-proton collider HERA is of particular interest for dedicated tests of perturbative QCD (pQCD). Experimentally heavy charm-quarks are identified via the decay of the D^* meson into charged particles, which allows the measurement of the production cross section of D^* mesons. The large charm mass provides a hard scale for reliable pQCD predictions, although difficulties arise from the additional hard scales, which are provided by the photon virtuality Q^2 and the transverse momentum $p_T(D^*)$. However, in the context of the present analysis one can distinguish between two strategies: a precise experimental cross section restricted to a detector acceptance confronted with a theoretical prediction, which inherits large errors from the phase space restriction during the calculation; the other strategy is to extrapolate the experimental measurement to the full phase space, which involves large uncertainties usually assigned to the experimental error. However, a precise theoretical prediction is calculable for the full phase space. These two strategies have been pursued in the present analyses and are discussed shortly in the following.

High statistic D^* Cross Sections

The D^* cross section data in DIS provides a scale, which is in between the two different heavy flavor schemes[3] where either the charm-quarks are treated completely massless valid for $Q^2 \gg m^2(c)$ (ZM-VFNS) or massive most applicable at threshold $Q^2 \lesssim m^2(c)$ (FFNS) and thus ideally suited to study pQCD predictions in a certain scheme[4]. In order to get a handle on these various theoretical schemes for the heavy flavor treatment in pQCD differential or double-differential D^* cross section measurements as presented in this analysis are helpful to further understand the underlying threshold and mass effects. The full available HERA II data statistics allows the determination of precise

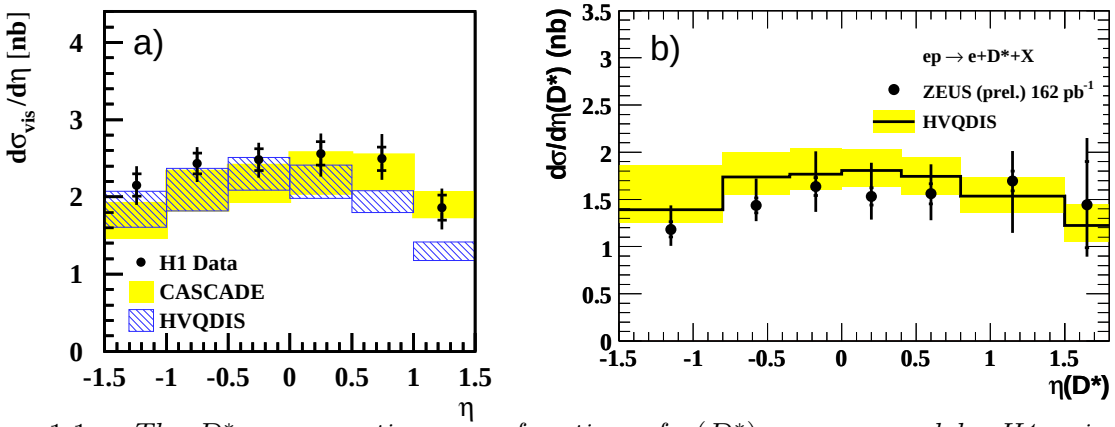

Figure 1.1.: *The D^* cross section as a function of $\eta(D^*)$ as measured by H1 using the luminosity of the whole HERAI data taking (left) and from ZEUS as measured using the luminosity of the years 2003 – 2005 (right) [Z+07].*

cross section data. These are utilised to further understand regions of the phase space

[3] These schemes are also applicable to b- and t-quarks.

[4] In addition there exist schemes with interpolating features known as GM-VFNS which give good descriptions of photoproduction data.

where previous measurements have observed an excess compared to the NLO QCD predictions. This is for instance the case for the $\eta(D^*)$ cross section measurement, which is depicted in figure 1.1a) for the last H1 publication [A+07] and in b) for the latest ZEUS preliminary result. The interesting region is the forward ($\eta(D^*) > 0$) region where H1 starts to see a small deficit of the HVQDIS NLO prediction compared to data. This effect is not so clear for ZEUS even in a more forward going measurement [Z+07]. However, the NLO QCD prediction used by ZEUS utilises a proton PDF derived from data, containing also DIS F_2^c measurements and thus the ZEUS PDF is made to better describe the data by construction. This is not the case for the CTEQ5f3 proton PDF [L+00], which was used by H1.
To some extend differences between PDFs are related to the treatment of heavy quark mass effects in the global analyses of the PDF fitter groups. A global fit of the inclusive structure function data to obtain the PDFs of the proton relies, amongst others, on a correct theoretical treatment of charm quark production in DIS. In particular the size of the strong coupling constant α_s makes it difficult to achieve reliable pQCD calculations, because the next higher order might still be non-negligible, i.e. the perturbation series does not converge fast. In order to account for this several heavy flavor schemes have been developed, which are different in the treatment of mass effects. As a drawback these schemes enter global fits of parton distributions and accordingly they influence the light parton distributions. By that predictions from different PDF sets

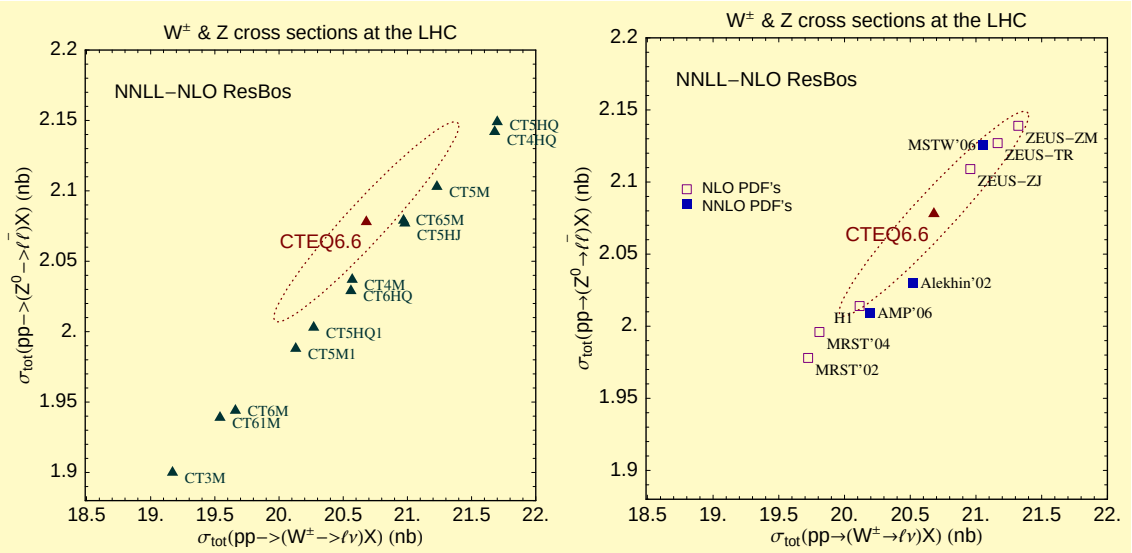

Figure 1.2.: *Predictions for $W^{\pm}$ and Z^0 production at the LHC using different proton PDFs of the CTEQ collaboration (left). The CTEQ61m implements a massless scheme, while the CTEQ65m predictions implements a general mass scheme as explained in the text. The right figure shows the comparison of the CTEQ PDFs to PDFs from other groups. Plot taken from [Nad08].*

can change by more than the individual stated error of a single PDF set as displayed in figure 1.2 (left) illustrating the influence of the heavy quark treatment on cross section predictions [Nad08]. The predictions for $W^{\pm}$ and Z^0 production at the LHC are depicted for different proton PDF sets where for instance CTEQ6 and CTEQ61m [P+02]

use a zero-mass prescription and CTEQ65m [T+07] implements a general-mass scheme incorporating heavy quark mass effects. Although the LHC centre-of-mass energy is far away from the c-quark production threshold, the treatment of charm production at the threshold influences the high scale behaviour significantly.

Extraction of the Charm content $\mathbf{F_2^c(x, Q^2)}$ of the Proton Structure

The only ep collider HERA operating at high centre-of-mass energies provides the ideal kinematic conditions for measurements of the structure function of the proton at small x in a wide range of Q^2. Moreover the measured differential D^* cross sections can be used to derive the charm contribution to the proton structure: $F_2^c(x, Q^2)$. Charm contributes up to 30% to the total structure function F_2^p at small Bjørken x, which has been observed in previous measurements at HERA [A+02]. Figure 1.3 illustrates the extracted F_2^c from D^* cross section data utilising a luminosity of $\mathcal{L} = 18.6$ pb^{-1} for the DGLAP evolution scheme (left) and for the CCFM evolution scheme (right). The data

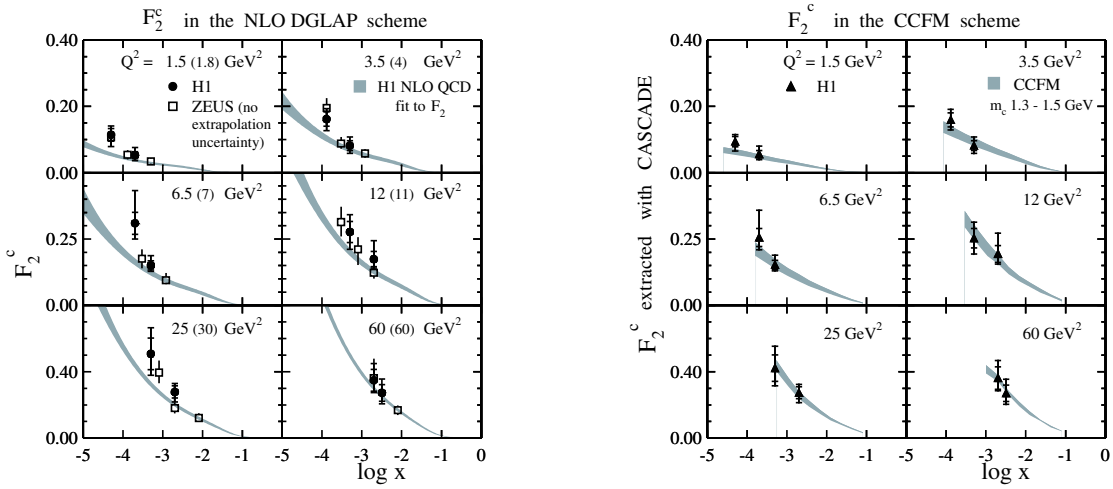

Figure 1.3.: *The derived charm contribution F_2^c to the proton structure using a luminosity of $\mathcal{L} = 18.6$ pb^{-1} for the DGLAP evolution scheme (left) and for the CCFM evolution scheme (right). For the H1 measurement a extrapolation uncertainty (outermost error) is assigned and added in quadrature on top of the experimental errors. The theory prediction uses a uncertainty band where the exact parameters are described elsewhere [A+02]. The left plot includes results from the ZEUS collaboration.*

are compared to the theory prediction of the model adopted for the extraction and illustrate a reasonable description. The amount of statistics included in the present analysis of D^* cross section data and the extraction of F_2^c uses a luminosity of $\mathcal{L} = 347$ pb^{-1} which is a factor of 18 larger. Nevertheless in order to have an impact on the global analyses of parton distribution functions performed by the fitter groups (e.g. CTEQ, MSTW, GJR) the data must have the highest possible precision in order to compete with the inclusive structure function measurements. Due to the increased

precision of the D^* cross section measurement also the present F_2^c measurement gains in terms of systematic errors compared to the previous H1 publication and further constrains the partonic structure of the proton.
In addition the charm production at HERA offers the possibility to extract the gluon distribution in the proton from a measurement of F_2^c, which can be confronted with the prediction from the global analyses where the gluon distribution is derived from the scaling violations at small Bjørken x.
One of the highly non-trivial tests of perturbative QCD is the comparison of the gluon density derived from inclusive $ep \to eX$ processes with the gluon initial state of the reaction $ep \to eD^*X$ and its consistency. The experimental access to the gluon initial state can be done via the measurement of F_2^c or via a direct measurement of the gluon density as done by H1 in 1998 [A+99] where D^* mesons are utilised as a probe to test the gluon density. These comparisons are from the theoretical point of view complex as different model assumptions are involved.

Organisation of the Thesis

The thesis is split up into two large parts. The physics analysis of D^* production in deep inelastic scattering is discussed in part one with chapters 2 to 13 where the first three chapters give the theoretical and experimental introduction to the measurement. A short overview of charm tagging methods utilised at H1 is added in chapter 5 where also the different reconstruction methods for the event kinematics are introduced and an optimal choice of the reconstruction method for the present analysis is motivated. By means of control distributions discussed in chapter 7 a good description of the selected event sample, as described in chapter 6, is ensured. The cross section determination and its features is covered by chapter 8 and followed by a detailled discussion of the studied systematic error sources in chapter 9. Finally the measured D^* cross section data are presented and compared to various pQCD predictions in chapter 10. Preliminary results of the D^* cross section measurement have been presented at [Jun08a; Jun08b]. The tables providing the measured single and double-differential cross section data with the statistical and systematical errors are given in appendix 15.6. Furthermore the cross section data are utilised to derive the charm contribution, F_2^c, to the proton structure where detailled studies and the results are discussed in chapter 11. Before drawing a conclusion of the present measurement, studies for an extended phase space of the D^* cross section measurement are presented, which help to solve several drawbacks of the F_2^c extraction. Results of these studies are discussed in chapter 12.
The second part of the thesis or chapters 14 and 15 is devoted to the hardware project successfully completed in the scope of the thesis. The hardware project consists of the commissioning and optimisation of the third level of the H1 Fast Track Trigger. A detailled discussion of the level three concept and its realisation is given. It is followed by a discussion of the performance that finally has been achieved for the FTT trigger system. In order to use the hardware like FTT simulation in a comfortable way, H1 has developed a post-processing scheme for the MC production. This required the re-simulation of the H1 central trigger simulation, which has been implemented within the FTT simulation. Results and the scheme implemented are discussed in chapter 14.

Results of the hardware project have been presented at [J+07] and will be published in a Nuclear Instruments and Methods paper.

Part I.

Measurement of the D^* Meson Production Cross Section and Extraction of $\mathrm{F}_2^{\mathrm{c}}(\mathrm{x}, \mathrm{Q}^2)$

2. Deep Inelastic electron-proton Scattering

In deep inelastic scattering (DIS) the interaction between the electron[1] e and proton p can be described by the exchange of virtual bosons. The process allows the measurement of the static and dynamic structure of the proton. The virtual bosons can be mediators either of the electromagnetic force or of the weak force. A Feynman graph of the lowest order DIS process is displayed in figure 2.1a) and b). It depicts the incoming electron with four-momentum $\mathbf{k}$, the virtual boson carrying a four-momentum $\mathbf{q}$ and the proton which carries a four-momentum $\mathbf{P}$. Thus the proton is probed with a four-momentum transfer squared $-q^2 = Q^2$ or virtuality. Depending on the mediating

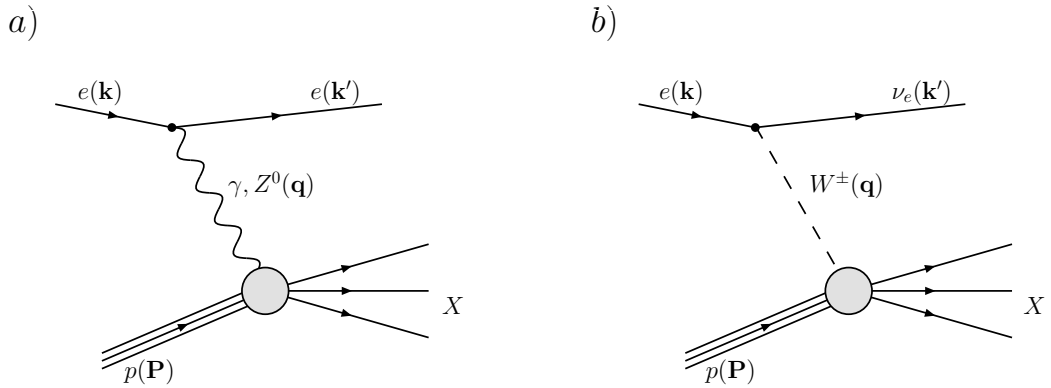

Figure 2.1.: *The leading order Feynman diagram for deep inelastic electron proton scattering (Bold letters indictate the four-momentum of a particle.). The exchanged virtual boson can be, depending on the four-momentum squared $-q^2 = Q^2$ of the interaction, a photon (γ) or Z^0 for the neutral current or a $W^\pm$ for the charged current.*

force the final state of the incoming electron can change. In case the mediating boson is a photon (γ) or a Z^0 (neutral current, NC) an electron can be observed as the final state. In case of the $W^\pm$ (charged current, CC) bosons the neutrino ν_e can not be directly observed. Due to the large mass of the weak force bosons, which enters a cross section calculation via the propagator, contributions from the weak force are strongly suppressed and negligible at a four-momentum transfer of $Q^2 \ll m^2(W^\pm, Z^0)$.

Next-to-leading order QED Corrections in DIS

The standard DIS NC process with the one-photon exchange as illustrated in figure 2.1a) is a QED leading-order (LO) process. Moreover higher orders of quantum electrodynamics (QED) have to be taken into account. The real next-to-leading (NLO) corrections in QED to the NC processes as depicted by the diagrams shown in figure 2.2 have to be considered. Furthermore there are virtual corrections at one-loop level

[1]The phrase electron is used as synonym for electron and positron.

QED which do also include electroweak corrections. These virtual graphs, which are dominated by the self-energy of the photon-line due to fermion-loops, can be included in the running of the electromagnetic coupling α_{em}.
For the real corrections one distinguishes between the initial state radiation (ISR) from

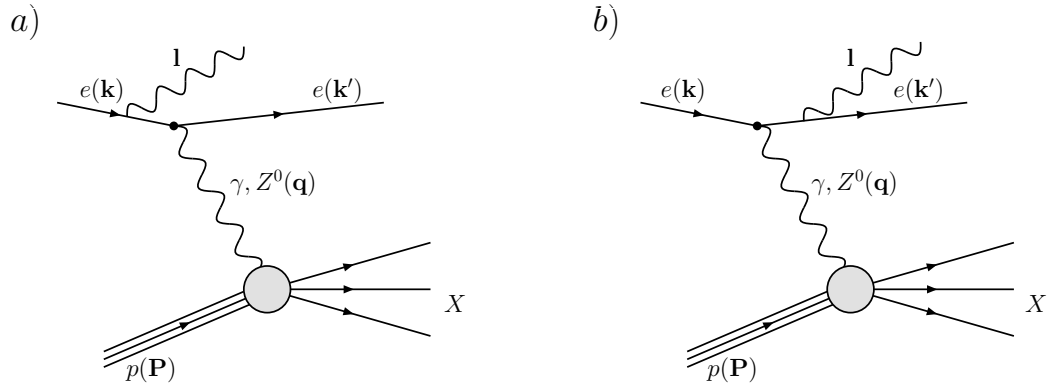

Figure 2.2.: *In deep inelastic scattering processes real next-to-leading order QED corrections to the cross section have to be considered: The initial state radiation (ISR) from the incoming electron line shown in a) and the final state radiation (FSR) from the outgoing electron line in b).*

the incoming electron and the final state radiation (FSR) from the outgoing electron. For the latter case the measurement of the electron is in most of the cases merged with the radiated photon since it is almost collinear to the electron. Events of this topology usually can not be distinguished experimentally from non-radiative events and have to be taken in account by the underlying model. The initial state radiation lowers the electron energy available for the interaction by $1 - E_\gamma/E_e$. Naturally both types of radiation influence the selection of DIS events and the cross section calculation. Therefore they are considered for the correction of the detector effects as it is explained in sections 4.1 and 8.2.

2.1. Kinematics

The ep scattering process $e+p \to e(\nu_e)+X$ is completely described with three Lorentz-invariant variables. Usually these are the Bjørken scaling variable x, the inelasticity y of the event and the four-momentum transfer squared Q^2 defined in the following way from the in and outgoing four-momenta of the electron:

$$Q^2 := -q^2 = -(\mathbf{k} - \mathbf{k}')^2 \ . \tag{2.1}$$

The dimensionless scaling variable Bjørken x can be interpreted as the fractional momentum of the proton which is carried by the struck quark:

$$x := \frac{Q^2}{2(\mathbf{p} \cdot \mathbf{q})}, \ 0 < x < 1 \ . \tag{2.2}$$

The limes of elastic scattering is approached for values of $x \to 1$. The second scale variable is y, which describes the relative energy loss of the electron in the proton rest

frame system, i.e. the energy fraction carried by the photon. y is a measure for the inelasticity of the scattering process and is defined by:

$$y := \frac{(\mathbf{p} \cdot \mathbf{q})}{(\mathbf{p} \cdot \mathbf{k})},\ 0 < y < 1\ . \tag{2.3}$$

The centre-of-mass energy is defined by the square root of the Mandelstam variable s:

$$s := (\mathbf{k} + \mathbf{p})^2\ , \tag{2.4}$$

With these definitions and neglecting the rest masses of the particles the square of the four-momentum transfer is given by:

$$Q^2 = sxy\ . \tag{2.5}$$

The photon-proton centre-of-mass energy is called $W_{\gamma P}$ and defined by:

$$W^2_{\gamma P} := ys - Q^2 + m_p^2\ . \tag{2.6}$$

For a fixed centre-of-mass energy s only two of the introduced quantities are independent and have to be measured in order to deduce the full event kinematics (see section 5.4).

Definition of the Inclusive ep Cross Section

The deep inelastic *ep* cross section for the neutral current one-boson exchange, is called cross section in *Born approximation* (Born level). For deep inelastic scattering the Born level cross section, neglecting the masses of the incoming particles and contributions from the exchange of Z^0 or $W^\pm$ bosons (allowed for $Q^2 \ll m^2(W^\pm, Z^0)$), is defined by:

$$\frac{d^2\sigma^{\mathrm{NC}}_{\mathrm{Born}}}{dxdQ^2} = \frac{2\pi\alpha^2_{\mathrm{em}}}{xQ^4} \cdot \left\{ \left(1 + (1-y)^2\right) \cdot F_2(x, Q^2) - y^2 \cdot F_L(x, Q^2) \right\}\ . \tag{2.7}$$

The quantity α_{em} denotes the QED coupling constant, while the two quantities $F_1(x, Q^2)$ and $F_2(x, Q^2)$ parameterise the structure of the proton and are called structure functions of the proton. They are related as follows:

$$F_2(x, Q^2) - 2x \cdot F_1(x, Q^2) = F_L(x, Q^2)\ . \tag{2.8}$$

The contribution of the so-called *longitudinal structure function* $F_L(x, Q^2)$ to the inclusive *ep* cross section is predominantly at high y. This contribution originates from virtual photons which can have in addition to the transverse polarisations also longitudinal polarisations. In a large part of the phase space F_L can be neglected and the proton structure is described by F_2 alone. For processes that involve large $Q^2 \sim m^2(W^\pm, Z^0)$ the contributions from the weak force can no longer be neglected. Therefore the weak force gives rise to the definition of the parity violating structure function $xF_3(x, Q^2)$ and for neutral current processes interference terms of the Z^0 exchange with the γ exchange enter the definition of $F_1(x, Q^2)$ and $F_2(x, Q^2)$.

Naïve Quark Parton Model of DIS

The results of early deep inelastic scattering measurements as depicted in figure 2.3a) were explained in the naïve quark parton model (QPM) [Bjo66; Bjo69; BP69] with a physical interpretation from Feynman [Fey69]. In this model the constituents of the proton are considered to be non-interacting quasi-free particles. The underlying picture is the *infinite momentum frame* (IMF) where the proton is moving fast, such that the mass of the proton is negligible. A schematic Feynman graph of the deep inelastic scattering process in the QPM interpretation is depicted in figure 2.3b). Deep inelastic

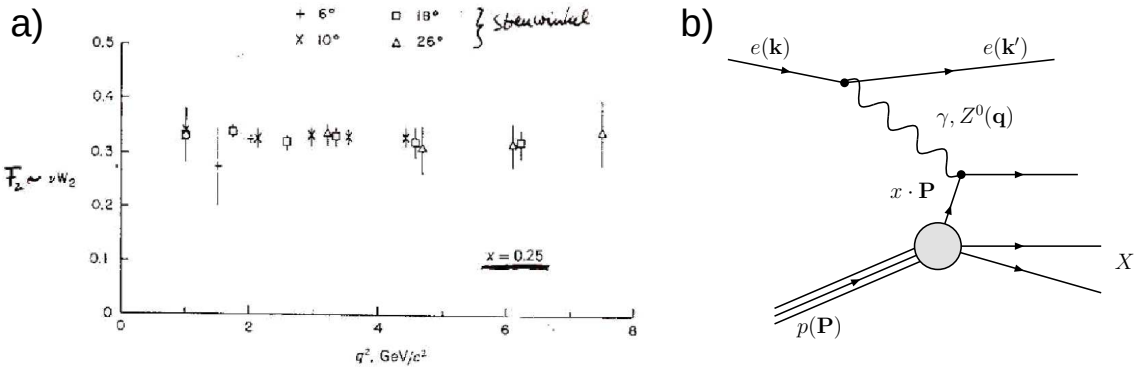

Figure 2.3.: *One of the first measurements of F_2 from fixed target experiments [FK72] at a fixed value of x a). The interpretation of the deep inelastic ep scattering process in the quark parton model as electron-parton scattering where the parton carries a fractional momentum x of the proton is illustrated b).*

electron-proton scattering in the IMF is described as elastic electron-parton scattering: The proton is interpreted as a loose cloud of point-like partons moving parallel with the proton and carrying momentum fractions x. These partons have later been identified with the three quarks of the proton necessary to explain the quantum numbers of the proton.
For partons with spin 1/2 the Callan-Gross relation [Cal70] uses the fact that a massless spin 1/2-particle can not absorb a longitudinally polarised virtual vector boson and consequently for non-interacting partons the longitudinal structure function $F_L(x, Q^2)$ is zero in the QPM:

$$F_2^{\mathrm{QPM}}(x, Q^2) - 2x \cdot F_1^{\mathrm{QPM}}(x, Q^2) = F_L^{\mathrm{QPM}}(x, Q^2) = 0 \ . \tag{2.9}$$

In this picture the structure functions $F_1^{\mathrm{QPM}}(x, Q^2)$ and $F_2^{\mathrm{QPM}}(x, Q^2)$ take the following form:

$$F_1^{\mathrm{QPM}}(x, Q^2) = \frac{1}{2} \sum_i e_i^2 f_i(x) \text{ and } F_2^{\mathrm{QPM}}(x, Q^2) = x \sum_i e_i^2 f_i(x) \ . \tag{2.10}$$

For each parton type of the proton the function $f_i(x)$ describes the probability to find a parton i carrying the fractional moment x_i. The electric charge of the parton i is given by e_i.
The structure functions can not be predicted by first principles and need to be measured. The result of deep inelastic scattering measurements [FK72] was interpreted to

be elastic electron-parton scattering, which explains all features of the measurement. The interpretation leads to the concept of scaling, meaning that there is no variation of the structure function with Q^2 whatsoever, or that the structure of the proton for a electromagnetic probe looks the same no matter how hard the scattering process was. Figure 2.3a) depicts the result of measurements of F_2 in deep inelastic scattering at a fixed value of $x \approx 0.25$ as function of Q^2, which indeed illustrate the scaling behaviour, i.e. a constant F_2. Already with improved fixed targets experiments significant deviations from the scaling behaviour have been observed [A+82] and the theoretical models confronted with these *scaling violations* had to be revised. Amongst others this led to the approach of *Quantum Chromodynamics* (QCD) with its key assumptions shortly summarised in the next section.

2.2. QCD based Model of Deep Inelastic Scattering

The basis of quantum chromodynamics is the concept of color and the underlying SU(3) symmetry group [FGML73; Wei73; GW73]. The color concept was introduced for the explanation of the wave function of the Δ^{++} meson (see [Y+06]) that needs to be asymmetric according to the Pauli principle. This wave function can only be constructed with a new degree of freedom in addition to space, spin and flavor: the color degree of freedom. Thus each quark carries color which is usually marked by an index $a = 1, 2, 3$ for the three colors. In contrast to the naïve quark parton model QCD incorporates interactions between the constituents of the proton mediated by the carrier of the strong force called gluons. These mediators are described in QCD as an octet of color-anti-color states.
Because of the non-zero probability that a quark emits a soft gluon the scaling behaviour of the proton structure function in the QPM is broken by logarithmic terms of Q^2 as higher and higher Q^2 resolve more and more partons. In addition gluons can split into $q\bar{q}$ pairs enhancing the quark content at small x even further. At the ep-collider HERA F_2 has been measured over a wide range of x and Q^2 with unprecedented precision. The F_2 proton structure function extracted from the inclusive neutral current cross section data is illustrated in figure 2.4a) utilising the data taken with the H1 detector in $1994 - 2000$. In addition the data from the early fixed target experiments at lower Q^2 and higher x values are depicted. For comparison also the H1 PDF 2000 fit is shown.
These structure function data are used to derive parton density functions from global fits, where also other data can be incorporated. Thus quark and gluon densities, as shown in figure 2.4b), are very well known to low x, while the gluon density is significantly less known. This is contributed to the fact that the gluon density, which is derived from the scaling violations $\partial\alpha_s/\partial \ln(Q^2)$, is only indirectly constraint from the fits to the inclusive F_2 structure function data. At high x the valence quark distributions dominate, while at low x the sea quark and, at most, the gluon densities dominate.

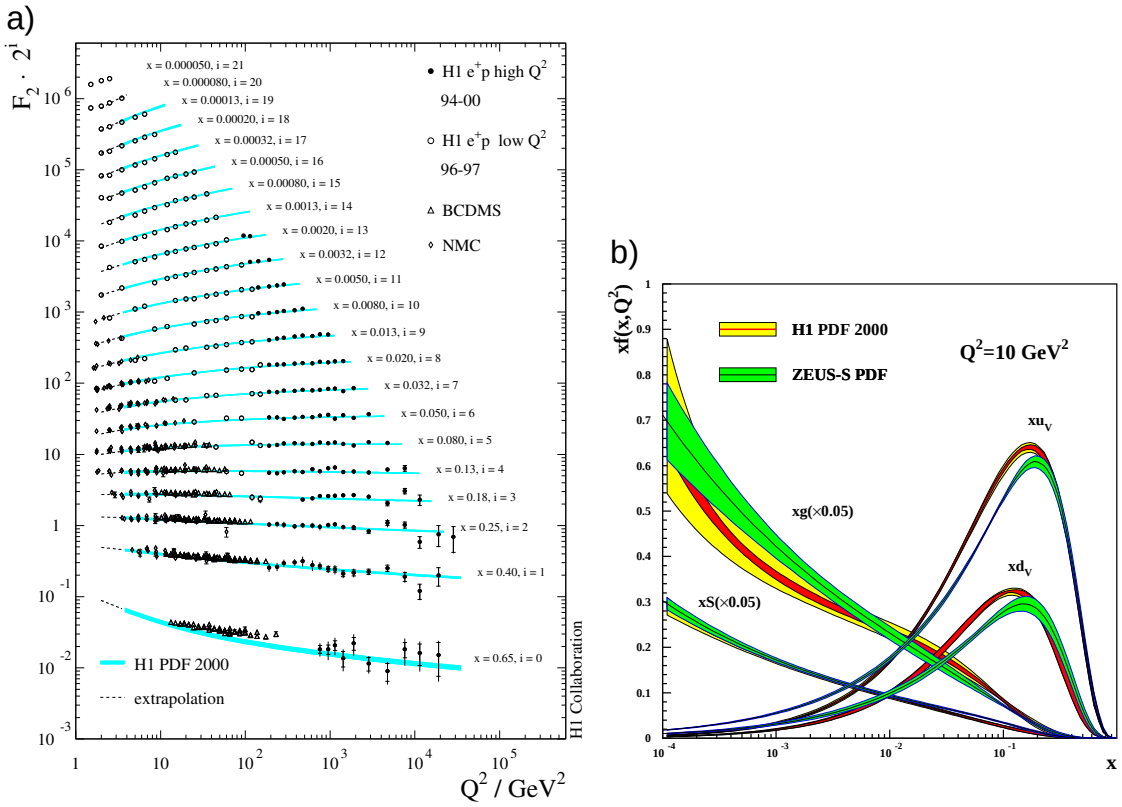

Figure 2.4.: *The proton structure F_2 a) for the combined $1994-00$ H1 e^+p (solid points) and previously published low Q^2 (open circles) data. The results are compared with the H1 PDF 2000 fit (error bands). Earlier fixed target data are added (BCDMS and NMC). The parton density functions derived from global analyses of structure function data are shown in b). Taken from [A+03].*

The Strong Coupling Constant

For the calculations of the QED or QCD coupling strength so-called *UV-divergences* arise from the fact that in quantum field theories as QED and QCD the propagator is corrected by closed fermion loops, or additionally in QCD: gluon loops. The momenta in loops are not restricted by any conservation law and lead to infinities if the integration over the whole momentum space is carried out. These un-physical infinities are removed by a method called renormalisation that introduces unmeasurable *bare* theoretical quantities. The measurable quantities are then defined after the renormalisation of a theory which depends now on the renormalisation scale parameter μ_r. Due to the renormalisation the coupling constants are no longer constant, i.e. depend on the ratio Q^2/μ_r^2 and are so-called effective *running couplings*. The special behaviour of the effective coupling constants can be further expressed by the renormalisation group

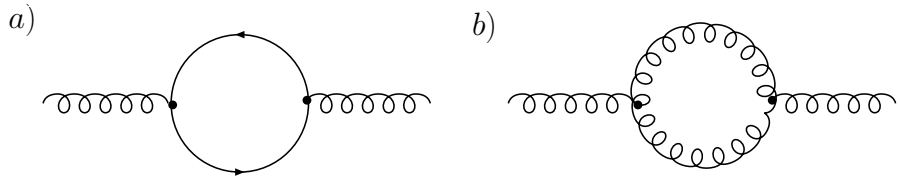

Figure 2.5.: *The $O(\alpha_s^2)$ loop corrections to the gluon propagator in QCD. a) shows the fermion-loop whereas b) shows the gluon-loop.*

equation (RGE) neglecting effects from the quark masses[2]:

$$\mu_r^2 \cdot \frac{\partial \alpha_s(\mu_r)}{\partial \mu_r^2} = \beta(\alpha_s(\mu_r)) \tag{2.11}$$

The RGE reflects the fact that for a quantum field theory the coupling does not depend on a certain gauge. For QCD the value of the strong coupling α_s at an arbitrary scale $\mu^2 = Q^2$ in the one loop approximation ($O(\alpha_s^2)$) is defined by:

$$\alpha_s(\mu_r^2) = \frac{1}{\beta^0 \cdot \ln(\mu_\mathrm{r}^2/\Lambda_\mathrm{QCD}^2)} \text{ with } \beta^0 = \frac{33 - 2 \cdot n_\mathrm{f}}{12\pi} \ , \tag{2.12}$$

where β^0 is the first coefficient in the perturbative expansion of the β function. The parameter Λ_QCD determines the scale where the running coupling becomes strong and n_f denotes the number of quark flavors. As there are six quark flavors β^0 is negative and stays negative up to 16 quark flavors in contrast to the β function in QED, which is positive. However, at a larger scale μ the effective coupling α_s decreases like the inverse power of $\ln(Q^2)$, which is also known as *asymptotic freedom* [GW73]. This remarkable feature of QCD is different to QED where the behaviour of the effective coupling is opposite, i.e. the effective coupling at low scales goes to α_em compensating for the fact that there are more and more soft photons. The RGE shows that the effective coupling in QED grows with increasing scales.
The parameter Λ_QCD in equation 2.12 refers to the fact that pQCD gives the scale dependence but not the absolute value of the scale itself and furthermore it determines the scale where pQCD is no longer valid because the next higher order is of comparable size to the one calculated. As the measured value[3] of Λ_QCD is around 200 MeV perturbative QCD breaks down at the mass scale of light hadrons. This might explain the *confinement* of quarks in the same spirit as the *asymptotic freedom* is explained.
In addition to the discussed UV-divergences there are other divergences arising in the calculation, for instance the *collinear divergences*. They arise if the gluon is emitted parallel (collinear) to the quark $k_T = 0$ which gives a singularity due to $1/k_T^2$ terms. It corresponds to the so-called long distance part of the strong interaction which is not calculable in perturbative QCD at all. As in the running of the coupling where the UV-divergences are hidden into a unmeasurable bare coupling at a renormalisation

[2]If quarks are treated massive additional terms enter the RGE and by solving it so-called running-masses $m(Q^2)$ are obtained.
[3]For all practical purposes natural units with $c = h = 1$ are used.

scale μ_r the collinear divergences are absorbed into a bare parton distribution $q_0(x)$ at some *factorisation scale* μ_f.

Factorisation and Evolution Schemes in DIS: DGLAP, BFKL and CCFM

The use of perturbative methods in QCD is based on the separation of short-distance (high-momentum) perturbative effects from long-distance (low-momentum) non-perturbative effects – a process which is known as factorisation. It is a fundamental property of the theory that the long and the short-distance part of the interaction can be factorised [CS87]. Although the proof exists only for a few processes, factorisation is assumed also for other processes. In section 2.3 the factorisation is explained in more detail for the heavy quark production, which is the topic of the present analysis. Furthermore factorisation is done in a distinct factorisation scheme like the DIS or $\overline{\text{MS}}$ scheme. In the DIS scheme all gluon contributions are absorbed into the quark distribution, while in the $\overline{\text{MS}}$ scheme only the collinear divergence is factorized out. The $\overline{\text{MS}}$ scheme is used for global analyses of parton distribution functions by fitter groups like MRST/MSTW or CTEQ (e.g. [T+07]). In order to simplify the calculations and for practical reasons in most applications the factorisation and renormalisation scale are treated to be the same: $\mu_f = \mu_r := \mu$.
The factorisation theorem allows the separation of the hard matrix element from the proton PDF and permits the use of measurements of the parton density as function of x at a scale Q_0^2 as input for general evolution equations. This method enhances the power of perturbative QCD enormously, because the evolution equations can be used to evolve the parton density functions to any scale. The different evolution schemata and their evolution in the $x - Q^2$ plane are sketched in figure 2.6a) together with the initial starting scale Q_0^2 and $ln(1/x_0)$ indicated by the dashed-dotted lines. The direction of evolution of the different evolution schemes provides also a certain ordering of the radiated partons, e.g. an evolution in Q^2 is ordered in k_T.

DGLAP The DGLAP evolution scheme is based on the work of Dokshitzer, Gribov, Lipatov and Altarelli, Parisi [Dok77; GL72; AP77] and provides an evolution prescription for the parton dynamics in Q^2. These prescription is realised via coupled integro differential equations:

$$\frac{\partial q_i(x,Q^2)}{\partial \ln Q^2} = \frac{\alpha_s(Q^2)}{2\pi} \cdot \int_x^1 \frac{d\xi}{\xi} \left[P_{qq}\left(\frac{x}{\xi}\right) q_i(\xi,Q^2) + P_{qg}\left(\frac{x}{\xi}\right) g(\xi,Q^2) \right] ,$$

$$\frac{\partial q_i(x,Q^2)}{\partial \ln Q^2} = \frac{\alpha_s(Q^2)}{2\pi} \cdot \int_x^1 \frac{d\xi}{\xi} \left[P_{gq}\left(\frac{x}{\xi}\right) q_i(\xi,Q^2) + P_{gg}\left(\frac{x}{\xi}\right) g(\xi,Q^2) \right] . \quad (2.13)$$

In leading-order α_s four splitting functions $P_{ab}(x/\xi)$ are used to describe the dynamic behaviour of the partons. The incident parton b with momentum fraction ξ radiates a new parton a with momentum fraction x as shown in figure 2.7. Certain sum rules ensure momentum and flavor conservation for the splitting functions. Due to the requirement that the momentum fraction x of the radiated

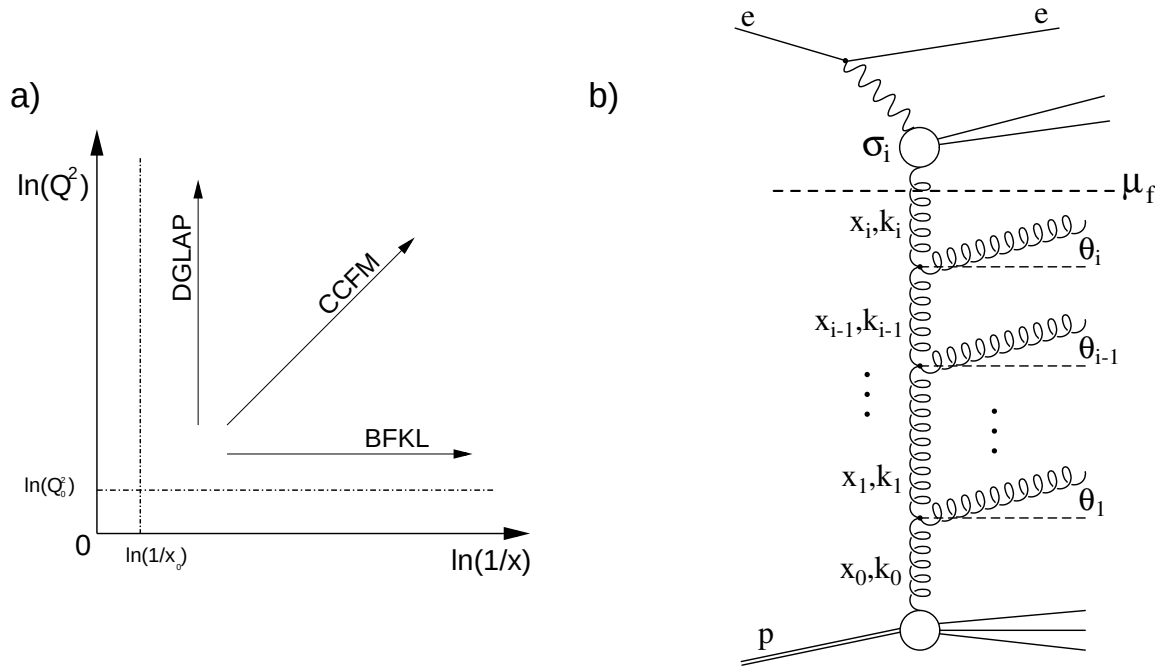

Figure 2.6.: *Figure a) shows the different evolution schemes and their direction in the $x - Q^2$ plane. The starting scale is indicated by the dashed dotted line for $ln(Q_0^2)$ and $ln(1/x_0)$ (Graph according to [KSD03]). The gluon ladder diagram of the QCD parton evolution shown in b) with the longitudinal momenta x_i, the transverse momenta k_i and the emission angle θ_i. The hard matrix element σ_i is separated from the evolution by the factorisation scale μ_f.*

parton is always smaller than the incident one, integrations can be carried out from any given non-zero x_0 starting point. The partons used in the gluon ladder as depicted in figure 2.6b) are strongly ordered in transverse momentum $k_{i,T}$: $Q^2 \gg k_{i,T}^2 \gg \ldots \gg k_{1,T}^2 \gg Q_0^2$. The DGLAP ansatz uses explicitly that the radiated partons are collinear to the incident ones, i.e. the longitudinal momentum fraction x_i is large compared to the transverse momentum k_T. Owed to this fact it is expected that the DGLAP evolution scheme fails at small x where k_T approaches values of the same order as x. By the evolution in Q^2 DGLAP resums terms proportional to $\ln^n(Q^2)$ but misses the rising contribution at very low x from large terms proportional to $\ln^n(1/x)$.

BFKL At small x values of 10^{-5} the term $\ln(1/x)$ can be treated as *large logarithm* and a re-summation of these large logarithms to all orders is applicable. This is implemented in the BFKL-scheme [BL78; KLF77] where the parton emissions are strongly ordered in the longitudinal momentum x_i: $x \gg x_i \gg \ldots \gg x_1 \gg x_0$, which describes the very low x regime by evolving x at fixed Q^2. However, BFKL is not able to describe the higher x regime. The BFKL evolution is not used in the present analysis.

CCFM A scheme, which combines the low x behaviour from the BFKL evolution and the high Q^2 behaviour from DGLAP, is the CCFM evolution scheme [Cia88;

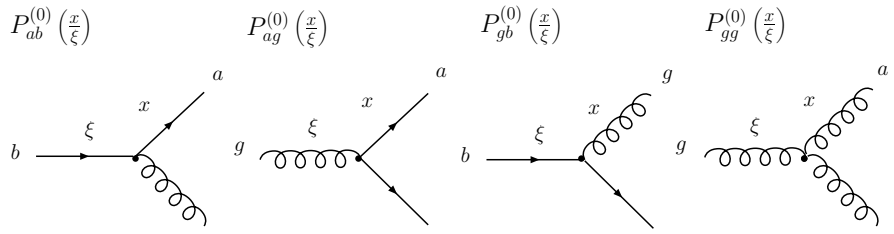

Figure 2.7.: *Each of the splitting functions $P_{ab}(x/\xi)$, shown with their corresponding process graph, describes the behaviour of an incident parton b radiating a new parton a.*

CFM90b; CFM90a; Mar95], which provides an evolution in x and Q^2 and resums terms in $\ln(1/x)$ and $\ln(Q^2)$ to all orders.
At small x the result of the CCFM evolution approaches the one from the BFKL evolution scheme which should be more appropriate at small x. The emission is strictly ordered in the angle θ_i as illustrated in figure 2.6b) which corresponds to an ordering in x and k_T: $Q^2 \gg k_{i,T}^2 \gg \ldots \gg k_{1,T}^2 \gg Q_0^2$ and $x \gg x_i \gg \ldots \gg x_1 \gg x_0$. However, for small angles and not too small x the same ordering as in DGLAP is achieved. Due to the k_T factorisation implemented in CCFM the k_T of a parton can be of the order of the k_T of the hard subprocess, thus it can not be neglected. CCFM provides partons with an intrinsic k_T that are expected to change the transverse momenta of the final state particles.

Even though HERA reaches very low x a clear break-down of the DGLAP scheme has not been observed, but there are indications that DGLAP indeed shows deficiencies for special event topologies like forward jet production. A recent H1 publication on three- to four-jet production at low x [A+08c] observes a better description of the data by the color dipole model [Lon95; AGLP89; Lon92] using gluons carrying un-ordered intrinsic k_T.

2.3. Heavy Quark Production Mechanisms in ep Scattering

The heavy quark production in DIS at HERA is dominated by the interaction between the exchanged virtual photon and a gluon from the proton side $\gamma g \rightarrow c\bar{c}$, the boson-gluon-fusion (BGF) process. In the following only c-quarks are mentioned here, although the theoretical concepts are applicable also for b-quarks. Because of the BGF process the measured charm cross section is directly sensitive to the gluon density in the proton.
The lowest order Feynman diagram for the direct BGF process of charm production is the first diagram shown in figure 2.8a), which corresponds to a next-to-leading order process in inclusive DIS. At small photon virtualities the so-called hadronic component of the photon emerges and produces a resolved contribution to the charm production. The present analysis uses a range in virtuality of $Q^2 > 5$ GeV^2 which suppresses the resolved component such that it is completely negligible [A+07]. Figure 2.8b) shows the direct process of charm production and highlights the theoretical ingredients and

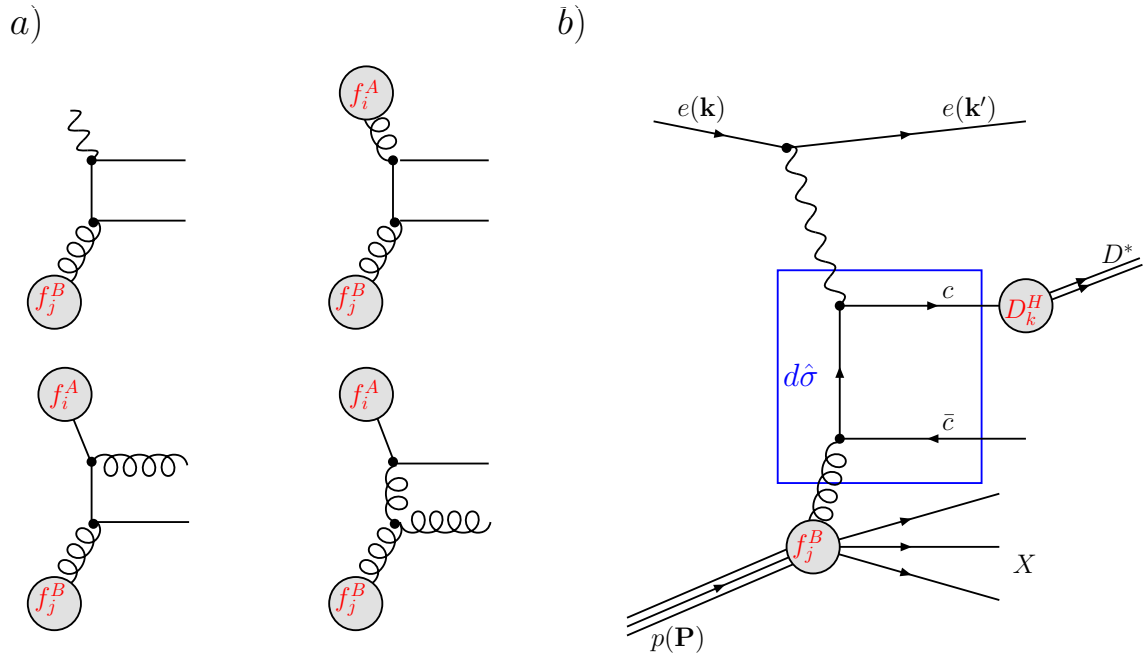

Figure 2.8.: *The leading order heavy quark boson-gluon fusion process for the direct production of the $c\bar{c}$-pair is the first diagram shown in a). In addition to this direct process there are also resolved processes where the photon has a hadronic structure indicated by a photon PDF f_i^A; the corresponding Feynman diagrams for resolved and excitation processes are also shown in a). Figure b) gives a theoretical picture of the direct BGF graph, which is explained in detail in the text.*

concepts needed for the calculation of charm production. A fundamental ingredient for the theoretical understanding of the production of D^* mesons or in general heavy hadrons is the factorisation theorem [Col98]. It has the following form:

$$d\sigma = \sum_{i,j,k} f_i^A(x_1, \mu_f) \otimes f_j^B(x_2, \mu_f) \otimes d\hat{\sigma}_{ij\to kX}(\mu_f) \otimes D_k^H(z, \mu_f) \ . \tag{2.14}$$

where the parameters for the calculation of the cross section $d\sigma$ are determined by:

- $d\hat{\sigma}(\mu_f, \alpha_S(\mu_r), \left(\frac{m_c}{p_T}\right))$: Matrix element of the hard scattering process of the partons i and j which is perturbatively computable. The long distance part of the interaction is removed by μ_f. The mass of the heavy quark m_c can be kept with a distinct heavy flavor scheme (see next section).

- photon PDF $f_i^A(x_1, \mu_f)$ and proton PDF $f_j^B(x_2, \mu_f)$: Probability to find partons i and j in the photon and proton provided by universal photon and proton PDFs (photon PDF only for resolved processes, for the direct BGF process it is simply the γ exchange).

- $D_k^H(z, \mu_f)$: Probability to produce a colourless hadron H from the initial quark k with a relative momentum z parametrised as fragmentation functions

For reliable pQCD calculations a hard scale is needed. But due to the presence of many scales (Q^2, p_T, m_c) in these kind of processes the precision of the predictability of the theory is decreased. Depending on the scale involved in the process different heavy flavor schemes for the calculation of the process do exist. This schemes are explained in more detail in the following section.

Treatment of Heavy Quarks in perturbative QCD

The mass of the heavy quark that appears in the hard matrix element can be treated differently in perturbation theory. The scale involved in the process advocates the application of massive, massless or mixed heavy flavor schemes. This complicates the interpretations as well as calculations enormously and causes in addition misunderstandings. A simplified picture of the heavy flavor schemes is illustrated in figure 2.9 where the hard matrix element $d\hat{\sigma}$ shown in figure 2.8a) is interpreted in terms of the underlying theoretical concepts.

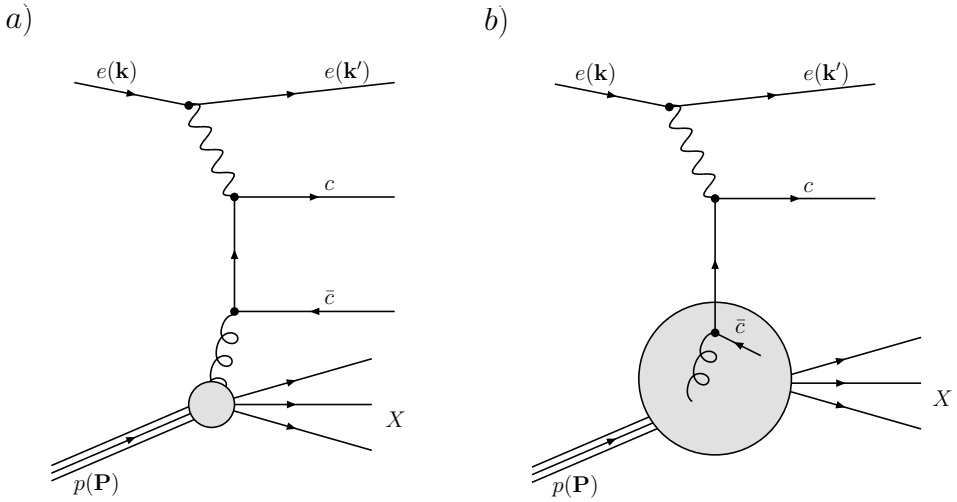

Figure 2.9.: *Heavy flavor schemes for the theoretical treatment of charm production where a) shows the perturbative production graph of massive charm quarks at production threshold via the BGF process, while b) shows the production graph of massless charm quarks valid far above the production threshold. More details are discussed in the text.*

FFNS The so-called *fixed flavor numbering scheme* (FFNS) assumes that only the light quark flavors ($q_i = u, d, s$) contribute to the dynamical structure of the proton as massless partons together with the gluons, i.e. the sum in equation 2.14 is up to the fixed number of flavors[4] $n_f = 3$. The massive charm quark relevant in the present analysis is thus produced entirely perturbatively as indicated in figure 2.9a). The heavy quark is treated in fixed order perturbation theory, i.e. at a finite order in perturbative calculation the FFN scheme inherits large logarithmic terms of the form $\log^n(Q^2/m_c^2)$ at order n of the perturbation series. Thus higher

[4]In case of bottom production also the c-quark is treated as light flavor.

order terms do not diminish and the perturbative expansion breaks down at higher scales. The FFNS is expected to describe data at threshold and at a scale μ^2 that is in the vicinity of m_c^2.

ZM-VFNS The region $m_c \to 0$ or $\mu^2 \to \infty$ is the domain of the *zero-mass variable* FNS (ZM-VFNS) [CG94; BKK98] where the light and heavy quarks are treated as massless partons. Thus the ZM-VFNS provides advantages for the calculation because the above mentioned large logarithms are absorbed into charm parton distribution functions and fragmentation functions at or close to a scale of m_c^2 as depicted in figure 2.9b) and are resummed to all orders by the DGLAP-evolution equations at higher scales. The ZM-VFNS is used in most conventional QCD parton model calculations. The flavors above $n_f = 3$ are switched on if $Q^2 > m_c^2$, by doing so the only left hard scale is Q^2. Exactly this behaviour causes unreliabilities or discontinuities at scales Q^2 of the size of the mass of the heavy quark m_c^2.

GM-VFNS In addition mixed schemes with a massive treatment at threshold and a massless treatment at high scales exist. Oversimplified the idea is to use the sum of the massive FFNS-term and the massless term from the ZM-VFNS and to account in a correct way the overlap term from gluon-splitting where the produced quark is collinear to the incident gluon. Such an ansatz is called *General mass*-VFNS where mass effects of the relevant partons are incorporated at the threshold region. The large logarithms from the mass at high scales $Q^2 \gg m_c^2$ are absorbed into a charm PDF and by that are resummed according to DGLAP like in the ZM-VFNS case. Different implementations of mixed schemes are available, which differ in the choice of theoretical assumptions and simplifications and are mentioned here for completeness only: ACOT [AOT94; ACOT94], ACOT(χ) [TKS02] and the Simplified-ACOT [KOS00] are used by the CTEQ group, whereas MRST/MSTW uses the mixed scheme [TR98b; TR98a].

From Quarks to Hadrons

As discussed in section 2.2 physically observable states are realised by the phenomenon of confinement that ensures that only colour neutral objects remain at observable time and distance scales. The outgoing partons from the hard interaction undergo a cascade of much softer interactions (fragmentation or hadronisation process) that lead to the formation of hadrons which are finally observed in a detector. This hadronisation process evolves at low scales where perturbative QCD can not be applied. Because of this lack of theoretical understanding phenomenological models are used to predict the hadronic final state of the parton interactions. For the present analysis the Lund string model [AM74; AGIS83] is utilised for the hadronisation of the light partons u, d, s.
The hadronisation of the charm quark to the heavy hadron: $c \to H(c\bar{q})$ can be split up in a part where pQCD in fixed order α_s according to the DGLAP evolution scheme is applicable and a part where only non-perturbative, i.e. phenomenological models are applicable. In order to describe this process several phenomenological functions are available: the *Peterson*-, *Kartvelishvili*- and *Bowler* fragmentation function

[Pet83; KLP78; Bow81] as defined in equations 2.15-2.17.

$$\text{Peterson} : D_H^c(z) \propto \frac{1}{z \cdot (1 - 1/z - \epsilon/(1-z))^2} \ , \tag{2.15}$$

$$\text{Kartvelishvili} : D_H^\alpha(z) \propto z^\alpha \cdot (1-z) \ , \tag{2.16}$$

$$\text{Bowler} : D_H^\alpha(z) \propto \frac{1}{z^{1+br_Q m_Q^2}} \cdot (1-z)^a \cdot \exp\left(\frac{bM_T^2}{z}\right) \ . \tag{2.17}$$

In the context of the analysis the Bowler and Kartvelishvili function using only one free parameter are of importance. All fragmentation functions describe the fraction z of energy (momentum) the produced hadron inherits from the initial quark state. The Bowler parametrisation utilises two free parameters a, b. Moreover m_Q denotes the mass of the heavy quark, $M_T = \sqrt{M_H^2 + p_T^2}$ is the so-called transverse mass with the mass M_H and transverse momentum p_T of the hadron and $r_Q = 1$ by default. Other fragmentation function parameters as adopted for the present analysis are discussed in section 4.1.

Properties of the Charmed Meson

Approximately one fourth of all charm quarks fragment into charged $D^{*\pm}$ mesons. The relative fragmentation probability was determined to be : $f(c \to D^{*\pm}X) = 0.224 \pm 0.028$ [Y+06]. In the present study the $D^{*\pm}$ meson is identified by the so-called *golden decay* channel:

$$D^{*\pm} \overset{(67.7\pm0.5)\%}{\longrightarrow} D^0 \pi^\pm_{\text{slow}} \overset{(3.8\pm0.07)\%}{\longrightarrow} K^\mp \pi^\pm \pi^\pm_{\text{slow}} \ , \tag{2.18}$$

where only charged tracks remain in the final state. Basic properties of the $D^{*\pm}$ meson are summarised in table 2.1. The selection of $D^{*\pm}$ mesons in the golden decay channel are further discussed in chapter 5.

name	value
Mass $m(D^{*\pm})$	(2010.0 ± 0.5) MeV
$I(J^P)$	$\frac{1}{2}(1^-)$
Full width Γ	96 ± 22 keV
Quark content	$(c\bar{d}) + c.c.$

Table 2.1.: Properties of the $D^{*\pm}$ meson taken from [Y+06].

2.4. The Charm Structure Function and the Connection to the Gluon Density

The charm contribution, $F_2^c(x, Q^2)$, to the proton structure is obtained by using the expression for the one-photon exchange cross section for charm production:

$$\frac{d^2\sigma^c}{dxdQ^2} = \frac{2\pi\alpha_{\text{em}}^2}{xQ^4} \cdot \left\{ \left(1 + (1-y)^2\right) \cdot F_2^c(x, Q^2) - y^2 \cdot F_L^c(x, Q^2) \right\} \ . \tag{2.19}$$

The longitudinal structure function $F_L^c(x, Q^2)$ contributes only at high y. At sufficiently high photon virtualities the production of charm quarks constitutes up to 30% of the total cross section [A+02]. The experimental and theoretical difficulties and the result of the extraction are explained in detail in chapter 11 and section 12.4. One of the intrinsic problems with these kind of measurements is the extrapolation to the full phase space needed to derive F_2^c. Even though this involves larger uncertainties compared to cross section data the charm structure function data can be utilised for global fits. Furthermore it can be utilised to extract a gluon density which can be compared to a gluon density derived from the scaling violation dependence: $\partial\alpha_s/\partial\ln(Q^2)$ of inclusive F_2 data.
If the D^* meson is measured as a final state and all theoretical implications arising

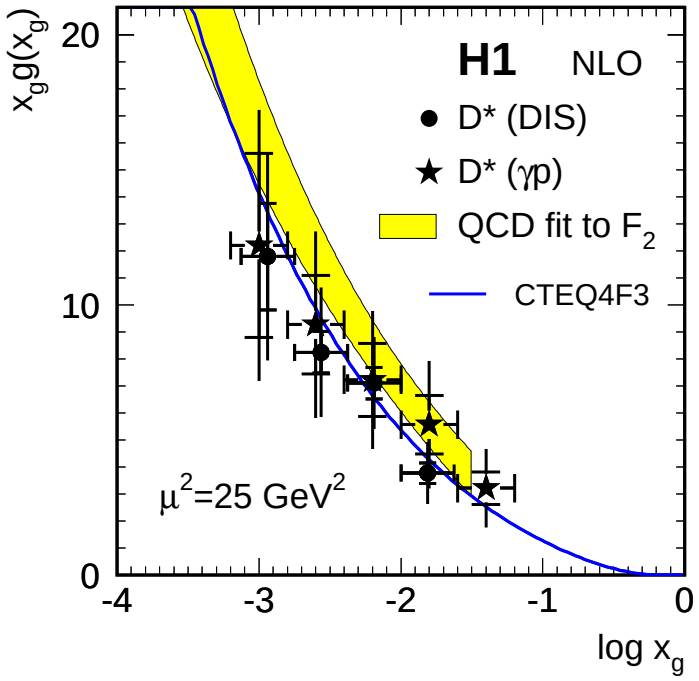

Figure 2.10.: *The gluon density as extracted from $D^{*\pm}$ meson measurement by H1 in DIS and photoproduction with a luminosity of* 9.6 pb^{-1} *at a average scale of* $\langle\mu\rangle = 25$ GeV^2 *[A+99] compared to the PDF used for the unfolding procedure and the gluon density as obtained by a QCD fit to the inclusive F_2 data.*

from massive heavy quarks in the calculation are considered, further insights on the gluon density are possible. As explained in section 2.3 the production of D^* mesons via the exclusive process $ep \to eD^*X$ is dominantly by the BGF process. Under the assumption that there is no or only a small contribution from intrinsic[5] charm the measurement of the exclusive process $ep \to eD^*X$ is directly sensitive to the gluon density. The H1 collaboration performed such a measurement in 1998 with an integrated luminosity of $\mathcal{L} = 9.6$ pb^{-1} and a statistical precision of $\sim 30\%$ [A+99]. The result for D^*

[5]Models exist which predict a non-zero charm density in the proton [BHPS80]. Unfortunately it contributes most at large x where the charmed hadron leaves the H1 detector through the beam pipe.

meson production in DIS ($Q^2 > 1$ GeV^2) and photoproduction ($Q^2 \sim 0$ GeV^2) at an average scale of $\langle \mu^2 \rangle = 25$ GeV^2 is illustrated in figure 2.10. The comparison is done to the PDF that has been used for the unfolding procedure and to the gluon density as obtained by a QCD fit to the inclusive F_2 data. Despite the large total error of up to 40% the measurement agrees quite well, although the data prefers in general the lower edge of the uncertainty band of the QCD fit to the inclusive F_2 data.

3. HERA and the H1 Detector

The only *ep* accelerator HERA was operated from 1992-2007 by DESY, which is one of the largest particle and photon science centers in the world. Figure 3.1 (left) shows the large HERA accelerator, which had a circumference of approximately 6.4 km and the necessary pre-accelerators PETRA[1] and DESY. The HERA machine was operated with contra rotating electron and proton bunch trains of each 180 bunches. The protons

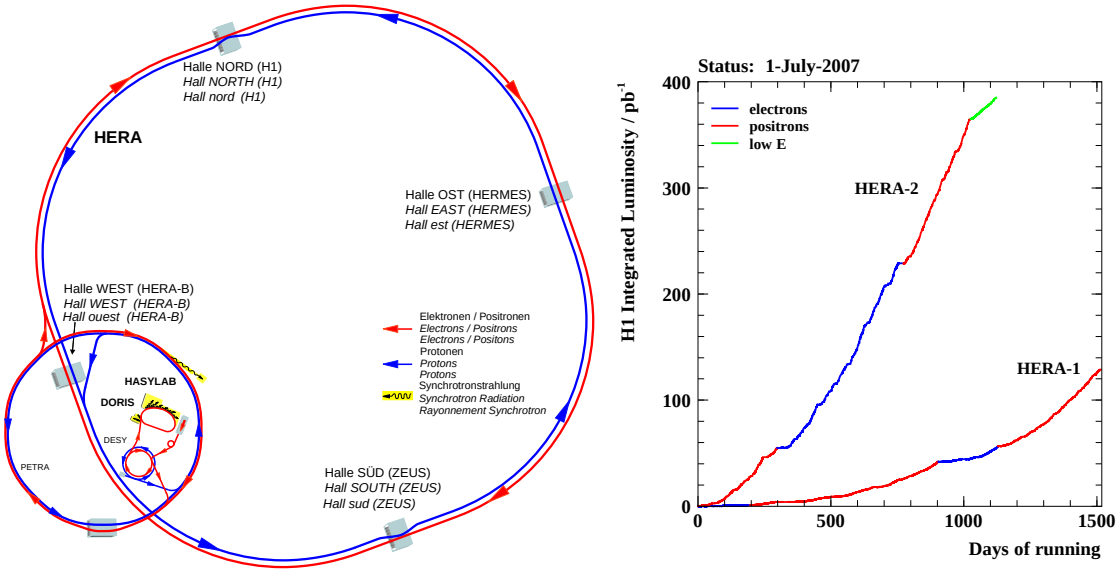

Figure 3.1.: *The HERA accelerator complex, running from 1992 - 2007, is shown left with its pre-accelerators PETRA and DESY. The large HERA experimental halls with the H1, ZEUS, HERMES and HERA-B experiment. The total collected luminosity by the H1 experiment from 1992 - 2007 including the low proton energy runs is shown right.*

have been accelerated to an energy of 920 GeV and electrons to an energy of 27.5 GeV which results to an available centre-of-mass energy of $\sqrt{s} \approx 319$ GeV. The design luminosity of the HERA II running period was $\mathcal{L} = 7.4 \cdot 10^{31}$ cm^{-2}s^{-1}.
In order to make best use out of the different particle beams the HERA storage ring had four large experimental halls (North, South, East and West) where the two collider experiments H1 and ZEUS and the fixed target experiments HERMES and HERA-B have been operated. The two fixed target experiments have been built-up as large complex spectrometers. HERA-B has measured the properties of heavy mesons by using a wire target made from materials of different density directed to the tails of the Gaussian proton beam profile. HERMES has used the electron beam, focused to a polarised gas target allowing detailled measurements of the spin structure of the proton. The two experiments H1 and ZEUS have been operated in a colliding mode allowing

[1]Currently being re-built to a 3rd generation synchrotron light source.

precise measurements of a large variety of particle physics aspects and in particular QCD. At the interaction points of ZEUS and H1 a bunch crossing rate of 10.4 MHz was achieved, which corresponds to time intervals of 96.5 ns (HERA clock). The H1 experiment looks for the debris of the electron proton collisions over a wide kinematic range of x and Q^2. The H1 experiment was active from 1992-2007 and has taken a total luminosity of 500 pb^{-1} as illustrated in figure 3.1 (right).

The H1 Detector

The H1 detector [A+97a] was technically designed such that the full solid angle is covered. The large asymmetry of the beam energies had a major impact on the H1 detector design and resulted in a more complex instrumentation in proton direction compared to the backward one.
In order to describe the event signatures of the detected particles a coordinate system is defined with its origin in the interaction point (IP). The z axis is aligned to the direction of the outgoing proton beam, whereas the x axis points to the centre of the HERA ring. As usual for a right-handed coordinate system the y axis points upwards. Furthermore two angles are of importance which are the azimuthal angle ϕ measured with respect to the x axis and the polar angle θ measured relatively to the proton beam direction. In order to allow a better orientation two projections are commonly used: orthogonal to the z axis ($r\phi$ plane) and aligned to the z axis (rz plane).
The central region of the H1 detector in the HERA II setup is depicted as a side view in figure 3.2, where all the labels and abbreviations are summarised in table 3.1. The detector subsystems are explained in more detail in the following. A more detailed description of the H1 detector is given in [A+97a].
The incoming proton beam is crossed at the IP 1 with the contra rotating electron beam. The beam bunches of the electron and proton beam are bend by the final focussing magnets located in backward 18 (GG) and forward 19 (GO) direction in order to get the small beam spot needed for the high luminosity of the HERA II running period.
The elliptical beam pipe is surrounded closest by the silicon tracking devices. These are the central silicon tracker (CST) 2 with an angular coverage of $30° \leq \theta \leq 150°$ relative to the IP. The resolution of the CST is $\sigma_{r\phi} = 12\,\mu$m in the $r\phi$ plane and $\sigma_{rz} = 22\,\mu$m in the rz plane [P+00]. Due to its superior resolution it measures not only the vertex of two or more particle tracks, but also secondary vertices, which originate from particles with relatively long life times, i.e. heavy quark hadrons. In addition to the CST two additional silicon detectors have been mounted for the HERA II running period: In forward direction the FST 4, which covers $8° \leq \theta \leq 16°$ [H+99a] and for the backward region the BST 3, which strengthens the identification of scattered electrons at large polar angles. For the BST large polar angles refer to an acceptance of $162° \leq \theta \leq 176°$ [Hen00].
More outwards in y direction the silicon detectors are followed by the central tracking system. The main components are the central jet chambers 1 7 and 2 8. Together with all other central tracking devices the CJCs are discussed in a more detailed way in section 3.3 because of the relevance of the tracking detectors for the present analysis. The FTD 9 with a polar angular acceptance of $7° < \theta < 25°$ [H+98] is a single detector

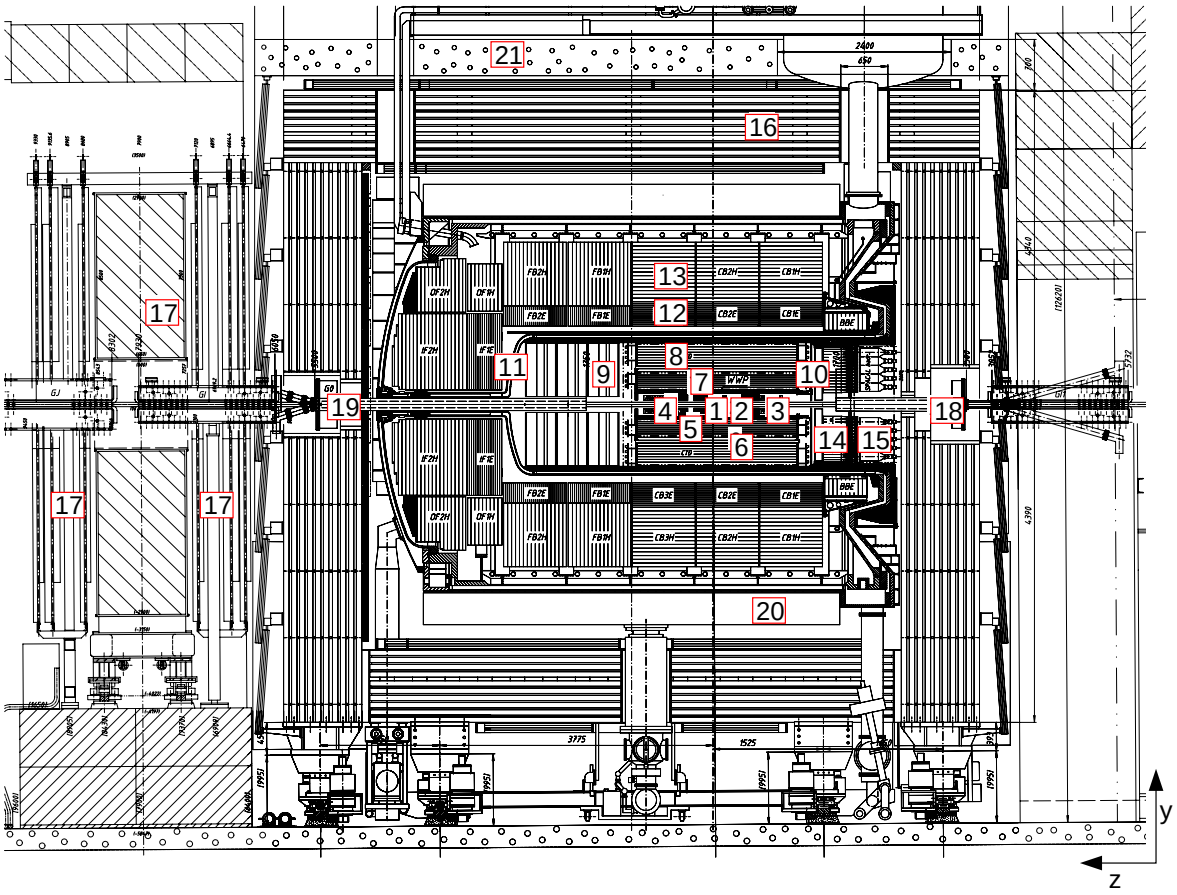

Figure 3.2.: *The H1 detector in the HERA II setup. The single detector components are listed in table 3.1 with their abbreviations and discussed in more detail in the text.*

component, which enhances the capabilities of H1 to measure the forward going tracks of the hadronic final state.

After the central jet chambers the Liquid Argon calorimeter (LAr) [A+93] covering a solid angle of $4° < \theta < 154°$ is arranged. The LAr is build as a sampling calorimeter with liquid argon as active medium between the absorption plates. The LAr consists of a electromagnetic part 12 and a hadronic part 13 and is situated in a cryostat 11 in order to achieve the low temperatures necessary to keep argon liquid. A more detailed discussion is given in section 3.1.

The main detector component in the backward direction of the H1 detector is the so-called spaghetti calorimeter (SPACAL), which consists of an electromagnetic 14 and a hadronic part 15. The notation SPACAL is derived from its construction method where active scintillating fibers are embedded in the absorption material lead [A+97b]. The SPACAL is described in more detail in section 3.2 because of its relevance for the present analysis. The SPACAL covers a solid angle of $155° < \theta < 175°$ and thus fills the gap in backward direction, which is not covered by the LAr calorimeter. In addition a backward proportional chamber (BPC) 10 enhances the possibility to detect the scattered electron in the backward region.

In order to measure the charge and the momentum of the particles a magnetic field

XX	Abbreviation	Detector component
1	IP	**I**nteraction **P**oint
Tracking Devices		
2	CST	**C**entral **S**ilicon **T**racker
3	BST	**B**ackward **S**ilicon **T**racker
4	FST	**F**orward **S**ilicon **T**racker
5	CIP2k	**C**entral **I**nner **P**roportional Chamber **2000**
6	COP	**C**entral **O**uter **P**roportional Chamber
7	CJC1	**C**entral **J**et **C**hamber **1**
8	CJC2	**C**entral **J**et **C**hamber **2**
9	FTD	**F**orward **T**racking **D**etector
10	BPC	**B**ackward **P**roportional **C**hamber
Calorimeters		
11	LAr cryostat	**L**iquid **Ar**gon cryostat
12	LAr (el.)	**L**iquid **Ar**gon Calorimeter
13	LAr (had.)	**L**iquid **Ar**gon Calorimeter
14	SPACAL (el.)	**Spa**ghetti **Cal**orimeter
15	SPACAL (had.)	**Spa**ghetti **Cal**orimeter
Muon system		
16	CMS	**C**entral **M**yon **S**ystem
17	FMS	**F**orward **M**yon **S**ystem & toroidal magnet structure
Miscellaneous		
18/19	GG/GO	super-conducting magnet (backward/forward)
20	–	super-conducting coil
21	–	concrete shielding

Table 3.1.: *List of the H1 detector components and their abbreviations with the corresponding number as illustrated in figure 3.2.*

with $B = 1.15$ T parallel to the z axis is produced by a super conducting coil 20. The coil surrounds all up to know described detector subsystems. This setup minimises the dead material between the IP and the calorimeters allowing for a good measurement of the energy of the produced particles and their decay products.
The outermost detector subsystem is the muon system consisting of two subsystems. The forward muon spectrometer 17, which measures the muon tracks with many drift chamber layers in a solid angle of $3° < \theta < 17°$. The magnetic field necessary to measure the momentum is produced by a toroidal magnet. The instrumented iron 16 builds up the central muon system (CMS), which consists of so-called streamer tubes with a quadratic profile and a sense wire in the middle. The setup is comparable to a track chamber, where the enclosed medium is filled with an ionisable gas. The CMS acceptance covers a solid angle of $4° < \theta < 171°$.

3.1. The LAr Calorimeter

The main detector component for energy measurements in the H1 detector is the liquid argon calorimeter, which covers a solid angle of $4° < \theta < 154°$. A transverse section of the upper half of the LAr calorimeter is depicted in figure 3.3. The calorimeter

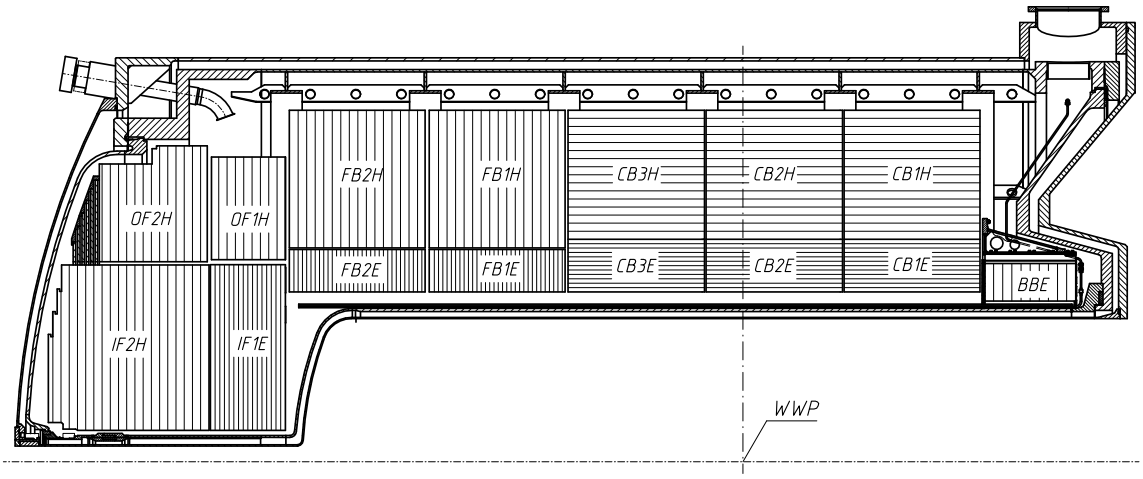

Figure 3.3.: *The transverse section of the upper half of the liquid argon sampling calorimeter with the inner electromagnetic and the outer hadronic section.*

is divided into an inner electromagnetic and an outer hadronic section. While both regions share liquid argon as the active medium, the two parts have different absorber materials: lead for the electromagnetic part and stainless steel for the hadronic part. Overall the material in the electromagnetic calorimeter amounts to 20 to 30 radiation lengths, whereas the hadronic part of the LAr calorimeter is 5 to 8 interaction lengths thick. The LAr provides fast trigger signals for level one decisions, which are based on energy thresholds.
The large amount of 45,000 readout channels provides a high spatial resolution. The energy resolution of the electromagnetic part of the LAr is $\sigma(E)/E \approx 12\%/\sqrt{E/\mathrm{GeV}} \oplus 1\%$ and for the hadronic part of the LAr it is $\sigma(E)/E \approx 50\%/\sqrt{E/\mathrm{GeV}} \oplus 2\%$. Both resolution have been determined from test beam measurements.

3.2. The SPACAL Calorimeter

The SPACAL calorimeter is utilised for the energy measurement in the backward region of the detector with a geometrical acceptance of $155° < \theta < 175°$. The SPACAL is separated in an electromagnetic and a hadronic part in order to identify electrons precisely and to estimate the hadronic energy flow in the backward region. The electromagnetic part is the main component of the SPACAL calorimeter, as the relatively thin (in terms of interaction lengths) hadronic part is only used as a veto of hadronic activity. The SPACAL is build as a sampling calorimeter where the active medium and the absorption material is composed in a sandwich structure. The active medium are scintillating fibres which are embedded in z direction in small notches in the absorption material lead.

Due to the HERA machine upgrade super-conducting magnet structures (GG) used for the final beam focussing towards the IP have been inserted, which in turn demanded a re-design of the inner region of the SPACAL. A schematic drawing of the SPACAL in the pre-upgrade layout is displayed in figure 3.4 (left). The modifications due to the HERA machine upgrade are indicated in the right figure. The inner radius of the SPACAL before the upgrade is indicated by the dashed line, thus inner cells had to be removed in order to accommodate for an elliptical beam pipe. With a depth of 28 radi-

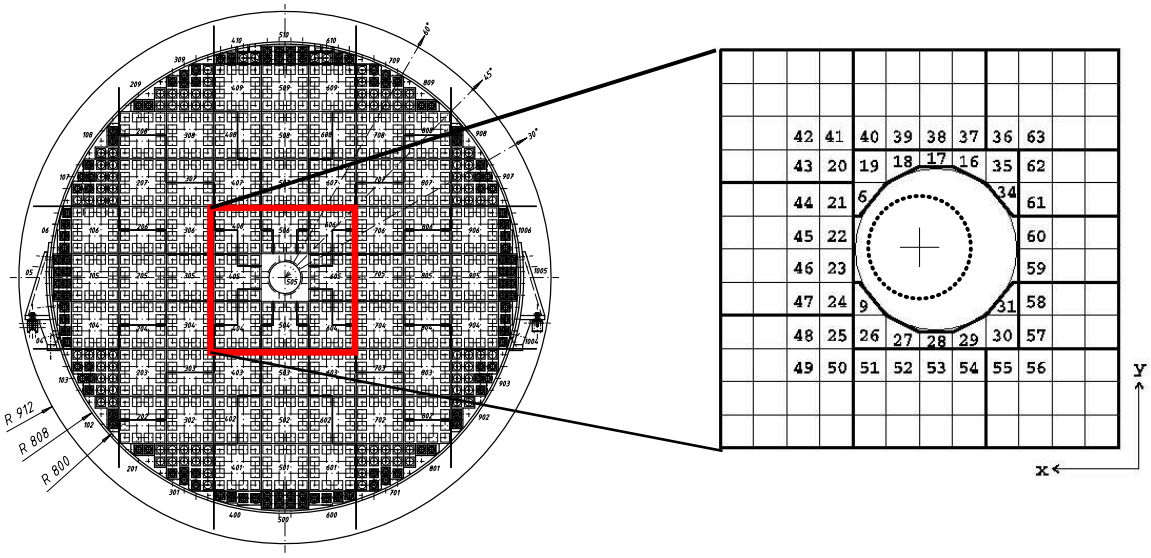

Figure 3.4.: *The geometry of the SPACAL calorimeter is displayed for the HERA I setup (left), whereas the right figure illustrates the modifications needed for the HERA machine upgrade. The inner radius of the SPACAL before the upgrade is indicated by the dashed line.*

ation lengths the electromagnetic part of the SPACAL is well suited to incorporate the electromagnetic shower of scattered electrons. The energy resolution of the SPACAL is $\sigma(E)/E \approx 7.1\%/\sqrt{E/\mathrm{GeV}}$. The electromagnetic part of the SPACAL is divided into $\sim$ 1150 readout cells as indicated in figure 3.4 (left). The SPACAL provides trigger signals at level one for the identification of the scattered electron which are based on energy thresholds.

3.3. The Central Tracking System

The central tracking system of the H1 detector consists of more components embedded between the CST and CJC1 and between the CJC1 and CJC2 as illustrated in figure 3.5. The five-layered CIP2k system [5] [C+98] was used for the fast determination of the event t_0 utilised for trigger decisions at level one. Between the CJC1 and CJC2 the outer chambers are placed, which are the outer z chamber (COZ) and the outer proportional chamber (COP) [6]. The COP was de-activated with the final comissioning of the third trigger level of the FTT and the full use of the L3Reject from 2006 onwards (see chapter 14). The COZ is the sole exception concerning the direction of the signal wires which are perpendicular to the beam axis. Due to this fact the resolution in rz is improved significantly to a z resolution of $\sigma_{rz} = 380$ μm

[A+97a]. The CIP2k and the COZ are additionally utilised for the fast estimation of the z position of the interaction, which is used for the trigger.

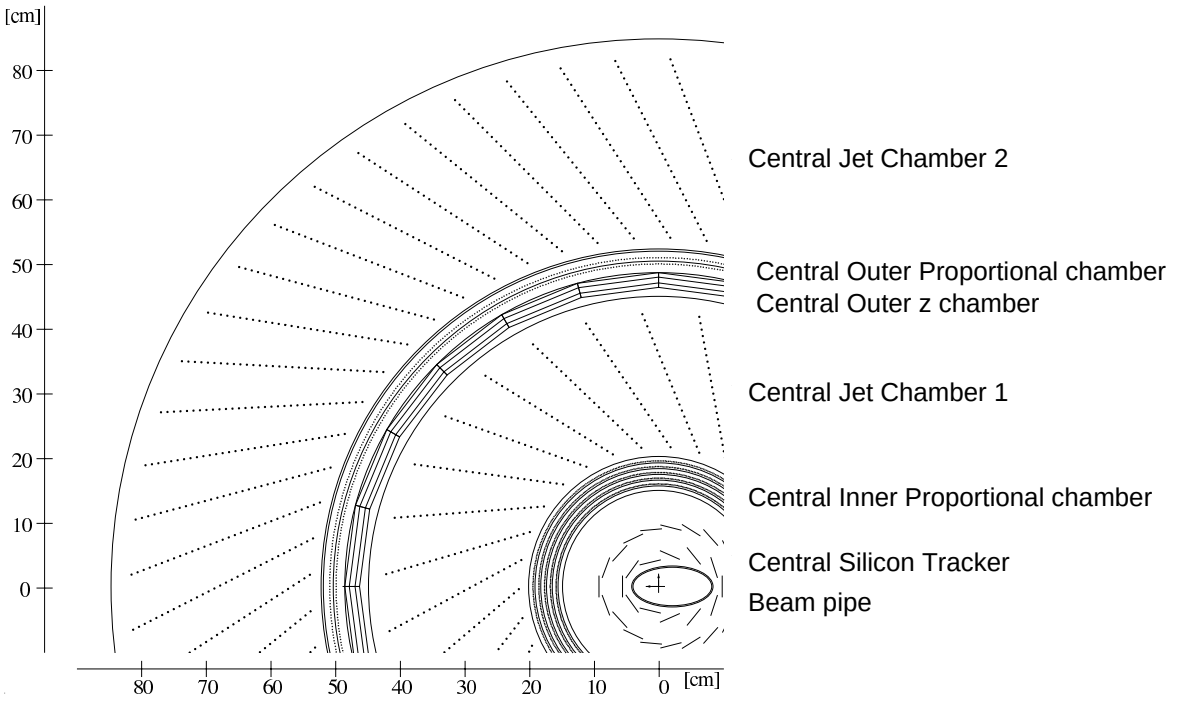

Figure 3.5.: *Lateral section in the xy plane of the central tracking devices of the H1 detector. The elliptical beam pipe is not centred with respect to the origin in x and y (taken from [H+04]).*

Central Jet Chambers

The main detector component of the central tracking system of the H1 detector are the two large central jet chambers CJC1 and CJC2. Figure 3.5 displays the lateral or $r\phi$ plane of the central tracking system. The signal wires of the CJCs are spanned parallel to the beam or z axis. The CJC1 is made out of 30 cells which consist out of 24 signal wires and the CJC2 has, due to the larger radii, 60 cells with 32 signal wires in each of the cells. The radial dimensions and other information of the CJCs is summarised in table 3.2.
Due to the presence of a magentic field, which penetrates both chambers in a homogeneous way, tracks of charged particles are curved which allows the measurement of transverse momenta. In turn the cells of the CJCs are tilted by 30°, which ensures for tracks over a wide range in transverse momentum, that the ionisation electrons drift perpendicular to the tracks. Moreover due to the tilt curved tracks cross the cell boundaries at least once, which allows a measurement based on two cells. The angle whereby the cells are tilted can be calculated for a given gas mixture and geometry of the chamber by considering also the drift velocity, the pressure, the magnetic field and the drift field.
The position of a hit in the transverse plane is derived from the measured drift time

	CJC1	CJC2
Total length	2500 mm	
Active length	2200 mm	
Inner radius	203 mm	530 mm
Outer radius	451 mm	844 mm
Number of cells	30	60
Number of sense wires	720	1920
Sense wire distance	10.16 mm	

Table 3.2.: *Mechanical parameters of the two central jet chambers [A+97a].*

and velocities and additionally the known wire positions and the angle in the magnetic field (Lorentz angle). Within a specific maximal drift time of ~ 1 μs the induced electrons produce a signal for the readout at both ends of a signal wire. Out of this signal the z position of a hit is determined with the method of charge division. In the $r\phi$ plane an ambiguity exist, because for each hit also a mirror hit is reconstructed, which is solved in most cases due to the tilt of the cells because two cells are utilised for the measurement.
The spatial resolution is given by $\sigma_{r\phi} = 170$ μm in the $r\phi$ plane and $\sigma_z = 4$ cm in z together with a p_T resolution of $\sigma_{p_T}/p_T^2 = 0.01$ GeV^{-1} [Tlu99].
For the data taking in 2004 the DC$r\varphi$ trigger [W+92] system was implemented, whereas for the data taking in $2005-07$ the Fast Track Trigger [B+01; Sch04] was active (see chapter 14). Both use the information of certain wire layers for the determination of trigger conditions based on the transverse momenta and multiplicity of tracks.

Reconstruction of Tracks

A simplified picture of a track in the $r\phi$ or xy plane is displayed in figure 3.6a). The charged particle is forced to a circular trajectory in the $r\phi$ plane due to the magnetic field. As the particles follows a linear trajectory in z the complete three-dimensional trajectory is described by five parameters ($\kappa,\ d_{\text{ca}},\ \phi,\ \theta,\ z_0$) of a helix trajectory.

- The track curvature κ is a measure for the transverse momentum of a track which can be deduced from:

$$p_T[\text{GeV}] = -Q \cdot \frac{0.3 \cdot B_z[\text{T}]}{\kappa[\text{m}^{-1}]}. \tag{3.1}$$

  Q denotes the charge of a particle track. In order to measure the transverse momentum p_T of a track a magnetic field B is used.

- The quantity d_{ca} (distance of closest approach) is the smallest distance in the $r\phi$ plane to the origin as indicated in figure 3.6a).

- The azimuthal angle ϕ of a track is measured between the x axis of the H1 coordinate system and the tangent to the circle in the point of closest approach d_{ca}, as depicted in figure 3.6a).

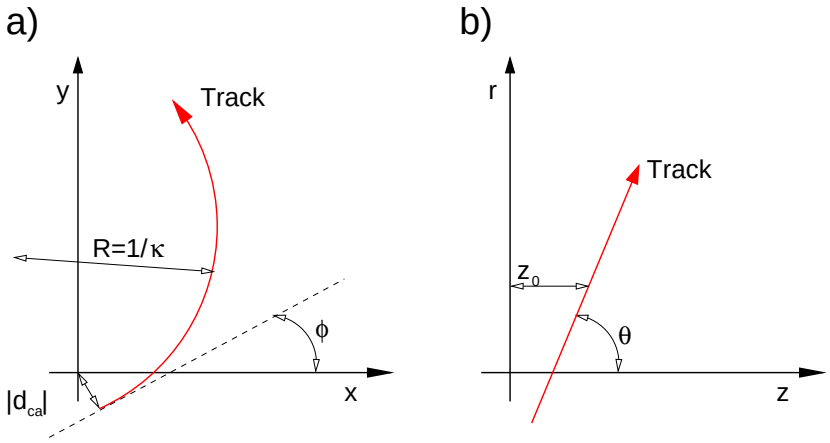

Figure 3.6.: *Projection of a track into the xy plane a) and into the rz plane b) of the H1 detector. The five parameters of a helix trajectory describe a three-dimensional track: κ, ϕ, d_{ca} in the xy plane and z_0, θ in the rz plane.*

- The polar angle θ is measured between the tangent to the circle in the point of closest approach d_{ca} and the z axis.
- The coordinate z_0 is the intercept with the z axis or the distance measured in z from the origin to the point of closest approach d_{ca} (see figure 3.6b)).

These parameters are determined with a circular fit in the $r\phi$ plane and a linear fit in the rz plane to the measured hits of the tracking devices [Blo05]. In a complicate iterative fit procedure the hit information of the CJCs in the $r\phi$ plane is utilised to determine κ, ϕ and the d_{ca}. Afterwards the procedure is repeated and information from other tracking devices is added. At the end of this fit procedure the event vertex in the $r\phi$ plane is determined with these tracks. The straight line fit in the rz plane determines the angle θ and the coordinate z_0. Moreover the whole fit procedure in the $r\phi$ plane and in the rz plane is iterated with the additional constraint of the event vertex for tracks that do not belong to a secondary vertex. Thus a higher performance is achieved because the vertex information has been determined from many tracks, which increases the resolution. As a result non-vertex fitted tracks and more precise vertex fitted tracks are available.

3.4. The Luminosity Measurement

The luminosity seen by the H1 experiment is determined via the measurement of the Bethe-Heitler process [BH34] where the electron and photon is scattered at very low angles. The scattering process is on the complete proton and thus only the electrical form factor is involved. The Bethe-Heitler process $ep \rightarrow ep\gamma$ is from the theory point of view very precisely calculable and therefore well suited for the determination of the luminosity of a colliding beam experiment using electrons. The produced photon from the Bethe-Heitler process is detected with the photon detector at $z = -101.8$ m. The photon detector is a sampling calorimeter consisting of scintillating fibres as active medium and tungsten as absorber material as depicted in figure 3.7. In order to suppress background a beryllium filter and a water Cerenkov counter are implemented.

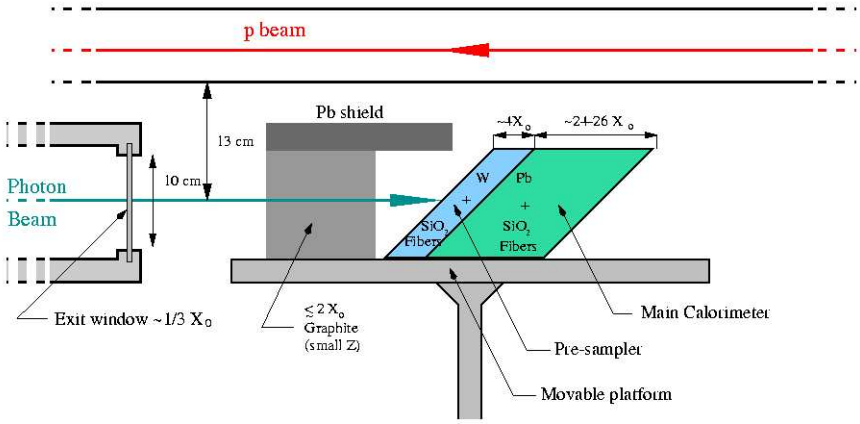

Figure 3.7.: *The photon detector system utilised to measure the luminosity as seen by H1 is situated at* $z = -101.8$ m. *The photon beam axis is* 13 cm *below the proton beam pipe. An absorber of roughly two radiation lengths reduces the synchrotron radiation directly hitting the presampler and the main calorimeter. All the detectors are mounted on a vertically movable table [H+ 04].*

The scattered electrons do not hit the photon detector because they are deflected by the HERA beam magnets. Nevertheless these deflected electrons are used for the cross check of the luminosity determination and are measured in the electron tagger at $z = -5.4$ m because of the energy loss during the deflection.

3.5. The Trigger Scheme

The trigger scheme of H1 implies a rate reduction of the bunch crossing rate of 10.4 MHz by about six orders of magnitude to allow the data storage. The readout of the H1 detector is not capable of rates higher than 50 Hz therefore the trigger system had to ensure that the rate reduction is sufficient to fulfil this requirement without loss of interesting physics. This is realised in H1 by means of a multi-level trigger system [A+97a; Els92]. The capabilities of the H1 trigger system have been largely extended in order to make the best possible use of the higher luminosity provided by the upgraded HERA collider. One of the upgrade projects of the H1 collaboration, which is also the topic of the hardware project of the thesis, was the Fast Track Trigger (FTT). It is integrated in the first three levels (L1 – L3) of the H1 trigger system and provides enhanced selectivity for events with charged particles and thus provides higher rate reduction. In photoproduction ($Q^2 \sim 0$) the electron leaves the detector volume undetected and thus electron based trigger conditions can not be used. In particular this kinematic region is a challenge for the trigger because of the strong increase of the cross section with decreasing Q^2 that yields high physics rates. Due to bandwith limitations the only way to identify interesting physics, e.g. heavy meson events, is by doing invariant mass calculations based on a precise on-line track reconstruction at trigger level. The second part of the thesis, which starts at chapter 14, describes the Fast Track Trigger system capable to do so and present the commissioning and optimisation effort for the FTT.

A schematic drawing of the complete H1 trigger scheme and its signals is given in figure 3.8. The first three levels of the trigger system are synchronous to the so-called HERA clock which is deduced from the frequency of the bunch crossing and gives time intervals of 96.5 ns.

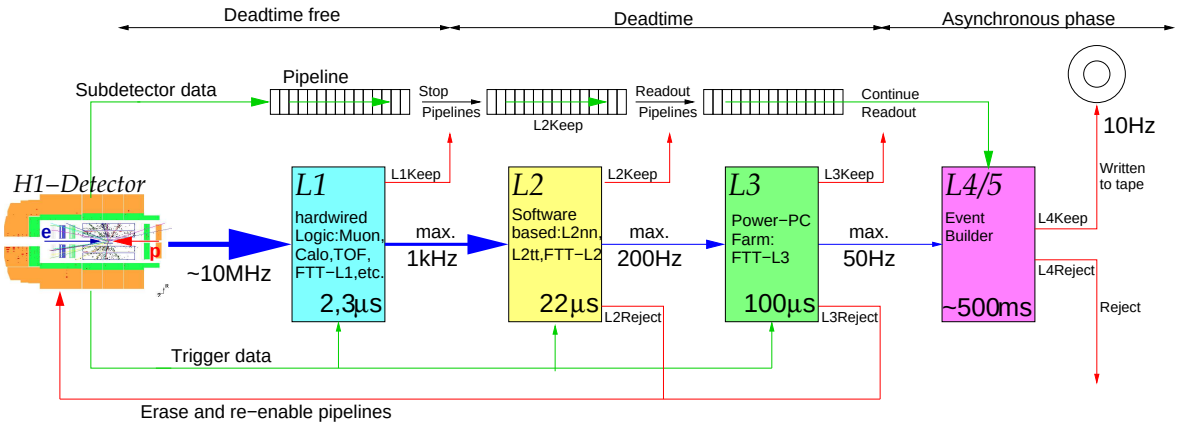

Figure 3.8.: *The H1 trigger system with its four trigger levels is shown together with important signals. The details are given in the text. (Sketch derived from [Nau03])*

The Level 1

The level one system is implemented as a dead time free trigger stage with a pipeline of 2.3 μs depth. The L1 trigger systems are implemented as hardware systems because of the short time available. The trigger signals delivered by the subdetectors are called trigger elements (TE). These elements are logically combined to subtriggers (s1 – s128) in order to select physics channels of interest. The 128 subtriggers are combined out of 256 trigger elements. The OR of all these subtriggers leads to a level one trigger decision (L1Keep). If the event is kept the frontend pipelines[2] are stopped and the dead time starts. The level one reject condition implies no signal at all, pipelines remain active. The level one output rate is O(1 kHz).

The Level 2

If a L1Keep was fanned out by the central trigger logic (CTL) the pipelines are stopped and the dead time of the detector starts. The level 1 trigger decision is than refined by the level 2 decision, which arrives 23 μs after the bunch crossing. It resembles the level one decision process: triggerelements from subdetectors are combined to the level two trigger decision by means of topological correlations (L2TT trigger [B+97]), by neuronal networks (L2NN trigger [K+97]) or track based quantities as estimated by the FTT L2 system [W+03]. These systems are implemented as software based trigger systems. The results of the trigger stages are fanned out by the central trigger to all subsystems. The actual readout of the frontend, which takes about 1.4 – 2 ms, is started on receipt of a positive L2 decision (L2Keep). The level two output rate is up to O(200 Hz).

[2]Embedded in the detector subsystems by a memory structure.

The Level 3

During the readout the level three trigger decision takes place. The system that contributes to the level three decision is the third trigger level of the FTT (FTT L3) [Nau03; Jun04; J+07] which utilises information from the calorimeter and muon systems in addition to track information (see chapter 14 for more details). A possible level 3 reject decision (L3Reject) is fanned out by the CTL within about[3] 100 μs. A L3Reject leads to an abort of the frontend readout, while the L3Keep signal validates the level one and two decision[4]. The typical L3 output rate is 50 Hz. In contrast to the first two levels the L3 trigger elements are technically on the CTL side subtriggers and can not be logically combined on CTL side. This is only possible within FTT L3 itself.

The Level 4

The data are transferred to the event builder at the fourth trigger level. It has the full detector information available and aims for a further reduction of the data logging rate and volume. The event builder rejects remaining background events originating from beam-gas or beam-wall interactions and classifies all events according to physics finders. Every event is sorted by the physics finders to different pre-defined physics classes. Events which can not be subjected to any of the given classes and have a four-momentum transfer below a certain threshold are weighted by a factor of 10 allowing off-line checks of the quality of the L4 decisions. This final step takes about 500 ms and reduces the rate to approximately $10 - 20$ Hz with a typical event size of 100 to 150 kByte.

The Concept of Prescales

If the cumulative rate reduction achieved by use of all trigger levels is not sufficient to preserve the rate constraints single subtriggers are *prescaled*. This *prescale* process reduces the rate of individual subtriggers in a deterministic way. It works as follows: each L1 subtrigger exist as *raw* and *actual* bit. If a prescale factor is assigned to a subtrigger during the data taking n raw bits are thrown away and only the n^{th} raw bit is taken, which is then marked as *actual*. Furthermore there is a global trigger concept which defines explicitly which kind of event topology is of interest and which subtriggers are of high priority (de facto no prescale) or become an acceptable low prescale of the order of 1 to 2 for triggers, which are of interest but have unfortunately a high rate. Examples for slightly prescaled triggers are the FTT L3 photoproduction triggers as discussed in section 15.5. A reliable trigger concept considers the different physics needs by the definition of physics channels where the subtriggers built for the same kind of physics processes are bundled. In addition to the definition of a prescale factor for each subtrigger individual weights are assigned for each physics channel such that the overall available total L4 input rate is matched. This process yields the best results

[3] A value of 130 μs for the L3Reject time was possible for the whole H1 detector system and was implemented for the $2006 - 07$ running where FTT L3 was fully activated.

[4] There have been subtriggers (muon triggers) implemented, where the validation by L3 is not considered if special conditions are fulfilled.

if executed in a dynamical and automatically way [SCEN+99] such that changes in the running conditions of the HERA machine can be adopted. A period with constant prescales and stable conditions is called *run*.

4. Event Generators

In general there exist two types of computer programs able to calculate or simulate *ep*-scattering. Both are based on random number generation utilised to simulate various physics processes for comparisons to experimental data. The difference between the two types is essentially that one type of programs simulates full events including parton hadronisation that can be forwarded to the detector reconstruction, so-called Monte Carlo (MC) event generators, while the other type of programs calculates next-to-leading order cross sections at parton level, i.e. the partons are not hadronised, by fixed order perturbation theory calculations. These are referred to as the NLO calculation programs. It is not expected that LO MC programs are able to produce the correct normalisation of a cross section prediction, which is the case for the NLO calculation programs.

4.1. Leading-order Monte Carlo Generators

The MC event generators include exact perturbative leading order calculations of the matrix element supplemented with parton showers (PS) according to one of the evolution schemes as described in section 2.2.
The generation of an *ep* event starts with the electron and the proton and follows the principles of the QCD factorisation theorem as discussed in section 2.2. First of all the hard subprocess is generated at a given factorisation scale. The hard matrix element corresponding to the hard subprocess is convoluted with the proton parton density distribution. If also resolved photon processes, as introduced briefly in section 2.3, have to be considered a photon PDF is added in addition. By applying the parton evolution equations a PDF can be evolved to an arbitrarily high scale given by the factorisation scale, which is usually defined as the hardest scale of the scattering process, like the virtuality Q^2. The hard subprocess or the so-called hard interaction determines the event kinematics of the process.
The initial state partons and final state partons from the hard interaction, the proton remnant and possibly the photon remnant are subject to parton showers realised by the DGLAP evolution equations, that end on the condition that only *on-mass shell*[1] partons are left from the virtual partons at the beginning.
As all outgoing partons are still colored objects they undergo a cascade of soft non-perturbative interactions (fragmentation or hadronisation process) where the confinement of quarks and gluons is realised and real hadrons are produced. At the end of the generation process all generated particles have a lifetime $\tau > 10^{-8}$ s and are available as four-momentum vectors which can be transfered to the detector simulation as discussed in section 4.3. The key concepts of the LO MC programs RAPGAP and CASCADE are briefly discussed in the following.

[1]Following the equation $E^2 = \overrightarrow{p}^2 + m^2$.

The RAPGAP Program

The RAPGAP generator [Jun95] uses leading-order (LO) matrix elements for the BGF process where the heavy quarks are treated massive. The LO matrix elements are matched to LO parton showers using the collinear DGLAP evolution scheme (see section 2.2) to generate ep events. In RAPGAP the possibility for the calculation of resolved contributions exist, where an additional DGLAP evolution from the hard scattering vertex to the photon side is made.
RAPGAP 3.1 is interfaced to HERACLES (version 4.4) [KSM92] for events with next-to-leading order QED processes as explained in section 2. The HERACLES interface has been utilised for MC event samples including NLO QED processes and samples where the NLO QED part has been switched off. The Lund fragmentation model is utilised by RAPGAP for the light quark flavors, while the Bowler fragmentation function is used for the heavy quark fragmentation. For RAPGAP only the direct contribution of the BGF process has been calculated as there is no evidence of a resolved component in the visible range analysed here [A$^+$07]. RAPGAP has been employed with two different proton PDFs, namely the leading-order CTEQ6ll [P$^+$02] and the next-to-leading order CTEQ65m [T$^+$07] where the GM-VFNS approach for the incorporation of heavy quark masses is utilised. For the CTEQ6ll proton PDF the ZM-VFN scheme has been adopted. As the CTEQ65m PDF is a NLO PDF it has naturally a lower gluon density as a LO PDF, because the matrix elements for the BGF process are larger. Due to the use in a LO MC program like RAPGAP a lower cross section is calculated compared to the use of a LO PDF. Moreover CTEQ65m incorporates an intrinsic charm distribution at the starting scale Q_0^2 of about 1% of the total PDF. This value gives the best χ^2 for the global fit [T$^+$07].
The RAPGAP MC program is chosen to correct the data for the acceptance and efficiency of the detector and furthermore to correct the measured cross sections, which include NLO QED contributions, to the LO QED one-photon exchange (Born-level cross section).

The CASCADE Program

CASCADE [Jun02] is, like RAPGAP, a MC program with LO matrix elements matched to LO parton showers and implements the CCFM evolution equations (see section 2.2) based on the assignment of an intrinsic k_T to the partons. The proton is parameterised by an un-integrated gluon density A0 [HJ03] which is obtained from fits to the inclusive F_2 data. There is no quark contribution in the PDF or in the parton radiation. By construction the CCFM evolution scheme and its implementation in the CASCADE generator is well suited for the low x region. The CASCADE program does not include resolved photon contributions, although one might expect that they are partially covered by the k_T factorisation approach.
Events have been generated with the CASCADE 1.2 and 2.0 program, which both use the Bowler fragmentation function for the heavy quark fragmentation. In order to estimate a model uncertainty the data correction is also made with CASCADE.

Common leading-order Monte Carlo Setup

The steering parameters and main options used for RAPGAP and CASCADE are discussed below[2]. The contributions to the golden decay channel from higher resonances have been taken into account by using the ALEPH tune [Kno96] for higher resonances derived from e^+e^- measurements. The renormalisation and factorisation scale have been set for both programs to: $\mu^2 = Q^2 + p_T^2 + 4m_c^2$ with a charm mass of $m_c = 1.5$ GeV. The fragmentation function has been chosen to obey the Bowler parametrisation (see equation 2.17) with parameters: $a = 0.400$, $b = 0.885$, which are also taken from the ALEPH tune. A summary of the individual settings for RAPGAP and CASCADE is given in table 4.1. The CTEQ65m PDF has been obtained from

RAPGAP:					
Luminosity [pb^{-1}]	Purpose	Proton PDF	NLO QED	m_c [GeV]	Miscellaneous
7307.32	Data correction	CTEQ65m	yes	1.5	dst3, dst5
14951.69	Born correction	CTEQ65m	yes	1.5	no rec. applied
14409.88	Born correction	CTEQ65m	no	1.5	no rec. applied
8940.68	Data comparison	CTEQ6ll	yes	1.5	dst3, dst5
613.20	Systematic unc.	MRST2004FF3nlo	yes	1.5	dst3, fully inclusive $c\bar{c}$
CASCADE:					
Luminosity [pb^{-1}]	Purpose	Proton PDF	NLO QED	m_c [GeV]	miscellaneous
11259.65	Data comparison	A0	no	1.5	no rec. applied
3853.53	Model uncertainty	A0	no	1.5	dst3, dst5
13267.75	F_2^c extraction	A0	no	1.5	no rec. applied
11850.35	F_2^c extraction	A0	no	1.3	no rec. applied
14837.48	F_2^c extraction	A0	no	1.6	no rec. applied
11707.89	F_2^c extraction	A0−	no	1.5	no rec. applied
12108.63	F_2^c extraction	A0+	no	1.5	no rec. applied

Table 4.1.: *Overview of the MC sets and its purpose for the presented analysis. The key parameters adopted for the generation and the amount of statistics is summarised here.*

global analyses of structure function data and other data (for details see [T+07]) by using a GM-VFNS for the correct treatment of the heavy quark mass at threshold, whereas for CTEQ6ll a ZM-VFNS has been used, which is more appropriate at higher scales, neglecting heavy quark masses.
For all MC sets a total statistics corresponding to > 100 fb^{-1} has been generated. Each set possesses a factor 20 times the data statistics in order to avoid statistical fluctuation of the MC samples. Except one all MC samples are selected at generator level to have D^* mesons in the golden decay channel and thus are called signal MC samples. The luminosity of the fully inclusive $c\bar{c}$ RAPGAP sample corresponds to 613.20 pb^{-1} or 20 million events. The last two RAPGAP MC samples in table 4.1 have not been generated by the author himself.

[2]The parameters chosen for the MC programs have been taken from an effort of the H1 Heavy Flavor Group to extract a common steering with most recent particle data group informations.

4.2. Next-to-leading Order Calculations

The next-to-leading order calculations include the α_s^2 corrections to the leading order α_s BGF process. A selection of the order α_s^2 Feynman graphs is shown in figure 4.1a) for the real NLO corrections and in b) for the virtual NLO corrections. A next-to-

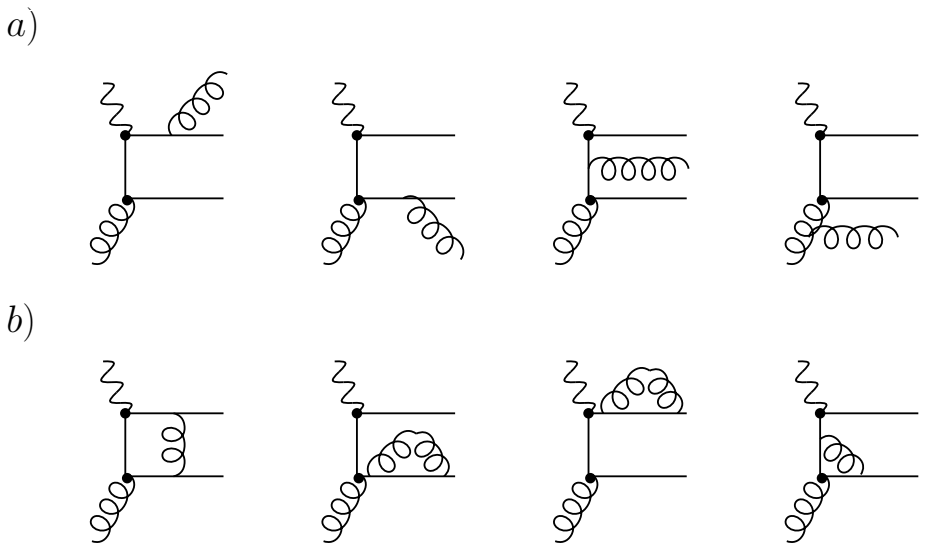

Figure 4.1.: *Feynman diagrams of the order α_s^2 corrections to the BGF process. Shown in a) is a selection of the real corrections and in b) a selection of the virtual corrections to the order α_s BGF process.*

leading order hard subprocess can not be directly supplemented with parton showers (MC@NLO) because of double counting problems. In order to develop a MC@NLO subtraction terms have to be identified, which has not been done up to now for DIS, although a first implementation is available for photoproduction [Tol08].
Therefore only NLO calculation programs without parton showers for heavy quark cross section predictions of the BGF-process up to order α_s^2 exist [Lae93]. The calculations can use different schemes for the treatment of the heavy quark mass, as introduced in section 2.3. In the following the implementations of the heavy flavor schemes and their use for the present analysis are discussed.

Calculation in the FFNS The HVQDIS [HS98; HS95] program implements the FFNS [Lae93] and produces up to three hard partons in the final state. The heavy quark is produced perturbatively from the boson-gluon fusion graph including NLO real and virtual corrections as discussed above. Two different proton PDFs have been utilised for HVQDIS from the CTEQ and MRST[3] group, namely the CTEQ5f3 [L$^+$00] and MRST04FF3 [MST06] proton PDFs. As HVQDIS needs proton PDFs in the FFNS both PDFs are derived from global analyses utilising FFNS. However it should be mentioned that the starting distribution of the MRST04FF3 PDF is taken from a global fit of MRST03 PDFs utilising a zero-mass-VFNS. Thus only the evolution is done in the FFNS which lead to a bad description of

[3]Now MSTW group.

the inclusive F_2 data, i.e. the χ^2/n.d.f. for H1 data is 2.8 as stated in [MST06]. Nevertheless it is used for the comparison to the data because it is the most recent FFNS PDF from the MRST group.
HVQDIS expects pole masses, i.e. for the charm quark $m_c \sim 1.6$ GeV which corresponds to a running mass of ~ 1.4 GeV [Y+06]. The fragmentation and renormalisation scale is chosen to be the same: $\mu_r^2 = \mu_f^2 = Q^2 + 4m_c^2$. The calculation for HVQDIS is in fixed order perturbation theory and produces fully differential distributions. The fragmentation process $c \to D^*$ is realised by a so-called independent fragmentation that does not take the color flow from the proton remnant into account as it is done for the Lund fragmentation model. For the independent fragmentation of the heavy hadron one of the discussed functions, like the Peterson, the Kartvelishvili or the Bowler fragmentation function, according to equations 2.15-2.17 is implemented.
The fully differential HVQDIS permits to restrict the phase space to the visible range of a measurement. Thus NLO predictions as single or double differential distributions of quantities of the produced D^* meson or event kinematic quantities, like Q^2 or y are possible. For the calculation the contribution due to b-quarks has been neglected as they contribute to less than 3% [A+07].
For a rough estimate of the theoretical uncertainty several parameters have been varied:

$$1.3 < m_c < 1.6 \text{ GeV}$$
$$0.5 < \mu_{r,f}/\mu_0 < 2, \text{ with } \mu_0^2 = Q^2 + 4m_c^2$$
$$2.9 < \alpha(\text{Kartvelishvili}) < 3.7$$

The mass of the charm-quark is varied within the given interval as well as a scale variation is done in order to get an impression on the possible contribution of higher orders. In addition to that also the value of the fragmentation parameter used in the independent fragmentation function has been varied.

Calculation in the ZM-VFNS There is no stand-alone program for the ZM-FVNS available, instead the calculation in the ZM-VFNS was kindly provided by G. Kramer and C. Sandoval [San08]. The calculation follows the basic principles as discussed in section 2.3.

Calculation in the GM-VFNS A fully differential calculation in the GM-VFNS for heavy quark production in ep deep inelastic scattering processes using NLO matrix elements is at the moment not available. According to a private communication [Sch08] the work for heavy flavor electroproduction is close to completion. Results in the GM-VFNS for heavy quark photoproduction have been presented [Kni08] and show good agreement to H1 photoproduction data [Urb09].

4.3. Detector Simulation

The events generated with one of the previously described LO MC event generators contain all required information for the `h1sim` package. This package tracks all the

generated four-momentum vectors of the particles trough the H1 detector whilst the detector response and electromagnetic interactions are given by the GEANT program [B+87]. After the digitisation step of the H1 detector simulation the whole event is forwarded to the H1 detector reconstruction step running the data reconstruction code of a certain run period. This period can be adjusted to the needs of the data analysis. The generated luminosity is than distributed over the chosen run period by a pre-processing step. Thus the acceptance and efficiency for the correction of the measured data can be calculated from a reconstructed LO MC event sample.
As the on-line data taking is based on the trigger scheme as introduced in section 3.5 also for the detector simulation the trigger system is simulated. The simulation of one of the most important[4] H1 trigger systems, the Fast Track Trigger (FTT), has been implemented within the scope of this thesis in a post-processing step. This step is executed by the FTT simulation package `fttemu` (see chapter 14.2). A general implementation into the H1 trigger simulation was not possible because of memory and data structure constraints given by the hardware-like simulation of the FTT system as explained in section 14.1. The implementation of the post-processing and its use for complex trigger mixtures is discussed in section 14.2.
For the analysis of track based final states, e.g. D^* mesons, it is of high importance that the amount of material is correctly implemented in MC. Otherwise the simulated detector response is not equivalent to the one in data. The presented analysis uses MC samples where the dead material description was improved significantly compared to previous versions used by H1 [Pit08]. In addition the random trigger noise simulation was added for the central tracking devices, which improves the description of the data by the MC.

[4]Trigger elements from the Fast Track Trigger have been implemented in more than 50% of all H1 subtriggers.

5. Open Charm Tagging and Experimental Methods

There are complementary experimental methods to identify or *tag* open charm production in *ep* scattering. The highest acceptance is achieved for measurements using secondary vertices of heavy mesons with large life times measured with the high resolution silicon trackers. These are identified by displaced tracks as indicated in figure 5.1a). This method allows to tag $> 80\%$ of open charm production at H1 [H+08]. A

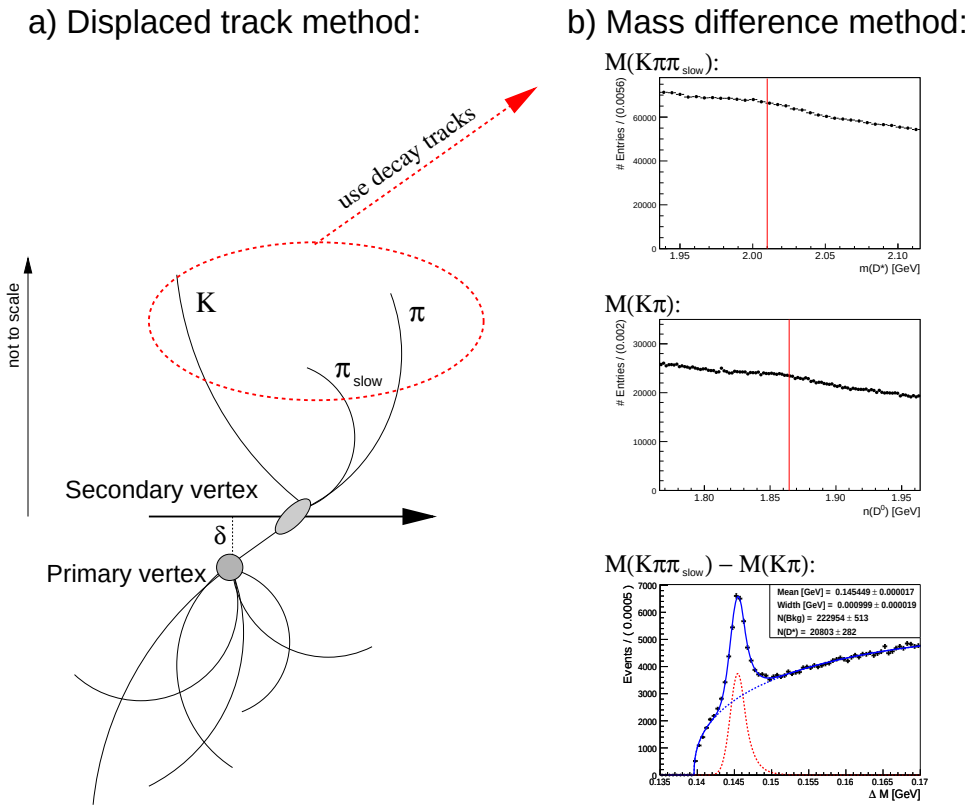

Figure 5.1.: *Different experimental methods for charm tagging at H1. The displaced track method using secondary vertices is indicated in a). The exclusive selection of D^* mesons from decay tracks using the mass difference method is shown in b). The nominal position of D^0 and D^* mesons in the mass distributions is marked by a solid line.*

complementary method for the identification of open charm is provided by the reconstruction of a $D^{*\pm}$ meson[1] thus open charm can be tagged. In addition, methods exist where the lifetime information of a charmed meson candidate is combined with the explicit reconstruction of charmed mesons for the decay under consideration, e.g. in order to identify D^+ mesons. The acceptance for this direct method depends on the

[1] If not stated otherwise D^* refers to both charged states of this meson: $D^{*\pm}$.

analysed phase space and is about $35-65\%$ which is discussed in more detail in chapter 11. However one has to keep in mind that the branching fraction and the fragmentation ratio (see section 2.3) have a large impact on the small acceptance. Nevertheless, the direct D^* tag has advantages as it provides very good background suppression which is utilised for the present analysis: a measurement of D^* meson production in DIS, where the D^* meson is directly reconstructed by its decay products.
In the present analysis, as well as in the on-line trigger system, the so-called *golden decay* channel: $D^{*\pm} \to D^0\pi^{\pm}_{\text{slow}} \to K^{\mp}\pi^{\pm}\pi^{\pm}_{\text{slow}}$ is used for the identification of the D^* mesons. The $D^0 \to K^{\mp}\pi^{\pm}$ decay is reconstructed from two oppositely charged tracks by applying the kaon and pion mass hypothesis. If the two candidates have a transverse momentum above a certain threshold the invariant mass is calculated. Those $K\pi$ pairs having an invariant mass consistent with the D^0 mass hypothesis within a certain D^0 mass window are sequentially combined with a third track (π_{slow}), which is requested to charge of opposite sign to that of the kaon candidate and to which the pion mass hypothesis is assigned. These track combinations are called *right charge* (RC) combinations. If the tracks fullfil the requirements, the right charge mass difference $\Delta M = M(D^*) - M(D^0)$ is calculated where D^* mesons peak at the expected value of 145.4 MeV [Y+06]. The small value of the mass difference, which is only slightly above the pion mass of $m(\pi^{\pm}) = 139.57$ MeV, restricts the available phase space for the D^* decay and thus implies very low momenta for the π_{slow}.
The advantage is that for the subtraction of the two masses part of the symmetric systematic errors from the track measurement of the π and K track cancels. Hence the resolution for ΔM is much better than for $m(D^{*\pm})$ or $m(D^0)$ distributions separately as illustrated by figure 5.1b). Thus the measurement of D^* mesons using the mass difference $\Delta M = M(D^*) - M(D^0)$ is dominated by the measurement of the π_{slow} track. Even though the total branching ratio of $D^{*\pm}$ mesons into $K^{\mp}\pi^{\pm}\pi^{\pm}_{\text{slow}}$ amounts to only $\sim 2.6\%$, this channel has its advantages, because its reconstruction from only charged tracks is comparably easy and due to the ΔM method has low background.
In order to understand the non-resonant background of the ΔM distribution, which is due to random combinations of three tracks, a so-called *wrong charge* (WC) decay is used. This wrong charged decay is selected from $D^{*\pm}$ decays where the D^0 decays as follows: $D^{*\pm} \to {}'D^{0\prime}\,\pi^{\pm}_{\text{slow}} \to K^{\pm}\pi^{\mp}\pi^{\pm}_{\text{slow}}$ and therefore does not show a resonance in a ΔM distribution. This wrong charge ΔM distribution is of particular use for the determination of the behaviour of the non-resonant background in the right charge ΔM distribution. In the following the on-line event selection of DIS events containing a D^* meson is described.

5.1. On-line Event Selection

As described in section 3.5 the H1 data taking is based on a large number of subtriggers for different kinds of physics channels. For the on-line selection of D^* mesons in DIS the subtrigger 61 (s61) is employed. A typical DIS event triggered by s61 containing a D^* meson candidate is illustrated in figure 5.2, where the scattered electron deposits its energy in a well pronounced cluster in the SPACAL and the central tracking devices contain high track multiplicities, which is common to D^* events.
The trigger conditions of s61 reflect this event topology, where a level one condition

on an isolated energy deposition in the SPACAL above 9 GeV (SPLe_IET > 2 || SPCLe_IET_Cen_3) and a track condition for a track in the CJCs are required. The track

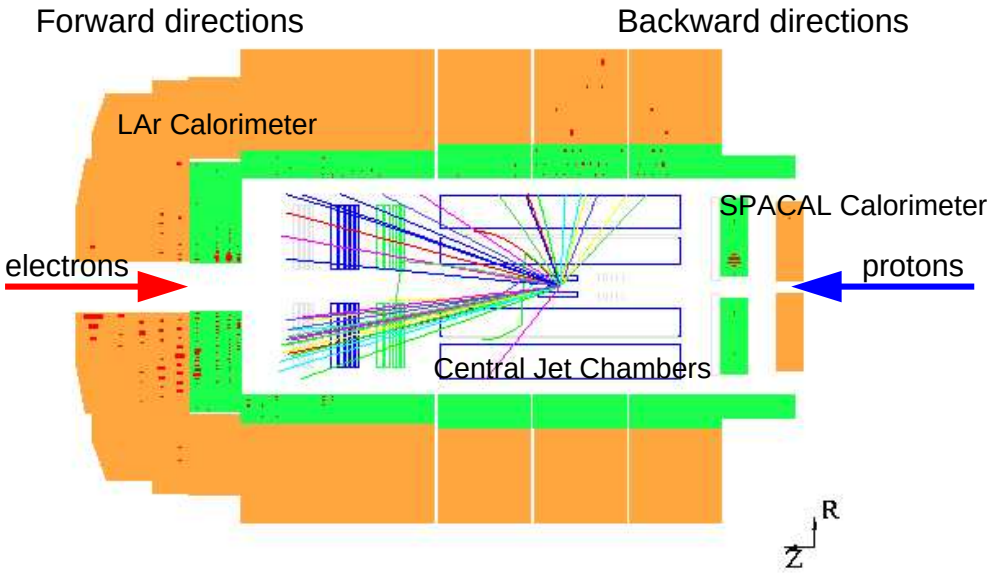

Figure 5.2.: *Event display of a typical DIS event with a well pronounced cluster in the backward calorimeter SPACAL and a high number of tracks in the central tracking devices. Out of which a D^* candidate can be identified by the methods described previously in the text.*

condition is calculated from two different track trigger systems, namely the DC$r\varphi$ system with a transverse momentum (p_T) threshold of 800 MeV (DCRPh_THig) for 2004 running and the FTT system during the $2005-07$ data taking with a p_T threshold of 900 MeV (FTT_mul_Td > 0). The track trigger efficiency is not affected by the slight change of the p_T threshold [Loh06]. Furthermore, the yield or in other words the efficiency is higher due to the better performance of the FTT trigger system, as discussed in section 8.1. In addition veto conditions at level one are implemented to suppress background from non-ep scattering events. These veto conditions are common to most of the H1 subtriggers. From mid 2006 an additional CIP veto was added to s61 to suppress very high multiplicity events. The s61 subtrigger does not use any conditions from the level two or three system as the rate is comparably low, but it is validated and filtered at L4.
As mentioned in section 3.5 events are classified at L4 by physics finders. The physics finder of importance for D^* meson events is the open charm finder. The basic principle follows the D^* selection outlined in the opening of this chapter, using cuts relaxed as much as possible that allow stable and efficient data taking. Because of continuous optimisations of the data taking the cuts implemented for the open charm finder have been relaxed with time to lower values. In the signal region of the ΔM distribution a D^0 window cut of 400 MeV is adopted, while it is tightened in case of the non-signal region to 100 MeV. Furthermore different cuts on the transverse momentum p_T of the D^* meson are applied which also depend on the ΔM distribution. An overview of the cuts as implemented for the 2007 data taking is given in table 5.1. The open

charm finder classifies the WC ΔM distribution where events contribute as described above. If the event is not classified by the open charm finder but the scattered electron

name	value
$p_T(K)$	> 0.40 GeV
$p_T(\pi)$	> 0.25 GeV
$p_T(\pi_{\text{slow}})$	> 0.07 GeV
ΔM	> 0.155 GeV
$M(D^0)$window	± 0.40 GeV
$p_T(D^*)$	> 1.50 GeV
ΔM	< 0.155 GeV
$M(D^0)$window	± 0.15 GeV
$p_T(D^*)$	> 0.70 GeV

Table 5.1.: *Selection cuts on the transverse momenta and invariant masses as implemented for the open charm finder at the L4 event builder for the year 2007 of the data taking.*

has an energy of more than 7 GeV the event is kept regardless. Otherwise another physics finder may classify the event as valid, if not it is downscaled with a factor of 10. Two different methods to extract the amount of D^* mesons from the right charge ΔM distribution are discussed in the following.

5.2. Signal Extraction Methods

Due to the combinatorial background the number of D^* mesons has to be determined using statistical methods. For the present analysis two different methods are implemented: The statistical subtraction method is applied for the determination of control distributions. The other method, based on fits with different parameterisations to the ΔM distribution, is used for the determination of the cross sections and some of the control distributions.
The idea of the subtraction method is to subtract the wrong charge background distribution from the signal distribution such that the distribution of the D^* meson signal remains. In order to do this, it is necessary to normalise the wrong charge background to the background of the signal distribution. This is done by a fit to the background region in the right and wrong charge ΔM distribution where the fraction of the fit parameterisations for $\Delta M > 0.155$ GeV is used as normalisation factor c. For data $c = 1.02$ is determined, whereas for MC a factor of $c = 0.74$ is calculated. The MC normalisation factor is low because the MC was selected at generator level to have only D^* mesons in the golden decay channel. Thus the wrong charge distribution is not expected to be at the same height as the right charge non-resonant background.
The subtraction method is illustrated in figure 5.3, where a) displays the wrong and right charge distribution of the scattered electron energy and b) shows the subtracted distribution. In order to reduce as much background as possible prior to the subtraction a cut on the ΔM mass difference of ± 0.002 GeV is applied.

The second method for the extraction of the amount of D^* mesons is based on a fit to the full ΔM distribution. A sum of two functions, one for the signal and one for

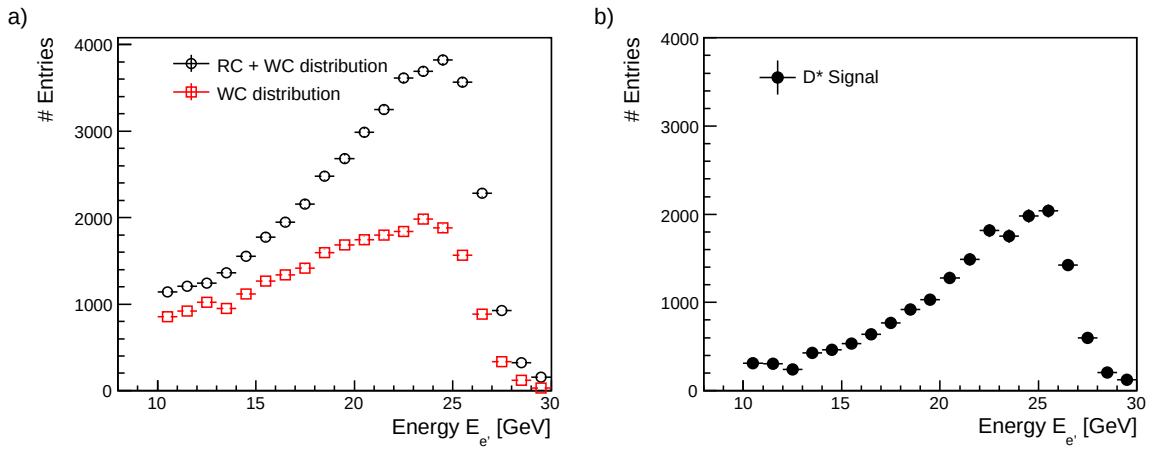

Figure 5.3.: *Illustration of the subtraction method using the distribution of the energy of the scattered electron. In a) the amount of events per bin for the right (filled symbols) and wrong charge distribution (open symbols) is depicted whereas b) shows the subtracted distribution as a function of the scattered electron energy.*

the background, is adopted to separate the signal from the background. This sum is then simultaneously fitted to the signal distribution and to the wrong charge ΔM distribution. Here the relative normalisation of the background function for the two data samples is left free. For the background the Granet parametrisation [G+78] is applied:

$$f(m) = (\delta m)^{p_1} \cdot \exp\left(-p_2 \delta m - (-p_3 \delta m^2)\right) \text{ with } \delta m = (m - m_\pi) \ . \tag{5.1}$$

δm denotes the difference of the mass $m = \Delta M$ subtracted by the pion mass $m(\pi)$, whereas p_1, p_2 and p_3 are left free for the fit procedure. The shape of the signal is asymmetric as illustrated in figure 5.4 therefore asymmetric parameterisations of the signal shape are applicable. In order to study systematic effects due to the a-priori not known exact signal shape, different fit parameterisations as described in chapter 9 are adopted. In the context of the previous analysis of D^* meson production in DIS [Boe07], extensive studies have been made with the conclusion that the *Crystal Ball* function [Gai82] (CB) is well suited to describe the peculiarities of the ΔM distribution. Therefore the standard signal extraction from the ΔM distribution follows this idea and implements the CB function:

$$f(m) = N \cdot \begin{cases} \exp\left(-\frac{1}{2}\left(\frac{m-\mu}{\sigma}\right)\right)^2 & \text{if } \frac{m-\mu}{\sigma} \leq -\alpha \\ \frac{\left(\frac{n}{|\alpha|}\right)^n \exp\left(-\frac{1}{2}\alpha^2\right)}{\left(\frac{n}{|\alpha|} - |\alpha| - \frac{m-\mu}{\sigma}\right)^n} & \text{if } \frac{m-\mu}{\sigma} > -\alpha \ , \end{cases} \tag{5.2}$$

as provided by the `RooFit` package [VK05]. The asymmetry of the fit is expressed by the parameter α which is a measure of the distance from the mean in σ where the Gaussian function changes to an exponential one. The sum of the CB- and the Granet function

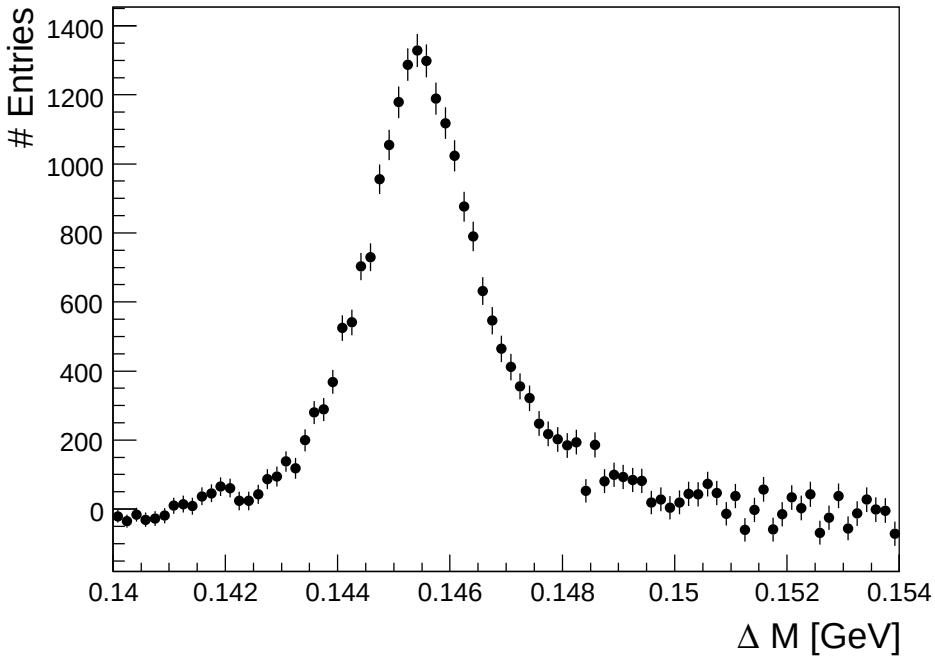

Figure 5.4.: *The signal region of the ΔM distribution. The background underneath the signal has been subtracted using a fit of the Granet function to the background only.*

has been fitted to the RC and the non-resonant WC ΔM distribution simultaneously in order to constrain the shape of the non-resonant background in the RC distribution as much as possible. If a ΔM distribution of a single bin for a measured quantity is fitted, the parameter α must be fixed to the value of the fit to the full data sample. Otherwise the fit converges badly because of low statistics and the result no longer describes the tail. The width of the signal is left free, because it can vary significantly for the different bins, especially for $p_T(D^*)$. For the minimisation the fit is performed as an unbinned negative log-likelihood fit ($\log(\mathcal{L})$ fit) where the likelihood is defined as:

$$\mathcal{L}(a) = \prod_{i=1}^{n} f(x_i|a) \ . \tag{5.3}$$

The likelihood gives the probability for a certain measured value x_i with a previously defined choice of the parameter a. The quantity $f(x_i|a)$ is normalised to one with respect to the parameter a. The unbinned negative log-likelihood-fit has the advantage that it maximises the use of available information to obtain the shape of a distribution. Furthermore there is no systematic bias due to a certain binning of the ΔM distribution which can arise if binned methods for limited data statistics are used [BL98]. Nevertheless the ΔM distributions depicted in the present thesis are binned to a reasonable value but the fit is always performed in an unbinned way. As mentioned the

minimisation of the fit uses the negative log-likelihood method $\mathcal{F}(a)$:

$$\mathcal{F}(a) = -\ln(\mathcal{L}(a)) = \sum_{i=1}^{n} \ln f(x_i|a) \ , \tag{5.4}$$

which is implemented in the `RooFit` package. `RooFit` is based on the `MINUIT` [Jam] package and provides an additional numerical integration for every step of the optimisation procedure. `RooFit` allows to compose fit functions in a very short and computational efficient way via the definition of probability density functions which are by definition positive definite and normalised to unity.
In order to make full use of the improved precision of the unbinned fit, it is necessary that the shape of the probability density $f(x_i|a)$ describes the data. The result of the fit of the sum of the asymmetric Crystal Ball function and the Granet background function is shown in figure 5.5 with a yield of more than $20,000$ D^* mesons in the signal. The signal to background ratio, calculated in the signal region from 0.142 to 0.152 GeV, is 0.35.

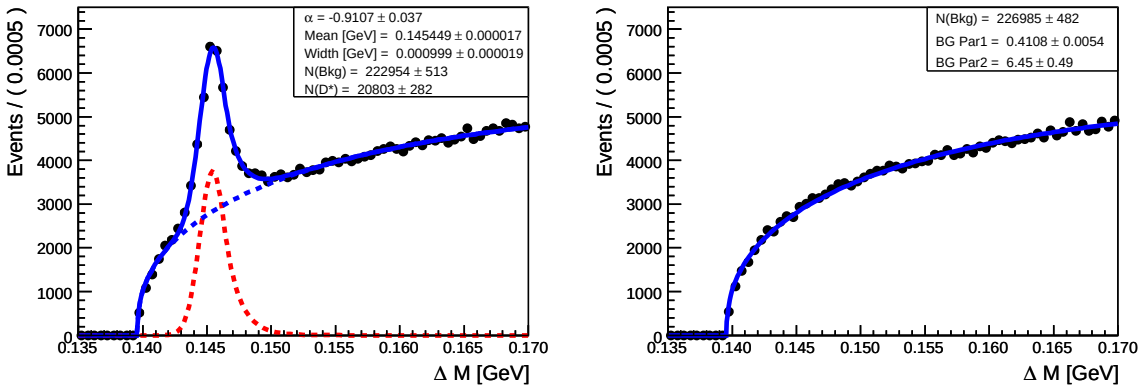

Figure 5.5.: *The ΔM distribution in data for the right charge sample with the combined signal and background fit indicated by the solid line (left). The signal and background contribution are drawn individually as the dotted lines. The wrong charge sample with the background fit drawn as the solid line (right). The parameters of the fits are given in the boxes.*

Toy Monte Carlo Studies

For the chosen combined shape (Crystal Ball + Granet function) it is of importance that it describes the ΔM distribution, otherwise a bias is introduced and the full advantages of the unbinned fit method is not exploited. In particular the dependence of the tail parameter α is studied as this is the most critical point.
The behaviour of the chosen probability density function has been studied by the generation of toy MC sets provided by the `RooFit` class RooMcStudy, which allows the generation of large samples for goodness-of-fit estimates. The starting parameters implemented for the toy MC generation are taken from the fit to the data as given in the box depicted in figure 5.5. As an example, one toy MC ΔM distribution is displayed

in figure 5.6 where the same fit function parametrisation as for data is adopted. The normalisation parameter N has a large negative effect on the convergence and time behaviour of the fit, which is why a fixation of this parameter is desirable. In order to

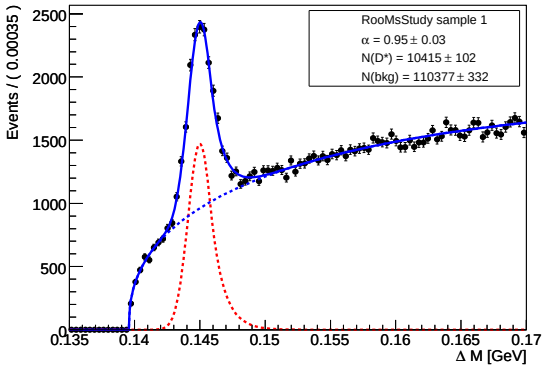

Figure 5.6.: *An example toy MC ΔM histogram as generated with the class RooMcStudy. The parameters for the generation are taken from the result of the combined fit to the ΔM distribution in data. The toy MC sample is itself fitted with the same fit parametrisation as the data are.*

fix it to an optimal value the dependence of N from the number of fitted $N(D^*)$ and from the asymmetry parameter α is studied with the toy MC samples. The result is illustrated in figure 5.7a) for the dependence from the fitted $N(D^*)$ and in b) for the dependence from α. The normalisation parameter N is fixed to $N = 120$, because at this value the fitted number of D^* is, within less than 0.5%, equal to $N(D^*) = 10400$, which has been used during the generation of the toy MC samples. Moreover this

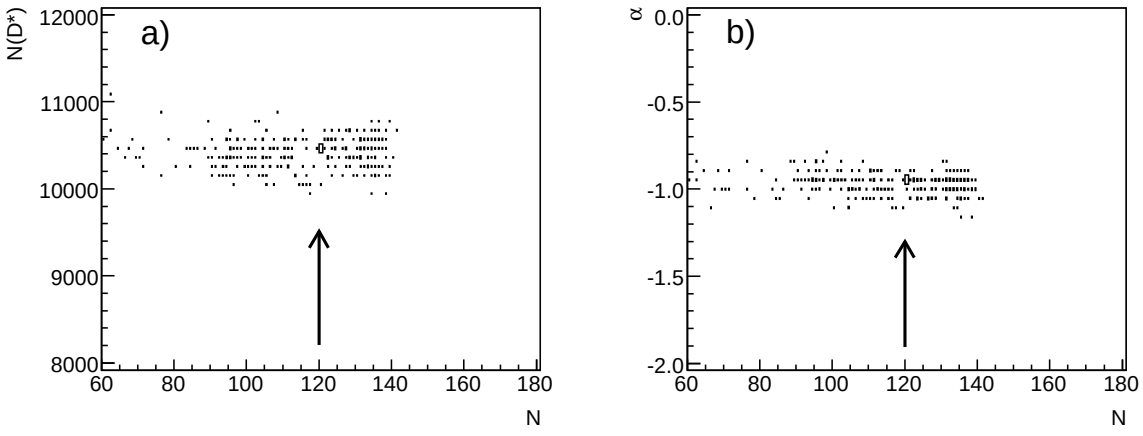

Figure 5.7.: *The fit results from* 500 *toy MC sets are illustrated as two dimensional scatter plots as a function of N and $N(D^*)$ a) and as a function of N and α in b).*

variability is most probably due to not optimal settings for `MINUIT`, which can be improved. For the dependence of α from the parameter N the optimal choice is also

$N = 120$ because the variability is again smallest for this value, as illustrated in figure 5.7b). Therefore N has been fixed to 120 for all following fits. An additional internal check is done by looking at the distribution of the pulls: the difference between the theoretical and the fitted values, divided by the estimated standard deviation. As it should be, the distribution of the pulls can be fitted precisely by a Gaussian centred at zero with a width equal to one.

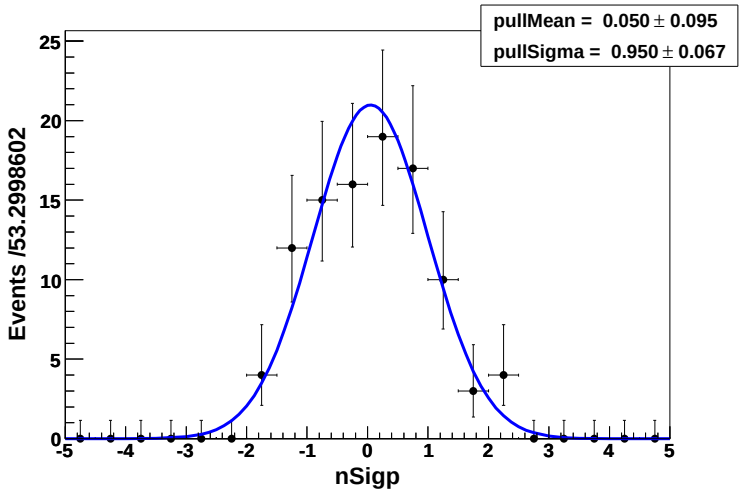

Figure 5.8.: *The distribution of the pulls for the toy MC sets.*

5.3. Unfolding of Detector Effects

A measurement in high energy physics faces the problems of limited acceptance, efficiency and resolution. In order to take these effects into account, different methods of data correction can be used depending on the complexity and behaviour of the measured quantity. Mathematically the problem can be expressed as:

$$y_i = \mathbf{A}_{ij} \cdot x_j \ , \tag{5.5}$$

where the measured distribution is given by y_i and the true distribution is x_j multiplied by a matrix $\mathbf{A}_{ij}$, which takes into account all effects mentioned above. The distribution y_i is usually derived from MC sets describing the detector response in all details. Roughly speaking, the matrix needs to be inverted in order to reconstruct the true distribution x_j but matrix inversion has well known problems and is therefore called mathematically and statistically "ill-posed" because: „small perturbation of the data can cause an arbitrary large perturbation of the solution" [Blo84]. The true distribution x_j can thus be obtained with different mathematically sophisticated methods [Blo84] that overcome inversion problems. Basically there are two completely different philosophies:

1. *Matrix unfolding*: Use the full migration and resolution information of the matrix $\mathbf{A}_{ij}$, i.e. perform matrix inversion,

2. or *Bin-by-bin unfolding*: Use only the diagonal elements of the matrix $\mathbf{A}_{ij}$, control migrations by using special assumptions.

For the first case a variety of techniques and methods are available needed to control fluctuations from off-diagonal elements of the matrix in an efficient way. Matrix inversion provides valuable information and reduces the dependence on the input MC distribution (or model) used in the MC generation process. Although matrix unfolding is the preferred way it is common and traditional to high energy physics experiments to use the bin-by-bin unfolding method which assumes no migrations between bins. Thus it is a comparatively simple method and is discussed in the following whereas the matrix correction method is presented in chapter 12.

Bin-by-bin Unfolding: Acceptance and Efficiency, Purity and Stability

The bin-by-bin unfolding assumes that there are no migrations between bins. If this is the case, the correction of detector effects like deficiencies and limited acceptance follows a simple approach. The correction is given by a simple factor or the inverse factor which is applied bin-wise. For clarity the correction is split up in a acceptance part and a efficiency part. The acceptance $\mathcal{A}$ is defined as follows:

$$\mathcal{A}_{\text{det}} = \frac{N^i_{gen} \ \&\& \ N^i_{acc}}{N^i_{gen}} \ , \tag{5.6}$$

where N^i_{gen} denotes the total number of generated D^* mesons and N^i_{acc} the number of generated events after a set of certain acceptance cuts. Thus it is a measure for the

fraction of events visible to the full detector, which is ensured by the acceptance cuts. The efficiency corrects the data for detector effects via the following definition:

$$\epsilon_{\text{det}} = \frac{N^i_{rec}}{N^i_{gen} \;\&\&\; N^i_{acc}} \;, \tag{5.7}$$

where N^i_{rec} is given by the sum of events which are generated and reconstructed in that bin and the number of events, which are generated in another bin but are reconstructed in that bin due to smearing effects. Moreover all acceptance cuts are applied for the calculation of N^i_{rec}. The results of the bin-by-bin unfolding method in terms of efficiency and acceptance used in the analysis are given and discussed in chapter 8. In order to account for lost information of the response matrix and a possible bias due to the dependence of the correction (efficiency and acceptance) from the input MC distribution, an uncertainty is assigned. This uncertainty is part of the model dependence discussed in chapter 9.
In reality migrations are present, i.e. there are non-diagonal elements in the detector response matrix $\mathbf{A}_{ij}$. In order to quantify these migrations within the bin-by-bin unfolding two variables called stability $\mathcal{S}$ and purity $\mathcal{P}$ are introduced. The purity $\mathcal{P}$ is given by:

$$\mathcal{P} = \frac{N^i_{gen} \;\&\&\; N^i_{rec}}{N^i_{rec}} \;. \tag{5.8}$$

It is defined as the number of events which are generated and reconstructed in the same bin $N^i_{gen} \;\&\&\; N^i_{rec}$ divided by the number of reconstructed events N^i_{rec} in the same bin i. As N^i_{rec} contains reconstructed events, which are generated inside and outside bin i the purity is a measure for the fraction of events in a given bin i which actually belong there. The other quantity to monitor migration effects is the stability $\mathcal{S}$:

$$\mathcal{S} = \frac{N^i_{gen} \;\&\&\; N^i_{rec}}{N^i_{gen} \;\&\&\; N^i_{acc}} \tag{5.9}$$

and is the fraction of events which are generated but not reconstructed in the same bin or to be more explicit it is the fraction of events which remains in a given bin.
In general for low migrations or $\mathcal{P} > 75\%$ the presented scheme is acceptable, but the statistical error is underestimated. In case of purities less than 30% the result in these bins of the measurement can be completely meaningless. In order to allow a reliable measurement the standard method is to optimise the binning in such a way, that the purity and stability as defined in equations 5.8 & 5.9 is above a certain threshold as discussed in section 8.1.

5.4. Reconstruction Methods for the Event Kinematics

At HERA the measurement of deep inelastic scattering events is overconstrained because the measurement relies not only on the scattered lepton. The measurement of the hadronic final state provides a redundancy for the estimation of the independent quantities x, y or Q^2. An event reconstruction method at HERA can thus be based on the use of the lepton final state or the hadronic final state or mixed methods as dis-

cussed in [BB95]. In order to minimise systematic errors, it is useful to first choose the reconstruction method providing the best detector resolution over the whole kinematic range of interest which in addition allows finer binning of a measurement. There are several reconstruction methods available, each of them having unique properties that give advantages or disadvantages for a measurement. In order to visualise the behaviour of a reconstruction method the following technique is used. The ratio $y_{\text{method}}/y_{\text{true}}$ is plotted against y_{true} where y_{true} is the fraction of energy available for the hard interaction as defined in equation 2.3. Each of the y_{true} bins projected on the y axis is fitted with a Gaussian function; this method is referred to as fit-in-slices method. The fitted values of the mean and resolution σ of a reconstruction method are plotted as function of y_{true}. This study is done using a large MC sample generated with RAPGAP including next-to-leading order QED corrections from HERACLES.
The different methods for the reconstruction of the event kinematics can be compared easily in figure 5.9a)-b) for the inelasticity y and in figure 5.10a)-b) for the virtuality Q^2 where the resolution and the mean for all reconstruction methods obtained by the fit-in-slices method are illustrated. The results are discussed together with a short introduction of the respective reconstruction methods in the following:

The electron-method (e-method)

The electron-method (e-method) of reconstruction of the event kinematics in deep inelastic scattering uses only the angle $\theta_{e'}$ and the energy $E_{e'}$ of the scattered electron, making it experimentally simple. The virtuality Q_e^2 is reconstructed as follows:

$$Q_e^2 = 2E_e E_{e'} \cdot (1 + \cos(\theta_{e'})) \tag{5.10}$$

and the inelasticity y and Bjørken x:

$$y_e = 1 - \frac{E_{e'}}{2E_e} \cdot (1 - \cos(\theta_{e'})) \text{ and } x_e = \frac{Q_e}{y_e \cdot s} \ . \tag{5.11}$$

The e-method is a very precise method for not too small values of $y_e > 0.10$ where the resolution is given by:

$$\frac{\delta y_e}{y_e} = \frac{(1 - y_e)}{y_e} \left(\frac{\delta E_{e'}}{E_{e'}} \oplus \frac{\delta \theta_{e'}}{\tan(\theta_{e'})} \right) \ . \tag{5.12}$$

The resolution degrades drastically if $y \to 0$ because of the $1/y_e$-term in the error propagation[2]. At low y this degraded resolution of the e-method, which has been used in previous D^* analyses, creates large systematic errors originating from the uncertainty of the $E_{e'}$ and $\theta_{e'}$ measurement deduced from the scattered electron. At least for low y the e-method should not be used for a precision measurement that aims for small systematic errors. By use of the e-method a further increase of the phase space towards lower y is not possible.
The result of the fit-in-slices method for the e-method is illustrated for the resolution in figure 5.9a), which shows a very good resolution at medium and large y with mean

[2]With $A \oplus B \equiv \sqrt{A^2 + B^2}$

values close to one. However, the adverse behaviour of the e-method at small y with resolutions of larger than 60% and a shift of the mean by 20% is clearly visible in figure 5.9b).
Although the e-method is rather insensitive to FSR QED radiation (see chapter 2 or section 8.2), as experimentally the photon is merged with the electron cluster, it is sensitiv to ISR QED radiation due to the presence of the beam energy in the calculation of the event kinematics. In case of an initial state radiated photon the incident electron energy is lowered by the photon energy: $E_e = E_{\text{beam}} - E_\gamma$, which hast the most influence at high y.
The resolution and mean for the virtuality Q^2 are displayed in figure 5.10a)-b), where the e-method shows a good resolution and a mean of one for almost the whole Q^2 range, except for lowest values of Q^2.

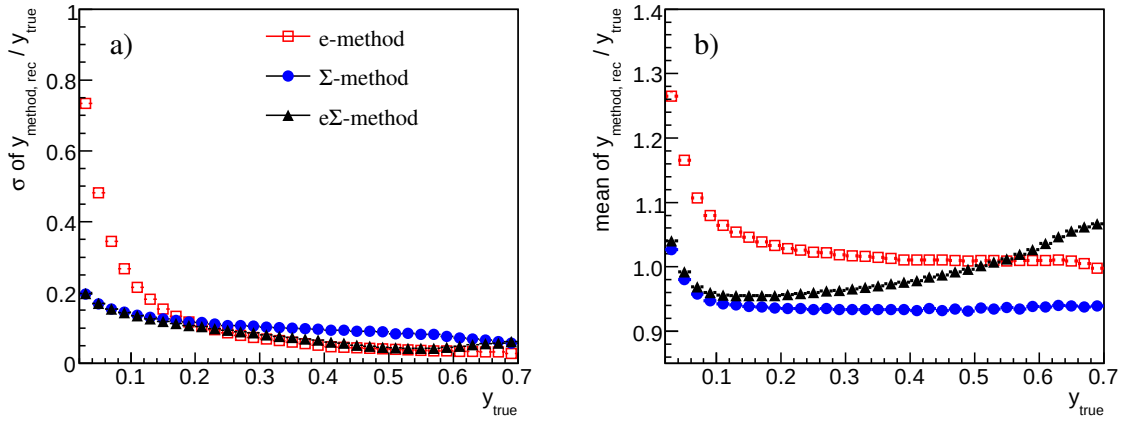

Figure 5.9.: *Resolution a) and mean b) of the different reconstruction methods as a function of the true y derived from fitted distributions of the fraction $y_{\text{method}}/y_{\text{true}}$ in a certain y_{true} bin.*

The Σ-method

A method which provides advantages in terms of resolution and also a vanishing sensitivity to ISR QED radiation is the Σ-method, which uses the hadronic final state for the reconstruction of the incident electron energy and is thus completely safe against ISR. The radiative corrections to the Σ-method are thus smallest compared to other methods. For a 4π detector energy-momentum conservation can be used to define the measured quantity Δ which is twice the electron beam energy: $\Delta = \Sigma + E_{e'} \cdot (1 - \cos(\theta_{e'})) = 2E_e$. The Σ-method for y is defined by:

$$y_\Sigma = \frac{\Sigma}{\Sigma + E'_e(1 - \cos(\theta_{e'}))} \text{ with } \Sigma = \sum_a (E - p_{z,\,a}) = \sum_a E_a \cdot (1 - \cos_a) \; . \qquad (5.13)$$

Σ is the difference of energy and longitudinal momenta of all hadronic final state particles and is by construction insensitive to losses in forward direction. The virtuality

Q^2 and Bjørken x are measured by:

$$Q^2_\Sigma = \frac{E^2_{e'} \sin^2(\theta_e)}{1 - y_\Sigma} \text{ and } x_\Sigma = \frac{E^2_{e'} \sin^2(\theta_e)}{s \cdot y_\Sigma (1 - y_\Sigma)} \,. \tag{5.14}$$

The resolution of the Σ-method is given by:

$$\frac{\delta y_\Sigma}{y_\Sigma} = (1 - y_\Sigma) \left(\frac{\delta \Sigma}{\Sigma} \oplus \frac{\delta E_{e'}}{E_{e'}} \oplus \frac{\delta \theta_{e'}}{\tan(\theta_{e'}/2)} \right). \tag{5.15}$$

High resolutions are achieved with the Σ-method for x_Σ whereas Q^2_Σ is slightly worse compared to the e-method (see figure 5.10a)-b)). In figure 5.9a)-b) the resolution and the mean for the Σ-method as obtained by the fit-in-slices method is illustrated. A flat behaviour for almost the whole y range is observed although the mean is systematically shifted towards lower values by 8%. At smallest y a dependence on the true y is observed where the mean, depicted in figure 5.9b), is shifted towards higher values by about $10 - 15\%$. The resolution as illustrated in figure 5.9a) gets worse but not as much as for the e-method.

The $e\Sigma$-method

The $e\Sigma$-method is a mixed method where the e-method is used at high $y_{e\Sigma}$ and the Σ-method is used at low $y_{e\Sigma}$. Due to the use of the e-method the $e\Sigma$-method gets slightly affected by QED radiative corrections. The $e\Sigma$-method is defined with the following prescriptions:

$$Q^2_{e\Sigma} = Q^2_e \tag{5.16}$$

$$y_{e\Sigma} = \frac{2E_e \Sigma}{\left(\Sigma + E_{e'} \cdot (1 - \cos\theta_{e'})\right)^2} \tag{5.17}$$

$$x_{e\Sigma} = x_\Sigma. \tag{5.18}$$

The resolution of the $e\Sigma$-method as obtained by the fit-in-slices method is illustrated in figure 5.9a) demonstrating the improved behaviour of the $e\Sigma$-method for the resolution over the whole y range compared to other reconstruction methods. Although the mean values for the $e\Sigma$-method as depicted in 5.9b) depend on the true y value the distance to the mean of the e-method is always smaller than the one of the Σ-method. This fact further strengthens the choice of the $e\Sigma$-method. Part of the dependence of the mean with the true y originates from the imperfect knowledge of the hadronic and electromagnetic calibration, which is taken into account by a hadronic and electromagnetic energy scale uncertainty assigned to the measurement (see chapter 9). For the virtuality the $e\Sigma$-method and the e-method coincide as for the $e\Sigma$-method Q^2 is reconstructed by the e-method (see figure 5.10).

In summary, the $e\Sigma$-method combines the region with good resolution from the Σ-method at low y and the one from the e-method for medium and high y. The significantly increased resolution at low y allows for an extension of the visible phase space down to $y = 0.02$, which increases the event yield and extends the measurement to a new phase space as previous D^* measurements started at $y > 0.05$ [A+07].

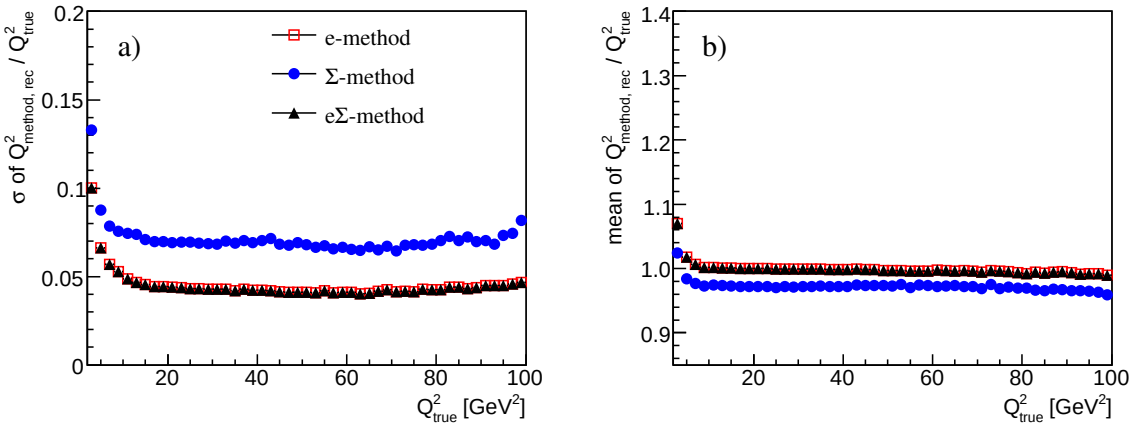

Figure 5.10.: *Resolution a) and mean b) of the different reconstruction methods as a function of the true Q^2 derived from fitted distributions of the fraction $Q^2_{\text{method}}/Q^2_{\text{true}}$ in a certain Q^2_{true} bin.*

Furthermore, the increased resolution reduces systematic uncertainties significantly, as discussed in chapter 9.
It should be mentioned for completeness, that the double angle method [BB95] has been discarded because it possesses a flat resolution of about 30% over the whole y range.
In order to study the different reconstruction methods, particularly with regard to the optimal use in the presented analysis, the effect of a reconstruction method on the resolution of a measured quantity is discussed. These measured quantities are discussed in the following.

Reconstructed Quantities of the Charmed Heavy Meson

The results of the study discussed above suggests that the mixed $e\Sigma$-method is an optimal choice for the event reconstruction. Nevertheless, as the reconstruction method affects the resolution of a D^* meson quantity and therefore alters the behaviour of the efficiency and purity of this D^* meson quantity, the choice of the reconstruction method is revised.
For the D^* meson cross section measurement, as discussed in chapter 10.2, the following reconstructed D^* quantities are of interest: η, p_T, z, x_g^{obs}. The pseudo-rapidity of the D^* meson is related to the polar angle θ and defined as:

$$\eta = -\ln\left(\tan\left(\frac{\theta}{2}\right)\right) \quad , \tag{5.19}$$

whereas p_T denotes the transverse momentum of the D^* meson in the laboratory system, which has also been measured in the photon-proton centre-of-mass frame. This quantity is labelled p_T^*. The fragmentation variable z as defined in equations 2.15-2.17 is experimentally not accessible in a direct way. A accessible quantity, which is related to the fragmentation, measures the fraction of energy that is transferred from the γ to the D^* meson in the photon-proton rest frame. This inelasticity of the D^* meson is

called $z(D^*)$ and calculated by:

$$z = \frac{E(D^*) - p_z(D^*)}{2 \cdot yE_e} \ . \tag{5.20}$$

As discussed in section 2.4 the D^* meson production is directly sensitive to the gluon density. In addition to the extraction of the charm structure function also a more direct measurement of the gluon density is possible. The basis is the measurement of the quantity $x_{\mathrm{g}}^{\mathrm{obs}}$:

$$x_{\mathrm{g}}^{\mathrm{obs}} = \frac{\frac{\left(p_T^2(D^*) + m^2\right)}{(z \cdot (1-z))} + Q^2}{y \cdot s} \quad \text{with} \quad z = \frac{E(D^*) - p_z(D^*)}{2 \cdot yE_e} \ . \tag{5.21}$$

In order to extract the gluon density from $x_{\mathrm{g}}^{\mathrm{obs}}$ means of an unfolding procedure using NLO QCD predictions as discussed in [A+99] are needed.
The resolution of quantities is influenced by the different reconstruction methods, where

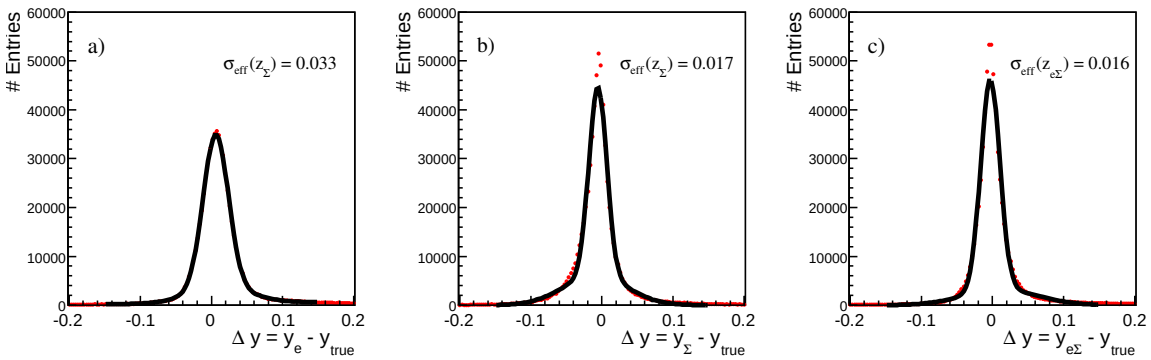

Figure 5.11.: *Effective resolution* σ_{eff} *of* y *obtained from Gaussian fits to the* $\Delta y = y_{\mathrm{method}} - y_{\mathrm{true}}$ *distribution for the different event reconstruction methods.*

y is either directly or indirectly involved, e.g. for $z(D^*)$. Moreover quantities, like $x_{\mathrm{g}}^{\mathrm{obs}}$, are affected because they need boosts where the four-momentum vector of the photon is used, as it relies on the electron four-momentum vector before and after the hard interaction. Figure 5.11 illustrates the resolution of y for different event reconstruction methods. The resolution is obtained from a fit to the $\Delta y = y_{\mathrm{method}} - y_{\mathrm{true}}$ distribution with a double Gaussian parametrisation. The effective peak resolution is calculated by:

$$\sigma_{\mathrm{eff}} = \frac{A_1\sigma_1 + A_2\sigma_2}{A_1 \cdot A_2}, \ \text{where} \ f_{1,2}^{\mathrm{Gauss}}(x) = A_{1,2} \cdot \exp\left(\frac{-0.5 \cdot (x - \mu_{1,2})^2}{\sigma_{1,2}^2}\right) \ . \tag{5.22}$$

For the e-method (see figure 5.11a)) an effective resolution of $\sigma_{\mathrm{eff}(e)} = 0.033$ is determined, while the Σ- and $e\Sigma$-method, as depicted in figure 5.11b)-c), illustrate an improved resolution with $\sigma_{\mathrm{eff}(\Sigma)} = 0.017$ and $\sigma_{\mathrm{eff}(e\Sigma)} = 0.016$. Although only slightly better than the Σ-method both are a factor of two better compared to the e-method.

For $z(D^*)$ the improvement in terms of the resolution is not as much as one could expect, although the tails of the $\Delta z = z_{\text{method}} - z_{\text{true}}$ distribution are reduced for the $e\Sigma$-method (see figure 5.12c)) compared to the e-method which is shown in figure 5.12a). In summary the $e\Sigma$-method provides an improved resolution for the measured

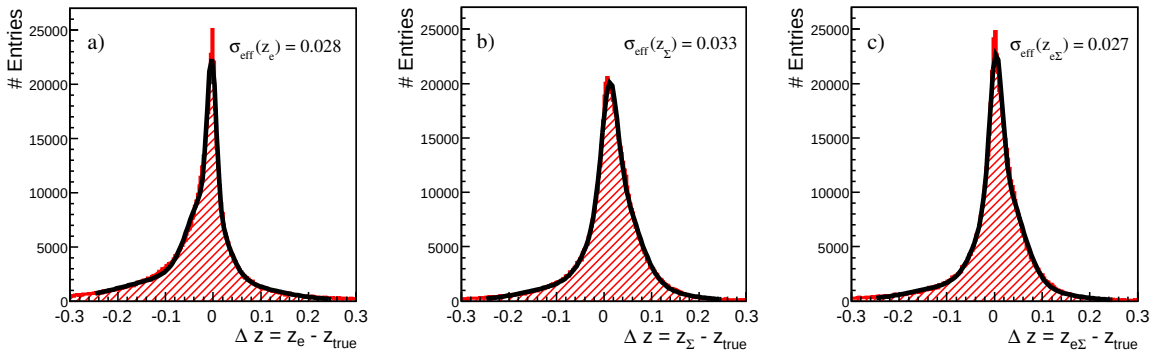

Figure 5.12.: *Effective resolution* σ_{eff} *of* $z(D^*)$ *obtained from Gaussian fits to the* $\Delta z = z_{\text{method}} - z_{\text{true}}$ *distribution for the different reconstruction methods.*

D^* quantities compared to other reconstruction methods. The resolution of a reconstructed quantity affects the correction of the detector effects as outlined below.

Influence of the Reconstruction Method on the Detector Correction

The efficiency and purity as defined in equations 5.6-5.8 of measured quantities is affected by the reconstruction method because of different resolutions. As an example the efficiency and purity for y and $z(D^*)$ is discussed, which are displayed in figure 5.13. They illustrate the improved behaviour of the $e\Sigma$-method. In particular for the high statistics region at low y the resolution of the e-method is worse and thus a lower efficiency a) and purity c) is determined. For the low y region the Σ- and $e\Sigma$-method have both better resolutions and accordingly give 20% higher efficiencies and $> 10\%$ higher purities (see figure 5.13a) and c)) compared to the e-method. This advantage of the $e\Sigma$-method at low y allows the increase of the measurement towards lower y compensating for the fact that the $e\Sigma$-method has on average a 10% lower efficiency at medium and high y compared to the e-method, which is acceptable. The efficiency of the Σ-method drops down drastically at high y as depicted in figure 5.13a).
The impact on $z(D^*)$, where y is used directly for the calculation according to equation 5.20, is not as much in terms of a higher efficiency but rather in terms of a flat efficiency. The efficiency for $z(D^*)$ as shown in figure 5.13b) illustrates a strong $z(D^*)$ dependence if the e-method is adopted, whereas the $e\Sigma$-method improves the distribution significantly to a more reasonable and desirable flat efficiency. Furthermore a flat and even higher purity as displayed in figure 5.13d) is achieved for the $e\Sigma$-method where the e-method shows deficiencies at low $z(D^*)$.

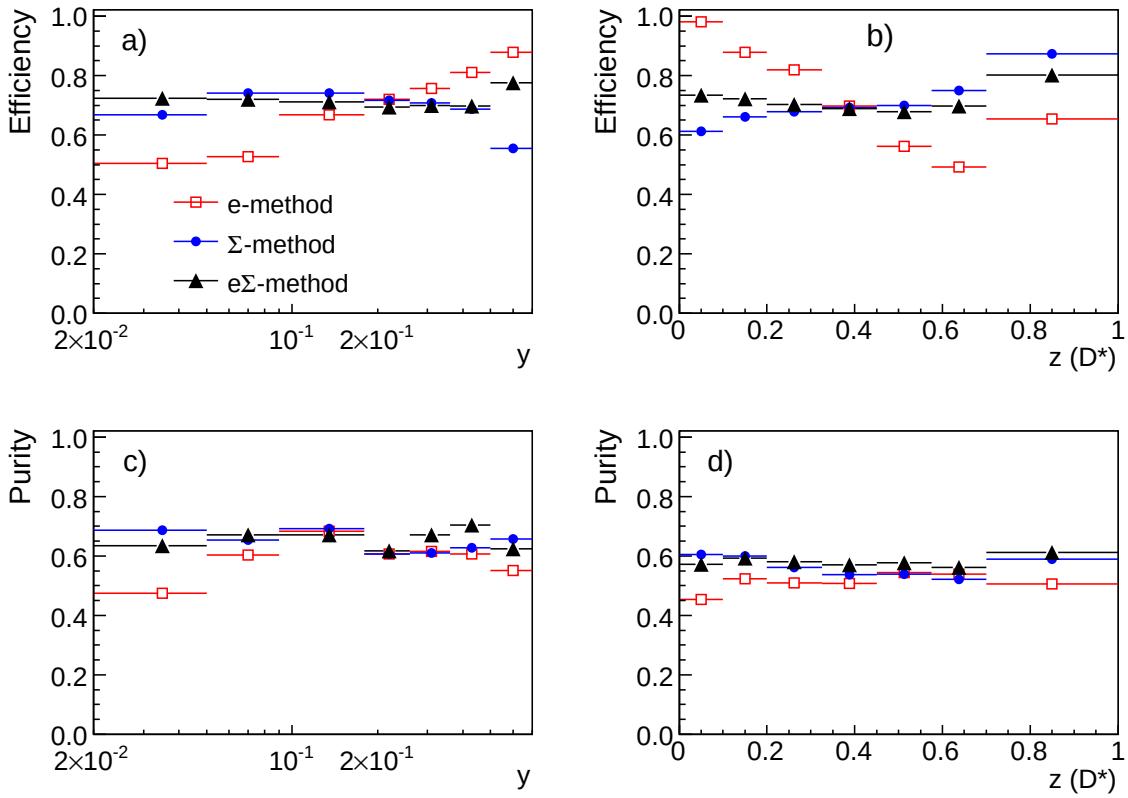

Figure 5.13.: *The effect of different event reconstruction methods used for the measurement is shown for the reconstruction efficiency a)-b) and the purity c)-d) calculated for y and $z(D^*)$, where y is directly used for the calculation.*

Final Choice of the Reconstruction Method for the Event Kinematics

The studies of the characteristics of the e-, Σ- and $e\Sigma$-method in terms of the correlation with the true variables, their resolutions and finally their purities and efficiencies for certain quantities motivated the mixed $e\Sigma$-method as the optimal choice. The $e\Sigma$-method provides overall good resolutions allowing finer binning and in addition shows flat and even higher purities and efficiencies compared to the e- or Σ-method. Furthermore the correction factors needed to specify the cross section for the one-photon exchange are small compared to the e-method as outlined in more detail in section 8.2.

6. Run and Event Selection

In order to ensure a stable and efficient detector configuration during data taking in general only good and medium quality runs are included for the analysis. Furthermore a trigger phase larger equal two is requested, which ensures that only runs are included where the HV is 100% on and stable prescale settings have been derived. Moreover the high voltage of the following subdetectors is requested: CJC1 & CJC2, LAr, SPACAL, VETO, LUMI, CIP and TOF. The integrated luminosity is corrected for the HV settings. Furthermore a z vertex within 35 cm of the expected primary vertex is requested. The subtrigger for the present analysis is s61 as introduced in section 5.1. The data were taken with the H1 detector in the years 2004 to 2007 and correspond to an integrated, for prescale and HV settings corrected, luminosity of $\mathcal{L} = 347.6$ pb^{-1}. The luminosity of the individual years and the corresponding average prescale factor together with the lepton type is summarised in table 6.1. The luminosity is shared almost equally between positrons and electrons.

year	lepton type	luminosity $\mathcal{L}$ [pb^{-1}]	avg. prescale
2004	positron	48.8	1.02
2005	electron	107.8	1.02
2006	electron	55.1	1.00
2006	positron	88.4	1.01
2007	positron	47.5	1.00

Table 6.1.: *The prescale corrected luminosity and the average prescale factor of the used subtrigger 61 taken in the HERA II running period of* $2004 - 07$ *with the lepton type.*

6.1. Off-line Event Selection

The deep inelastic scattering events are selected with the cuts summarised in table 6.2. The cut on the electron energy is motivated by the energy threshold of the SPACAL trigger element SPCLe_IET of $E_{e'} > 9$ GeV [Fer04] during the HERA II data taking. The the cut on the electron angle is motivated by the geometrical acceptance of the SPACAL detector, which corresponds to an angle of $153° < \theta_{e'} < 177°$. Additional geometrical cuts are applied run-dependent to remove inefficient regions of the SPACAL. As an example the distribution of the cluster position of all selected events in the SPACAL is depicted per year (indicated at the top) in figure 6.1. To avoid edge effects the inner part of the SPACAL is not used and a radius cuts of 12 cm is applied. In addition inefficient regions in terms of dead SPACAL cells, which are marked in figure 6.1 by light-colored (red) boxes or hot SPACAL cells not implemented for the trigger

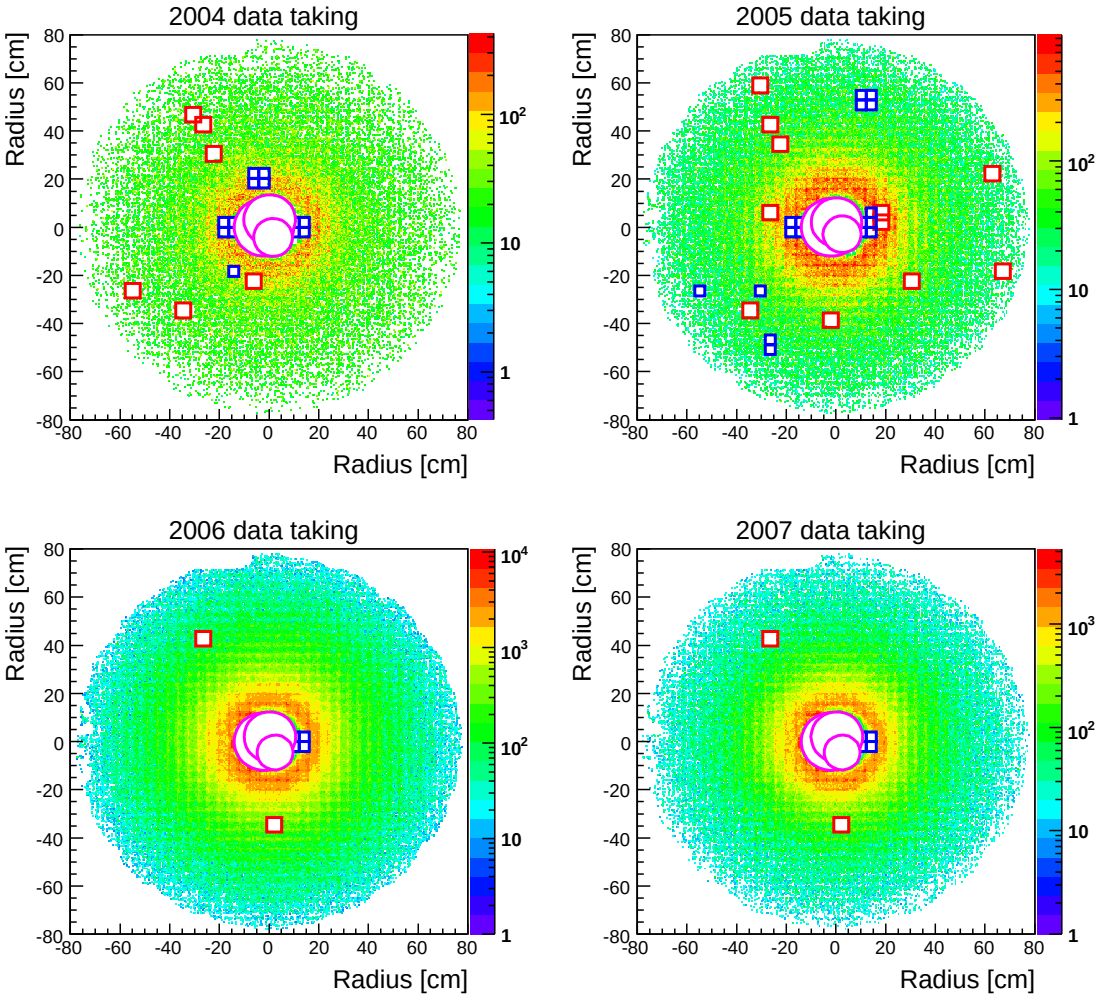

Figure 6.1.: *Distribution of the cluster position in the SPACAL for all years of the data taking. The inner region are cut out by circular cuts. Furthermore regions with decreased sensitivity, i.e. dead cells (light-colored red boxes) or hot cells excluded from the trigger (dark-colored blue boxes), are discarded by fiducial cuts as indicated.*

name	value
Virtuality	$5 < Q^2 < 100$ GeV^2
Inelasticity	$0.02 < y < 0.70$
Electron energy	$E_e^{'} > 10$ GeV
Electron angle	$153° < \theta_{e'} < 177°$

Table 6.2.: *Cuts for the selection of deep inelastic scattering events.*

(dark-colored blue boxes) are discarded. These fiducial cuts are the same for the 2007 and 2006 data taking because the SPACAL configuration was basically the same for both years.
All cuts on the transverse momenta, pseudo-rapidity and invariant masses of the D^* meson and its decay products are summarised in table 6.3. The cuts on the transverse momenta are applied to ensure an efficient track reconstruction. Furthermore light quark background is suppressed due to the fact that the decay particles of the D^* meson have on average a higher transverse momentum than other hadrons. To suppress more background an additional cut on the scalar sum of the p_T of the decay products of the heavy D^0 meson is applied, which makes use of the additional transverse momentum due to the decay into two light mesons. As the direction of the decay particles is

name	value
$p_T(K)$	> 0.3 GeV
$p_T(\pi)$	> 0.3 GeV
$p_T(\pi_{\text{slow}})$	> 0.120 GeV
$p_T(K) + p_T(\pi)$	> 2.0 GeV
$\lvert\eta(K, \pi, \pi_{\text{slow}})\rvert$	< 1.7
$\lvert M(K\pi) - M(D^0)\rvert$	< 0.08 GeV
ΔM	< 0.170 GeV
$p_T(D^*)$	> 1.5 GeV
$\lvert\eta(D^*)\rvert$	< 1.5

Table 6.3.: *Selection cuts on the transverse momenta and pseudo-rapidity of the D^* track and the tracks of its decay particles. Additional cuts for the invariant masses of the reconstructed heavy mesons are applied.*

correlated with the direction of the original D^* meson a cut on the pseudo-rapidity of the decay tracks is applied, which ensures a track measurement in an efficient η region. For the decay particles of the D^* meson a relaxed $|\eta|$ cut of 1.7 is done in order to not constrain the $|\eta|$ range of the D^* meson where $|\eta| < 1.5$ is requested. The selection cuts of the right charge D^* sample are additionally used to select a wrong charge sample, which is utilised to study the non-resonant background of the right charge sample as outlined in chapter 5. Furthermore for the $M(D^0)$ histogram a stringent ΔM window cut of ± 0.002 GeV around the nominal ΔM value for D^* mesons of 0.1454 GeV is applied. This histogram is only used for cross checks, while the ΔM distribution is used for the statistical determination of the number of D^* mesons.
For the D^* meson cross section measurement presented in chapter 8 the covered phase space is defined by so-called visibility cuts summarised in table 6.4. Within the visibility cuts the measured D^* cross sections are corrected for detector effects, which allows a comparison to theoretical models.

Yield of the D^* Meson Selection

The run quality and data selection stability is checked by a common method that examines the flatness of the production yield of the analysed event type. For this purpose

variable	value
Virtuality	$5 < Q^2 < 100$ GeV^2
Inelasticity	$0.02 < y < 0.70$
Transverse momentum	$p_T(D^*) > 1.5$GeV
Pseudo-rapidity	$\|\eta(D^*)\| < 1.5$

Table 6.4.: *The phase space coverage (visible range) of the cross section measurement as presented in chapter 8 is defined by these so-called visibility cuts.*

all selection cuts (see table 6.2 and 6.3) are applied and the amount of D^* mesons as determined by a fit in bins of constant luminosity of the analysed subtrigger (s61, see section 5.1) is plotted as a function of the run number. This distribution is called *yield plot*, which is an efficient technique to spot deficits or other problems in a certain run range quickly, because the yield is expected to be flat within the statistical precision. The yield plot for the present analysis that covers the full HERA II data taking period with a run range of $367259 - 500611$ is illustrated in figure 6.2. The first step at run

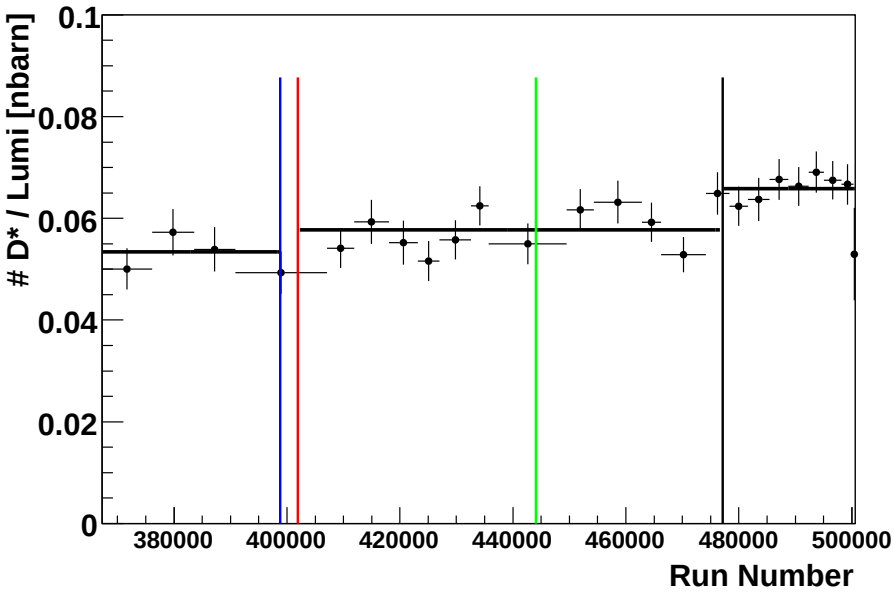

Figure 6.2.: *The yield of D^* mesons selected according to table 6.2 and 6.3 in bins of constant luminosity covers the full HERA II data taking period (*runrange : $367259 - 500611$*). The lines correspond to major changes during the data taking which are explained in the text.*

~ 401924 indicated by the first two lines[1] corresponds to the change from the DC$r\varphi$ trigger to the Fast Track Trigger for the track condition implemented in subtrigger s61 at the beginning of the year 2005 (also seen in [Boe07]). The improved reliability and

[1]The gap between the lines corresponds to a larger HERA shutdown.

trigger efficiency of the FTT (see section 8.1) lead to a yield increase of about (8±0.5)% compared to the yield where the DC$r\varphi$ trigger was implemented. If only the almost constant region of the yield with stable trigger and luminosity conditions (2005 to mid 2006) is fitted a yield of $(5.77 \pm 0.11) \cdot 10^{-2}$ D*/nb^{-1} is determined. The second step at approximately run number 477000 is related to the luminosity measurement. The step is currently not fully understood but investigated by a special luminosity task force (see for instance [NS+08]). This step is seen by all H1 analyses more or less significant because of the different amount of statistics. The statistics of the D^* data sample is not large enough to constrain the jump reasonably. From high statistic inclusive data samples an increase of around 8% has been observed (see chapter 9).

7. Control Distributions for DIS Events

A control distribution allows to check for imperfect descriptions of the data by the full detector simulation. Basically there are two possible reasons for disagreements between data and MC: First of all the generated distribution can be wrong, which is solved by reweighting the MC and second the efficiency is wrong in a localised region. The latter is the difficult case where the MC simulation needs to be corrected or the doubtful region has to be excluded from the analysis. In addition the description of the data by the MC in general is of interest, as a good agreement is the basis for the bin-by-bin method of data correction (see section 5.3). The reconstruction version adopted for data and MC is dst3[1]. The method to suppress the wrong charge background in the data is either the statistical subtraction method or the fit method as introduced in section 5.2 and is stated in the caption of a control distribution. This choice depends on whether the width of a signal peak is expected to change as a function of the controlled quantity, which it does for instance for $p_T(D^*)$, or not. The normalisation is done according to the number of D^* events in data. The data are only compared to a RAPGAP MC sample with QED NLO corrections from HERACLES (see table 4.1 for details on the generation) because of the method applied for the conversion of the cross section to the Born level (see section 8.2). Thus CASCADE is not utilised for the data correction as it does not provide an interface for QED NLO contributions from HERACLES. However, CASCADE is used to study the model dependence of the D^* cross section measurement as it is discussed in chapter 9.
For the present analysis no reweighting because of wrongly generated distributions is

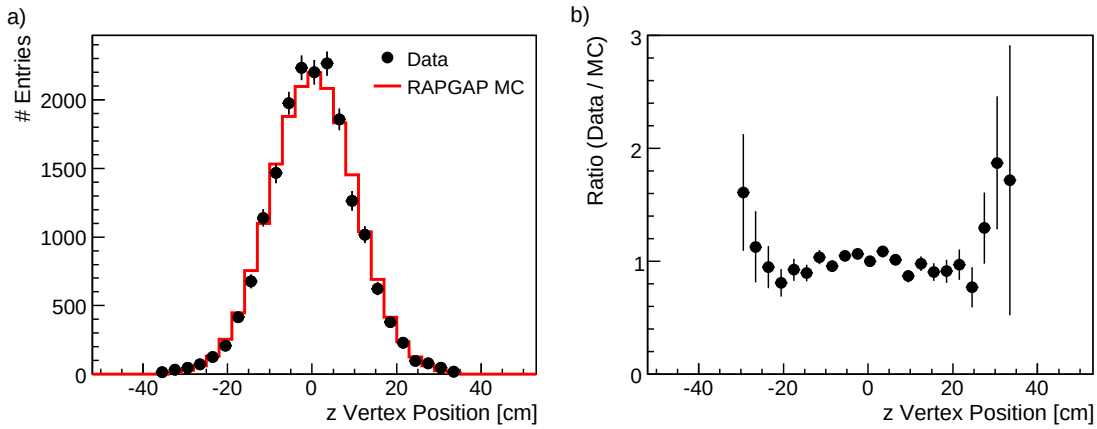

Figure 7.1.: *Distance in z direction of the interaction point to the nominal z vertex position a) for data (filled circles) compared to MC (solid line). The combinatorial background in data is subtracted using the statistical subtraction method. The ratio b) between data and MC is adopted for the MC reweighting.*

[1]Except for the studies made for the extended phase space region where dst5 is used.

needed with the sole exception of the z vertex distribution. This distribution is not expected to describe the data by default, as it is smeared during the generation process such that it is broad enough to overlap with any z vertex distribution of a physics analysis. Thus a reweight of the z vertex distribution described in the following is needed. Background caused by interactions of the protons with remaining dust particles due to the not perfect vacuum or the beam pipe itself are suppressed by a cut on the z vertex position of $|z_{\text{vtx}}| < 35$ cm compared to the expected position. In figure 7.1a) the distance in z direction of the interaction point to the nominal z vertex position for the selected events in data (filled circles) compared to MC (solid line) is displayed. The combinatorial background in data is subtracted with the statistical subtraction method. Although there is only a small difference between data and Monte Carlo the z vertex is reweighted according to the function that is fitted to the fraction $z_{\text{data}}/z_{\text{MC}}$ as illustrated in figure 7.1b).

7.1. Control Distributions for Electron Quantities

The control distributions of the electron quantities, which are based on the measurement of the scattered electron in the SPACAL, are discussed here. Figure 7.2 focuses

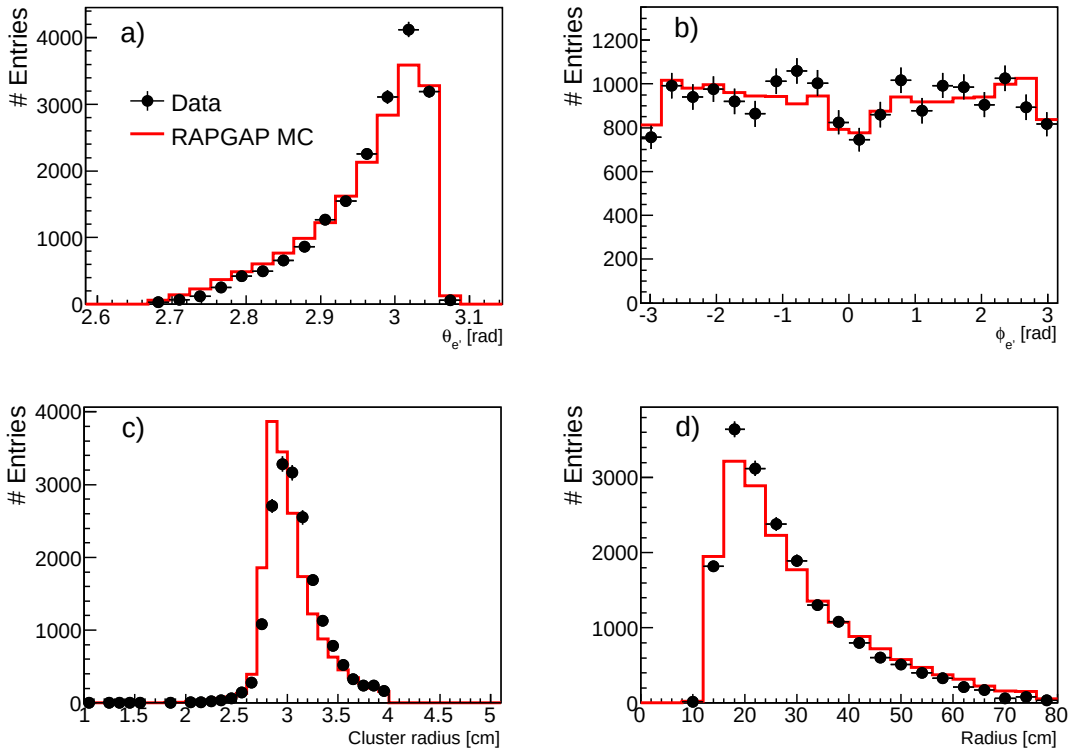

Figure 7.2.: *Control distributions of quantities of the electron final state, which are measured in the SPACAL for data (filled circles) and MC (solid line). The background has been subtracted using the statistical subtraction method.*

on the angles $\theta_{e'}$ a) and $\phi_{e'}$ b) of the scattered electron, the radius c) of the cluster associated to the scattered electron and the radial position of this cluster d). A nice

description of the data by the Monte Carlo is achieved although there is a slight undershoot of the MC at large $\theta_{e'}$ or low radii. The dips in the $\phi_{e'}$ distribution at zero and $\pm\pi$ are due to deactivated SPACAL trigger cells as indicated in figure 6.1.
In figure 7.3 control distributions of the reconstructed kinematic quantities are de-

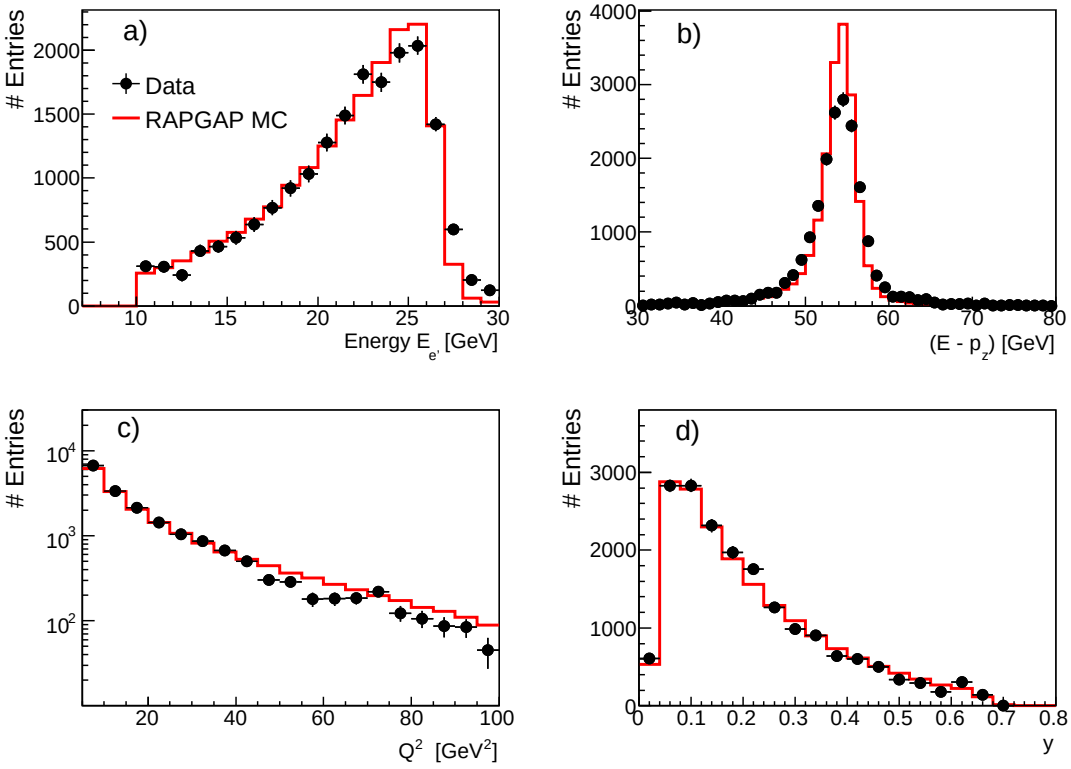

Figure 7.3.: *Control distributions of quantities which are either directly measured or deduced from measurements in the SPACAL. Data are always drawn as filled circles and the MC as solid line. The background has been subtracted using the statistical subtraction method.*

picted. The distribution of the energy of the scattered electron a) is in general nicely reproduced by the MC. However, the edge at high energies of the scattered electron is sharper in MC than in data, which is possibly due to an overestimated resolution in MC. The distribution of $(E - p_z)$ b) is, because of energy & momentum conservation, expected to peak at $2 \cdot E_e = 55$ GeV if all particles have been detected. This quantity is well suited to suppress photoproduction background, which is expected to be at values of $(E - p_z) < 30$ GeV. However, a cut on $E - p_z$ against photoproduction is not needed because there are hardly any events below 35 GeV. The Q^2 distribution c) is reasonably well described but shows some deficits in the description at medium Q^2 range above 40 GeV^2. The y distribution is in general nicely described by the MC. The slight missmatch between the edge in data and MC at high energies of the scattered electron energy does not affect the y distribution at small y because the $e\Sigma$-method is implemented for the reconstruction of the event kinematics and by that also the hadronic final state is used at low y. This improves the description at low y.

7.2. Control Distributions for D^* Meson Events

The description of the transverse momentum of the D^* meson and the D^0 meson originating from the decay of the D^* meson is a useful test of the generated distribution. The combinatorial background is taken into account using a fit to the ΔM distribution

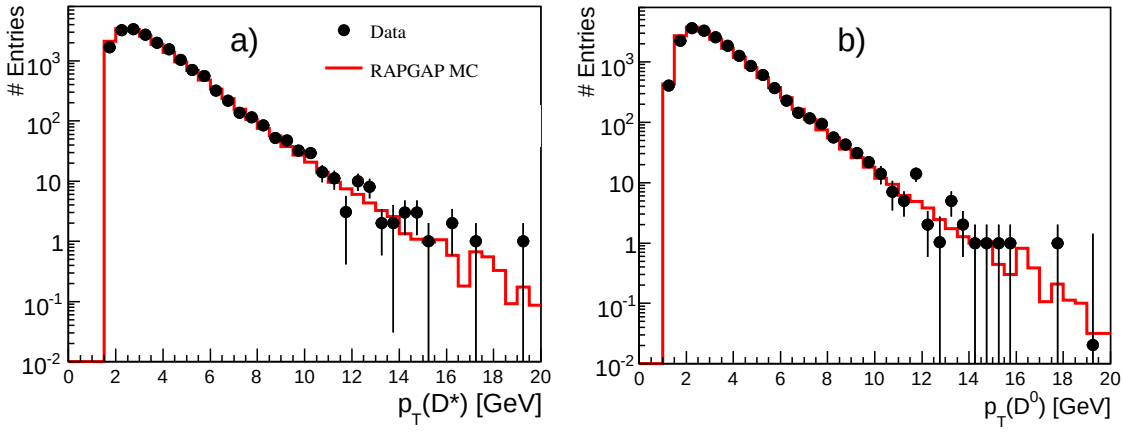

Figure 7.4.: *Comparison of the p_T spectra in data (filled circles) and Monte Carlo (solid line) for D^* mesons shown left and for D^0 mesons originating from the decay of the D^* meson shown right. The background has been subtracted using a fit to the ΔM distribution for every bin.*

in bins of $p_T(D^*)$ or $p_T(D^0)$. The Monte Carlo distribution is normalised to the number of D^* mesons in data. Figure 7.4a) illustrates the good description of the p_T spectrum of the D^* meson by the MC. Also the p_T spectra of the D^0 meson of the D^* decay is well described as illustrated in figure 7.4b). The ratio of data to MC for the $p_T(D^*)$

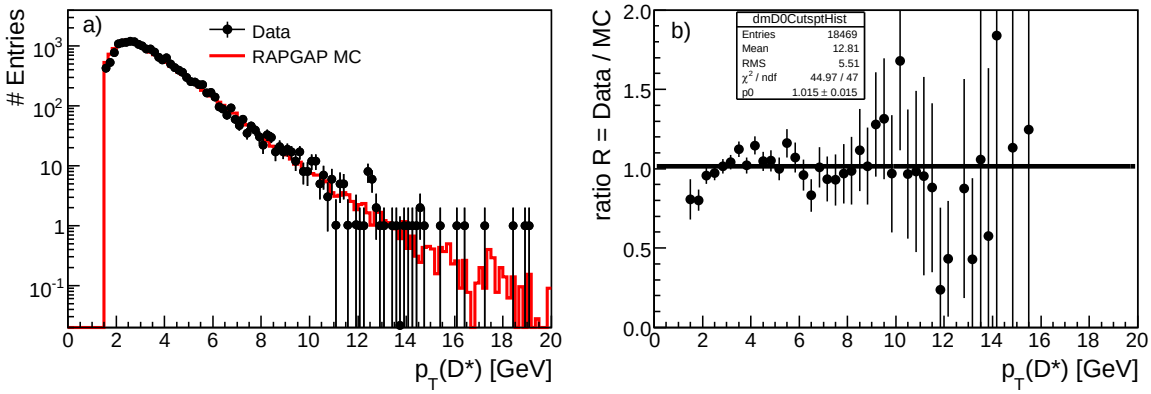

Figure 7.5.: *In a) the data (filled circles) is compared to Monte Carlo (solid line) dependence from the transverse momentum of the D^* meson. b) depicts the ratio of data to MC. The background has been subtracted using a fit to the ΔM distribution for every bin in $p_T(D^*)$.*

distribution is shown in figure 7.5b), no need to reweight the p_T of the D^* meson is observed. However, the first two $p_T(D^*)$ bins are slightly overestimated by the MC. Within the statistical precision of the data there is no different $p_T(D^*)$ slope in MC, which was also seen in a previous measurement of D^* meson production in DIS [Boe07]. Therefore it is assumed that the D^* production process is well described by the Monte Carlo simulation.

Tracks of the Decay Particles

The description of the transverse momentum of the tracks originating from the decay of the D^* meson is a crucial test for the implementation of the CJCs and the dead material in MC. The p_T spectra of the decay particles of D^* mesons are displayed in figure 7.6a)-c). Because of a cut on the scalar sum of the p_T of the kaon and pion track the corresponding distribution is added as figure 7.6d). No significant deviation between data and Monte Carlo is observed, except a overshoot of the MC in the p_T distribution of the kaon track below 0.5 GeV whereas the slow pion track is described nicely down to 0.12 GeV. Thus an inefficiency of tracks below 500 MeV is not likely the cause for the discrepancy in the $p_T(K)$ distribution. In order to localise inefficiencies

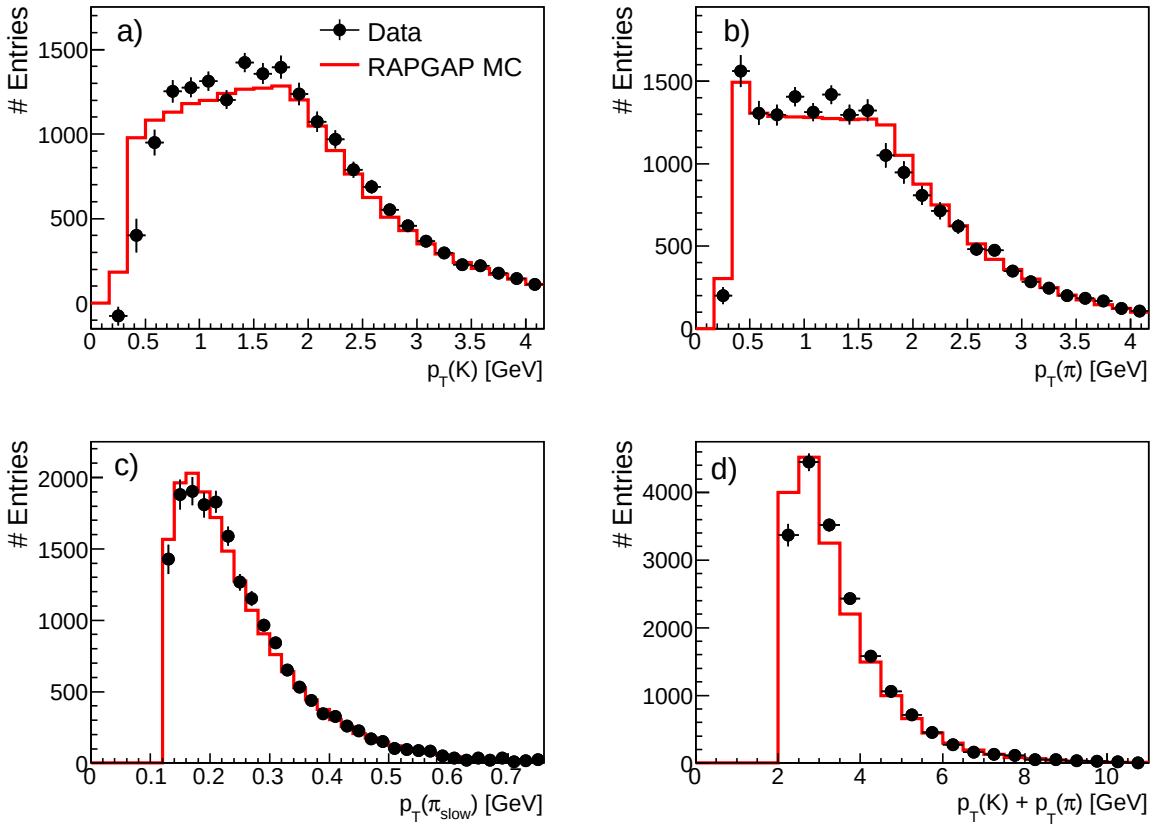

Figure 7.6.: *The p_T spectra of the three decay particles of the D^* meson a)-c) and the scalar sum d) of the p_T of the kaon and pion depicted for data (filled circles) and MC (solid line). The background has been subtracted using a fit to the ΔM distribution for every bin.*

between data and Monte Carlo the control distributions of the polar and azimuthal angle are useful and illustrated in figure 7.7. The combinatorial background in data

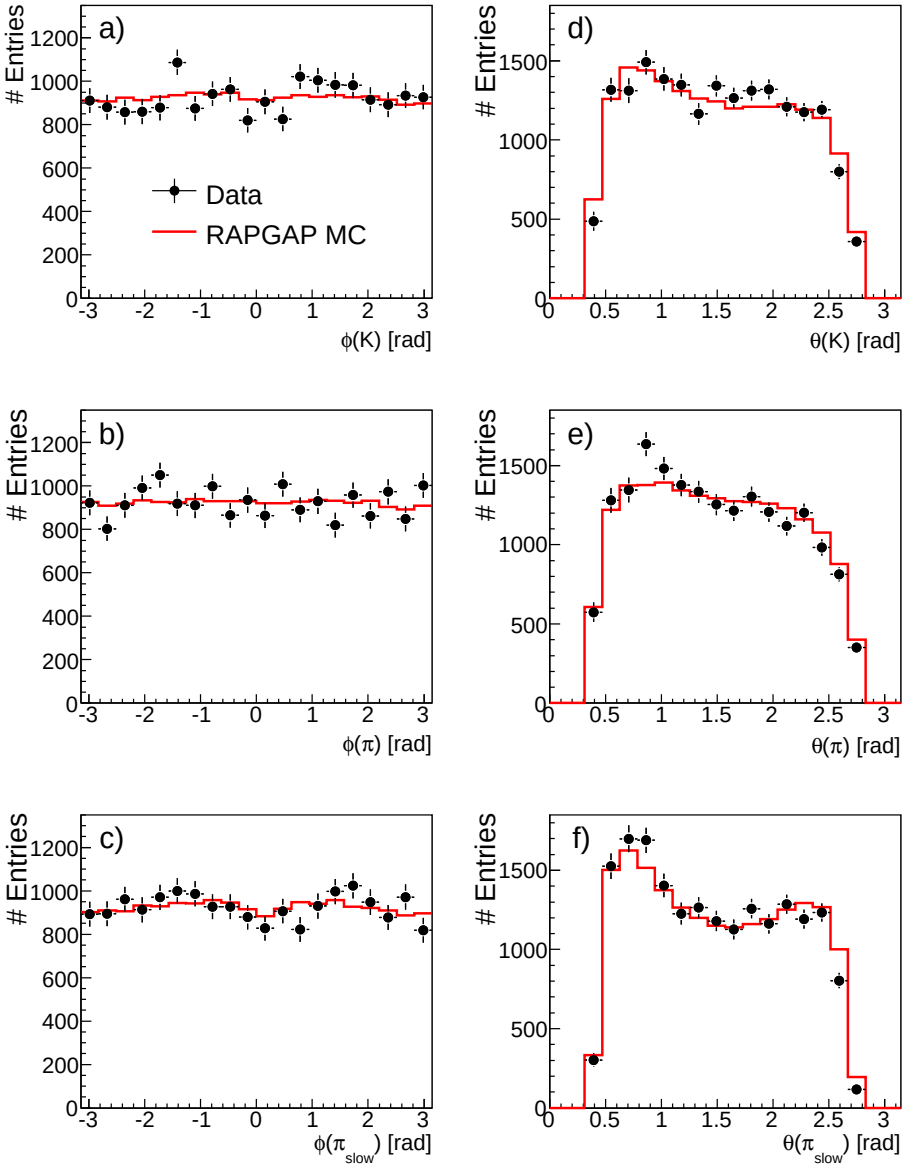

Figure 7.7.: *Distribution of the azimuthal a)-c) and polar angle d)-f) for the three decay particles of the D^* meson depicted for data (filled circles) and MC (solid line). The combinatorial background in data has been subtracted using the statistical subtraction method.*

has been subtracted using the statistical subtraction method. There is no significant difference seen with the exception of a larger fluctuation for the θ of the pion track at low values as illustrated in figure 7.7e). Compared to the other decay tracks the slow pion track as shown in figure 7.7f), shows a more pronounced structure in θ. Partially this is due to the θ dependent tracking efficiency at low momenta and also due to the strong correlation to the direction of the D^* meson. Also this effect is well described by the Monte Carlo.

The tracking efficiency is highly dependent on the amount of hits associated to a track and the radial lengths of the track itself. Therefore these distributions are displayed in figure 7.8, which are in general rather well described by Monte Carlo. The double peak

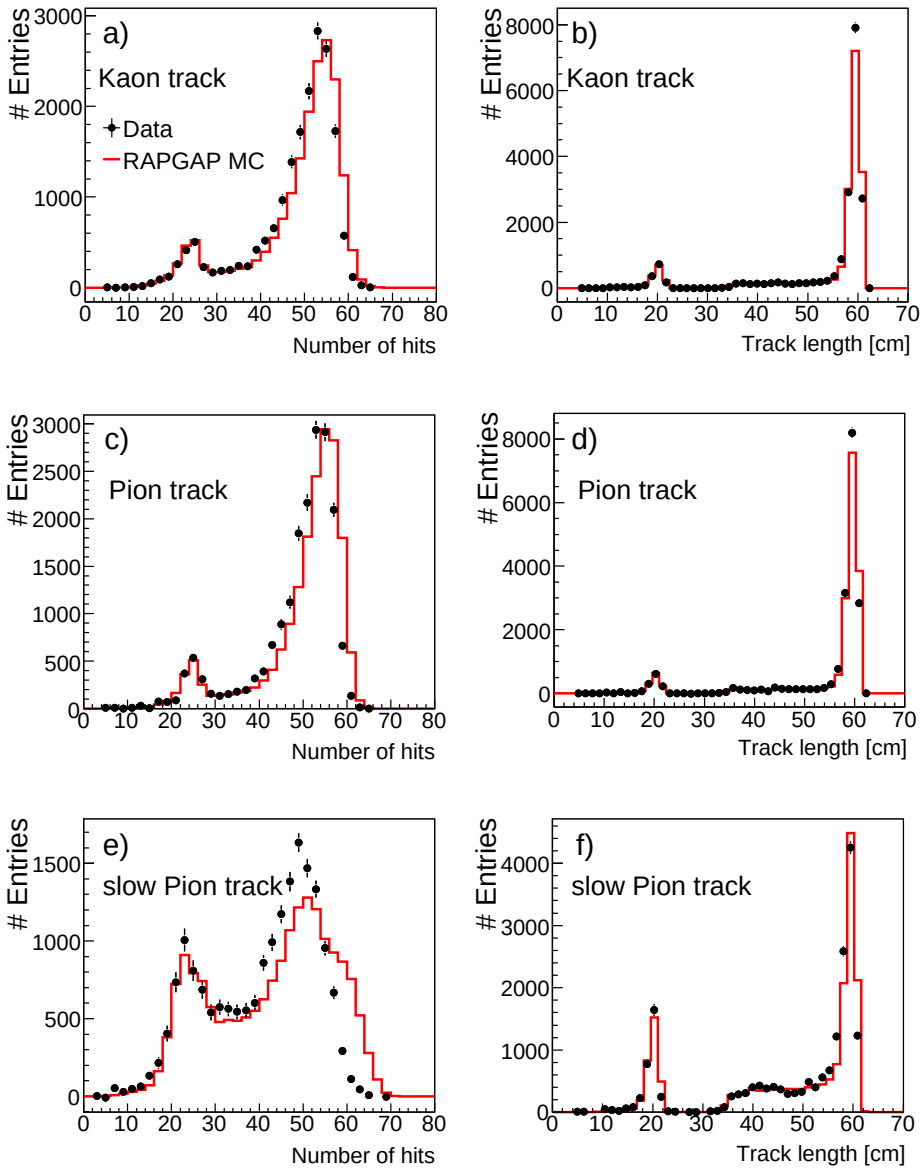

Figure 7.8.: *The number of hits along the track a),c),e) and the length of the track b),d),f) is shown for the pion, kaon and slow pion track displayed for data (filled circles) and MC (solid line). The combinatorial background in data has been subtracted using the statistical subtraction method.*

structure of the hit distribution is owed to the fact that not all tracks are reconstructed within both CJCs which causes the peak at around 24 hits, while tracks reconstructed in both chambers peak at 56 hits. The cause for a track being not reconstructed by both chambers has different reasons, for instance the momenta is not large enough as illustrated by the slow pion track in figure 7.8e). In addition the track reconstruction can simply miss the second part of a track for various reasons, like multiple interactions

or regions that are densely populated with hits. A larger difference between data and MC is seen for the slow pion track in figure 7.8e) located at large numbers of hits where the MC extends to even larger numbers compared to the data. A possible explanation[2] is that the MC overestimates the amount of hits for low momentum tracks that start to loop in the tracking chambers. These tracks have than multiple hits on a wire, which leads to a shift towards more hits compared to the higher momentum track of kaon and pion where no significant tail is observed. This has no large effect on the measurement as the transverse momentum of the slow pion track, shown in figure 7.6c), is well described down to smallest p_T. The track length, as shown in figure 7.8, is nicely described for all decay particles of the D^* meson.
Due to the overall nice agreement between data and Monte Carlo down to 0.12 GeV for the tracks of the decay particles it is expected that the tracking is well described by the Monte Carlo.

[2]Also the efficiency is slightly charge dependent at very low track momenta.

8. Cross Section Determination

For the calculation of the D^* meson production cross section the following formula is used:

$$\sigma_{\mathrm{tot}}^{\mathrm{vis}}(ep \to eD^*X) = \frac{N(D^*) \cdot (1-r)}{\mathcal{L} \cdot \mathcal{B}(D^* \to K\pi\pi_{\mathrm{slow}}) \cdot \epsilon \cdot \mathcal{A} \cdot (1+\delta_{\mathrm{rad}})} \; . \tag{8.1}$$

The cross section is calculated using the number of D^* mesons $N(D^*)$, which is determined from a combined signal and background fit to the ΔM distribution as introduced in section 5.2. Beside the correction of the detector acceptance $\mathcal{A}$ and efficiency ϵ, including the trigger efficiency, the number of D^* mesons is corrected for two effects: the amount of reflections r from other decay modes of the D^0 meson (see section 8.3) and the effect of radiative events as introduced shortly in chapter 2 (or better section 8.2). The D^* cross section includes decays from B hadrons to D^* mesons which are expected to contribute to less than 2%, which is neglected for the present analysis.
First of all the results of the method for the correction of the detector effects are presented. Afterwards the method for the correction of the effect of radiative events is introduced and the term $(1+\delta_{\mathrm{rad}})$ is derived, which is used to convert the cross sections to the Born level. In section 8.3 the method to determine the contribution from the reflections is discussed and a correction factor for the cross section is calculated.

8.1. Correction of Detector Effects

The bin-by-bin method as introduced in section 5.3 is utilised for the correction of the detector effects. The bin-by-bin correction is based on a good description of the data by the MC that is used for the data correction. A overall nice agreement of the data with the MC has been demonstrated in chapter 7. Moreover the measurement is optimised in a way that migrations between the bins are small. The subsequent acceptance and efficiency corrections of the bin-by-bin method follow the formulae presented in equation 5.6 and 5.7. As mentioned the standard bin-by-bin method has been utilised here, but moreover studies for the use of the matrix correction method in an extended phase space are performed (see section 12.2).

Results of the bin-by-bin Method

The MC utilised for the determination of the purity, stability, acceptance and efficiency has been simulated and reconstructed with version table row 47[1]. The MC has been generated with the RAPGAP program using the proton PDF CTEQ65m, because of a significantly better description of the $\eta(D^*)$ shape than for RAPGAP with the CTEQ6ll proton PDF. The parameters used during the generation process are discussed in section 4.1.

[1] VT47 in MC corresponds to dst3 data, which is the reconstruction version of the whole presented data sample.

From the MC the number of bins has been optimised such, that the purity is typically above 70% for single-differential measurements and above 50% for double-differential measurements with only small exceptions. The number of bins exploited for the measurement of a certain variable is large enough to provide extensive tests of pQCD.
The purity for all quantities measured single-differentially is indicated as solid line in

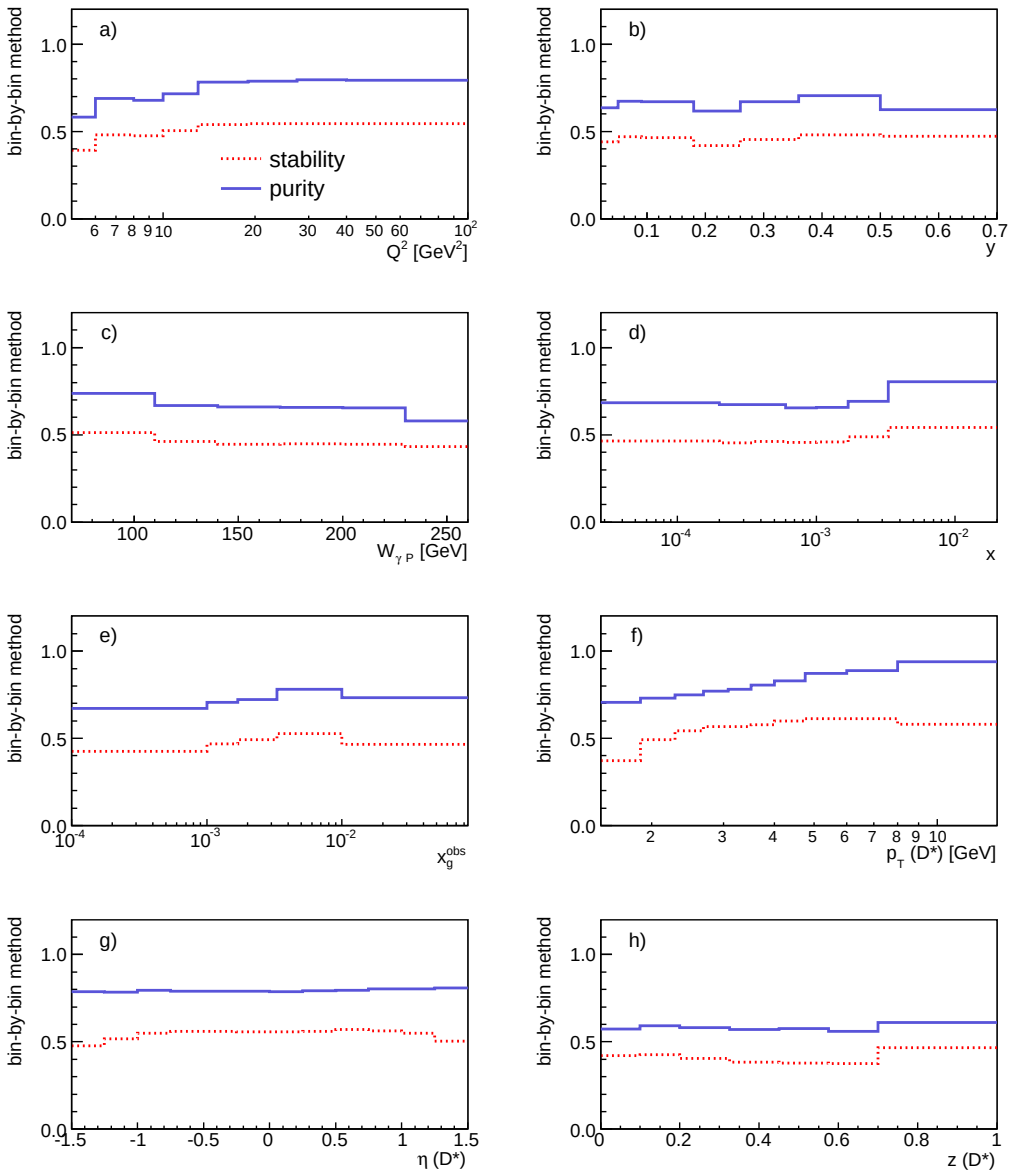

Figure 8.1.: *The purity (solid line) and the stability (dotted line) as defined in equation 5.8 and 5.9 for all quantities measured single-differentially.*

figure 8.1a)-h) together with the stability (dotted line). In general the goal of purities around 70% for single-differential distributions is achieved with the exception of single bins in some distributions. For instance at low Q^2 a value of only 60% is reached and the purity of the inelasticity y is on average at around 65% whereas the purity for $W_{\gamma P}$ shows a decrease towards high $W_{\gamma P}$. The purity as a function of D^* quantities like p_T or η is on average even at 80%. Whereas for the purity in $z(D^*)$ in general only 60%

is achieved for all measured bins, which is most probably due to the direct use of y for the calculation, see equation 5.20, of $z(D^*)$.
The stability (dotted line) is displayed in figure 8.1 for the same distributions as it was done for the purity. For all bins the stability is above 40% which is lower than the purity because of the efficiency.
For the double-differential distributions in $y - Q^2$ and $\eta(D^*) - p_T(D^*)$ the purity is in

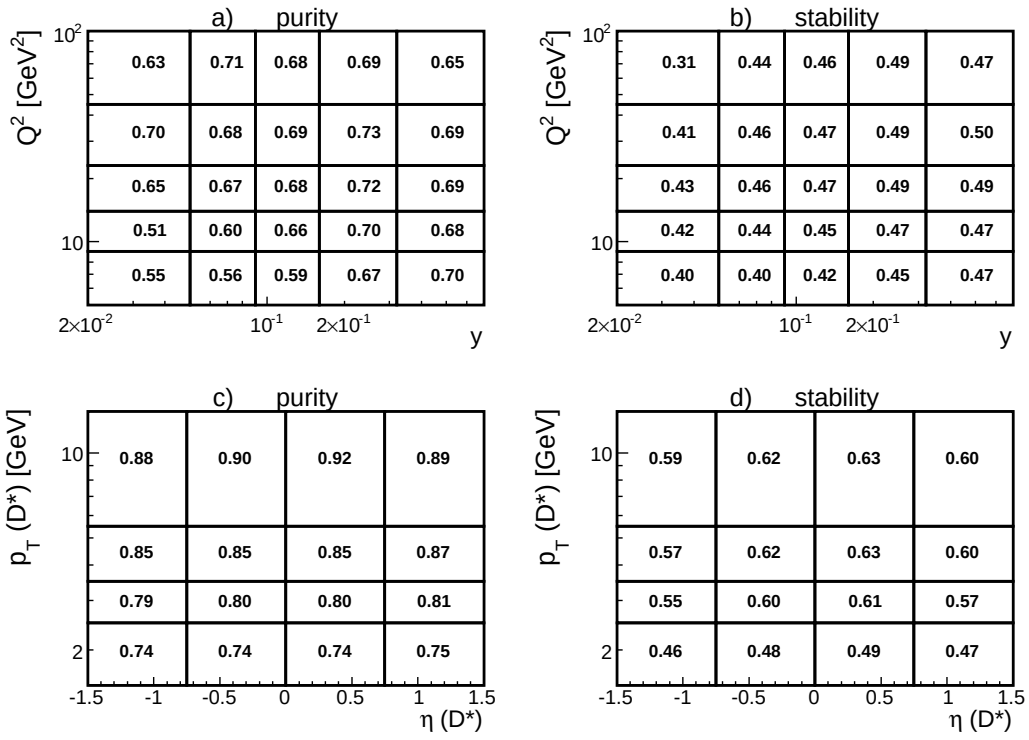

Figure 8.2.: *The purity and stability of the H1 detector for the double-differential cross section measurement in $y - Q^2$ a)-b) and $\eta(D^*) - p_T(D^*)$ c)-d). The bin borders are indicated by the thick solid lines.*

general above 60% as displayed in figure 8.2a) and c). The thick solid lines indicate the bin borders of the measurement. Only at low y and low Q^2 values of around 52% are achieved whereas for the purity as a function of $\eta(D^*) - p_T(D^*)$ on average 80% are achieved with lowest values at low transverse momenta. As for the stability of single-differential distributions also here the stability is lower than the purity because of the efficiency.
The efficiency needed to correct the data for detector effects is split up in an acceptance and an efficiency part. First of all the acceptance $\mathcal{A}$ as defined in equation 5.6 is discussed; which is a measure for the fraction of events that is visible for the detector at all. The cuts separating the acceptance and efficiency are called acceptance cuts and are defined in table 8.1. The acceptance is illustrated for the single-differential distributions in figure 8.3a)-h) and is for all distributions at values of around 60%. Exceptions are located at small transverse momenta of the D^* meson as depicted in figure 8.3f), which are caused by the acceptance cut on the transverse momentum of the slow pion track. Furthermore the most forward and backward bins of the $\eta(D^*)$ distribution as displayed in figure 8.3g) are affected by the acceptance cuts on θ(track).

quantity	Value
$p_T(K)$	> 0.3 GeV
$p_T(\pi)$	> 0.3 GeV
$p_T(\pi_{\text{slow}})$	> 0.120 GeV
θ(track)	$20 < \theta < 160$
energy of the scattered electron	$E_{e'} > 10$ GeV
polar angle of the scattered electron	$153^\circ < \theta_{e'} < 177^\circ$

Table 8.1.: *Definition of the selection criteria for the detector acceptance.*

For the double-differential distributions in $y - Q^2$ and $\eta(D^*) - p_T(D^*)$ the acceptances as illustrated in figure 8.4a) and c) are in general above 65% with exceptions located at low Q^2 and low y and at low $p_T(D^*)$ in most backward and forward directions. A higher acceptance for these regions is possible by an extension of the $\eta(D^*)$ and $p_T(D^*)$ range, which is discussed in chapter 12.

The Detector Efficiency

The total detector efficiency includes the reconstruction efficiency defined in equation 5.7 and the trigger efficiency ϵ_{trig}:

$$\epsilon_{\text{tot}} = \epsilon_{\text{rec}} \cdot \epsilon_{\text{trig}} \ , \tag{8.2}$$

where ϵ_{rec} is determined from MC and ϵ_{trig} usually from data[2]. Therefore a D^* data sample, which is selected by the subtrigger used for the analysis (s61) logically combined (AND) with an independent reference subtrigger and a D^* sample only selected by the reference subtrigger is used. The fraction gives the trigger efficiency:

$$\epsilon_{\text{trig}} = \frac{N_{\text{s61}}(D^*)\&\&N_{ref}(D^*)}{N_{ref}(D^*)} \ . \tag{8.3}$$

To provide enough statistic the reference trigger (or a subset of reference triggers) and the subtrigger used for the analyses should have a reasonable phase space overlap, but they have to be independent. In case a trigger efficiency depends only on one quantity the trigger efficiency correction can be applied easier by the determination of an event weight, which is included in the reconstruction efficiency. In the following the determination of the trigger efficiency for the present analysis is discussed.

[2]For the estimation of an uncertainty of the trigger condition implemented in a subtrigger MC is utilised.

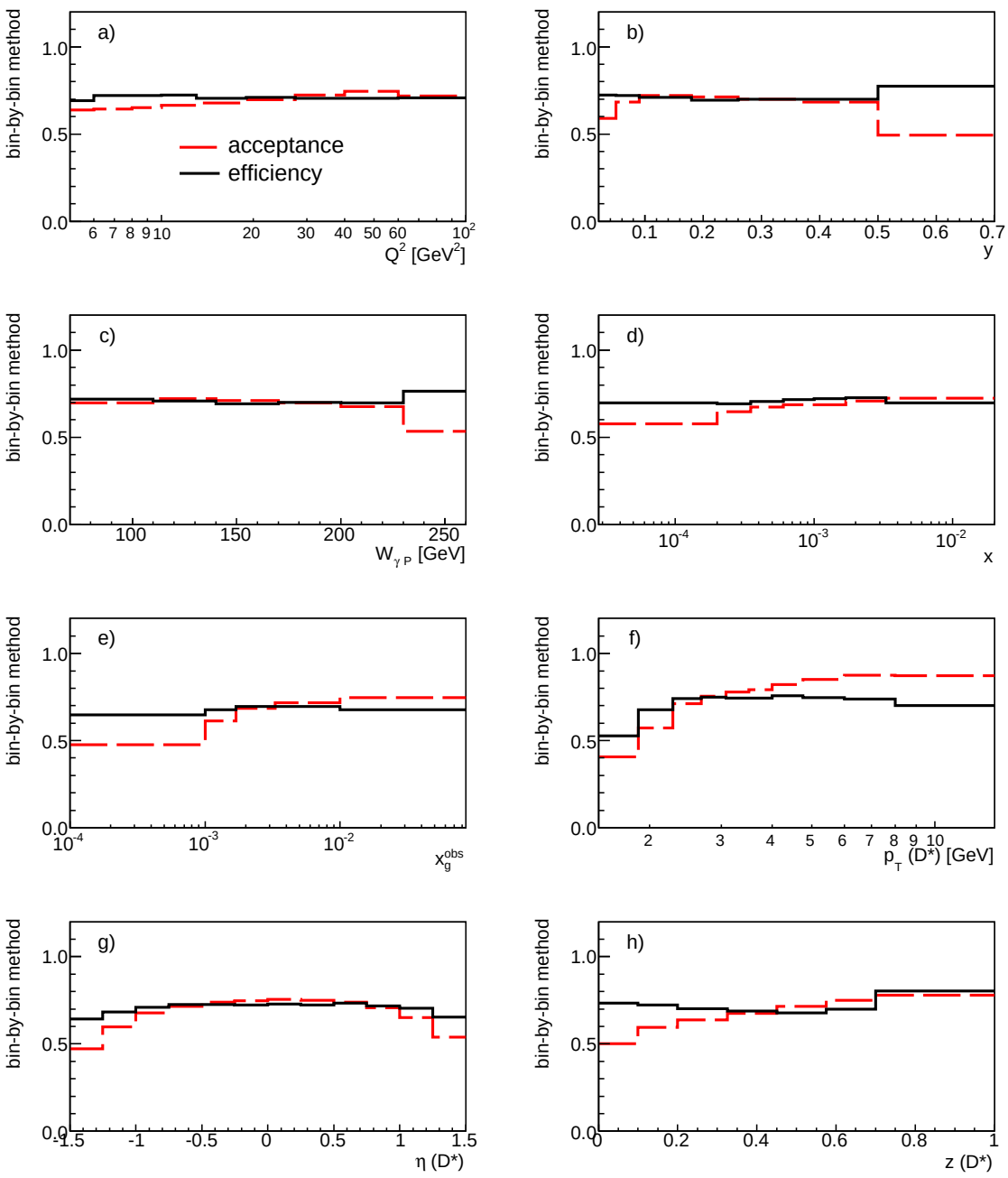

Figure 8.3.: *The acceptance (dashed line) and the efficiency (solid line) of the H1 detector as function of all quantities of the cross section measurement.*

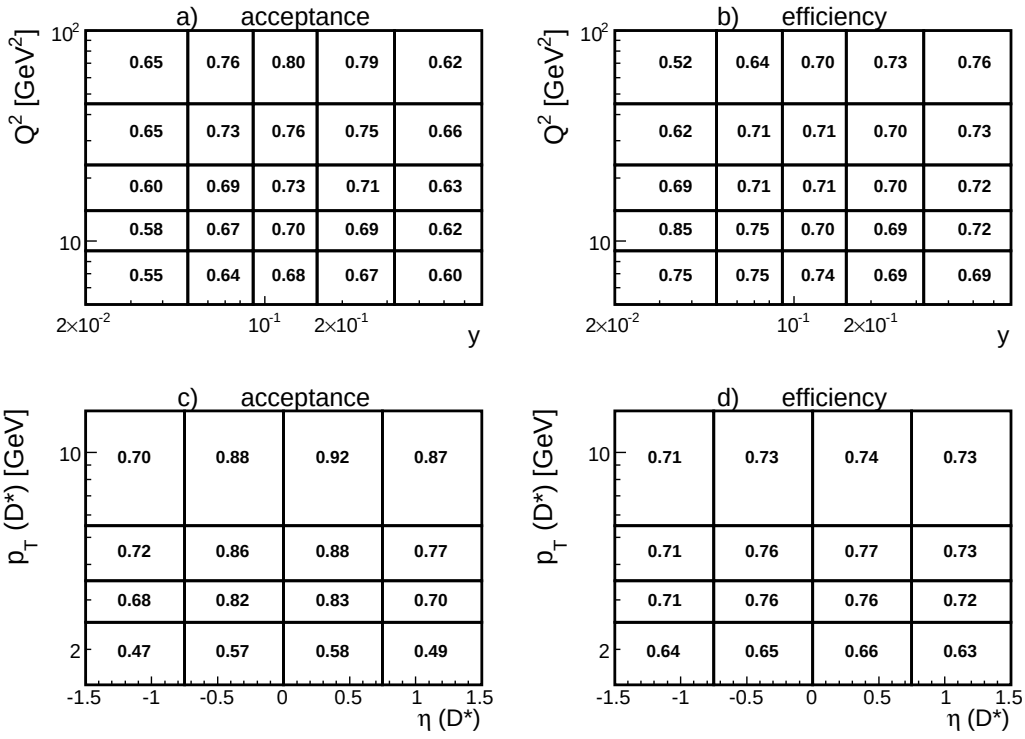

Figure 8.4.: *The acceptance and efficiency of the H1 detector for the double-differential cross section measurement in $y - Q^2$ a)-b) and $\eta(D^*) - p_T(D^*)$ c)-d). The bin borders are indicated by the thick solid lines.*

The Trigger Efficiency

The subtrigger s61 implements trigger conditions based on track informations and informations of the scattered electron. Thus the total trigger efficiency ϵ_{trig} is determined from the track trigger efficiency and the SPACAL trigger efficiency:

$$\epsilon_{\text{trig}} = \epsilon_{\text{trig}}^{\text{SPACAL}} \cdot \epsilon_{\text{trig}}^{\text{TRACK}} \ . \tag{8.4}$$

Both trigger efficiencies are determined according to equation 8.3 with independent subsets of reference triggers for each of the two trigger efficiency calculations. Overall the track and SPACAL conditions implemented in s61 are 98% efficient thus the trigger efficiency has not a large impact on the data correction of the present analysis.
Nevertheless it is corrected with the previously described procedure: the SPACAL part of the trigger efficiency is used to determine an event weight, which is included in the reconstruction efficiency and the track trigger efficiency is determined from data and applied as additional correction to the data. First of all the SPACAL trigger efficiency determination is discussed followed by the track trigger efficiency.
The SPACAL trigger conditions ((SPLe_IET > 2 || SPCLe_IET_Cen_3)) translate to an energy threshold of 9 GeV combined with a topological criterium for inner radii. The SPACAL trigger efficiency as a function of variables related to the scattered electron is illustrated in figure 8.5. Within the statistical precision it is flat as a function of the radius b), the polar angle of the scattered electron $\theta_{e'}$ c) and the virtuality Q^2 d).

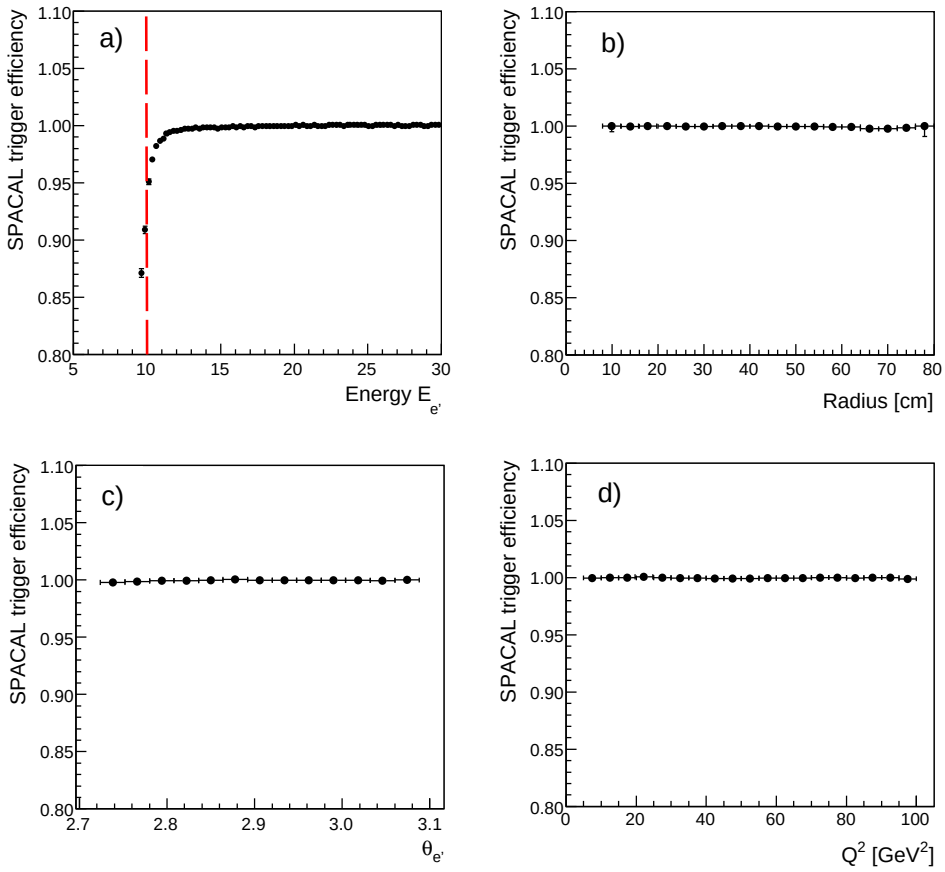

Figure 8.5.: *Trigger efficiency of the SPACAL trigger element implemented within subtrigger s61 as function of variables related to the scattered electron determined for the year 2007. The dashed line in a) indicates the cut on the energy of the scattered electron adopted for the analysis (and for b),c) and d)). Take note of the zero-suppressed y axis.*

In contrast the SPACAL trigger efficiency as a function of the energy of the scattered electron as displayed in figure 8.5a) demonstrates the expected threshold behaviour of the trigger condition. Only for the latter a relaxed $E_{e'}$ cut of 8 GeV has been used in order to be able to fit the threshold. The dashed line indicates the acceptance cut $E_{e'} > 10$ GeV adopted for the other efficiencies shown in figure 8.5, which is also done later for the analysis. The $E_{e'}$ distribution is ideally suited to determine the event weight. In order to determine the event weight the distributions of the SPACAL trigger efficiency as a function of $E_{e'}$ are fitted per year with a Fermi function which is defined by:

$$f(E_{e'}) = \frac{a}{\exp(\frac{b-E_{e'}}{c}) + 1} \ . \tag{8.5}$$

The parameter a describes the plateau of the trigger efficiency and b the threshold position with the threshold widths c. The results of the fits for the individual years

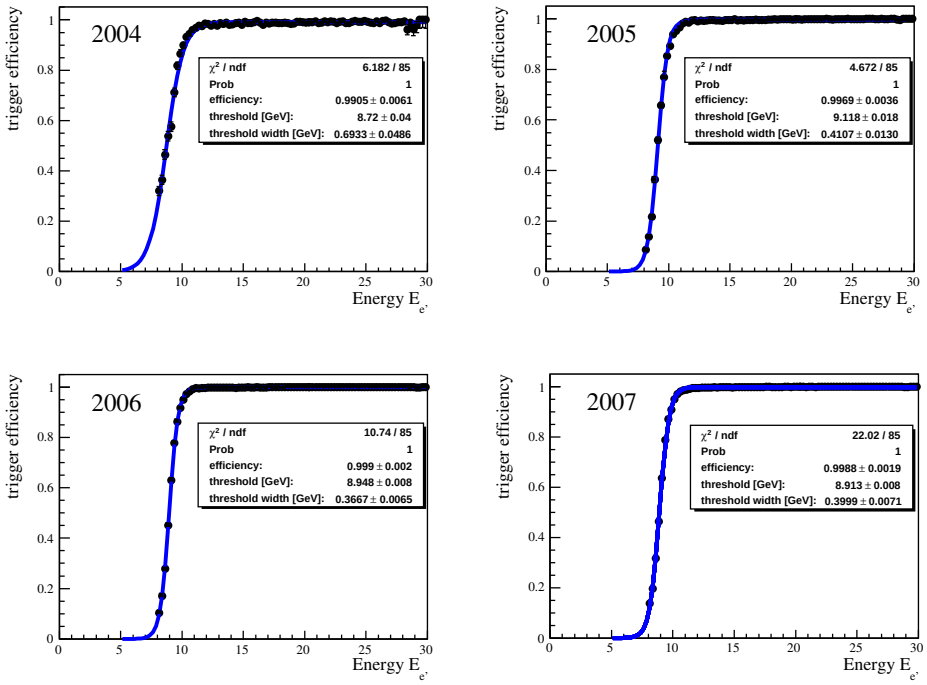

Figure 8.6.: *The SPACAL trigger efficiency as function of the energy of the scattered electron $E_{e'}$ is fitted with a Fermi function for all years. The results of the fits are summarised in the boxes.*

2004 − 07 are summarised in table 8.2. These parameters are utilised to calculate an

year	Plateau value a	Threshold position b [GeV]	Threshold width c [GeV]
2004	0.991 ± 0.006	8.72 ± 0.04	0.69 ± 0.05
2005	0.997 ± 0.004	9.12 ± 0.02	0.41 ± 0.01
2006	0.999 ± 0.002	8.95 ± 0.01	0.37 ± 0.01
2007	0.999 ± 0.002	8.91 ± 0.01	0.40 ± 0.01

Table 8.2.: *Results and errors of the Fermi fit (see equation 8.5) to the distribution of the energy of the scattered electron for the individual years as illustrated in figure 8.6.*

event weight, which is included in the detector reconstruction efficiency calculation. Thus the cross section measurement is corrected for the SPACAL trigger efficiency. The systematic uncertainty of the SPACAL trigger condition is roughly estimated to be 1%.

The reconstruction efficiency that includes the correction due to the SPACAL trigger efficiency as discussed above is illustrated for all single-differential distributions of the cross section measurement in figure 8.3. In general efficiencies of more than 70% are achieved. Some exceptions mainly at low transverse momenta of the D^* meson are observed. The efficiency for the double-differential distributions in $y - Q^2$ and

$\eta(D^*) - p_T(D^*)$ are illustrated in figure 8.4b) and d) with an average efficiency of 70%. Smaller efficiencies are located at high Q^2 and low y with a value of 52% and at low transverse momentum in most forward and backward directions where 64% are achieved.
Because of the sharp threshold of the trigger condition at 9 GeV (see section 6.1) an electron energy cut of greater 10 GeV can be implemented for the event selection. This cut leads to a restriction of the accessible y range. Figure 8.7 illustrates the distribution of the energy of the scattered electron against the inelasticity y indicating that the electron energy cut of 10 GeV allows a mean value for the first $E_{e'}$ bin above 10 GeV of 0.64. Thus higher y are not directly accessible for the measurement, but as long as the extrapolation is small this can be corrected within the reconstruction efficiency (see equation 5.7). The average extrapolation factor used in the reconstruction efficiency for $y = 0.64 \rightarrow y = 0.70$, which is the visible range of the present measurement, is less than 1.5%. This fraction is determined from MC where the difference in the highest y analysis bin (defined from 0.5 to 0.7) with and without a cut of 10 GeV on the energy of the scattered electron is derived.
The trigger efficiency of the track condition of s61 is determined from data for all

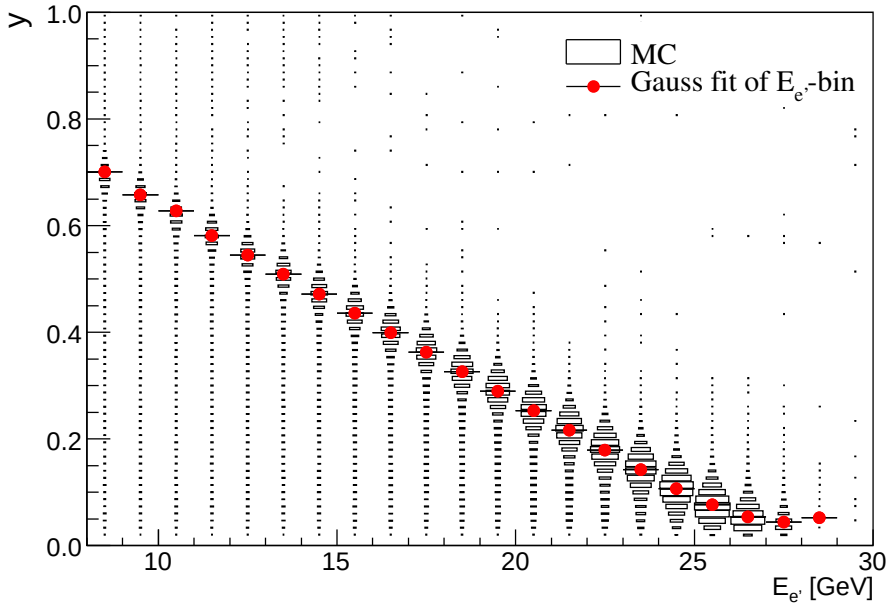

Figure 8.7.: *Distribution of the energy of the scattered electron against the inelasticity for the Monte Carlo event sample within the acceptance cuts summarised in table 6.3 with the exception of a lower $E_{e'}$ cut of only* 8 GeV. *Gaussian fits are applied to slices of $E_{e'}$ and the mean (filled circle) is drawn for each slice.*

distributions of the cross section measurement and applied as bin wise correction to the data. The track condition asks for one track above a certain p_T threshold and is calculated either from the DC$r\varphi$ trigger (DCRPh_THig) for the 2004 data taking or from the FTT trigger (FTT_mul_Td) for the 2005-07 data taking. For the DC$r\varphi$

trigger a p_T threshold of 800 MeV was implemented whereas the FTT implemented a 900 MeV p_T threshold. Tunings of the s61 track trigger setup have been studied in detail elsewhere [Loh06].
The track trigger efficiency is calculated according to equation 8.3 with a subset of

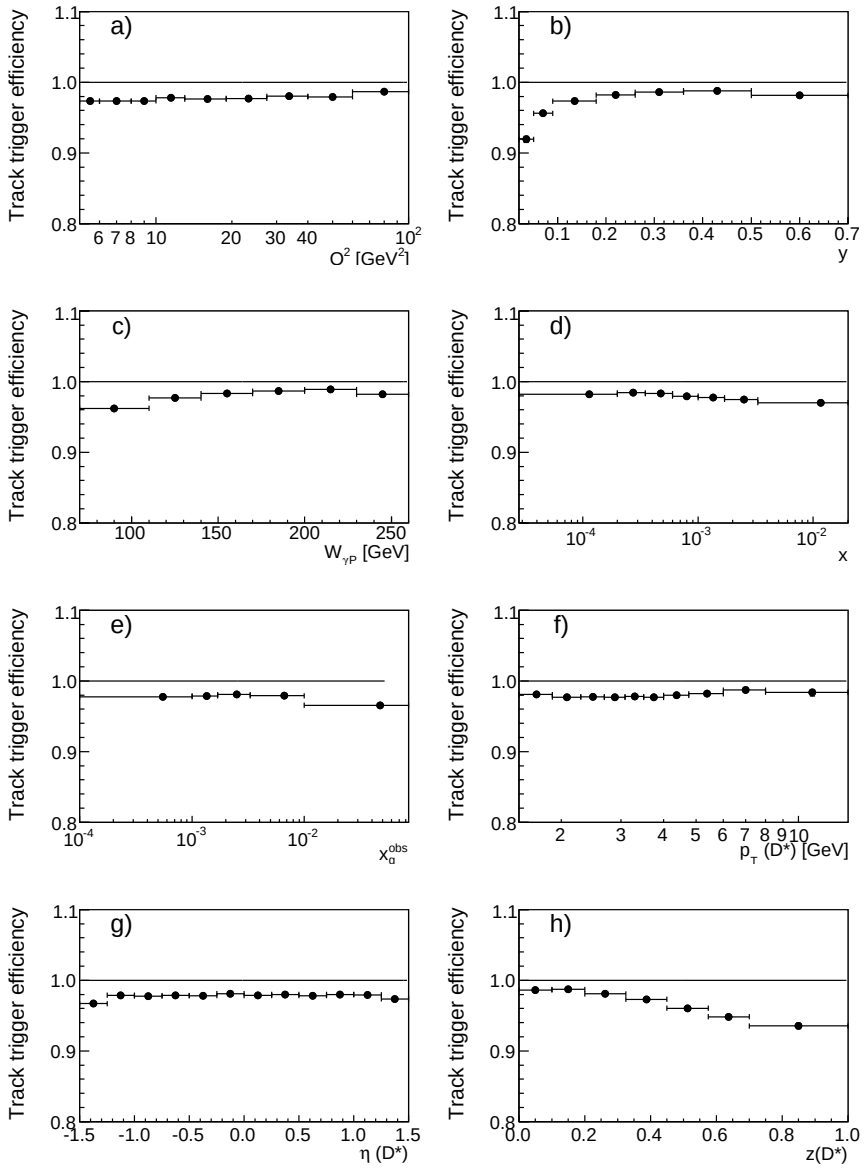

Figure 8.8.: *The trigger efficiency of the track condition of s61 in data as function of single-differentially measured quantities determined for the whole data period* $2004 - 07$. *Take note of the zero-suppressed y axis.*

independent reference triggers based on calorimeter information (subtrigger: s0,s3,s9) and is illustrated in figure 8.8. The track trigger efficiencies are reasonably flat as expected with an average track trigger efficiency of $\epsilon_{\text{trig}}^{\text{TRACK}} > 97\%$ with the exception that for low y b) and high $z(D^*)$ h) it drops down to values of around 92%.
To further study these dependencies the track trigger efficiency is split up into two

parts for the different track trigger systems because 87% of the D^* data have been taken with the FTT track condition. For further insights on the track trigger efficiency it is discussed as a function of the p_T of selected tracks (p_T(selTrack)) and the number of the central tracks (multiplicity) where the track conditions depends on. The trigger efficiency in MC is calculated according to equation 8.3 where also the reference triggers (s0, s3, s9) are used from the simulation. The FTT trigger efficiency is illustrated

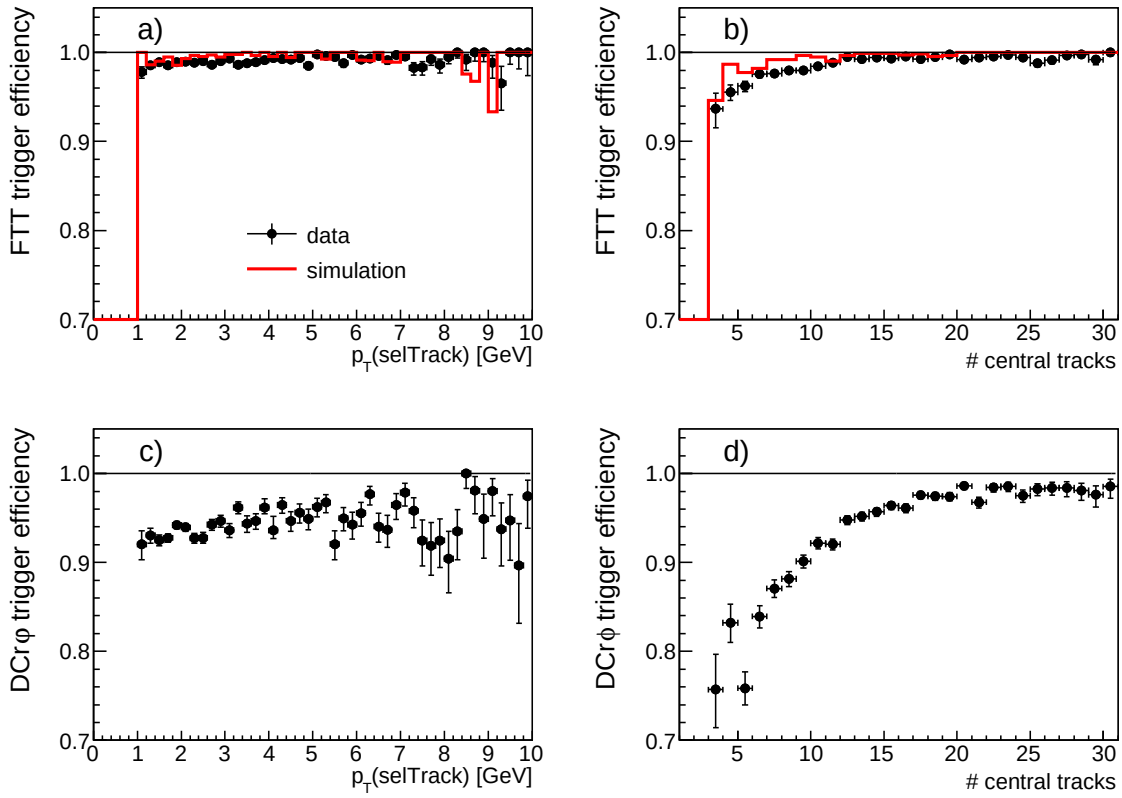

Figure 8.9.: *The trigger efficiency of the FTT track condition a)-b) in data (filled circles) and FTT simulation (solid line) as a function of* p_T(selTrack) *and the number of central tracks. For comparison the trigger efficiency of the DCr*φ *track condition from data is depicted in c) and d). Take note of the zero-suppressed y axis.*

in figure 8.9a) as a function of p_T(selTrack) and of the multiplicity b) for data (filled circles) and MC (solid line) with the use of the `fttemu` package (see chapter 14.2) that fully simulates the Fast Track Trigger system. For the calculation in MC the MC post-processing step as introduced in section 14.2 has been used, which largely simplifies the use of the FTT information in the H1 software framework. An overall track trigger efficiency of $> 98\%$ for the FTT was determined, which is nicely described by the FTT simulation. Moreover it is almost flat for p_T(selTrack) with only a slight dependence on the multiplicity where 94% are achieved at low multiplicities of three tracks. This can be explained from the fact that the FTT simulation slightly overestimates the single track efficiency, which has an impact foremost at small track multiplicities. This region does not influence the present analysis much as the average multiplicity of D^* events

is around 12 tracks where the efficiency is already at the level of 98%.
Compared to the DCrφ trigger, which is utilised for only 13% of the data taking, the FTT system has provided a significant improvement as one can see from figure 8.9c)-d). The DCrφ trigger efficiency is derived in the same way as for the FTT and shows efficiencies of 91% at low p_T(selTrack) combined with a strong dependence on the multiplicity. Because of the change from the DCrφ trigger to the FTT trigger in 2004 no tuning for the simulation of the DCrφ trigger has been done, which is why a simulation of the DCrφ trigger is not available.
Overall there is only a small difference of less than 1.0% between the FTT trigger efficiency in data compared to the full FTT simulation. Even if a larger value of around 2% (taken from [Sch03]) is assigned for the DCrφ data taking the track trigger uncertainty of the subtrigger 61 is still at a level of 1% because of the small fraction of DCrφ triggered data.
As discussed in section 5.1 a refined final trigger selection is applied at the fourth level of the H1 trigger system (see section 3.5). For the present analysis and kinematic range the L4 weights of all selected events are equal to one, equivalent to a fully efficient level four filter.
The total detector correction applied for the cross sections presented in chapter 10 includes the detector acceptance and the weighted reconstruction efficiency (see figure 8.3) to account for the SPACAL trigger efficiency. In addition the effect of the track trigger as discussed above is corrected by the determined track trigger efficiency (see figure 8.8).

8.2. Correction of next-to-leading Order QED Contributions

In order to convert the measured D^* cross sections to the Born level (one-photon exchange) they are corrected for the virtual and real NLO QED contributions, i.e. event topologies where a photon is radiated incident to the interaction (ISR) or after the interaction (FSR) as it was outlined in chapter 2. The virtual NLO QED corrections are of the order 5% to 13% for a Q^2 range of $5 - 10^4$ GeV^2 and are included in the running of the electromagnetic coupling constant α_{em} [KSM92]. For the real NLO QED corrections the ISR from the lepton line is the dominant contribution as the FSR is almost always merged with the measured electron cluster.
The difference to the Born level is usually expressed by $(1 + \delta_{\text{rad}})$:

$$\sigma_{\text{Born+NLO}} = (1 + \delta_{\text{rad}}) \cdot \sigma_{\text{Born}} \ . \tag{8.6}$$

Thus the conversion to the Born level is given by a correction factor $c_{\text{rad}} = (1 + \delta_{\text{rad}})^{-1}$ applied to the measured cross sections, which is determined from different RAPGAP MC samples (see table 4.1):

$$c_{\text{rad}} = \sigma^{\text{gen}}_{\text{non-rad}} / \sigma^{\text{gen}}_{\text{rad}} \ . \tag{8.7}$$

The cross section $\sigma^{\text{gen}}_{\text{rad}}$ is determined from a D^* sample generated by RAPGAP interfaced to HERACLES [KSM92], while $\sigma^{\text{gen}}_{\text{non-rad}}$ has been calculated from a D^* sample where RAPGAP was utilised with a non-radiative setup. In order to be save against

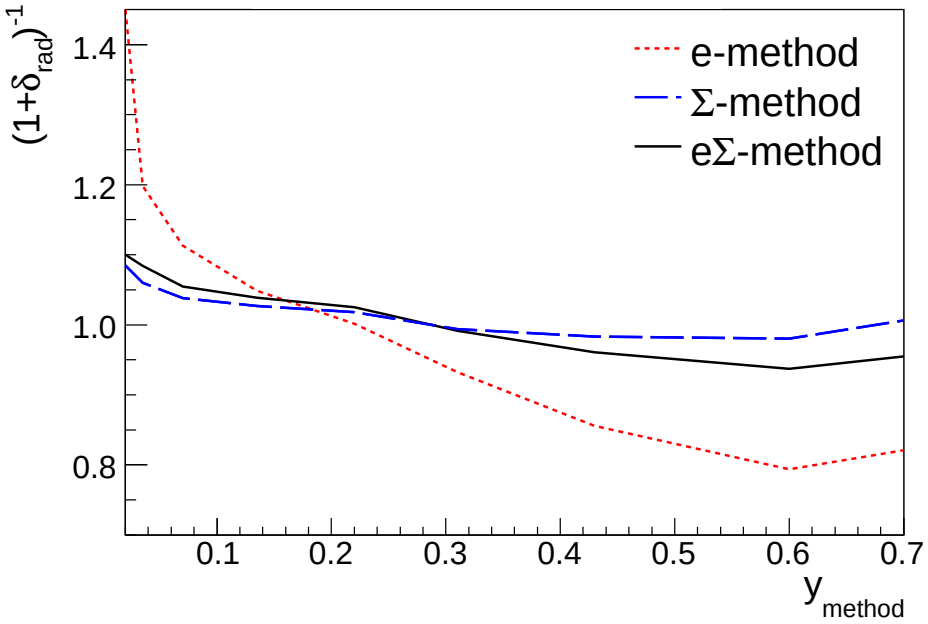

Figure 8.10.: *Radiative corrections* $(1+\delta_{\mathrm{rad}})^{-1} = \sigma_{\mathrm{non-rad}}/\sigma_{\mathrm{rad}}$ *as function of* y_{method} *for different reconstruction methods of the event kinematics.*

statistical effects a large number of events has been generated, which corresponds to a ratio $\mathcal{L}_{\mathrm{MC}}/\mathcal{L}_{\mathrm{data}}$ of above 60. Both cross sections are calculated within the visible range (see table 6.4).
For the calculation of the correction factor c_{rad} the reconstruction method of the event kinematics has a large influence. The radiative correction as function of y_{method} is depicted in figure 8.10 for different reconstruction methods. The $e\Sigma$-method is almost insensitive to the initial state radiation because it uses the hadronic final state for the calculation of the centre-of-mass energy, which turns into a smaller radiative correction compared to the e-method. Thus the $e\Sigma$-method largely reduces the influence of radiative effects and the radiative correction for the $e\Sigma$-method is much smaller and flat over the whole measured y range. The factor for the Σ-method is even smaller and only shown for comparison.
The factor c_{rad} is applied as bin wise correction to convert the measured D^* cross sections to the Born level. For the single-differential distributions it is illustrated in figure 8.11. Only for x_g^{obs} the correction factor as depicted in figure 8.11e) deviates from unity by up to 20% at low and large x_g^{obs}. This effect might be due to the explicit use of y, which is needed for the boost to the photon-proton rest frame and might have a large impact for the calculation of x_g^{obs}. For the bulk of the data the radiative corrections are of the order of $2-3\%$, except for some corners of the phase space like high y, low x, high $W_{\gamma P}$ and low $z(D^*)$. The statistical precision in the individual bins is of the order of 0.5% such that the fluctuations between the bins are not consistent with statistical effects. Figure 8.12a)-b) illustrates the radiative correction for the double-differential distributions in $y - Q^2$ and $\eta(D^*) - p_T(D^*)$ where at most 6% are observed at high p_T or high y. For all other bins correction around $2-3\%$ are seen. The systematic

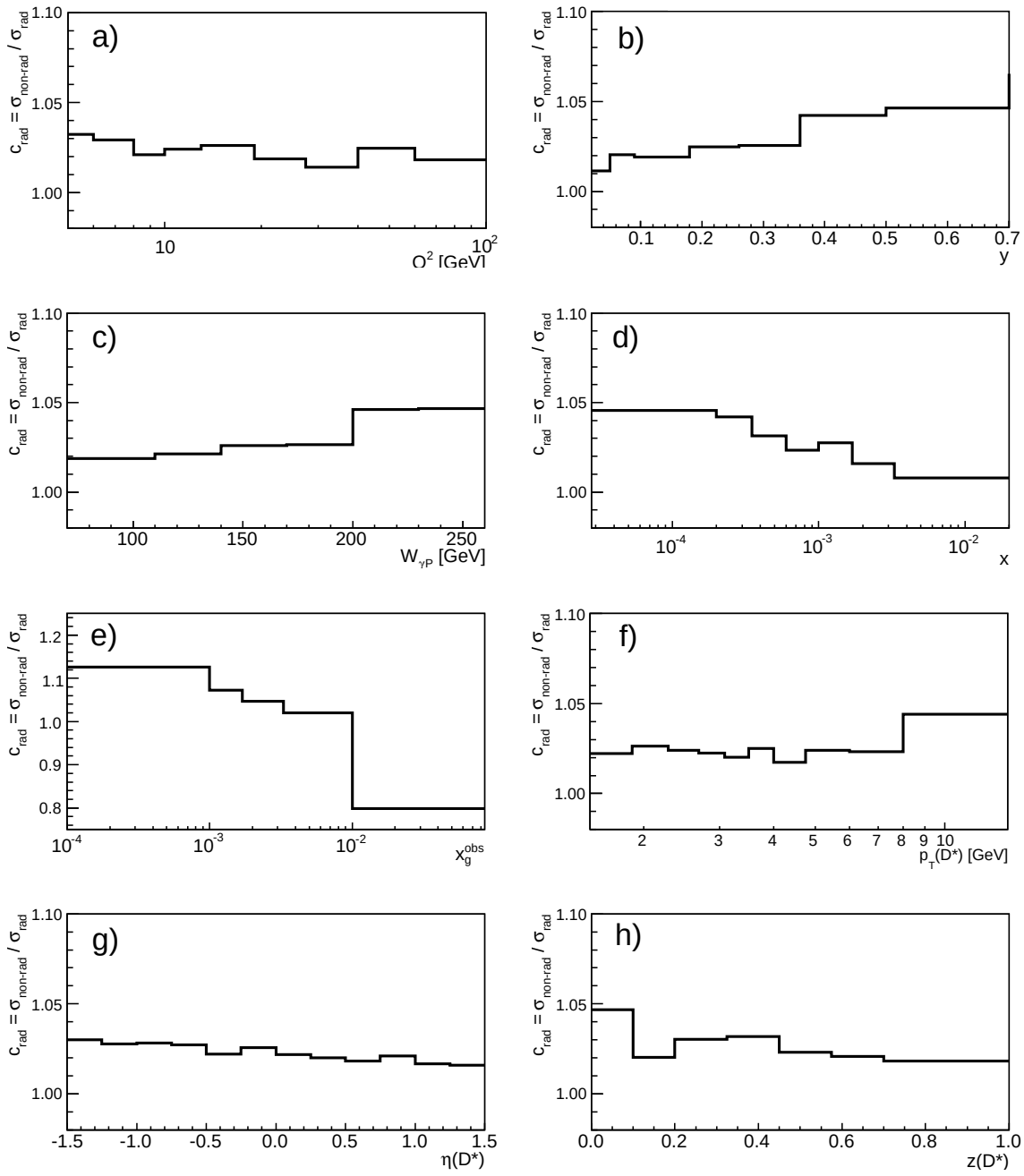

Figure 8.11.: *The radiative correction factors for Q^2, y, $W_{\gamma P}$, x and for quantities of the D^* meson like x_g^{obs}, $p_T(D^*)$, $\eta(D^*)$ and $z(D^*)$ calculated from the ratio of the D^* cross sections from radiative and non-radiative MC samples.*

uncertainty of the radiative corrections covering the non-smooth behaviour is discussed in chapter 9.

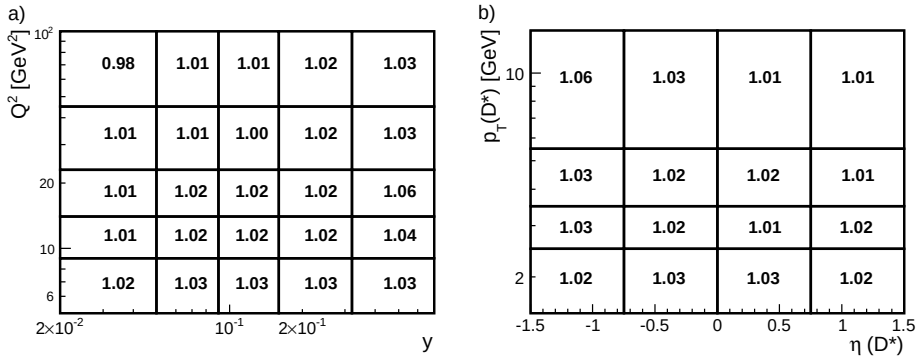

Figure 8.12.: *The radiative correction factors for the double-differential distributions in $y - Q^2$ a) and $\eta(D^*) - p_T(D^*)$ b). The bin borders are indicated by the solid lines.*

8.3. Correction due to Reflections

The calculated D^* cross sections are corrected for the branching fraction of the golden decay channel of the D^* meson as defined in equation 8.1. However, in general also other decay modes of the D^* or D^0 meson might contribute to the signal determined from the ΔM distribution. A contribution due to other D^* decays is not relevant because only three decay channels exists and furthermore the ΔM method ensures the D^* decay into $D^0\pi_{\text{slow}}$ because of the mass constraint from the slow pion. But for the D^0 decay many other decay channels exist therefore possible contributions have to be studied.
The $M(D^0)$ mass distribution is illustrated in figure 8.13 for events with a mass difference of $|\Delta M - 0.1454| < 0.002$ GeV to the nominal expected position of D^* mesons at 145.4 MeV [Y+06]. In addition to the right charge combinations (filled circles) also the wrong charge combinations (solid line) are shown. The D^0 decay channel which is chosen by the golden decay channel of the D^* meson creates a peak at the expected position of 1864.5 ± 0.4 MeV. Whereas other D^0 decay channels are located at around 1.6 GeV and create a broad signal. The decay channels of the D^0 meson listed in table 8.3 have two charged particles in the D^0 decay. These decays are called reflections because they can peak at other masses due to wrong mass assignments and thus can also contribute to the signal of the golden decay channel. Although the reflections are suppressed by the $|M(D^0) - 1864.5| < 80$ MeV window cut they contribute to the measured D^* meson cross section and can not be separated in data. Therefore a method is applied, based on a fully inclusive charm MC sample, which determines the contribution of the reflections from a selection at generator level. The ΔM distribution of D^* mesons in the golden decay channel including the reflections is depicted in figure 8.14a). The amount of reflections from other decay channels of the D^0 meson is determined from a fit to the ΔM distribution where the reflections are selected at generator level as depicted in figure 8.14b). The final correction is given by the fraction

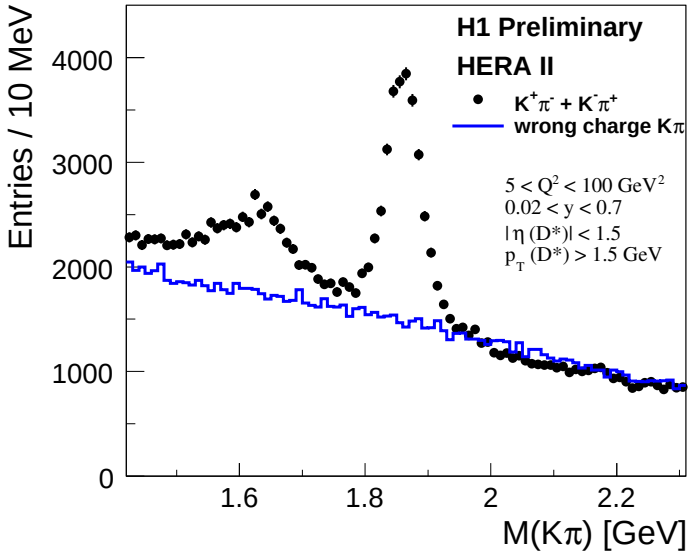

Figure 8.13.: *The D^0 mass distribution for the total D^* sample for the right charge combination (filled circles) and as solid line for the wrong charge combinations. D^0 decays in the golden decay channel of the D^* meson peak at* 1864.5 ± 0.4 MeV *whereas the other D^0 decay channels cause the broader peak at around* 1.6 GeV*.*

of the two fit results:

$$r = \frac{N^{\text{only refl.}}(D^*)}{N^{\text{all}}(D^*)} = 0.04 \ . \tag{8.8}$$

A correction factor of 4% is applied for the cross section calculation. The method to determine the contribution of reflections was already used in [Boe07] with the constrain of rather limited MC statistics. The statistics that has been utilised here is a factor five larger. This does not change the central value of the contribution but constrains the systematic error of the contribution from reflections as discussed in section 9.

	decay	Branching fractions
golden channel:	$D^{*\pm} \to D^0 \pi^{\pm}_{\text{slow}}$	$(67.7 \pm 0.5)\%$
	$D^0 \to K^{\mp}\pi^{\pm}$	$(3.8 \pm 0.07)\%$
other channels:	$D^0 \to K^{\pm}K^{\mp}$	$(3.84 \pm 0.10) \times 10^{-3}$
	$D^0 \to K^{\mp}\pi^{\pm}\pi^0$	$(14.1 \pm 0.5)\%$
	$D^0 \to \pi^{\mp}\pi^{\pm}$	$(1.36 \pm 0.03) \times 10^{-3}$
	$D^0 \to \pi^{\mp}\pi^{\pm}\pi^{\mp}\pi^{\pm}$	$(7.31 \pm 0.27) \times 10^{-3}$
	$D^0 \to \pi^{\mp}\pi^{\pm}\pi^0$	$(1.31 \pm 0.06)\%$
	$D^0 \to K^{\mp}e^{\pm} \overset{(-)}{\nu}_e$	$(3.51 \pm 0.11)\%$
	$D^0 \to K^{\mp}\mu^{\pm} \overset{(-)}{\nu}_\mu$	$(3.19 \pm 0.16)\%$
	$D^0 \to \pi^{\mp}e^{\pm} \overset{(-)}{\nu}_e$	$(2.81 \pm 0.19) \times 10^{-3}$
	$D^0 \to \pi^{\mp}\mu^{\pm} \overset{(-)}{\nu}_\mu$	$(2.4 \pm 0.4) \times 10^{-3}$

Table 8.3.: Branching fractions of the golden decay channel of the $D^{*\pm}$ meson and of other D^0 decay channels – taken from [Y+06].

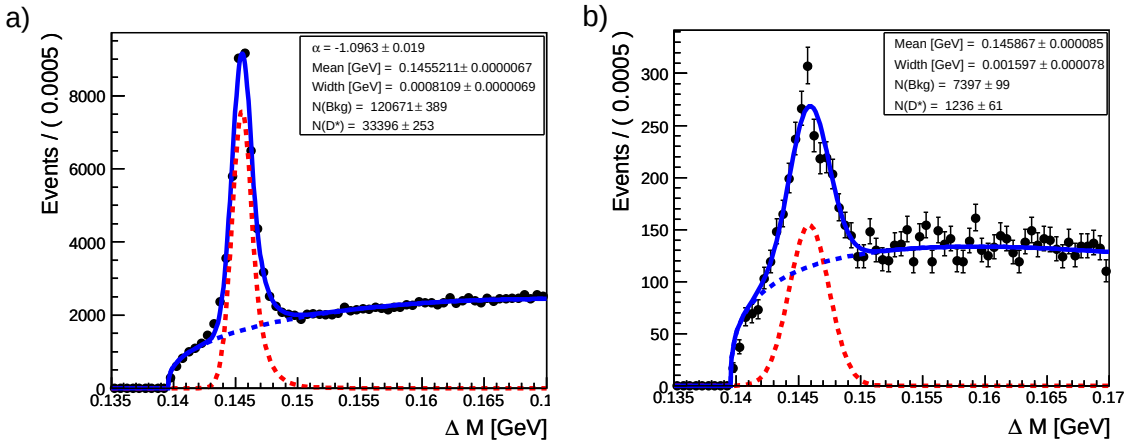

Figure 8.14.: *The ΔM distribution filled from D^* mesons in the golden decay channel including other decay channels (see table 8.3) of the D^0 meson a) determined by a fully inclusive charm MC. The ΔM distribution b) only for other decay channels of the D^0 meson are selected at generator level.*

9. Systematic Uncertainties

For the present analysis the systematic error is dominant for almost the whole phase space. Only for large transverse momenta of $p_T(D^*) > 8$ GeV or large photon virtualities of $Q^2 > 80$ GeV^2 the statistical error dominates the measurement. The systematic uncertainties summarised in table 9.1 are divided into uncertainties which are bin-to-bin uncorrelated and uncertainties which are bin-to-bin correlated. First of all the bin-to-bin uncorrelated systematic error sources are discussed.

Uncorrelated errors:		
Track efficiency	2% per track	6%
Luminosity		3.2%
Radiative correction		2.5%
Branching ratio		2.3%
Primary-vertex fit efficiency		2.5%
Signal extraction		2%
Trigger efficiency		1.4 %
D^0 meson mass cut		1.0%
PDF uncertainty	Cteq6ll vs. Cteq65m	1%
Reflections		$< 1.0\%$
Photoproduction background		$\sim 0.15\%$
Correlated errors:		
Model uncertainty	CCFM vs. DGLAP	$< 3\%$
Electromagnetic energy scale	$\pm 1\%$	1-2.5 % (6% at high y)
Scattering angle θ	± 1 mrad	$\sim 2\%$
Hadronic energy scale	$\pm 4\%$	1.0 % (10% at low y)

Table 9.1.: *Summary of all systematic errors with the breakdown into bin-to-bin uncorrelated and bin-to-bin correlated uncertainty sources.*

9.1. Uncorrelated Uncertainties

Track Efficiency Uncertainty

The uncertainty of the track reconstruction efficiency is the dominant systematic error of this measurement. At high transverse momenta of the track the LAr calorimeter can be used as additional detector component to cross check the tracking system. Such a study observes a difference between the track finding efficiency in data and MC of 2%. This uncertainty is applicable for the transverse momentum range that is analysed here [Boe07].

The determination of the track finding efficiency at low momenta is a difficult issue because there is no other detector component to cross check the tracking system. Instead a direct determination is possible from studies of tracks with low momenta, which start to curl inside the CJCs where a part of the track is reconstructed within the CJC1 and another part in the CJC2 after penetrating the dead material in between. These studies suffer from background and are at the moment not final for the HERA II data taking [Bri08].
For the time being 2% per track is assigned as systematic uncertainty of the track finding efficiency. Thus the presented measurement has a total track efficiency error of 6%. For the normalised ratio of the cross section in data to MC the track efficiency error has been reduced by 1.4% because half of the error arises from an unknown dependence and the rest is due to normalisation, which is not present in a normalised distribution.

Luminosity Measurement Uncertainty

The luminosity measurement and its uncertainty is under investigation by a luminosity task force because all high-statistics analyses observe a jump in the event yield around run number 477000. As an example figure 9.1 illustrates the high statistics yield of a DIS analysis where the scattered electron is detected by the SPACAL. The whole HERA II data taking was analysed and the step (vertical solid line) is observed at around 477000. The currently assigned uncertainty of the luminosity measurement of $L/\delta L = 2.5\%$ before the step and $L/\delta L = 5\%$ afterwards are indicated by two underlayed bands. These bands cover the spread of the yield including the step. At

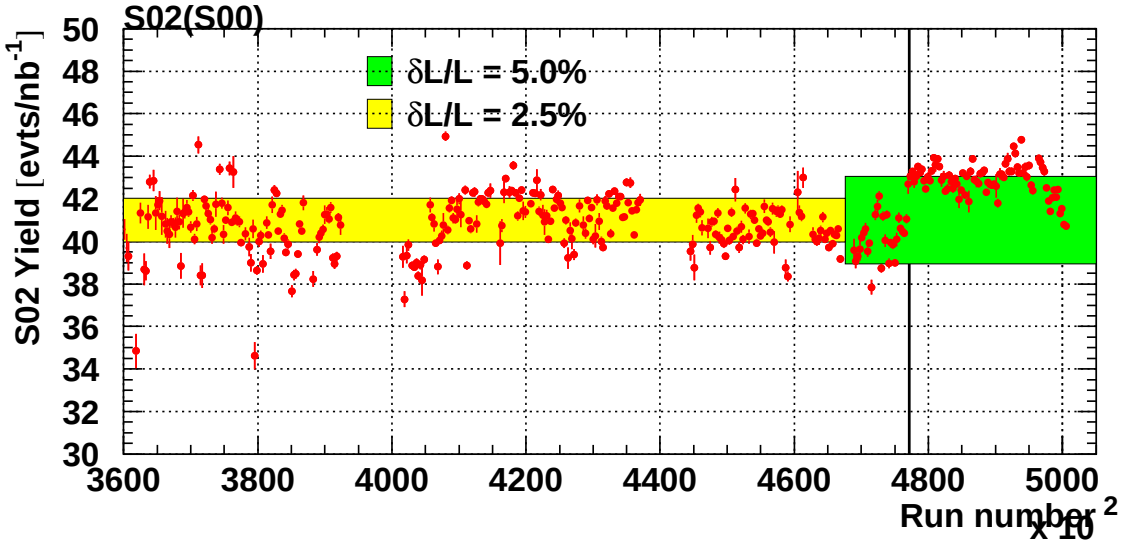

Figure 9.1.: *The high statistics yield of a DIS analysis where the scattered electron is detected by the SPACAL is shown for the whole HERA II period. An error on the luminosity measurement as indicated by the two shaded bands with* 2.5% *and* 5% *covers the spread of the yield. A step in the yield is observed at around* 477000 *and indicated by the solid line.*

the last collaboration meeting the most probable reason was identified to be a subtle acceptance problem of the detector, which has been used for the measurement of the

luminosity [NS+08].
The luminosity uncertainty error for this analysis is 3.2%, which is calculated as a weighted error, based on the amount of luminosity taken in the two different run periods of uncertainty.

Radiative Correction Uncertainty

For the conversion of the measured cross section to the *Born level* cross section as discussed in section 8.2 the RAPGAP program interfaced to HERACLES has been utilised. The corrections applied are of the order of 2.5%. A conservative uncertainty of 2.5% has been assigned, which is of the same order, because a detailed study comparing the radiative correction factors calculated by two different programs, like HECTOR and HERACLES, has not been performed. For the presented analysis this radiative correction uncertainty is not the dominant one therefore it does not harm to be conservative. Nevertheless, the recent H1 publication about the measurement of F_L [A+08a] includes such a study and concludes a uncertainty of 1.0%.

Primary-vertex Fit Uncertainty

The uncertainty of the primary-vertex fit is estimated from a dedicated almost background free D^* sample in data and a high statistics D^* signal MC sample. These two samples are used as an input to the D^* finder utilising primary-vertex fitted tracks and non-primary-vertex fitted tracks. Accordingly the ΔM distributions in data and MC are filled from primary-vertex fitted tracks and non-vertex fitted tracks. The primary-vertex fit efficiency is determined by the fraction $N(D^*)_{\text{vertex}}/N(D^*)_{\text{non-vertex}}$ for data and MC. A difference of 2.5% has been observed [Boe07] and is adopted here as the primary-vertex fit uncertainty.

Signal Extraction Uncertainty

The method for the estimation of a signal extraction uncertainty has previously been used in [Boe07] and is adapted here. The basic principle is to check the stability of the fit to the ΔM distribution. Therefore different fit parameterisations of the combined fit are utilised to determine the number of D^* mesons from data and MC samples. The full data sample has been used in order to minimise the dependence of the fit from statistical effects. The fit uncertainty is than estimated on the spread of the different fit results.
The sum of the Crystal Ball signal parametrisation as defined in equation 5.2 and the Granet background parametrisation (see eqn. 5.1) are defined as standard fit. Apart from that the Bukin signal function parametrisation has been used:

$$f_{\text{Bukin}}(x) = A \cdot \exp\left(-0.5 \ln^2\left[1 + \Lambda\tau(x - x_0)\right]/\tau^2 + \tau^2\right) \ . \tag{9.1}$$

As an additional parametrisation of the non-resonant background of the ΔM distribution the following polynomial parametrisation is employed:

$$f(x) = (x - m_\pi)^a \cdot (1 - b \cdot x^2) \ . \tag{9.2}$$

The fitted parameters are a and b, while the term $(x - m_\pi)$ models the threshold behaviour of the ΔM distribution with the allowed region $x > m_\pi$.
The signal extraction is based on two functions for the non-resonant background: the polynomial function or the Granet function (see eqn. 5.1) and two functions for the signal: the Bukin function or the Crystal Ball function (see eqn. 5.2). Thus the

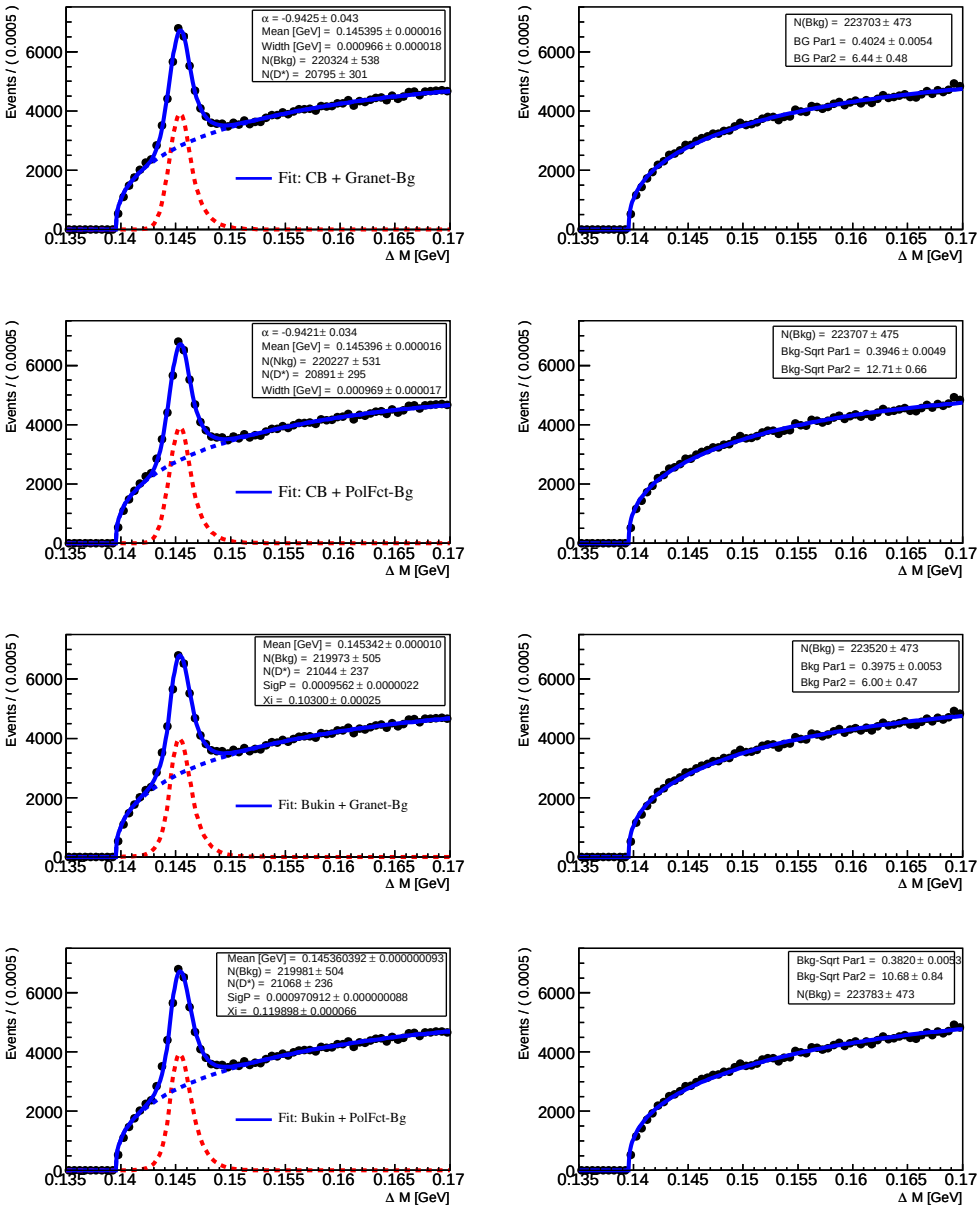

Figure 9.2.: *The ΔM distribution in data for right charge (left column) and wrong charge (right column) fitted with different parametrisations of the signal and background function as stated in the legend of a ΔM histogram.*

study to estimate the fit extraction uncertainty implements in total four combinations of signal and background functions as illustrated in figure 9.2 for data where the fit parametrisations are indicated. The description of the ΔM distribution is reasonably good by all combinations and furthermore the derived number of D^* mesons agrees

well with the number of D^* mesons derived by the default setup (Crystal Ball + Granet function). These fit combinations are applied to the whole data sample, to a signal MC sample and to a fully inclusive MC sample where the result of the different parametrisation combinations is summarised in table 9.2. The systematic uncertainty

data		Crystal Ball	Bukin
	Granet	20795 ± 301	21044 ± 237
	Pol.Fct.	20891 ± 295	21068 ± 236
signal MC		Crystal Ball	Bukin
	Granet	669864 ± 856	677273 ± 869
	Pol.Fct.	671108 ± 838	681456 ± 867
incl. MC		Crystal Ball	Bukin
	Granet	32869 ± 253	33329 ± 247
	Pol.Fct.	32965 ± 255	33450 ± 256

Table 9.2.: *Fit results using different parameterisations for the right charge ΔM distribution for data, a signal MC and a fully inclusive $c\bar{c}$ MC sample.*

on the signal extraction is taken from the largest difference between the fit result to the nominal Crystal Ball + Granet parametrisation. In data the largest difference is $\sim 1.3\%$, while the signal MC sample gives a values of $\sim 1.8\%$. The fully inclusive $c\bar{c}$ MC sample shows a largest difference between the fit results of 1.4%. All values agree within 2% which is assigned as systematic signal extraction uncertainty.

Branching Ratio Uncertainty

The systematic error on the branching ratio of the D^* meson decaying in the golden decay channel: $D^* \to D^0\pi_{\text{slow}} \to (K\pi)\pi_{\text{slow}}$ is 2.3% [Y+06].

Trigger Efficiency Uncertainty

The estimation of the uncertainty of the two trigger conditions implemented in s61 has been described in section 8.1 and is conservatively 1% per condition. Thus a systematic uncertainty of 1.4% covers the trigger uncertainty of s61.

D^0 Mass Cut Uncertainty

Due to slightly different resolutions in data and Monte Carlo the efficiency of the D^0 mass window cut of ± 80 MeV around the nominal D^0 mass can be different. In order to estimate an uncertainty for this cut the $M(D^0)$ distribution from data and MC is studied in bins of the transverse momentum of the D^* meson. Each $M(D^0)$ distribution is fitted with the sum of a Gaussian function and a polynomial function to account for the background. The result of the fit is illustrated in figure 9.3 as a function of

$p_T(D^*)$: The mean denotes the D^0 mass position, while the error bar is the width of the D^0 mass peak as obtained by the fit to data (filled circles) and MC (open squares). Overall the data shows a slightly broader D^0 mass peak as expected due to the worse

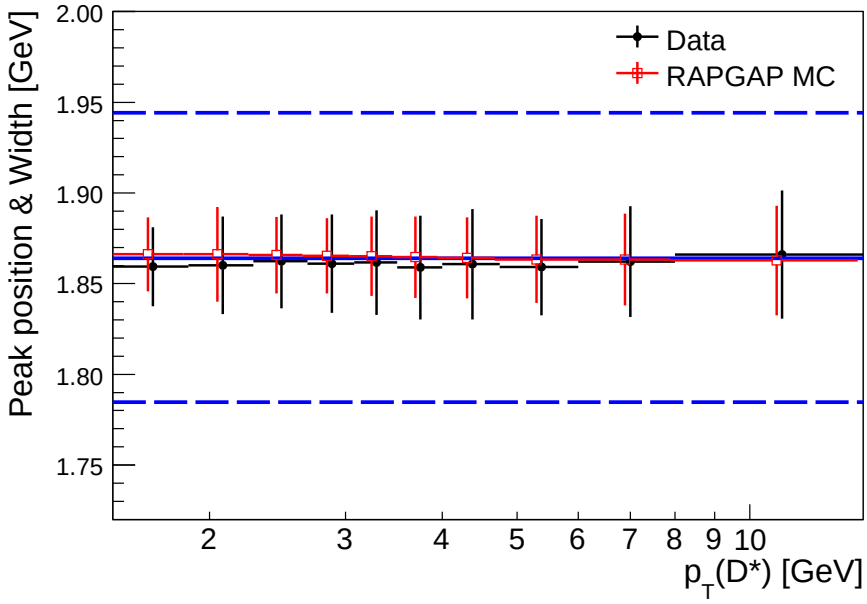

Figure 9.3.: *The $M(D^0)$ distribution in bins of $p_T(D^*)$ for data (circles) and MC (squares) has been fitted with the sum of a Gaussian and polynomial function. The result of the fit as a function of $p_T(D^*)$ is shown here. The error bar denotes the width of the D^0 mass peak. The solid horizontal lines indicate the nominal D^0 mass value (solid line) and the ± 80 MeV cut (dashed lines) as implemented for the D^* selection.*

resolution in data compared to MC and in addition the data shows a systematic shift to lower D^0 masses. In order to estimate the uncertainty of the D^0 mass cut the integral of the Gaussian fit in bins of the $p_T(D^*)$ distribution is used to calculate the relative loss which is the fraction of events that is not inside the ± 80 MeV cut around the nominal D^0 mass. This method relies on the simplified assumption that a single Gaussian function describes the signal. Figure 9.4 depicts the relative loss for data compared to MC where the fit error has been taken into account in terms of relative losses. Overall the relative loss in data is small $< 1\%$ besides the highest $p_T(D^*)$ bin, which has also a large fit error for the data. The difference to the relative loss in MC is well below 1% within the statistical precision of this study and therefore a correction is not applied but 1.0% is taken as an uncertainty of the D^0 mass cut.

Systematic Uncertainty due to Reflections

The method for the determination of the contribution of the reflections from non-golden decay channels to the D^* signal in the golden decay channel has been described in section 8.3 where the full statistics of the fully inclusive MC sample has been utilised. The systematic uncertainty due to reflections is estimated from the dependence of the contribution with $p_T(D^*)$. The high MC statistics utilised for this study allows a good

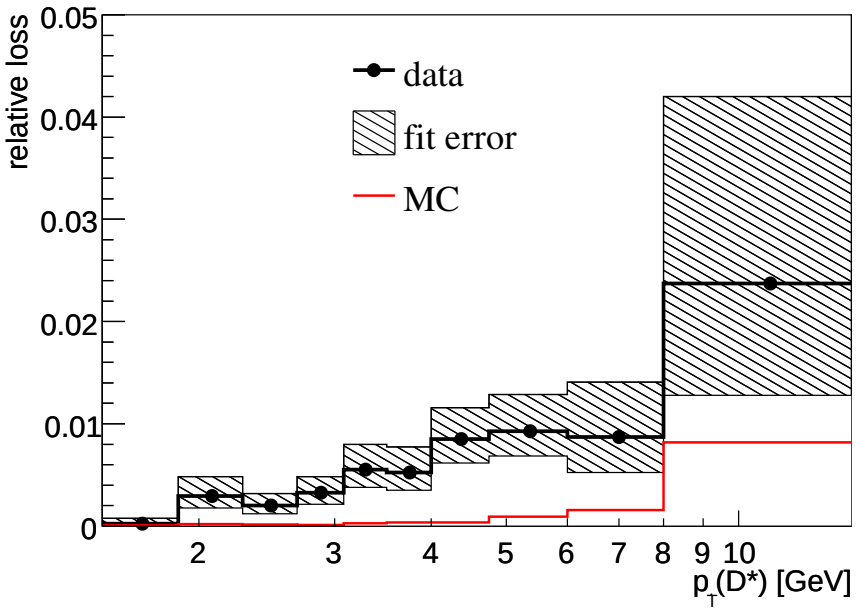

Figure 9.4.: *The relative loss due to the D^0 cut window as a function of $p_T(D^*)$ for data and MC, which is estimated from the integral of a Gaussian fit to the $M(D^0)$ distribution within and without the* ± 80 MeV *cut around the nominal D^0 mass.*

constraint of the dependence, which is expected because of the width of the D^0 peak that changes with transverse momenta. A broader D^0 peak contains more and more reflections with increasing transverse momenta of the D^* meson, which is illustrated in figure 9.5. Nevertheless, within the statistical precision the distribution is compatible with a flat distribution; 1% covers all differences to the 4% correction applied to the cross sections and is assigned as a systematic uncertainty to cover a dependence of the reflections.

Proton PDF Uncertainty

A proton PDF uncertainty has been estimated in bins of the cross section measurement utilising different parameterisations for the proton PDF, namely CTEQ6ll and CTEQ65m, with the RAPGAP MC program. The difference of the detector acceptance (see eqn. 5.6) from RAPGAP MC samples generated with different proton PDFs to the nominal acceptance is assigned as proton PDF uncertainty. The relative errors for the $Q^2, y, W_{\gamma P}$ and x distributions are illustrated in figure 9.6a)-d), while figure 9.6e)-h) depicts the relative error estimated for the $x_g^{\text{obs}}, p_T(D^*), \eta(D^*)$ and $z(D^*)$ distribution. Overall the uncertainty due to different proton PDFs is less than 1% for all distributions. As there is no strong dependence of the relative error for a certain variable on the usage of different PDFs a uncorrelated systematic uncertainty of 1% is assigned.

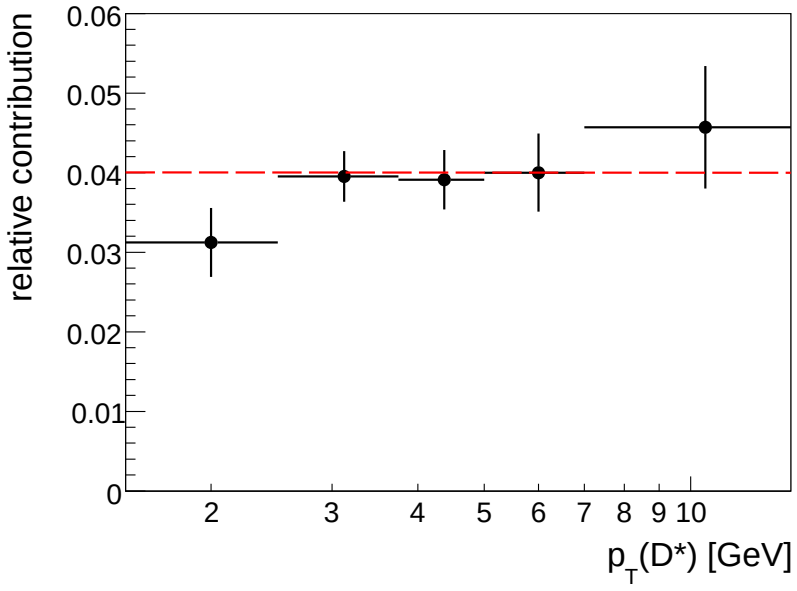

Figure 9.5.: *The relative contribution of the reflections from non-golden decay channels to the D^* signal in the golden decay channel as function of the transverse momentum of the D^* meson. The dashed line indicates the flat correction assigned to the cross sections to account for the contribution of the reflections (see section 8.3).*

Photoproduction Background Uncertainty

An uncertainty of the background from photoproduction is estimated from a photoproduction PYTHIA MC (signal D^*) with an upper Q^2 cut as high as the lower Q^2 cut during the generation of the DIS MC, which was 3.5 GeV^2. As this analysis starts at 5 GeV^2 migrations of DIS events from $3.5-5$ GeV^2 into the measured region are taken into account by the DIS MC during the correction of detector effects. The amount of D^* mesons originating from the photoproduction process is determined from the full selection and analysis chain used with the photoproduction MC. Thus a yield of 0.09 D* mesons/pb^{-1} from photoproduction processes is calculated and compared with the DIS yield for this analysis of about 58 D* mesons/pb^{-1} (see section 6.1). The fraction of photoproduction background is less than 0.15% for the presented analysis which has been assigned as systematic uncertainty.

9.2. Correlated Uncertainties

In case of the correlated uncertainties the relative error that arises from a certain variation in MC is calculated using the nominal cross section value of a certain quantity and the cross section value of the up- and down variation:

$$\delta^{\pm} = \frac{\sigma^{\pm} - \sigma_{\text{nom}}}{\sigma_{\text{nom}}} \,. \tag{9.3}$$

The change of the reconstruction method from the e-method to the $e\Sigma$-method (see section 5.4) combined with the lowered y cut gives a significant reduction of the systematic

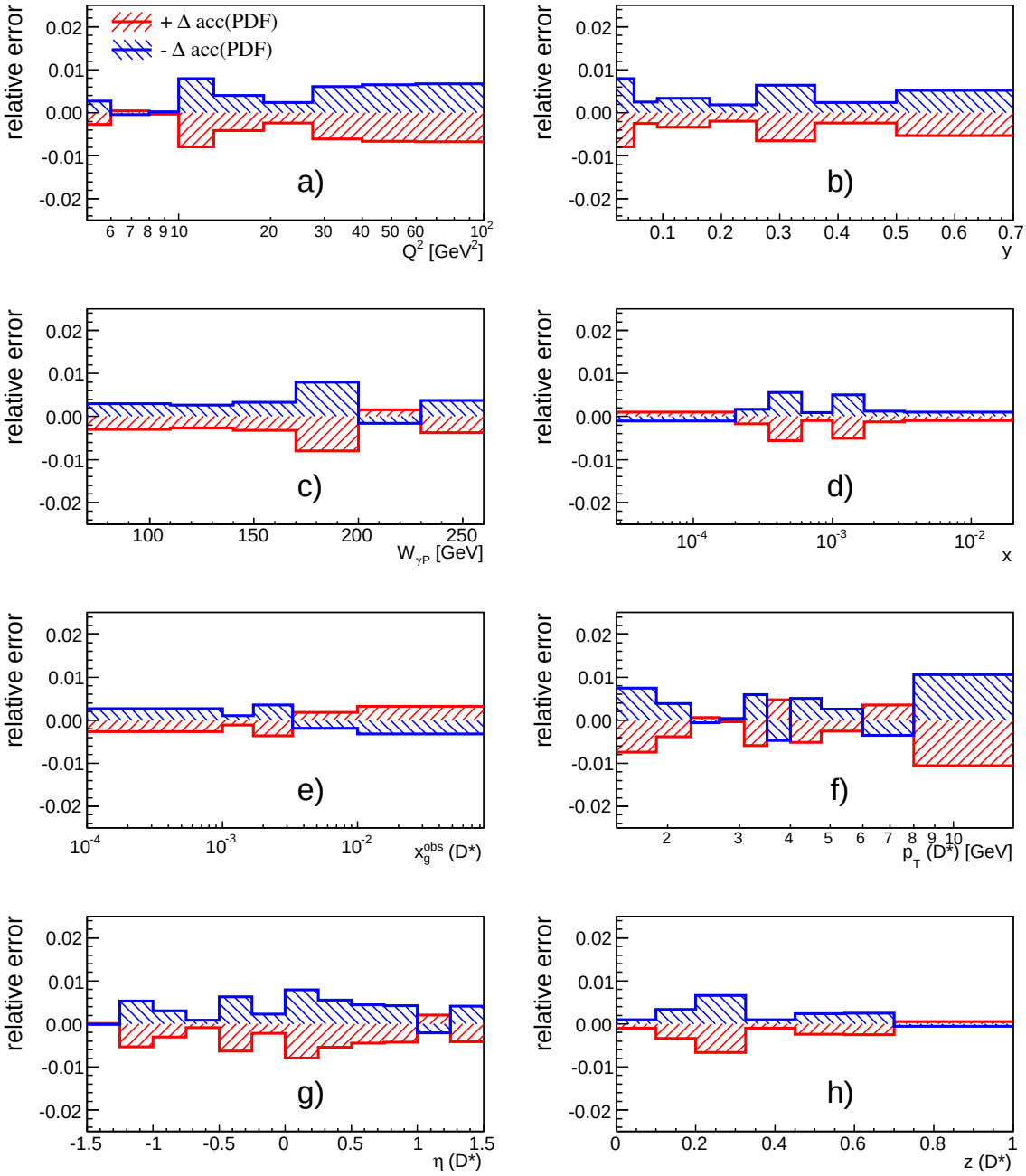

Figure 9.6.: *The relative error due to different proton PDFs for event kinematic quantities like Q^2, y, x and for quantities of the D^* meson like $p_T(D^*)$, $\eta(D^*)$ and $z(D^*)$.*

uncertainty from the energy scale uncertainty, although in addition to the electromagnetic energy scale also the hadronic energy scale has to be varied. As an example the relative error according to equation 9.3 for the $\eta(D^*)$ distribution is displayed in figure 9.7. The filled band illustrates the uncertainty from the electromagnetic energy scale variation utilising the e-method and the hatched band (inside the thick solid lines) illustrates the uncertainty from the electromagnetic and hadronic scale variation added in quadrature for the $e\Sigma$-method. In previous D^* analysis at H1 the e-method has been used together with a higher y cut of > 0.05 which led to uncertainties of up to 15% in forward directions. This is owed to the fact that D^* mesons produced at low y, which corresponds to large x, go predominantly in forward directions or $\eta(D^*) > 0$. The uncertainty arising from the energy scale uncertainty is negligible for the $\eta(D^*)$ distribution if the $e\Sigma$-method is used and the y range is extended. Therefore an exten-

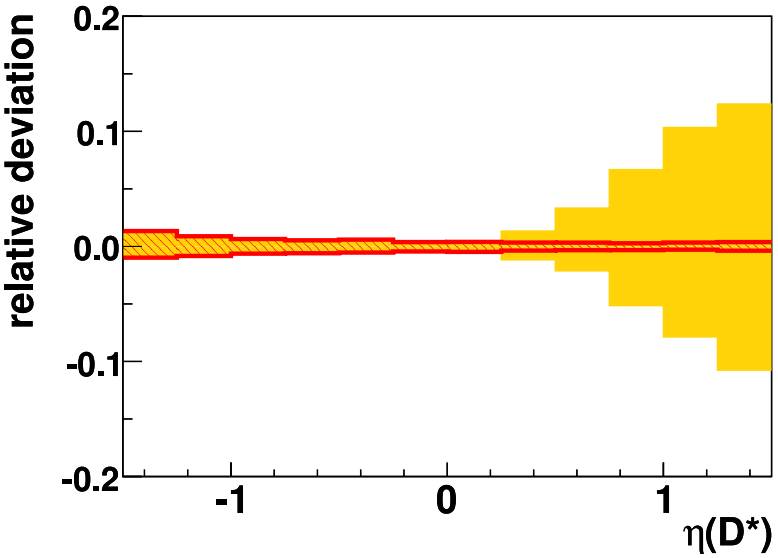

Figure 9.7.: *Comparison of the relative uncertainty from the energy scale uncertainty in bins of $\eta(D^*)$ if the $e\Sigma$-method (hatched band) in the kinematic range $0.02 < y < 0.70$ or the e-method in the range $0.05 < y < 0.70$ is used (filled band).*

sion of the phase space towards lower y has been done for the present analysis. In the following the bin-to-bin correlated errors are discussed in more detail for the presented cross section measurement.

Systematic Errors from the Electron & Hadron Measurement

The values of the uncertainty of the scale of the electromagnetic and hadronic energy scales are utilised to estimate the influence on the measurement of D^* meson production. The systematic uncertainty on the electromagnetic energy calibration has been measured to be about 1%, whereas the angular precision of the SPACAL and BPC is about 1 mrad and the systematic uncertainty on the hadronic energy calibration has been determined by H1 to be about 4% [Kru08]. For an estimation of the influence of these scale uncertainties on the measurement three scale variations are applied to

MC. The advantage due to the $e\Sigma$-method for the analysed phase space is illustrated in figure 9.8, which shows the uncertainty from the relevant energy scale uncertainty for the e-method and the $e\Sigma$-method exemplarily for the y and $z(D^*)$ distribution. In

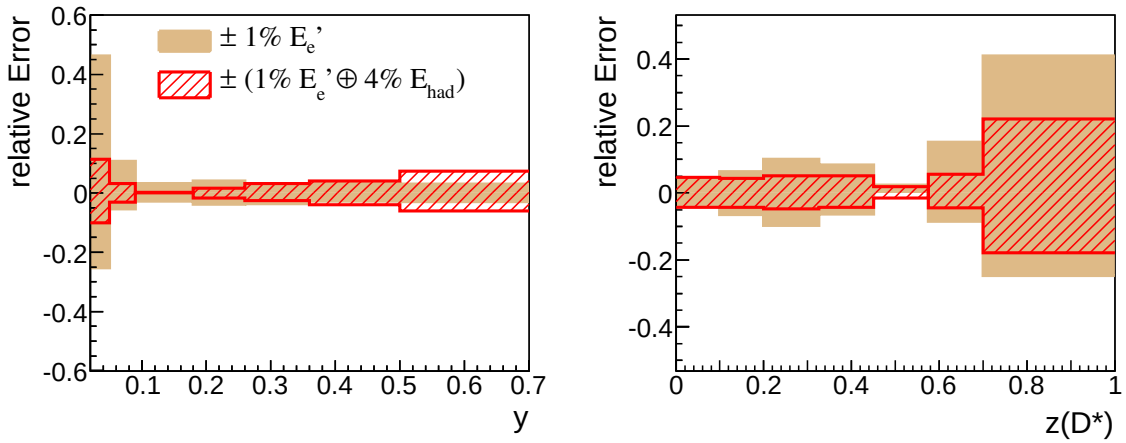

Figure 9.8.: *The relative error, which arises from the energy scale variation for the e-method (shaded band) where only the electromagnetic scale is varied and for the eΣ-method (red hatched band) where electromagnetic and hadronic energy scale are varied individually. In this case the relative errors are added in quadrature.*

the case of the e-method the error due to the variation of the electromagnetic energy scale is indicated as shaded band. The overlayed hatched band displays the error from the electromagnetic and hadronic energy scale variation added in quadrature if the $e\Sigma$-method is utilised. As the $e\Sigma$-method is less sensitive to the measurement of $E_{e'}$ it shows, in particular at low y, a better behaviour. At large y the $e\Sigma$-method is slightly worse but still acceptable. For the $z(D^*)$ distribution the $e\Sigma$-method illustrates an improvement over almost the whole $z(D^*)$ range. Especially at large $z(D^*)$ a reduction of the error of nearly a factor two for the $e\Sigma$-method is achieved. Thus the $e\Sigma$-method provides significantly reduced errors (see also figure 9.7) estimated from the energy scale variations.
In the following the results of the three scale variations are discussed in more detail. According to equation 9.3 the relative error is than calculated from the difference of the nominal cross section compared to the cross section values after a scale variation. The relative errors are assigned as an additional correlated systematic error source of the cross section measurement.
A variation of the electromagnetic energy scale by $\pm 1\%$ is utilised to estimate the uncertainty for the present measurement from the electromagnetic energy scale. Figure 9.9 illustrates the relative errors calculated from the difference of the nominal cross section value in MC to the one optained after a variation of the electromagnetic energy scale by $\pm 1\%$. The statistical precision in a certain bin of the data sample is indicated by the error bar. The direction of the variation is stated in the legend. For the Q^2 distribution, depicted in figure 9.9a), the error is within 1% as expected with the exception of the highest Q^2 bin ($< 1.5\%$). For the inelasticity y as depicted in figure 9.9b) it is largest (around 5%) at high y where predomiantly the measurement

of the electron has an impact. As $W_{\gamma P}$ is directly correlated with y it shows almost the same dependence as illustrated in figure 9.9c). As high y translates to small x

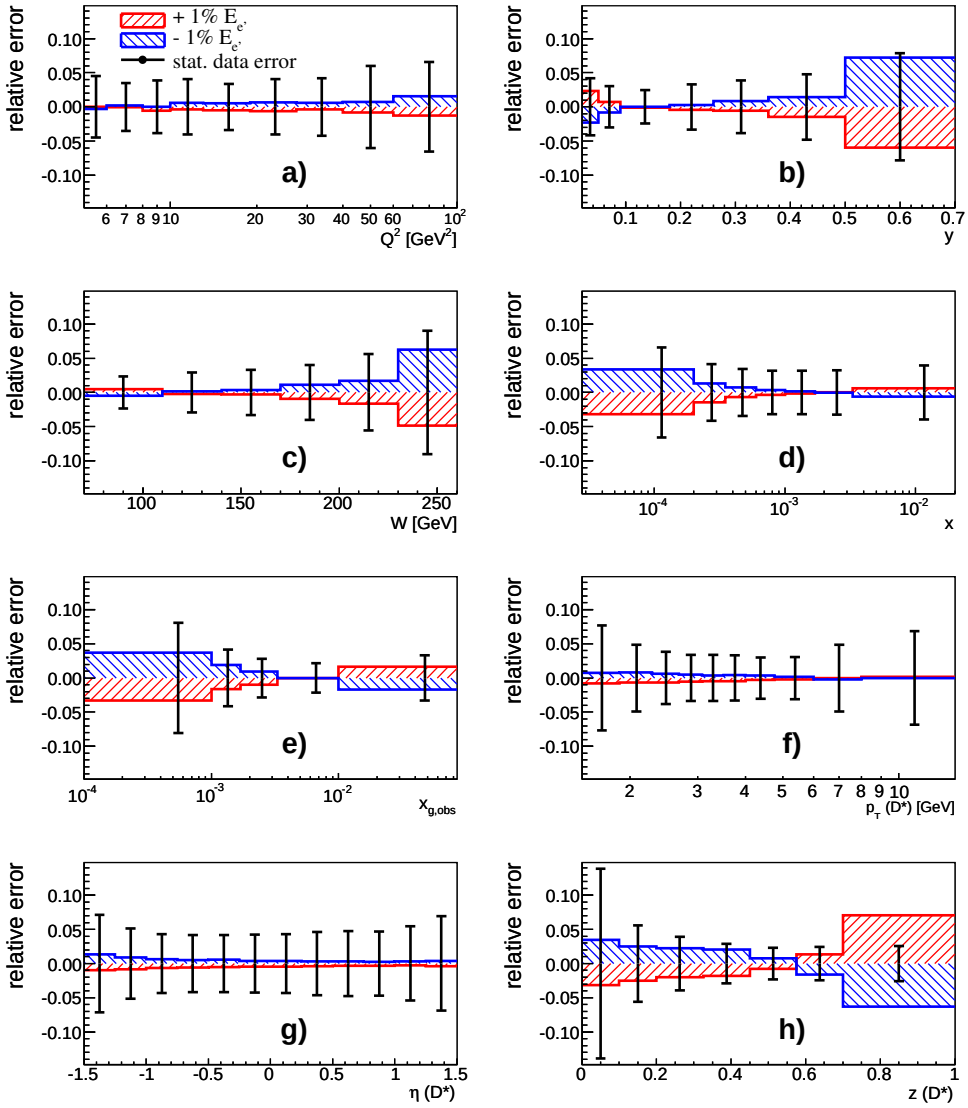

Figure 9.9.: *Variation of the electromagnetic energy scale by ±1% for event kinematic quantities like Q^2, y, x and for quantities of the D^* meson like $p_T(D^*)$, $\eta(D^*)$ and $z(D^*)$. The statistical precision of the data sample in a certain bin is indicated by the error bar.*

(and also small x_g^{obs}) the largest error for these distributions is located at small values as displayed in figures 9.9d)-e). The D^* distributions for example $p_T(D^*)$ and $\eta(D^*)$ are shown in figures 9.9f)-g) and inherit only minor errors from the variation of the electromagnetic scale variation. The $z(D^*)$ distribution, see figure 9.9h), shows larger errors of around $4-7\%$ as expected because the calculation of $z(D^*)$ depends directly on y. Together with the high y region this is the only bin where the uncertainty from the electromagentic energy scale is close to or even larger than the statistical error of the data.

Figure 9.10 illustrates the errors that arise from the variation of the hadronic energy

scale within the uncertainty of ±4% in the same way as it was done for the electromagnetic scale variation. As expected there are variables which do not depend on the hadronic energy and by that do not inherit any sizeable error. This is the case for

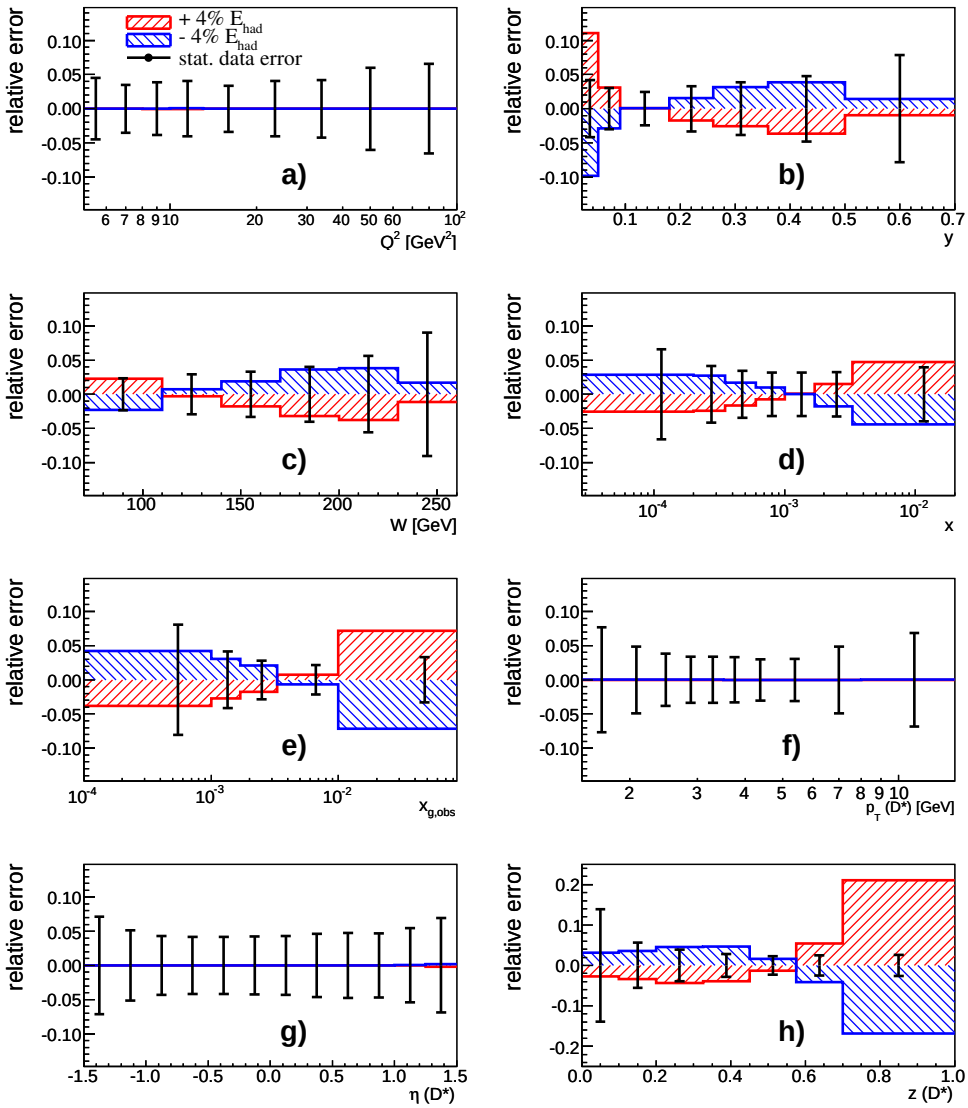

Figure 9.10.: *Variation of the hadronic energy scale by ±4% for event kinematic quantities like Q^2, y, x and for quantities of the D^* meson like $p_T(D^*)$, $\eta(D^*)$ and $z(D^*)$. The statistical precision of the data sample in a certain bin is indicated by the error bar. Take note of the different y axis for $z(D^*)$.*

Q^2 as depicted in figure 9.10a) and for D^* quantities like $p_T(D^*)$ or $\eta(D^*)$ displayed in figures 9.10f)-g). Other quantities depend on the hadronic energy scale and have sizeable errors. Due to the use of hadronic quantities for the y reconstruction at low y the error is here, with up to 11%, larger than the statistical error. For the medium and large y region the error is around 3% as depicted in figure 9.10b). The error from the hadronic energy scale for $W_{\gamma P}$ is around 3% with no large excursions as shown in figure 9.10c). For x and x_g^{obs}, see figure 9.10d)-e), the error is up to 5% at high x and up to 8% at high x_g^{obs}. In case of the x distribution this is reasonable because the

high x domain corresponds to low y region with large errors from the hadronic scale uncertainty. The calculation of x_g^{obs} depends directly on the inelasticity and inherits large errors. The $z(D^*)$ distribution shows the largest errors of up to 20% at large $z(D^*)$. The statistical errors are of comparable size to the hadronic scale uncertainty and at high $z(D^*)$ even smaller, thus the measurement in $z(D^*)$ is dominated from the hadronic scale uncertainty.
In addition to the uncertainty of the energy scale the uncertainty of the angular pre-

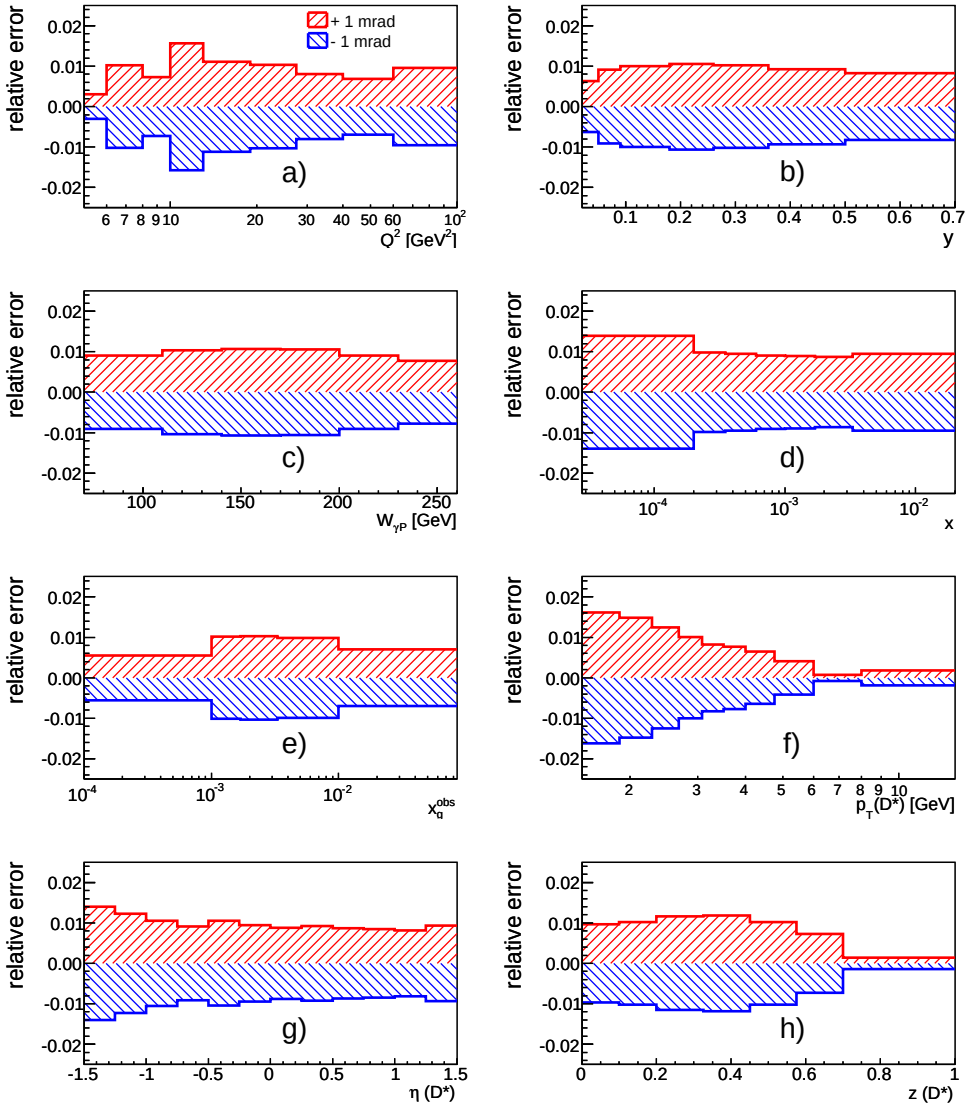

Figure 9.11.: *Variation of the scattered electron angle in the interval of the angular precision of ±1% of the SPACAL & BPC for event kinematic quantities like Q^2, y, x and for quantities of the D^* meson like $p_T(D^*)$, $\eta(D^*)$ and $z(D^*)$.*

cision of the SPACAL (and BPC) for the measurement of the angle of the scattered electron has to be taken into account. This is done by a variation of the angle of the scattered electron by ±1 mrad. The relative errors are calculated according to equation 9.3 and are illustrated in figure 9.11. As expected there is no strong dependence for

any quantity. Furthermore all errors are less than 1.5%, which is why the comparison to the statistical precision of the data is not made.

Model Uncertainty

The model uncertainty is estimated from different MC programs which utilise different parameterisation for the evolution equation, namely the DGLAP scheme versus the CCFM scheme. The difference of the acceptance (see eqn. 5.6) calculated from

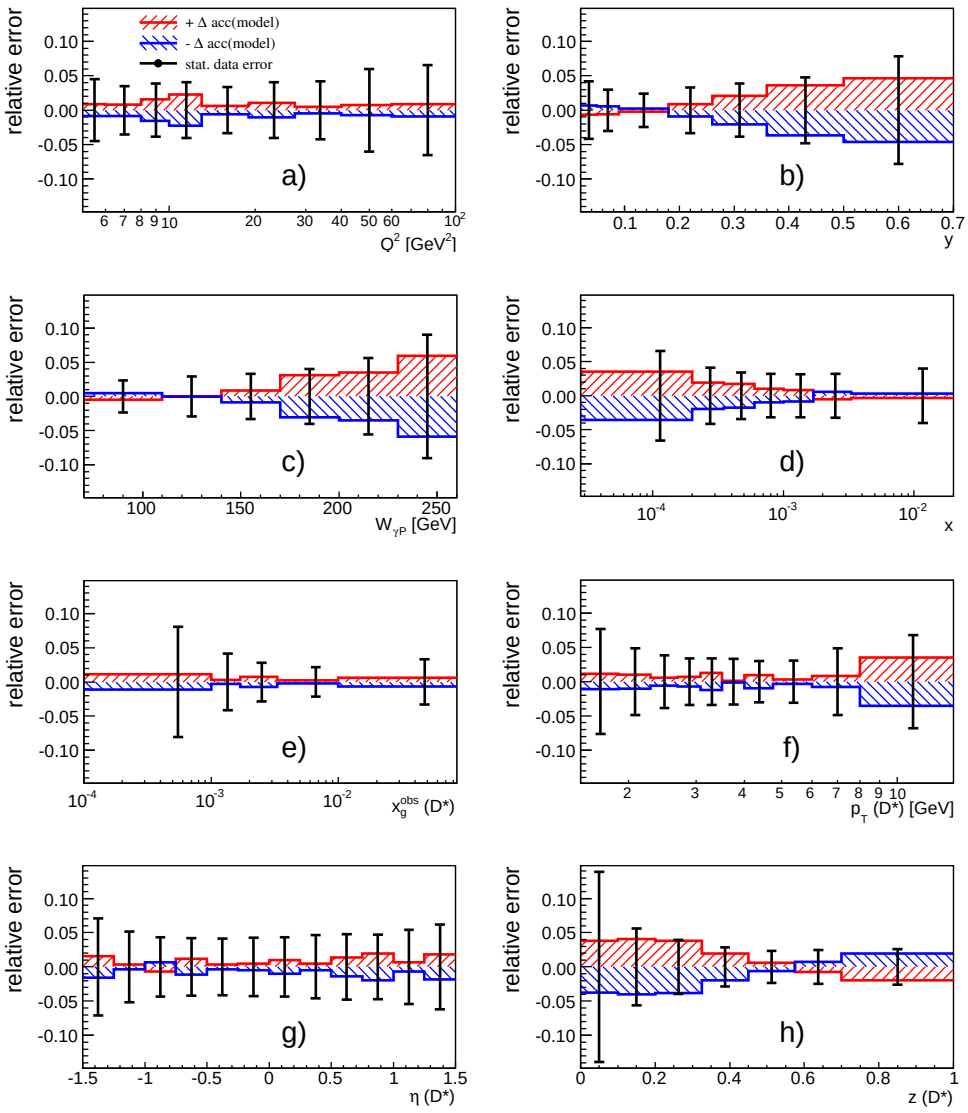

Figure 9.12.: *A model uncertainty is calculated from RAPGAP and CASCADE MC samples for event kinematic quantities like Q^2, y, x and for quantities of the D^* meson like $p_T(D^*)$, $\eta(D^*)$ and $z(D^*)$. More details are given in the text. The statistical precision of the data sample in a certain bin is indicated by the error bar.*

RAPGAP and CASCADE MC samples to the nominal acceptance is assigned as relative error $\pm\Delta acc$ in bins of the cross section measurement. The relative errors for

the $\eta(D^*)$, $p_T(D^*)$ and Q^2 distributions as illustrated in figure 9.12 are reasonable flat, except for the highest $p_T(D^*)$ bin where an error of 4% is observed. As the nominal acceptance is calculated from a RAPGAP with NLO QED contributions one expects small differences to CASCADE predominantly at low y. The inelasticity y shows a slight dependence on the used model and an error of up to 4.5% at high y due to the different models. The errors arising from different models for the $z(D^*)$ distribution have a clear structure and sizeable errors of up to 4% located at small $z(D^*)$. For the x and x_g^{obs} distribution the largest errors of up to 4% are located at small x. For the $W_{\gamma P}$ distribution the errors are 6% at large values of the centre-of-mass energy in the photon-proton rest frame and minor for values smaller than 170 GeV. Because of the dependence of certain variables, e.g. the inelasticity y, on the used MC a correlated systematic uncertainty on the use of different models is assigned per bin of the cross section measurement.

9.3. Fragmentation Uncertainty

The parametrisation of the fragmentation function (see equations 2.15-2.17) and its parameters assumed for the fragmentation process from $c \to D^*$ have an influence on the data correction. The Bowler fragmentation function (see equation 2.17) is used for the MC samples with parameters adopted from the ALEPH tune [Kno96] which were derived from e^+e^- measurements of the fragmentation function. In addition H1 did a measurements of the fragmentation function in $ep \to eD^*X$ processes [A+08b]. A good agreement of the parameters between ep and e^+e^- measurements is observed. But the H1 measurement sees problems for the QCD models and the NLO predictions

fragmentation function	value
Bowler	$a = 0.400$, $b = 0.885$
Kartvelishvili	$\alpha = 4.84 \pm 0.01$
$\hat{s}$ fragmentation:	
low $\hat{s} < 70$ GeV^2	$\alpha = 8.2 \pm 1.1$
high $\hat{s} > 70$ GeV^2	$\alpha = 4.6 \pm 0.6$
$\hat{s}$ threshold	70 ± 20 GeV^2

Table 9.3.: *The parameters of the Bowler fragmentation function used for the generation of the CASCADE sample corresponds to the given α value of the Kartvelishvili fragmentation. The $\hat{s}$ fragmentation with its parameters is given in addition.*

to describe the data at different photon-gluon centre-of-mass energies ($\hat{s}$) with the same parameters of a fragmentation function. The $\hat{s}$ dependence corresponds to significantly different parameters of a fragmentation function if D^* mesons are produced near the production threshold (low $\hat{s}$), with almost no additional activity in the event, or far above the threshold (high $\hat{s}$) where enough energy is available to produce additional particles. In the measurement [A+08b] the two regions are distinguished by demanding or vetoing two jets with a transverse momentum above a certain threshold which

corresponds roughly to $\hat{s} = 70$ GeV^2 [Lip08].
For this study a CASCADE sample has been utilised, since for CASCADE a part of the fragmentation information[1] is stored during the generation process. CASCADE is generated with the Bowler fragmentation function, which depends on z and p_T. Since only z is stored for further studies, the z distribution has been fitted with a Kartvelishvili parametrisation and a value of $\alpha = 4.84 \pm 0.01$ as given in table 9.3 has been obtained. The z distribution is reweighted to the measured values of α for the two $\hat{s}$ regions (see table 9.3). Thus a $\hat{s}$ dependent fragmentation function ($\hat{s}$ *fragmentation*) is constructed, which is expected to describe the data better. Figure 9.13 (left) illustrates the generated fragmentation function parametrised as a Kartvelishvili distribution (solid line) and in addition the z distributions for $\hat{s} > 70$ GeV^2 and $\hat{s} < 70$ GeV^2. These

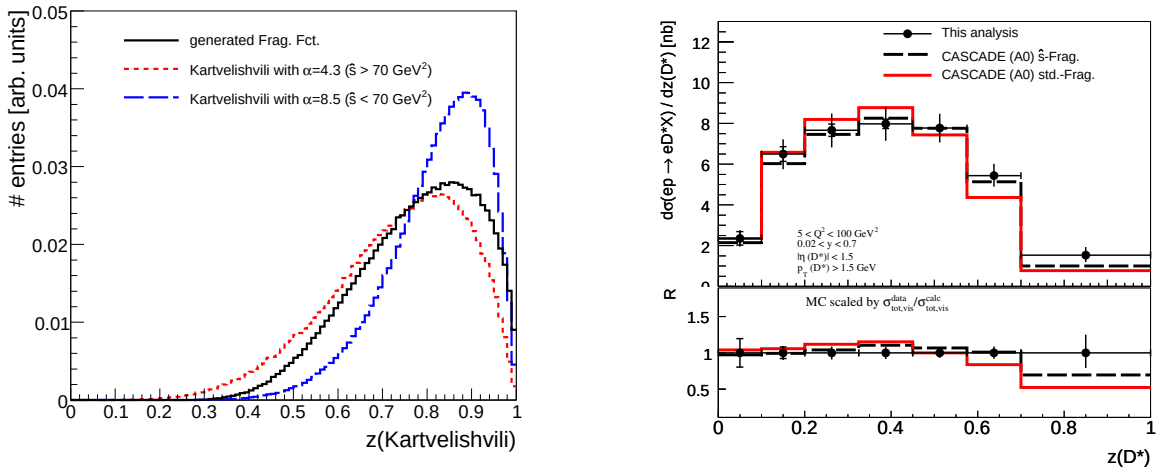

Figure 9.13.: *The z distribution of the standard Bowler fragmentation utilised during the generation of the CASCADE MC is equivalent to a Kartvelishvili fragmentation with an obtained value of $\alpha = 4.84$ (solid line) as depicted in the left histogram. The z distributions at low $\hat{s}$ (long dashed line) and high $\hat{s}$ (short dashed line) are shown for comparison. CASCADE has been re-weighted according to the $\hat{s}$ fragmentation as shown in the right histogram together with the not weighted CASCADE and the differential cross section as a function of $z(D^*)$. The ratio shown at the bottom is normalised to the total cross section according to equation 10.2.*

two different z distributions with a threshold of $\hat{s} = 70$ GeV^2 are utilised to reweight CASCADE to the $\hat{s}$ fragmentation function.
A quantity which is correlated to the fragmentation function is the $z(D^*)$ distribution. Therefore the cross section in $z(D^*)$ is compared to CASCADE as depicted in figure 9.13 (right). CASCADE with the Bowler fragmentation function is indicated by the solid line and CASCADE re-weighted to the $\hat{s}$ fragmentation is shown as dashed line. The description is in general improved but deviations remain at high $z(D^*)$. This is the region that enhances D^* mesons produced at low $\hat{s}$ as the D^* takes most of the available energy.
In order to quantify the influence on the data correction an independent variation of α

[1]The z quantity that is mentioned here is not the inelasticity of the D^* which is called $z(D^*)$.

and $\hat{s}$ of the $\hat{s}$ fragmentation as summarised in table 9.3 is done. Thus a fragmentation uncertainty of the cross section measurement has been estimated from the full error of α and the $\hat{s}$ threshold error in bins of the cross section measurement. The full difference of the acceptance (see eqn. 5.6) calculated from four re-weighted CASCADE samples to the nominal acceptance of the CASCADE sample with the standard Bowler fragmentation is assigned as relative error. For the fragmentation uncertainty illustrated in figure 9.14 the relative errors of the two variations are added in quadrature. This

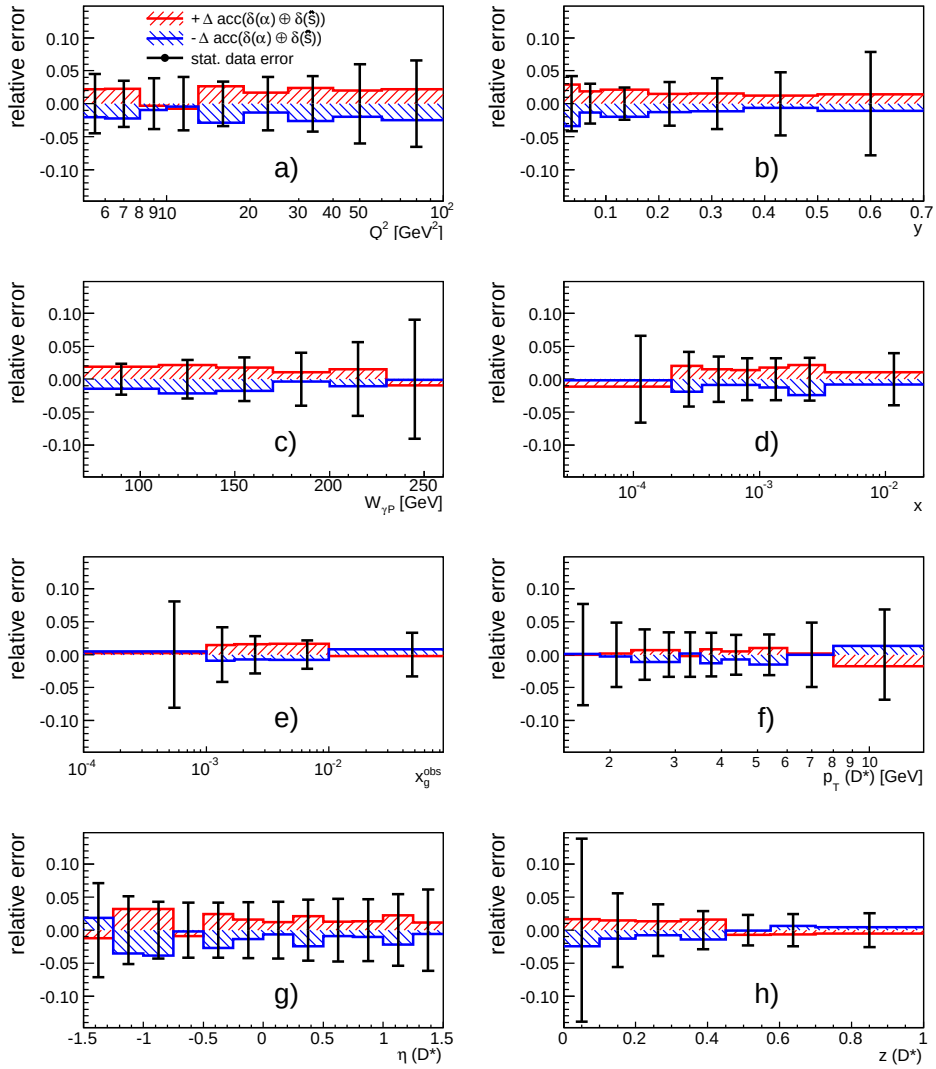

Figure 9.14.: *The relative error of the fragmentation uncertainty (for details see text), is depicted for event kinematic quantities like Q^2, y, x and for quantities of the D^* meson like $p_T(D^*)$, $\eta(D^*)$ and $z(D^*)$. The statistical precision of the data sample in a certain bin is indicated by the error bar.*

uncertainty is not added to the other systematic error sources but kept as single column in the cross section tables presented in the appendix 15.6. This has been done on purpose, as the preliminary results have been derived before the final conclusion of the fragmentation function measurement has been made, which lead to the introduction of the ad-hoc $\hat{s}$ fragmentation.

10. Cross Section Results

The D^* meson production cross section in deep inelastic scattering is calculated from equation 8.1. The number of D^* mesons is determined from a fit to the ΔM distribution with an asymmetric peak parametrisation considering the tail. The data sample is selected as discussed in section 6. The measurement uses an integrated luminosity of $\mathcal{L} = (347.7 \pm 11.1)$ pb^{-1} corresponding to the full HERA II data taking period. The

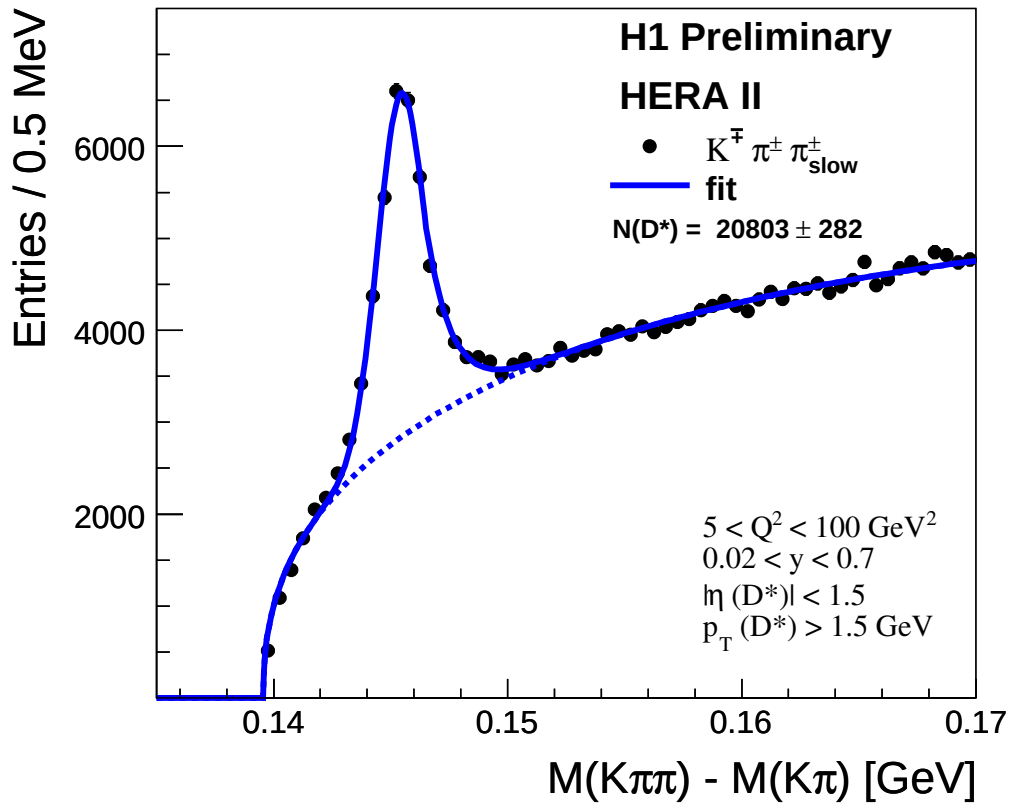

Figure 10.1.: *Distribution of the ΔM mass distribution of all selected D^* meson candidates. The combined signal and background fit (solid line) to the ΔM distribution uses the Crystal ball parametrisation whereas the background fit (dotted line) is according to the Granet parametrisation.*

D^* mesons decay in the golden channel $D^{*\pm} \to D^0 \pi^{\pm}_{\text{slow}} \to K^{\mp}\pi^{\pm}\pi^{\pm}_{\text{slow}}$ and are selected according to the cuts summarised in table 6.3. Table 6.2 summarises the cuts for deep inelastic scattering events. The ΔM distribution for the selected events is depicted in figure 10.1 and shows a large amount of D^* mesons. As mentioned previously due to the limited acceptance of an experiment the cross section measurement is restricted to a visible range (see table 10.1) within which the data are corrected for all detector effects. The presented cross section measurement is corrected for contributions from

variable	value
Virtuality	$5 < Q^2 < 100$ GeV^2
Inelasticity	$0.02 < y < 0.70$
Transverse momentum	$p_T(D^*) > 1.5$GeV
Pseudo-rapidity	$\|\eta(D^*)\| < 1.5$

Table 10.1.: *Definition of the visible range of the D^* cross section measurement.*

reflections, while contributions from b-quarks are neglected as they contribute only 2%. The cross section is converted to the Born level by correcting the NLO QED contributions from ISR and FSR events including virtual corrections as discussed in section 8.2.

10.1. The total Cross Section

The total cross section in the visible range (see table 10.1) is measured to be:

$$\sigma^{\text{tot}}_{\text{vis}}(e^{\pm}p \to e^{\pm}D^{*\pm}X) = 4.85 \pm 0.07\ (\text{stat.}) \pm 0.42\ (\text{syst.})\ \text{nb}. \tag{10.1}$$

The total systematic uncertainty error is 8.7% whereas the statistical precision is 1.4%. The total cross section predictions from the LO MC programs and the NLO calculation HVQDIS are summarised in table 10.2. For the same visible region RAPGAP using the

LO MC predictions:	proton PDF	$\sigma^{\text{tot}}_{\text{vis}}$ [nb]
RAPGAP	CTEQ6ll	4.89 nb
	CTEQ65m	3.65 nb
CASCADE	A0	4.72 nb
NLO calculation:	**proton PDF**	**$\sigma^{\text{tot}}_{\text{vis}}$ [nb]**
HVQDIS variations:		
$1.3 < m_c < 1.6$ GeV $0.5 < \mu_{r,f}/\mu_0 < 2,\ \mu_0^2 = Q^2 + 4m_c^2$ $2.9 < \alpha$(Kartvelishvili) < 3.7		
	CTEQ5F3	$4.43\ ^{+0.69}_{-0.47}$ nb
	MRST2004FF3nlo	$4.17\ ^{+0.59}_{-0.37}$ nb

Table 10.2.: *Summary of total cross section predictions from the LO MC programs and the NLO calculation. The used proton PDF is indicated before the value of the predicted total cross section. For the HVQDIS calculation the intervals of the parameter utilised for the estimation of the theoretical uncertainty have been added.*

proton PDF CTEQ6ll [P+02] yields a cross section of $\sigma_{\text{vis}}^{\text{tot}} = 4.89$ nb and $\sigma_{\text{vis}}^{\text{tot}} = 3.65$ nb if used with the CTEQ65m [T+07] parametrisation. As outlined in section 4.1 it is expected that the NLO PDF CTEQ65m utilised with a LO MC program yields a lowish total cross section. CASCADE yields a cross section of $\sigma_{\text{vis}}^{\text{tot}} = 4.72$ nb. For all LO MC predictions the Bowler fragmentation parametrisation (see equation 2.17) with the ALEPH tune for higher resonances and a charm mass of 1.5 GeV has been used. For a detailed summary of the MCs and their parameters see table 4.1.
The NLO calculation HVQDIS is utilised with two different proton PDFs namely MRST2004FF3nlo [MST06] and CTEQ5f3 [L+00]. More details on the PDFs and the parameter used for HVQDIS are given in section 4.2. The MRST2004FF3nlo proton PDF gives a total cross section of $\sigma_{\text{vis}}^{\text{tot}} = 4.17 \pm^{0.59}_{0.37}$ nb. In the case of the CTEQ5f3 PDF HVQDIS predicts a cross section of $\sigma_{\text{vis}}^{\text{tot}} = 4.43 \pm^{0.69}_{0.47}$ nb. An estimate of the theoretical error is calculated from variations of the charm mass m_c, the scale $\mu_0^2 = Q^2 + 4m_c^2$ where factorisation and renormalisation scale have been varied simultaneously and the fragmentation parameter α as given in table 10.2.

10.2. Single-differential Cross Section Distributions

Single-differential cross sections are measured as a function of the kinematic quantities $Q^2, y, W_{\gamma P}, x$ and as a function of the D^* meson quantities $x_g^{\text{obs}}, p_T, \eta, z$. The corresponding figures are organised such that the data are compared with the LO MC predictions on the left and with the NLO calculation on the right side of a figure. Furthermore, in order to better judge on the shape of the different LO MC programs and NLO QCD predictions the ratio R between data and the predictions normalised to the corresponding total visible cross section is calculated for all single-differential cross section measurements. For a measured variable Y it is calculated like the following:

$$R = \frac{\frac{1}{\sigma_{\text{tot,vis}}^{\text{calc},Y}} \cdot \frac{d\sigma^{\text{calc}}}{dY}}{\frac{1}{\sigma_{\text{tot,vis}}^{\text{data},Y}} \cdot \frac{d\sigma^{data}}{dY}} \,. \tag{10.2}$$

For all single-differential distributions it is attached at the bottom of the presented figures. For the ratio the systematic errors that influence only the normalisation are subtracted. Therefore the systematic error of 3.2% of the luminosity measurement and half of the track uncertainty of 2% per track is subtracted from the total systematic error in each bin. Afterwards a typical total experimantal systematic error of 6.2% for the ratio is achieved.
The differential cross section as function of the photon virtuality Q^2 is depicted in figure 10.2a) for the LO MC predictions and in b) for the NLO calculation HVQDIS. Overall a good description of the shapes is observed and in general the same trends in normalisation are seen as for the total cross section predictions. As outlined in section 4.1 the CTEQ65m PDF is a NLO PDF, which results in a lower cross section if utilised in a LO MC program compared to the use of LO PDFs. The increased y range down to 0.02 allows for an additional bin compared to the standard y cut of > 0.05 used in previous H1 D^* meson cross section measurements (e.g. [A+07]). The cross section as a

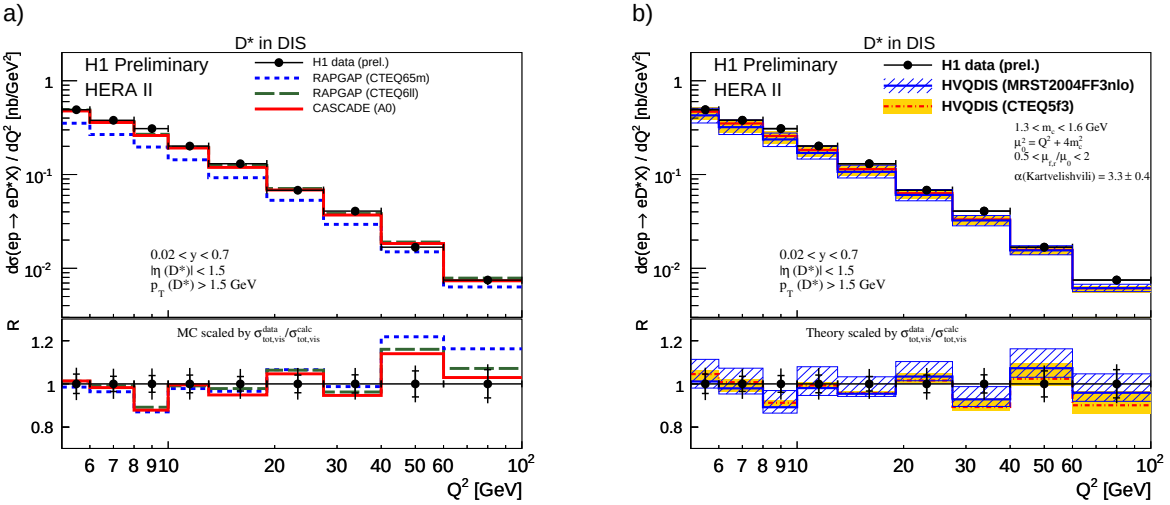

Figure 10.2.: *The differential cross section as a function of Q^2 in the visible range (see table 10.1). The measurements are given as filled circles; the inner error bars correspond to the statistical error of the measurement, while the outer error bars correspond to the statistical and systematic error added in quadrature. The data are compared to RAPGAP using two different proton PDFs and CASCADE a) and compared to the NLO calculation HVQDIS b). The bands for the expectation of HVQDIS for the MRST2004FF3nlo (hatched) and the CTEQ5f3 (shaded) PDFs are obtained by varying parameters according to table 10.2. The ratio attached at the bottom is calculated according to equation 10.2.*

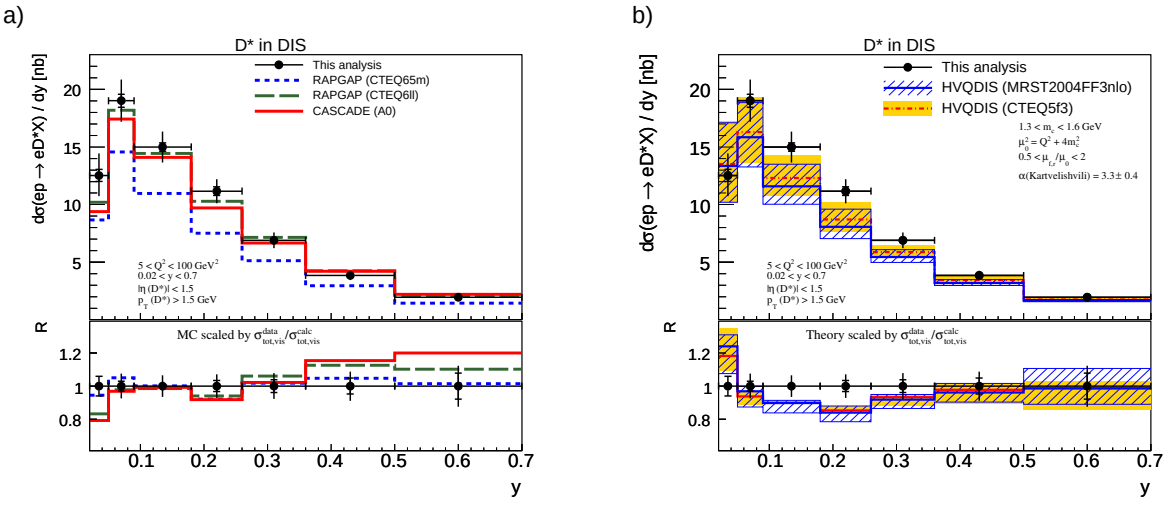

Figure 10.3.: *The differential cross section as a function of y in the visible range. The data are compared to RAPGAP using two different proton PDFs and CASCADE a) and compared to the NLO calculation HVQDIS b). See the caption of figure 10.2 for further details.*

function of y is illustrated in figure 10.3. Overall a reasonable description is seen. The predicted LO MC shape as depicted in 10.3a) and is for CASCADE and RAPGAP with CTEQ6ll not rising strong enough towards low y. RAPGAP with CTEQ65m gives a very good description of the shape in general and especially of the new y bin. The y distribution is reasonably described by the NLO predictions as displayed in 10.3b). But the rise towards low y is too strong for both PDFs.
The cross section as function of $W_{\gamma P}$ is depicted in figure 10.4. The normalised ratio

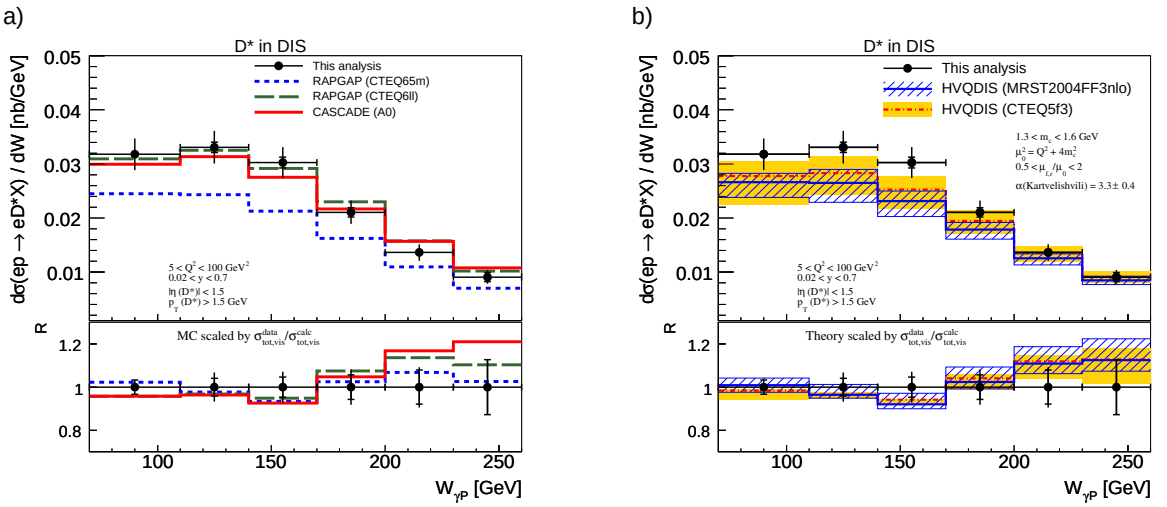

Figure 10.4.: *The differential cross section as a function of $W_{\gamma P}$ in the visible range. The data are compared to RAPGAP using two different proton PDFs and CASCADE a) and compared to the NLO calculation HVQDIS b). See the caption of figure 10.2 for further details.*

attached at the bottom of figure 10.4a) illustrates a good description of the shape at small $W_{\gamma P}$ by the LO MC programs, while for $W_{\gamma P} > 200$ GeV CASCADE and RAPGAP tend to provide a more shallow slope than the data. As $W_{\gamma P}$ is related to y, where RAPGAP with CTEQ65m provides a better description, also here especially at low $W_{\gamma P}$ the description is improved. The NLO prediction describes the $W_{\gamma P}$ dependence quite well, although a similar deficit at high $W_{\gamma P}$ can be seen in figure 10.4b), which is completely covered by the large theoretical uncertainty particularly in that region.
The lower y cut allows the access of higher Bjørken x. The measured cross section is shown in figure 10.5a) for the leading order MC comparison. The ratio illustrates the good description of the slope in x by the LO MCs, although there is a slight tendency for the RAPGAP using the CTEQ65m proton PDF to undershoot the data at low x and to overshoot at high x which is smaller if the CTEQ6ll proton PDF is used. The comparison of the measured cross section in x to the NLO QCD prediction from HVQDIS is illustrated in figure 10.5b). The CTEQ5f3 proton PDF provides a slightly better description at large x and a weaker one at low x compared to the MRST04ff3 proton PDF.
After the presentation of the D^* cross sections as a function of the event kinematic quantities, the D^* cross sections as a function of the D^* quantities are presented in the following. The cross section as a function of x_g^{obs} can be seen in figure 10.6a) for the

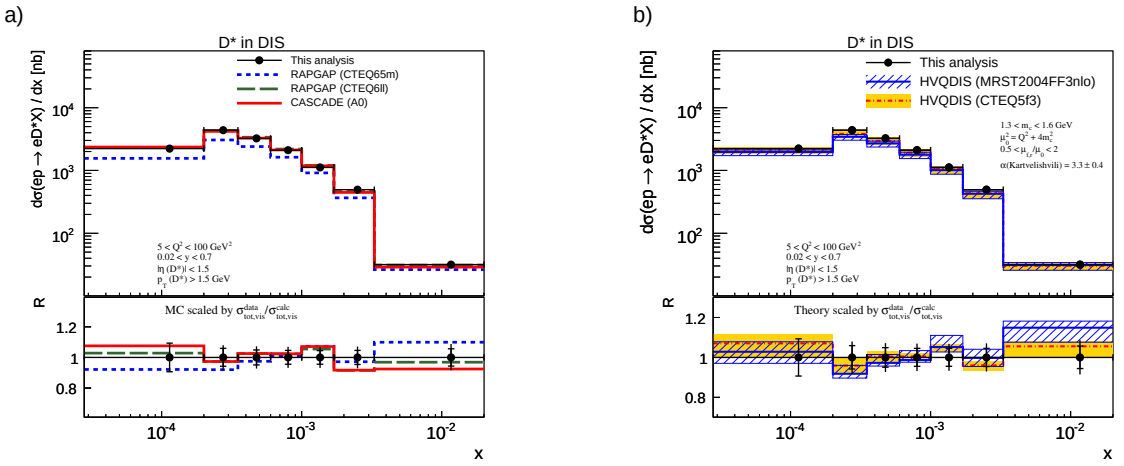

Figure 10.5.: *The differential cross section as a function of x in the visible range. The data are compared to RAPGAP using two different proton PDFs and CASCADE a) and compared to the NLO calculation HVQDIS b). See the caption of figure 10.2 for further details.*

LO MC programs and in b) for the NLO QCD predictions. Also here the observation is made that the CTEQ65m describes the shape of the cross section data better compared to the CTEQ6ll. For CASCADE the description of the shape is almost perfect. The NLO QCD prediction fails to describe the x_g^{obs} distribution.
For the cross section as a function of the transverse momentum p_T of the D^* meson,

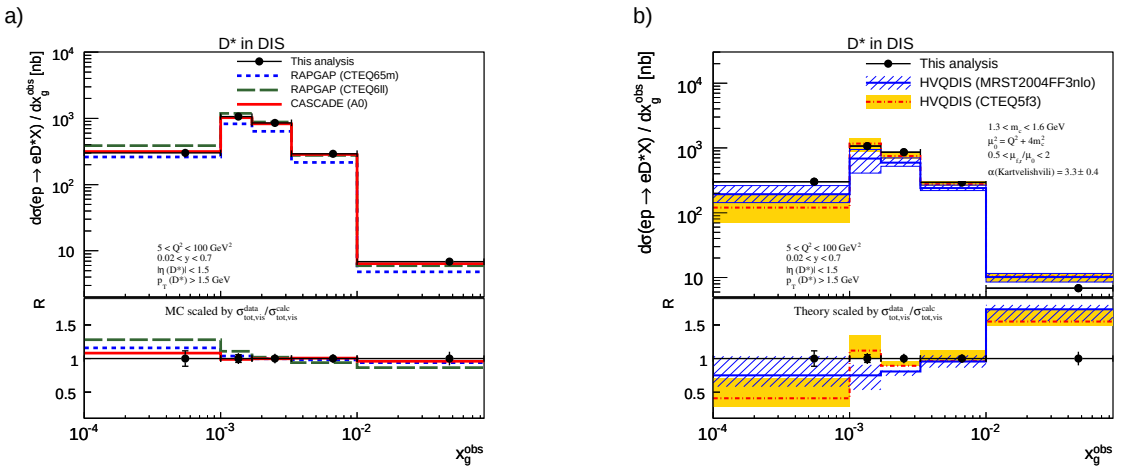

Figure 10.6.: *The differential cross section as a function of x_g^{obs} in the visible range. The data are compared to RAPGAP using two different proton PDFs and CASCADE a) and compared to the NLO calculation HVQDIS b). See the caption of figure 10.2 for further details.*

depicted in figure 10.7, a good description is observed. There is a tendency to not fully reproduce the shape of the distribution due to an undershoot of the data at medium $p_T(D^*)$ by the LO MC predictions and the NLO calculation. In general this effect is stronger for the NLO predictions, which can be a result of the fragmentation function used. For more insigths on the fragmentation issue of HVQDIS see section 11.2.

In figure 10.8 the differential cross section measurement as a function of $\eta(D^*)$ is depicted and compared to the LO MC predictions a) and the NLO predictions from HVQDIS b). The shape of the $\eta(D^*)$ distribution is very well described by the CAS-

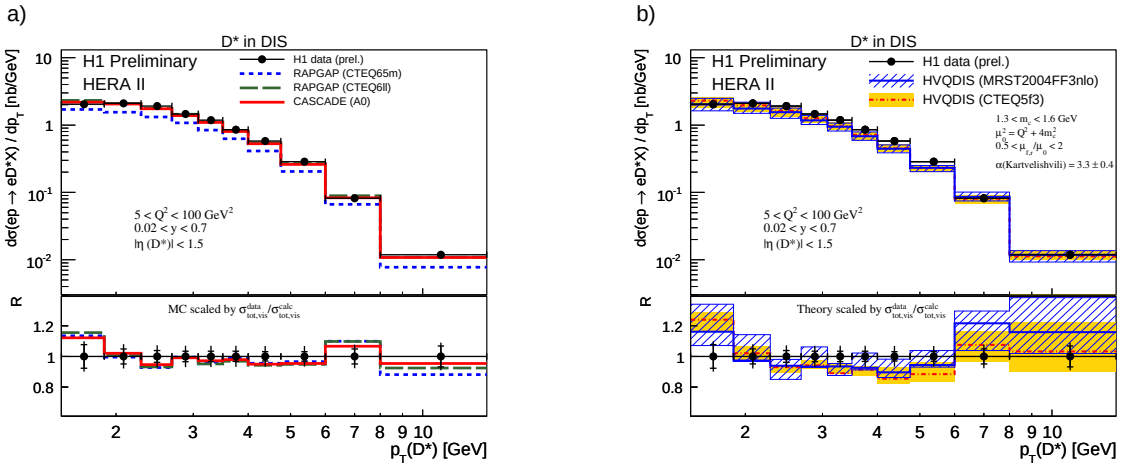

Figure 10.7.: *The differential cross section as a function of p_T in the visible range. The data are compared to RAPGAP using two different proton PDFs and CASCADE a) and compared to the NLO calculation HVQDIS b). See the caption of figure 10.2 for further details.*

CADE prediction, while RAPGAP with the CTEQ6ll proton PDF has difficulties in backward and forward directions of the produced D^* meson. This is reduced if RAPGAP with CTEQ65m is utilised but in contrast the description of the shape for x is better for RAPGAP with CTEQ6ll rather than with CTEQ65m (see figure 10.5a)). In

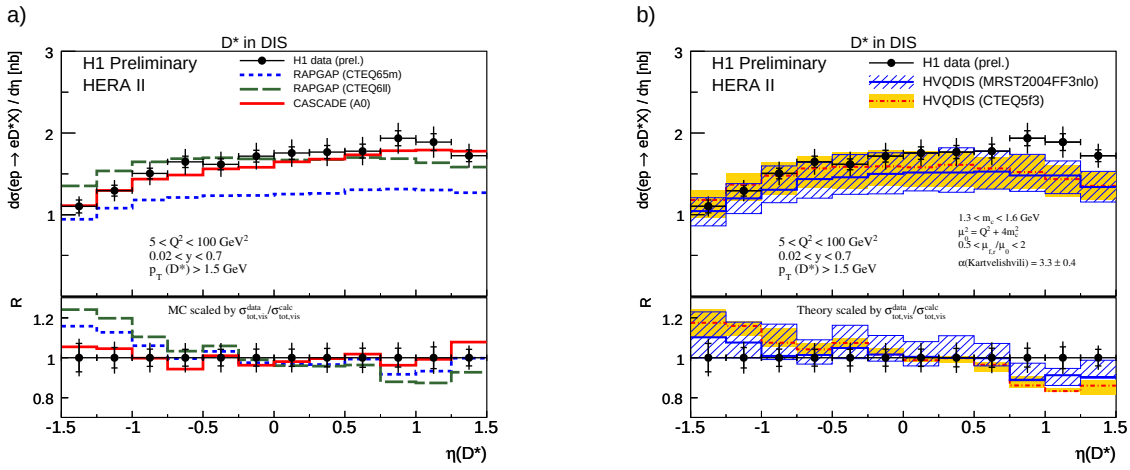

Figure 10.8.: *The differential cross section as a function of $\eta(D^*)$ in the visible range. The data are compared to RAPGAP using two different proton PDFs and CASCADE a) and compared to the NLO calculation HVQDIS b). See the caption of figure 10.2 for further details.*

addition ZEUS has observed a similar problem where the NLO prediction is utilised with a ZEUS PDF, which results in a good description of $\eta(D^*)$ (see figure 1.1), while

the description in x is suboptimal [Z+07]. Compared to the NLO predictions as depicted in figure 10.8b) there is a small excess in forward directions $\eta > 0$, which was observed already in previous H1 analyses [A+07; Boe07]. This excess turns out to be located at low p_T as it can be seen in comparison to the NLO calculation for the double-differential distribution in $\eta(D^*)$ and $p_T(D^*)$ as presented in section 10.3.
A sensitivity of the $\eta(D^*)$ distribution to the proton PDF is observed from the comparison of the shape in data to the shape of the RAPGAP prediction utilised with two different proton PDFs, CTEQ6ll and CTEQ65m, as illustrated in figure 10.8a). The normalised ratio at the bottom of the distribution illustrates a better agreement to the data if the CTEQ65m PDF is used, which was obtained by using a GM-VFNS for the correct treatment of the heavy quark mass at threshold. In contrast to that the CTEQ6ll proton PDF uses a ZM-VFNS as stated in [P+02], which is more appropriate at higher scales neglecting heavy quark masses. However, the RAPGAP MC generator

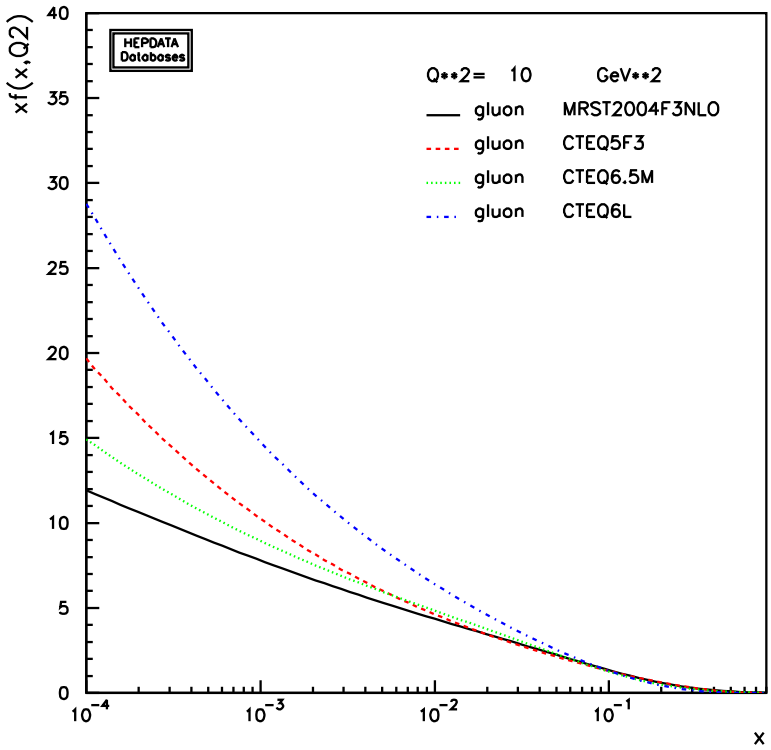

Figure 10.9.: *The gluon density from global analyses of structure function data from the CTEQ and MRST group for different proton PDFs, which are used in this analysis. They are plotted as a function of x for a fixed Q^2 of* 10 GeV^2 *[Dur].*

only implements the BGF process and misses contributions from massless production processes like the one illustrated in figure 2.9b). As CTEQ65m is a NLO PDF both PDFs are not fully appropriate. Hence the proton PDFs have different gluon distributions as illustrated in figure 10.9 as a function of x for a fixed $Q^2 = 10$ GeV^2 [Dur]. A direct comparison is only possible between the NLO proton PDFs, while the LO PDF CTEQ6ll is just added for completeness. As small x are, at least for low Q^2, located at backward directions the description of the $\eta(D^*)$ shape is better with the less steep gluon density provided by CTEQ65m. This observation is confirmed by the NLO pre-

dictions as illustrated in figure 10.8b). The $\eta(D^*)$ shape is better described with the NLO prediction using the MRST04FF3nlo proton PDF, while the use of the CTEQ5f3 proton PDF degrades the description of the $\eta(D^*)$ shape, but provides a slightly better description of the x shape (see figure 10.5b)). In summary the proton PDF with the less steep gluon density (MRST04FF3nlo) provides the better description in $\eta(D^*)$ and a degraded one in x, while the proton PDF with the steeper gluon density (CTEQ5f3) behaves exactly the other way around. However, the significance of the sensitivity is reduced by the relatively large theoretical uncertainties. Nonetheless the observation from the NLO predictions is similar to the situation observed for the LO MC case.
For the cross section as a function of $z(D^*)$ of the D^* meson, depicted in figure 10.10,

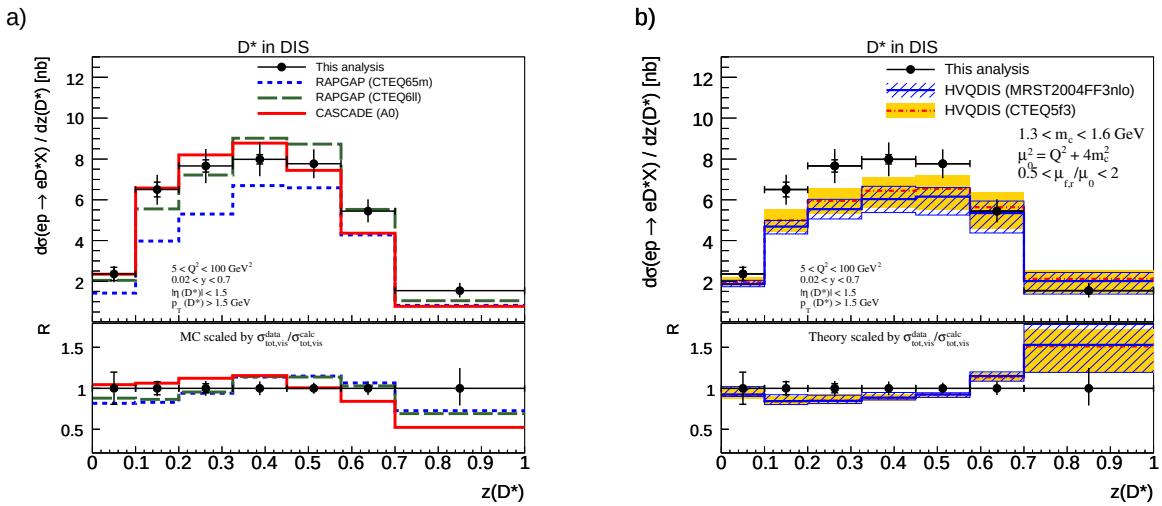

Figure 10.10.: *The differential cross section as a function of $z(D^*)$ in the visible range. The data are compared to RAPGAP using two different proton PDFs and CASCADE a) and compared to the NLO calculation HVQDIS b). See the caption of figure 10.2 for further details.*

in general a good description is observed. The description of the $z(D^*)$ shape by the LO MC programs illustrates features that are opposed to the description of the shape by the NLO calculation. In particular for the high $z(D^*)$ region the LO MC programs undershoot the data and the NLO calculations overshoot the data in the normalised ratio shown at the bottom of 10.10a) and b) respectively. However, the NLO prediction b) at medium $z(D^*)$ $(0.1 - 0.6)$ is always below the data and only the upper end of the error band slightly matches the data. As it was discussed for the LO MC CASCADE the description of the $z(D^*)$ shape is improved if the fragmentation treatment is changed to the $\hat{s}$ fragmentation (see section 9.3).

10.3. Double-differential Cross Section Distributions

The double-differential cross section is measured in $y - Q^2$ and in $p_T(D^*) - \eta(D^*)$. In figures 10.11 and 10.12 the double differential measurement in y and Q^2 is illustrated. The $y - Q^2$ measurement is used to derive the charm contribution, $F_2^c(x, Q^2)$, to the proton structure as discussed in chapter 11. The comparison to the LO predictions is depicted in figure 10.11 and illustrates that RAPGAP using the CTEQ6ll

or CTEQ65m proton PDF, as well as CASCADE, in general describe the data well. In particular they have difficulties to describe the lowest y bin at medium virtualities $14 < Q^2 < 45$ GeV^2. This y region has previously not been analysed for D^* cross sec-

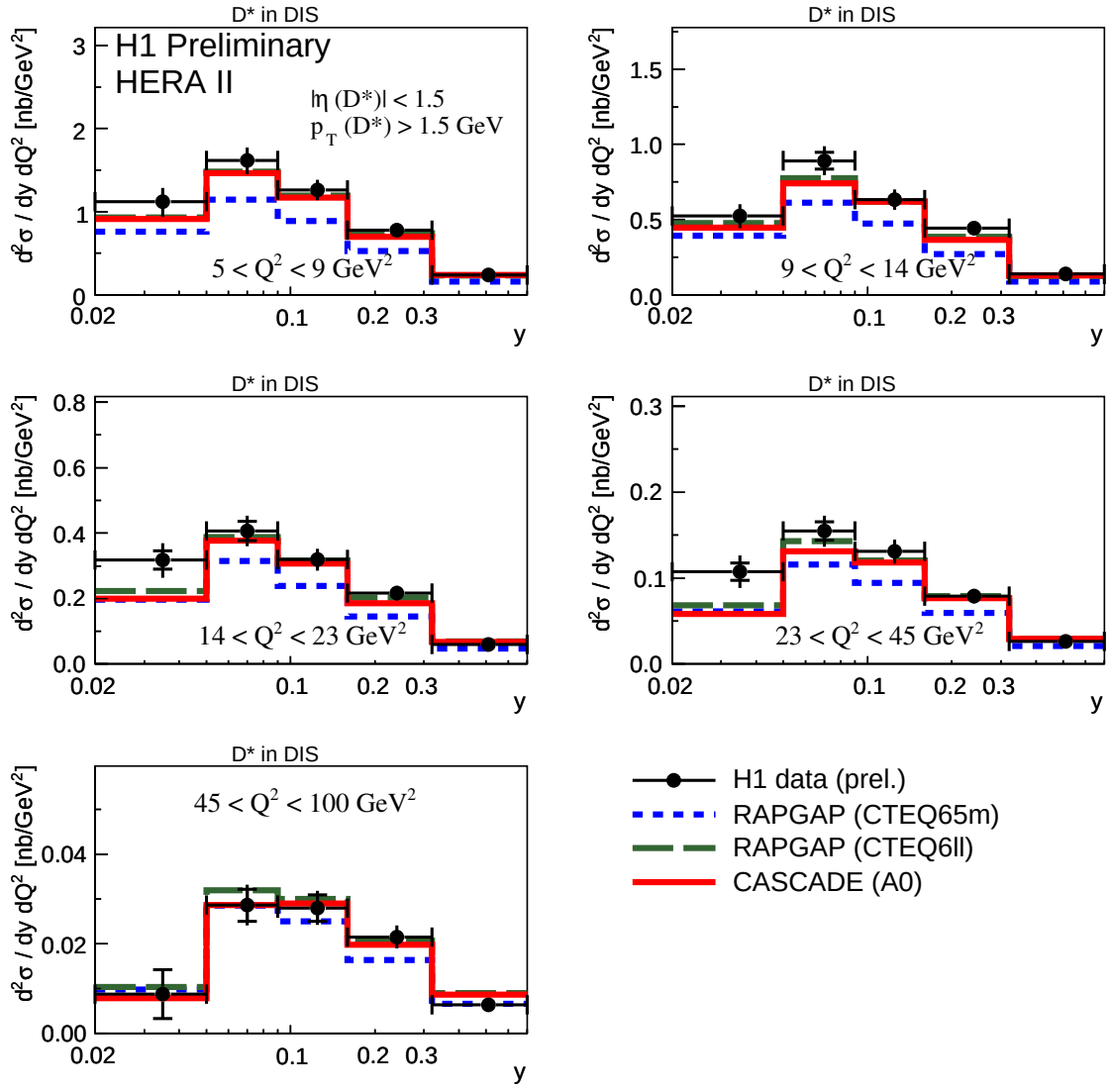

Figure 10.11.: *The double differential cross section as a function of inelasticity y and the virtuality Q^2 in the visible range. The data are given as filled circles; the inner error bars correspond to the statistical error of the measurement, while the outer error bars correspond to the statistical and systematic error added in quadrature. The data are compared to RAPGAP using two different proton PDFs and CASCADE.*

tion measurements at H1. At largest Q^2 all predictions agree with the data partially because of larger statistical errors, which exceed in the lowest y bin 60%. In this low y region a phase space extension towards larger $\eta(D^*)$ for the D^* meson could help. Within errors the HVQDIS prediction shown in figure 10.12 is able to describe the shape and normalisation of the y distribution for all Q^2 bins for both proton PDFs reasonably well. The bands reflect the theoretical uncertainty that arise from the vari-

ation of parameters as given in table 10.2, which increases especially towards low Q^2 and low y.
In order to investigate the undershoot of the NLO predictions compared to the data observed in the $\eta(D^*)$ distribution (see figure 10.8b)), a double differential measurement in $p_T(D^*)$ and $\eta(D^*)$ is performed. In figures 10.13 and 10.14 the cross section is

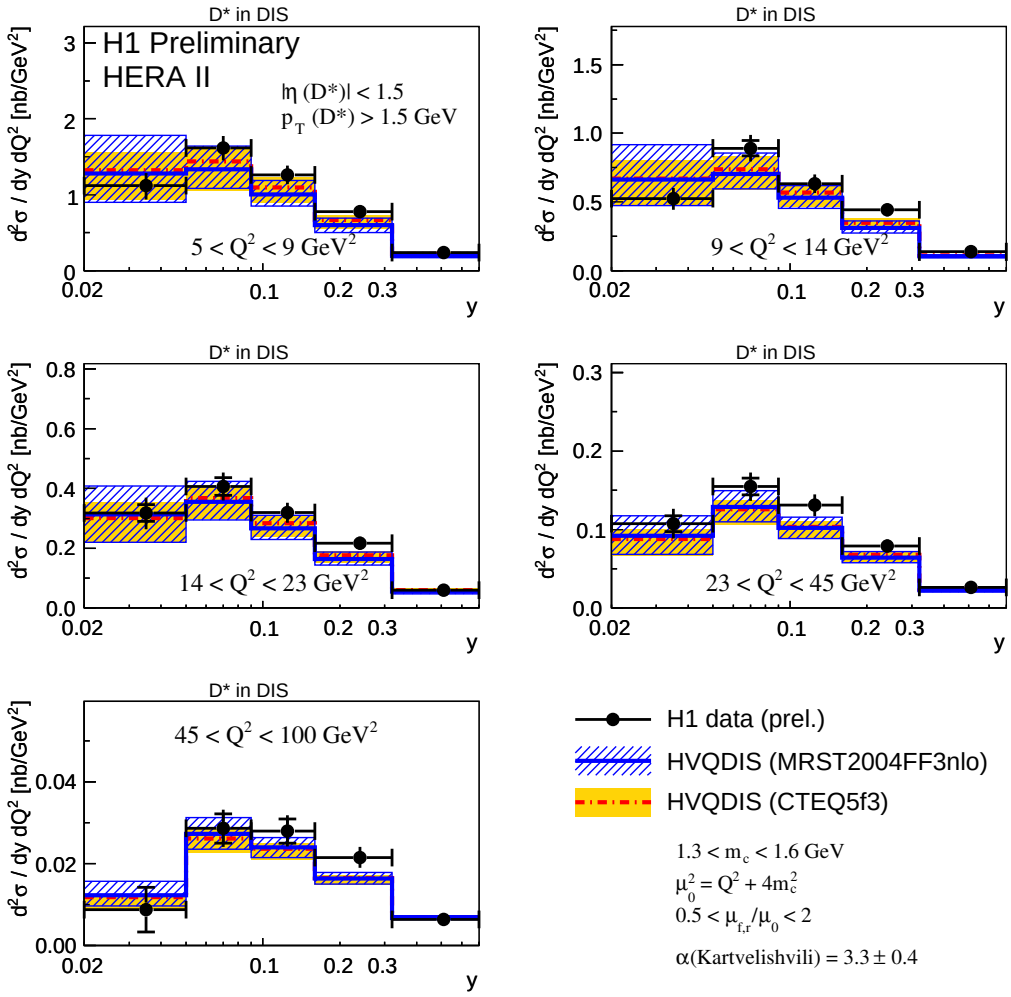

Figure 10.12.: *The double differential cross sections as a function of inelasticity y and the virtuality Q^2 in the visible range. The measurements are given as filled circles; the inner error bars correspond to the statistical error of the measurement, while the outer error bars correspond to the statistical and systematic error added in quadrature. The data are compared to the NLO calculation (HVQDIS) with two different Proton PDFs. The bands for the expectation of HVQDIS for the MRST2004FF3nlo (blue hatched) and the CTEQ5f3 (yellow filled) PDFs are obtained by varying parameters according to table 10.2.*

presented as a function of the pseudo-rapidity $\eta(D^*)$ in bins of the transverse momenta of the D^* meson $p_T(D^*)$ for the LO MC programs and the NLO QCD predictions, respectively. While the two RAPGAP predictions have a tendency to be too flat in $\eta(D^*)$ in all $p_T(D^*)$ regions, CASCADE describes the data reasonably well. The dis-

crepancy between the data and the HVQDIS predictions in forward direction is located at low transverse momenta $p_T(D^*) < 3.5$ GeV. Moreover also in the $p_T(D^*)$ range of

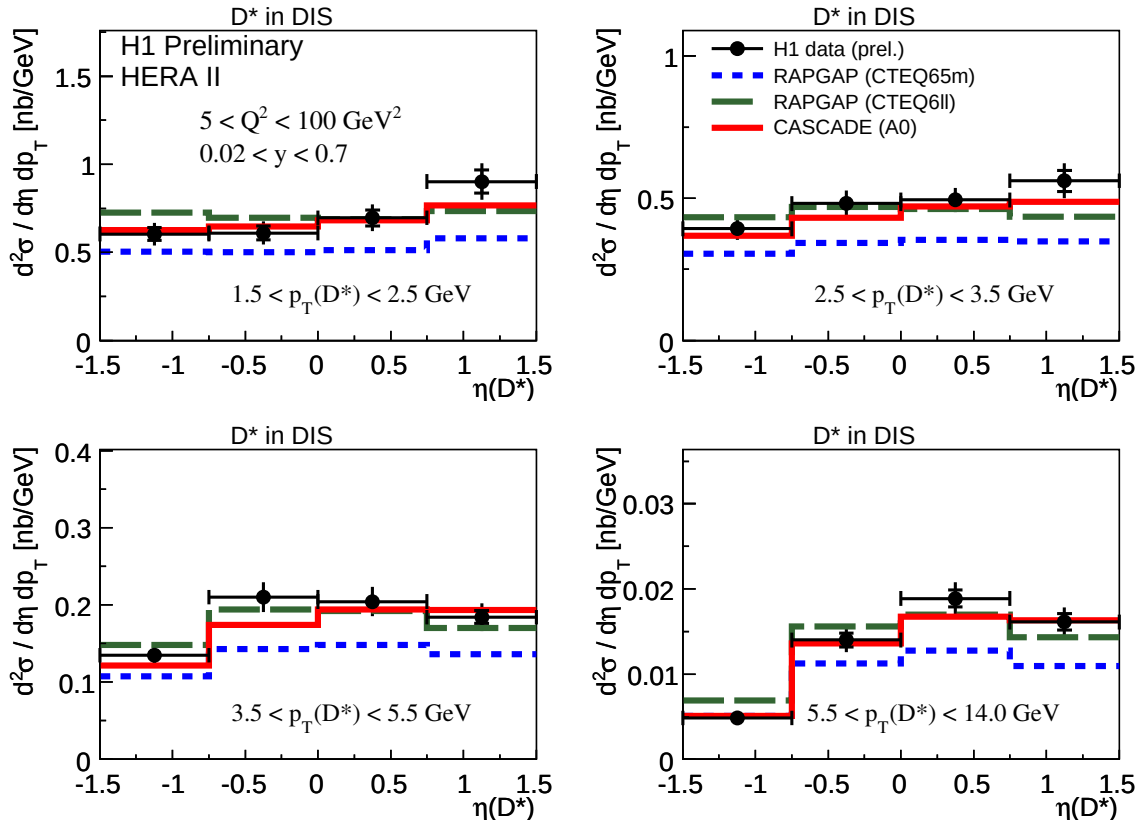

Figure 10.13.: *The double differential cross section as a function of p_T and η of the D^* meson in the visible range. The data are compared to RAPGAP using two different proton PDFs and CASCADE. See the caption of figure 10.11 for further details.*

3.5 GeV $< p_T(D^*) <$ 5.5 GeV the NLO prediction is slightly below the data for a wider range in $\eta(D^*)$. However, the upper end of the theoretical uncertainty band covers this excess almost.
In particular for the double differential measurement in $\eta(D^*) - p_T(D^*)$ a phase space extension towards lower transverse momenta and larger pseudo-rapidity of the D^* meson could help to further understand the underlying processes. A part of the necessary studies for a phase space extension towards lower $p_T(D^*)$ and larger $|\eta(D^*)|$ completed during the analysis is presented in chapter 12.

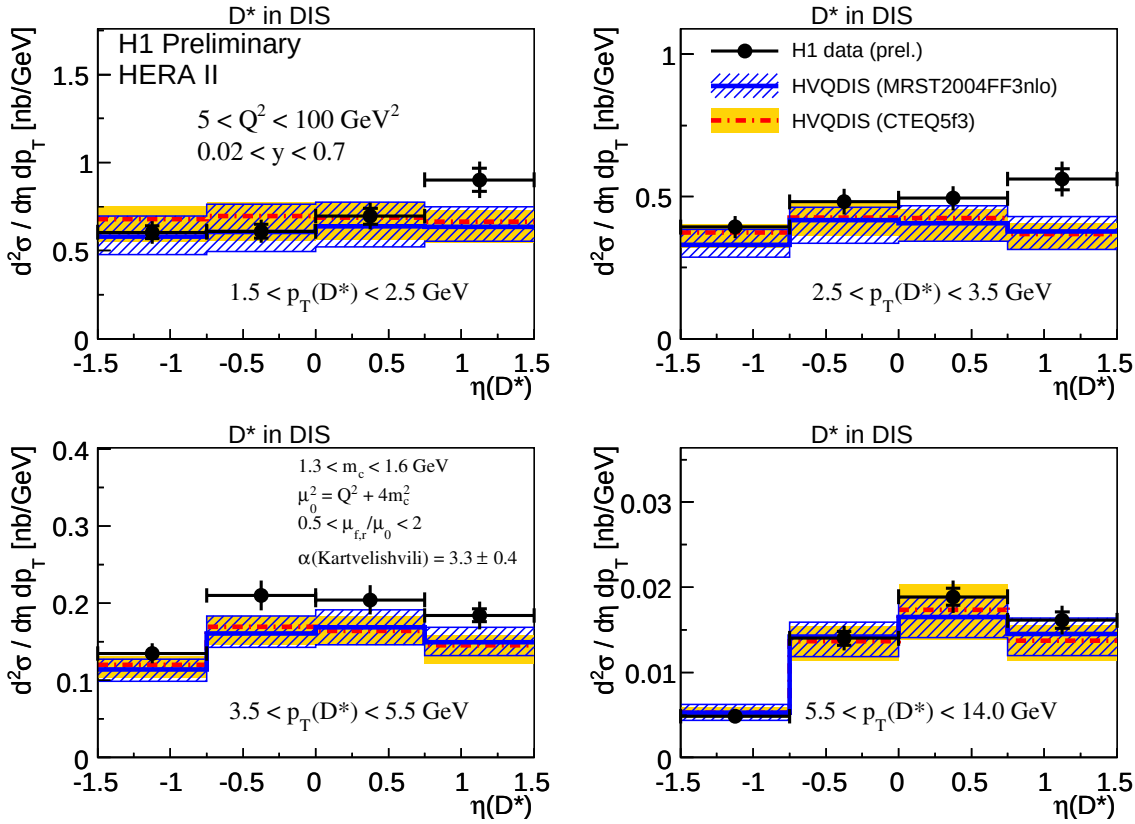

Figure 10.14.: *The double differential cross section as a function of p_T and η of the D^* mesons in the visible range. The data are compared to the NLO calculation (HVQDIS) with two different proton PDFs. See the caption of figure 10.12 for further details.*

11. The Charm Contribution to the Proton Structure

The D^* meson cross section data can be extrapolated to a charm cross section in the full phase space. Thus the charm contribution to the proton structure, i.e. the charm structure function $F_2^c(x, Q^2)$ as defined in equation 2.19, is derived. The longitudinal charm structure function, F_L^c, contributes only at high y, which is of the order of $2-3\%$ for the visible range of this measurement (see table 6.4) and is consequently neglected. The charm structure function is derived from the D^* meson cross section data by the following concept:

$$F_2^{c\ \mathrm{exp}}(x, Q^2) = \frac{\sigma_{\mathrm{vis}}^{\mathrm{exp}}(y, Q^2)}{\sigma_{\mathrm{vis}}^{\mathrm{theo}}(y, Q^2)} \cdot F_{2\ \mathrm{full}}^{c\ \mathrm{theo}}(x, Q^2) \ , \tag{11.1}$$

which was also previously adopted in [A+02; A+99]. The double-differential cross section measurement in $y - Q^2$ (see figure 10.11 and 10.12) is converted to a cross section in $x - Q^2$ using $x = Q^2/sy$ according to equation 2.5. The contribution from b-quarks to the proton structure in the present kinematic range is neglected, as F_2^b contributes of the order of 1-2% of F_2^c [CSvN00].
Different models can be utilised for the extraction if they describe the visible phase space reasonably well, as it is demonstrated for the predictions of the LO CCFM and NLO DGLAP models (see chapter 10). The theoretical prediction of the cross section $\sigma_{\mathrm{vis}}^{\mathrm{theo}}(x, Q^2)$ for the visible phase space is made either with the LO MC program CASCADE implementing the CCFM evolution equations or the NLO calculation HVQDIS using the DGLAP evolution equations. The theoretical prediction for the full phase space $F_{2\ \mathrm{full}}^{c\ \mathrm{theo}}(x, Q^2)$ is calculated with CASCADE for the CCFM based extraction without any cuts on the phase space of the D^* meson. The DGLAP based extraction uses the fully inclusive *Riemersma program*[1] [Lae93] which implements the order α_s^2 BGF process in the FFNS. Both theoretical predictions of $F_{2\ \mathrm{full}}^{c\ \mathrm{theo}}(x, Q^2)$ are computed at the bin centres in x and Q^2, which are calculated from the bin centres in y and Q^2 by $x = Q^2/sy$.
The use of a MC program supplemented with parton showers and a pure NLO calculation program is owed to the fact that there is no MC@NLO as shortly outlined in section 4.2, which would be the optimal choice. Instead there is HVQDIS, which provides the BGF process in NLO and considers effects of the charm mass by the FFNS, while CASCADE provides a massive calculation as well but computes only the LO BGF process supplemented with parton showers. Moreover the model assumption, i.e. CCFM versus DGLAP evolution equations, cause another contrary issue: CASCADE provides gluons in the initial state with a finite transverse momentum, which changes kinematic distributions of the final state, while HVQDIS treats also light quarks as partons inside the proton, which is in particular more appropriate at large x. The model assumption influence the extrapolation from the visible range of the measurement to the full phase space of the D^* meson, which is crucial for the determination

[1] The differential HVQDIS program is also based on this calculations.

of the charm contribution to the proton structure.

11.1. Phase Space Coverage & Extrapolation

The kinematic plane within the visible range defined in table 6.4 is depicted in figure 11.1 as a function of x and Q^2 a) and as a function of y and Q^2 b). A dependence as a function of x is observed, which originates from the inelasticity cut, which would involve truncated bins if the extraction of F_2^c is simply based on a rectangular $x - Q^2$ binning. Instead the double-differential measurement in $y - Q^2$ is utilised for the

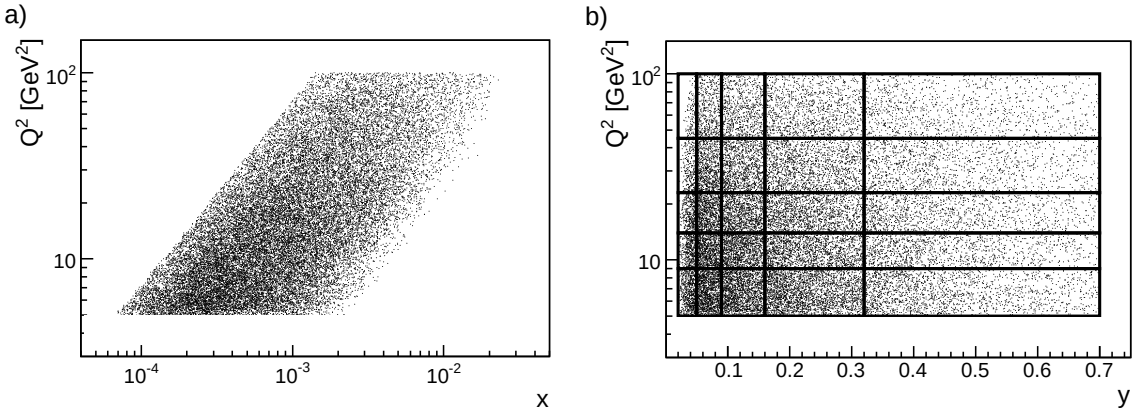

Figure 11.1.: *The phase space coverage within the visibility cuts (see table 6.4) as a function of a) x and Q^2 and as a function of b) y and Q^2 where the bin borders are indicated by the thick solid lines.*

extraction, as it possesses a good coverage of the phase space for the chosen binning (solid lines) as depicted in figure 11.1b). However at lowest y and highest Q^2 the phase space coverage is slightly affected by the geometrical acceptance of the SPACAL (see section 6.1). The detector acceptance, efficiency, purity and stability determined from the bin-by-bin method are discussed in section 8.1 for the $y - Q^2$ distribution.
The conversion from the $y - Q^2$ to the $x - Q^2$ binning for F_2^c is done according to equation 11.1. The fraction $\sigma_{\text{vis}}^{\text{exp}}(y, Q^2)/\sigma_{\text{vis}}^{\text{theo}}(y, Q^2)$ in the visible range is multiplied by the cross section prediction for the full phase space, which is computed at the bin centres in $x - Q^2$ from the bin centres in $y - Q^2$ by utilising $x = Q^2/sy$. Thus the cross section measurement in $y - Q^2$ is converted and extrapolated into a measurement of F_2^c in $x - Q^2$.

Extrapolation to the Full Phase Space

In order to judge on the size of the visible phase space compared to the full phase space, an extrapolation factor from the visible D^* meson cross section (see table 6.4)

to the full phase space is expressed by:

$$f^{\text{extra}} = \frac{\frac{d^2}{dydQ^2} \cdot \sigma^{\text{theo}}_{\text{full}}}{\frac{d^2}{dydQ^2} \cdot \sigma^{\text{theo}}_{\text{vis}}} \,. \tag{11.2}$$

The theoretical predictions are calculated from CASCADE or HVQDIS, for comparison also RAPGAP is utilised. Figure 11.2a) illustrates the extrapolation from the visible

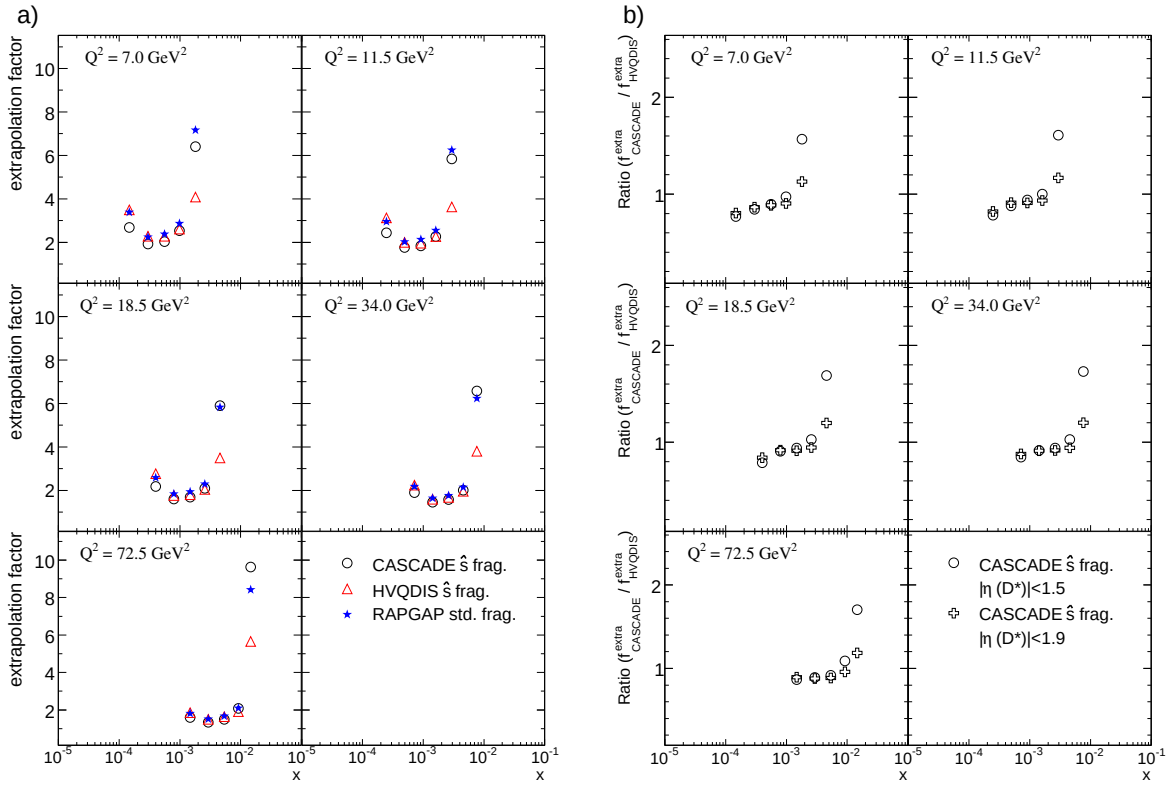

Figure 11.2.: *Extrapolation factors to the full phase space a) as determined by HVQDIS, CASCADE and RAPGAP in bins of the extracted F_2^c. For CASCADE and HVQDIS the ŝ fragmentation is implemented (see section 9.3). The extrapolation factors from CASCADE for the standard and an extended $\eta(D^*)$ range b) are normalised to the ones from HVQDIS.*

to the full phase space of the D^* meson in bins of the F_2^c extraction. On average the extrapolation factor is around 3.0, which corresponds to an average phase space coverage of $\sim$ 30%. The largest extrapolation factors are located at high x where the D^* mesons are mostly produced in forward direction and don't fulfil the pseudo-rapidity cut of $|\eta(D^*)| < 1.5$.
In general the three models show a similar behaviour, but at large and small x they differ. At small x RAPGAP is always closer to HVQDIS than CASCADE whereas at large x RAPGAP is closer to CASCADE, which might be due to the different QCD evolution schemes implemented in the different models. Moreover, the LO MC programs are supplemented with parton showers, which also might play a role. In

addition the two models have different assumptions about the distribution of D^* mesons in the unmeasured phase space, as illustrated by figure 11.2b). For better comparison the extrapolation factors of CASCADE in two different $\eta(D^*)$ ranges are normalised to the respective extrapolation factor determined from HVQDIS. In particular at high x different acceptances estimated by CASCADE and HVQDIS cause large differences of up to 80% that go down drastically if a larger $|\eta(D^*)|$ range of 1.9 is used. To overcome this problem an extension of the measurement towards larger $|\eta(D^*)|$ of 1.9 is needed, which increases the phase space coverage to $\sim 50\%$. Nevertheless for $|\eta(D^*)| < 1.5$ a large model uncertainty remains, as overall differences of $10-20\%$ are observed between the two models in the same $\eta(D^*)$ range. More insights to a F_2^c extraction from D^* cross sections measured in an extended phase space are discussed in section 12.4. Because of the large differences between the two models the extraction is performed for both models separately. Within each model an additional extrapolation uncertainty is assigned which is discussed in the following.

11.2. Theoretical Uncertainties of the Extrapolation Procedure

For the extrapolation to the full phase space extrapolation uncertainties, beside the discussed model choice, arise from the charm mass, the scale variation and from the fragmentation process. The extrapolation uncertainty is estimated from the change of the extrapolation factors for a parameter variation, which represents the uncertainty of a parameter as summarised in table 11.1. The nominal extrapolation factor f^{extra}

name	interval (HVQDIS)	interval (CASCADE)
charm mass	$1.3 < m_c < 1.6$ GeV	$1.3 < m_c < 1.6$ GeV
scale $\mu_0^2 = Q^2 + 4m_c^2$	$0.5 < \mu_{r,f}/\mu_0 < 2$	$0.5 < \mu_{r,f}/\mu_0 < 2$
PDF	CTEQ5f3 & MRST04FF3	A0−, A0 , A0+
$\hat{s}$ fragmentation:		
low $\hat{s}(< 70$ GeV$^2)$	$\alpha = 6.0^{+1.0}_{-0.8}$	$\alpha = 8.2 \pm 1.1$
high $\hat{s}(> 70$ GeV$^2)$	$\alpha = 3.3 \pm 0.4$	$\alpha = 4.6 \pm 0.6$
$\hat{s}$ threshold	70 ± 20 GeV^2	70 ± 20 GeV^2

Table 11.1.: *Uncertainty of certain quantities which is utilised for the estimation of the extrapolation uncertainty calculated from HVQDIS and CASCADE. The parameters of the $\hat{s}$ fragmentation are taken from [A+08b], while the threshold position is taken from [Lip08].*

(see eqn. 11.2) and the extrapolation factor f_i^{extra} calculated for a quantity i, from the uncertainty interval of that quantity, is utilised to calculate a relative error:

$$\delta_i^{\text{extra}} = \frac{f^{\text{extra}} - f_i^{\text{extra}}}{f^{\text{extra}}} \,, \quad \text{with} \quad f_i^{\text{extra}} = \frac{\frac{d^2}{dydQ^2} \cdot \sigma^{\text{theo}}_{\text{full } i}}{\frac{d^2}{dydQ^2} \cdot \sigma^{\text{theo}}_{\text{vis } i}} \,. \tag{11.3}$$

Thus the extrapolation uncertainty is estimated from the relative error of the extrapolation factor for the charm mass uncertainty, the scale uncertainty and the uncertainty of the $\hat{s}$ fragmentation, which was introduced in section 9.3. The relative errors are added in quadrature and assigned as extrapolation uncertainty to the F_2^c data. The extrapolation uncertainty is calculated for HVQDIS and CASCADE separately. For the latter large statistics of the MC samples that corresponds to a total luminosity of more than 100 fb^{-1} has been generated. Each of the eight final MC sets is equivalent to 40 times the statistics of the data, which reduces the statistical error of the CASCADE MC samples even in the worst bin to $< 1\%$. This is neccessary for the study of the dependence of the relative errors with the different sources of uncertainties.

Charm Mass Dependence

The uncertainty due to the charm mass variation in bins of the F_2^c extraction is illustrated in figure 11.3a) for CASCADE and in b) for HVQDIS. The upward variation is marked with a blue error bar, while a red error bar denotes the downward variation. For CASCADE the largest error of around 7% from the charm mass uncertainty is located at lowest Q^2 and x. With rising Q^2 and x the error decreases to values of around 1% at highest Q^2. Despite some fluctuations predominantly at large x, the NLO QCD

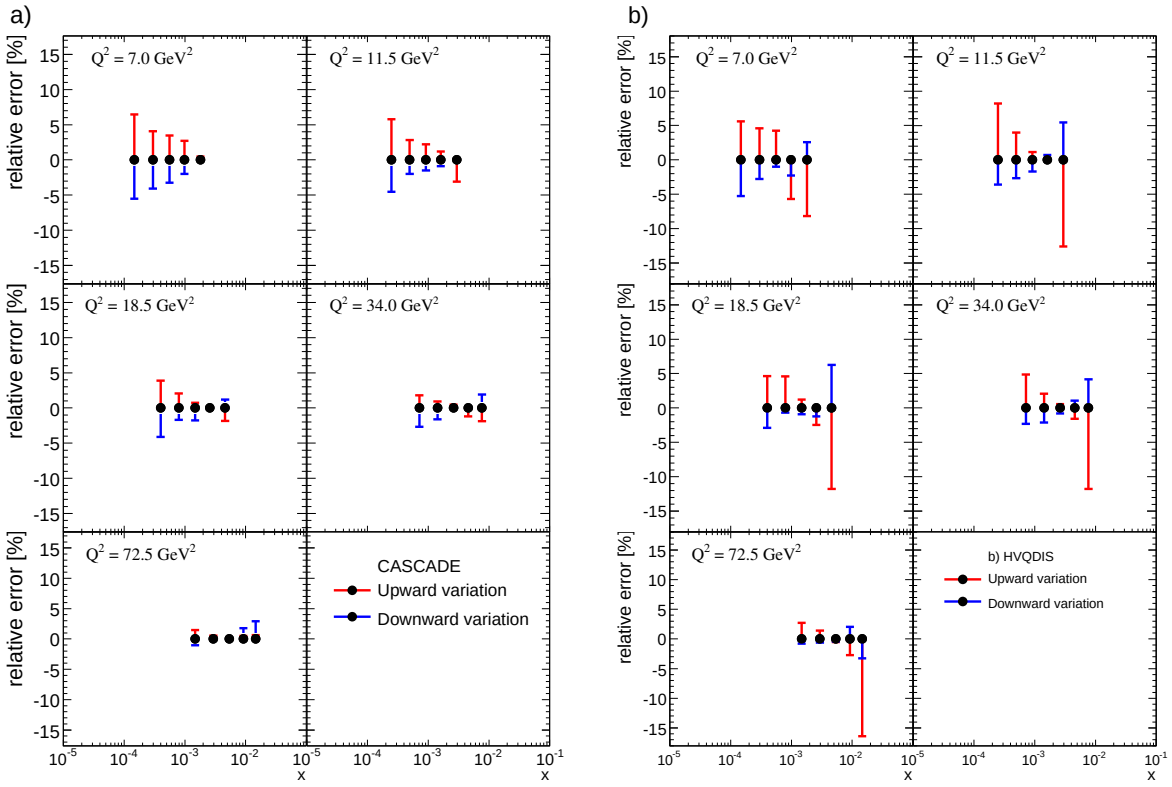

Figure 11.3.: *Uncertainty of the extrapolation factor from the charm mass uncertainty for CASCADE a) and for HVQDIS b) in bins of the extracted F_2^c. The assigned charm mass uncertainty is given in table 11.1.*

calculation HVQDIS predicts a similar behaviour. However, the A0 and CTEQ5f3 proton PDFs are extracted from global analyses with a fixed charm mass. Thus the

error is most probably overestimated. A better estimation would involve a re-fit of the PDFs with the chosen charm mass, which is beyond the scope of this analysis.

Scale Dependence

For the renormalisation scale uncertainty CASCADE is utilised with different sets of the proton PDF. For the default value the A0 proton PDF is taken, while the down- and upward variation is provided by the A0− and A0+ proton PDFs. These special proton PDFs are extracted from a global analysis at a lower and higher scale such that the variation of the scale inside CASCADE is accompanied by a similar change of the scale for the proton PDF extraction.
The extrapolation uncertainty due to the renormalisation scale uncertainty in bins of the F_2^c extraction is depicted in figure 11.4a) for CASCADE. The blue error bar denotes the upward variation and the red bar the downward variation. The uncertainty is very small for all bins of the extraction even at lowest Q^2 where the error is only 2%. This small error is due to the simultaneous change of the scale in CASCADE and the proton PDF. Owed to the fact that a variation of the factorisation scale results into a rather bad description of inclusive structure function data [Jun08c], it has not been varied within CASCADE. However, the size of these errors is expected to be at the same

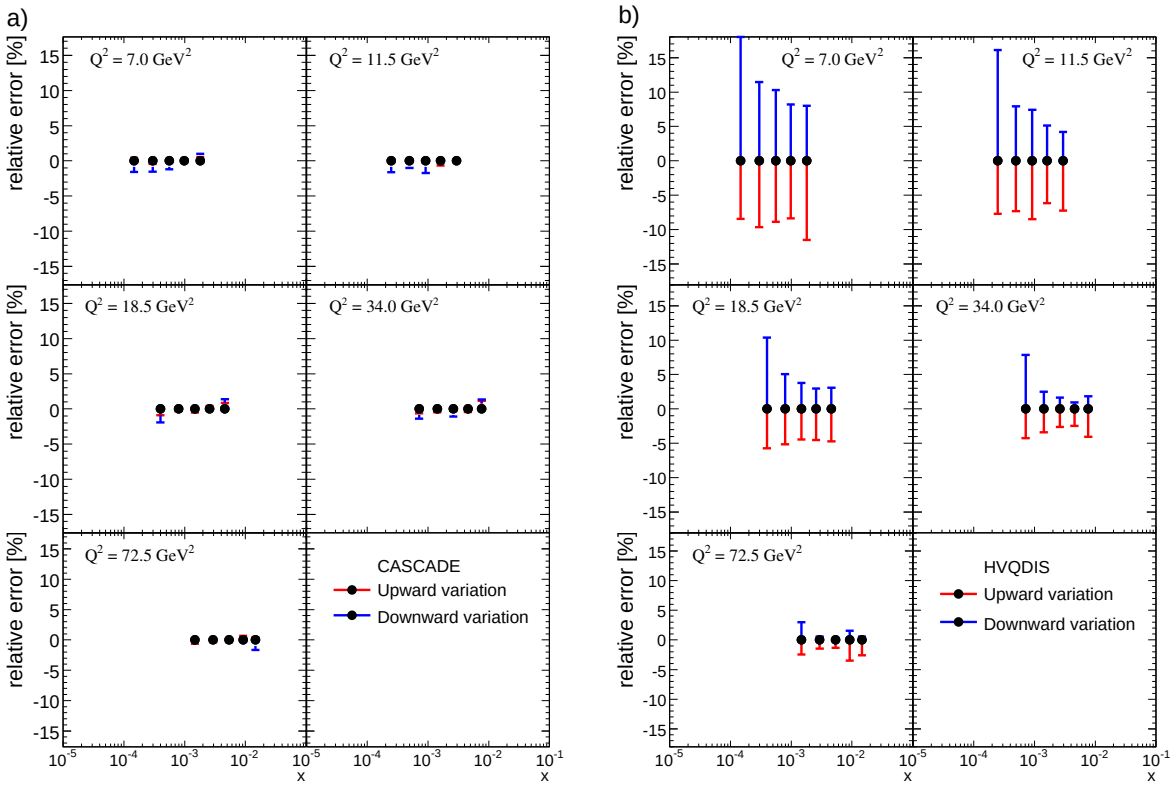

Figure 11.4.: *Uncertainty of the extrapolation factor in bins of the extracted F_2^c from the renormalisation scale uncertainty determined for CASCADE a) from different proton PDFs. For HVQDIS the extrapolation uncertainty b) includes renormalisation and factorisation scale uncertainty and is determined from the same proton PDF. The details of the variation are given in table 11.1.*

height.
The extrapolation uncertainty due to a simultaneous variation of the renormalisation and factorisation scale within HVQDIS is displayed in figure 11.4b). In general large uncertainties arise from the scale, which are due to the fact that for HVQDIS the same proton PDF is used for all scales, which is different from how it was done for CASCADE. As there is no FFNS proton PDF extracted at different scales the situation is not satisfactory. In addition it is controversial if the renormalisation and factorisation scales should be varied independently or simultaneously. At the present stage there exist no clear prescription, therefore the scale uncertainty illustrated in figure 11.4b) is assigned to the extraplation uncertainty.

Proton PDF Dependence

For the extraction in the DGLAP scheme the possibility to test the dependence on the proton PDF is utilised for the extrapolation to the full phase space. Within the CCFM scheme only the A0 proton PDF is available, thus the test is not performed for CASCADE. The two different proton PDFs, which are used for HVQDIS, are CTEQ5f3 and MRST04FF3. Figure 11.5 illustrates the relative error originating from the use of different proton PDFs. The central values correspond to the CTEQ5f3 proton PDF, while the relative error is determined from the use of the MRST04ff3 proton PDF. The full difference is used as proton PDF uncertainty for the extrapolation. At low Q^2 and small x the two proton PDFs differ most, as expected because the predictions of F_2^c from the two proton PDFs, see figure 11.10, are different at low Q^2 and get more similar with increase of Q^2.

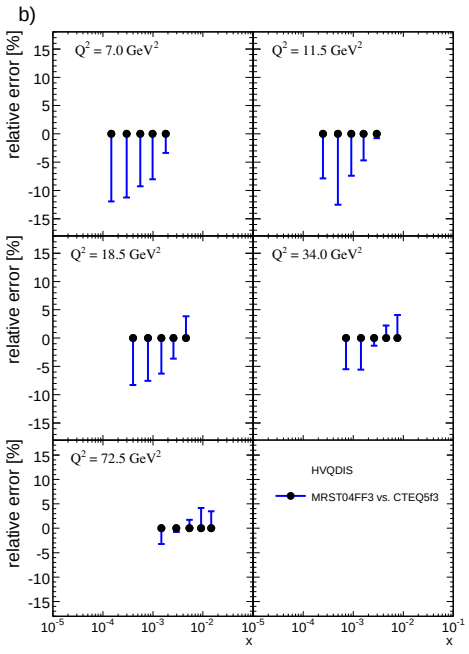

Figure 11.5.: *Uncertainty of the extrapolation factor in bins of the extracted F_2^c from the use of different proton PDFs in the case of HVQDIS. The central value correspond to CTEQ5f3 and the relative error is calculated from the use of MRST04FF3.*

Fragmentation Dependence

The calculation of the extrapolation uncertainty due to the fragmentation function follows the concept as described in section 9.3 for the inclusive cross section measurement. Because of the extrapolation down to $p_T(D^*) = 0$, a larger fragmentation uncertainty compared to the cross section measurement is expected.
The $\hat{s}$ fragmentation for CASCADE uses the values given in table 11.1, which improve the description of the inclusive cross section measurement as illustrated in figure 9.13. Also for HVQDIS a $\hat{s}$ fragmentation is implemented with the parameters summarised in table 11.1. The values are taken from [A+08b] and are quite different to the ones for CASCADE. The $\hat{s}$ fragmentation is an ad-hoc method to reproduce the measurement of fragmentation functions. Moreover the $\hat{s}$ fragmentation does not rely on a larger theoretical motivation. In order to check for an improved description of the data by HVQDIS the total and differential cross section predictions are used.
The NLO QCD prediction with CTEQ5f3 using the $\hat{s}$ fragmentation predicts a total visible cross section of 4.76 nb, which is an increase of 8% compared to the prediction of 4.43 nb if HVQDIS is used with the standard Kartvelishvili fragmentation (non $\hat{s}$ dependent). This difference is due to the harder fragmentation at threshold, i.e. D^* mesons inherit on average a larger p_T from the fragmentation process and thus more D^* mesons propagate into the visible range. The HVQDIS NLO predictions for $\eta(D^*)$

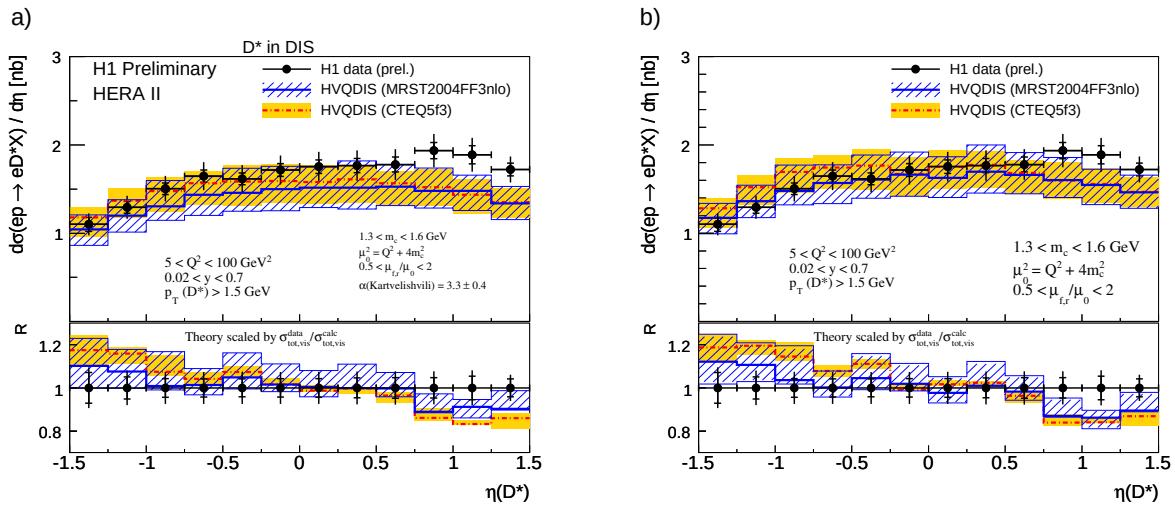

Figure 11.6.: *The HVQDIS NLO prediction using the standard Kartvelishvili fragmentation with $\alpha = 3.3 \pm 0.4$ a) and the $\hat{s}$ fragmentation b) are compared to the D^* cross section data. The theoretical uncertainty in case of the standard Kartvelishvili fragmentation is estimated according to table 10.2, while for the $\hat{s}$ fragmentation table 11.1 summarises the parameter uncertainties. The normalised ratio is calculated according to equation 10.2.*

in comparison to the D^* cross section data are illustrated in figure 11.6 where the prediction depicted in a) uses the standard Kartvelishvili fragmentation (not $\hat{s}$ dependent) with $\alpha = 3.3$, while in figure 11.6b) HVQDIS is utilised with the $\hat{s}$ fragmentation. The HVQDIS with the $\hat{s}$ fragmentation function is used with the two different proton PDFs. For figure 11.6a) only the theoretical uncertainties according to table 10.2 are applied, while b) illustrates the total uncertainty, which includes the uncertainty of the

$\hat{s}$ fragmentation as given by table 11.1. Although the normalization of the prediction compared to the data improves for both proton PDFs, the individual description of the shape is not significantly improved. However, a large improvement is not expected as the color flow from the proton side for the fragmentation process is not considered within HVQDIS, which it is in case of CASCADE where more prominent improvements are observed (see figure 9.13).
The extrapolation uncertainty from the fragmentation process is determined separately from the uncertainty of α and the $\hat{s}$ threshold. In case of the uncertainty of α the influence in bins of the extracted F_2^c for the extrapolation with CASCADE is displayed in figure 11.7a). Errors of the order of 7% arise, which are located at large x and decrease with increasing Q^2 to values of around 2%. Consistently a fragmentation uncertainty based on the error of α is determined also for HVQDIS, which is illustrated in 11.7b). The error is largest at low Q^2 and large x with values of up to 8%.
The threshold position of the $\hat{s}$ fragmentation where the hardness of the process changes

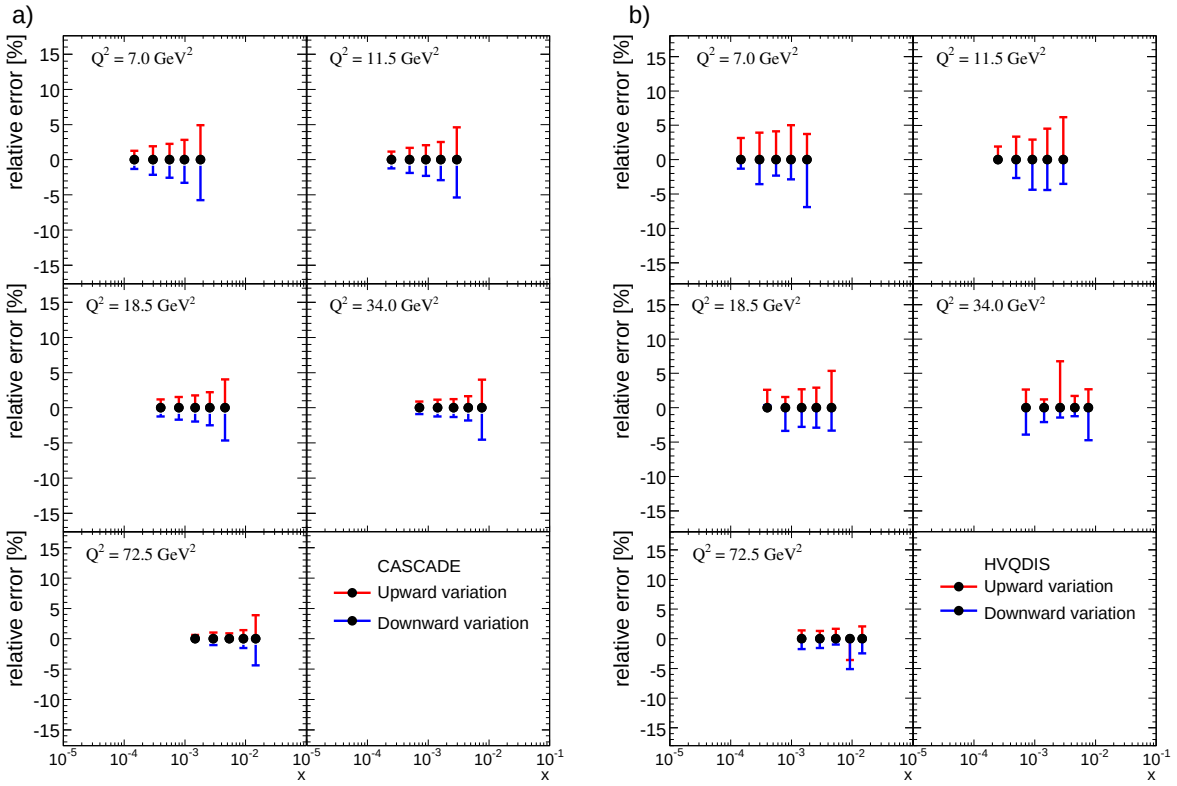

Figure 11.7.: *Uncertainty of the extrapolation factor determined from the error of the fragmentation parameter α in the $\hat{s}$ fragmentation for CASCADE a) and for HVQDIS b). The intervals of the different α variations are given in table 11.1.*

is varied by $\hat{s} = 70 \pm 20$ GeV^2. The effect of the uncertainty of the threshold position in bins of the F_2^c extraction is illustrated for CASCADE in figure 11.8a). The errors estimated are almost independent of Q^2 with small values of up to 3%. Figure 11.8b) displays the relative error from the uncertainty of the threshold position in case of the HVQDIS NLO extrapolation; only small errors are observed.

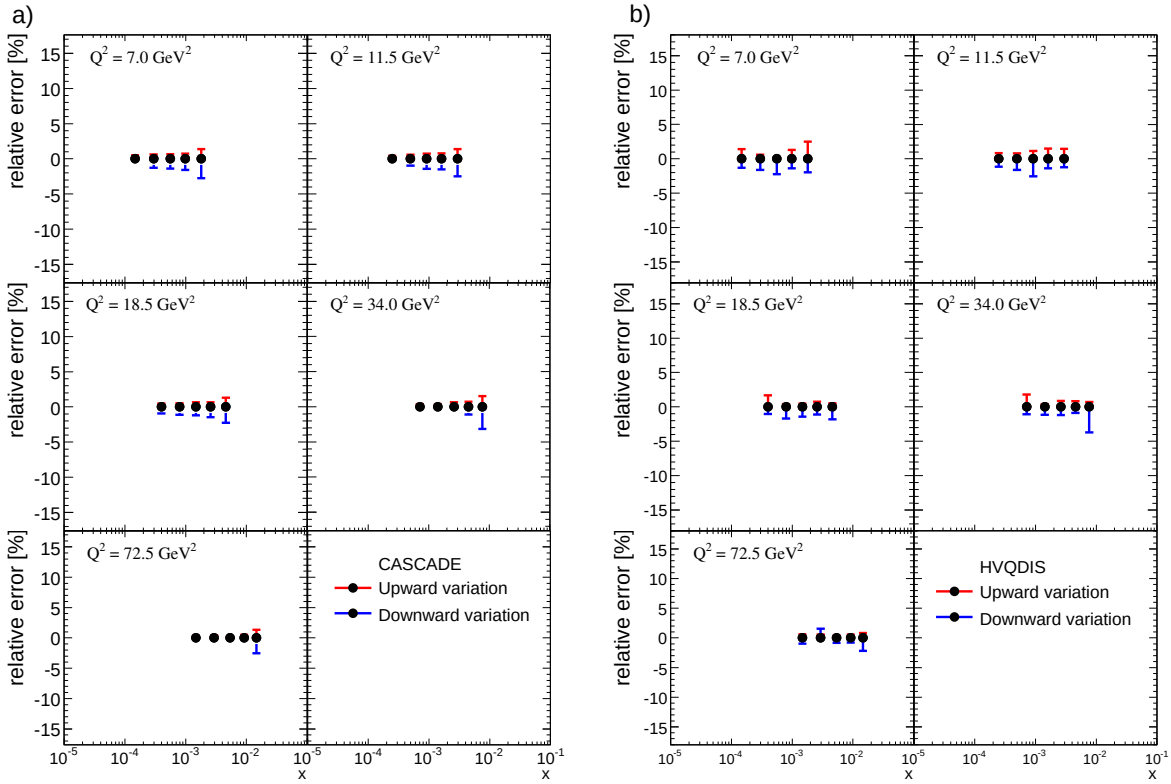

Figure 11.8.: *Uncertainty of the extrapolation factor from the uncertainty of the threshold position implemented for the $\hat{s}$ fragmentation for CASCADE a) and for HVQDIS b). The interval of the variation is given in table 11.1.*

11.3. The Charm Contribution to the Proton Structure

The inclusive D^* cross section data are extrapolated to the full phase space in order to derive the charm contribution F_2^c to the proton structure as a function of x for different Q^2 bins. The extrapolation uncertainty of the extraction follows the procedure presented in the previous section and is added as a shaded band at the bottom of a certain Q^2 bin, with the exception that the fragmentation uncertainty is added in quadrature to the experimental systematic uncertainty.
For the presented F_2^c extraction the D^* cross section measurement results of the high Q^2 analysis are added. The high Q^2 measurement is performed within the same visible phase space, except for the photon virtuality Q^2 where $100 < Q^2 < 1000$ GeV^2 is analysed [Bri08]. Moreover all Q^2 bin centres are shifted to a value that allow a later combination with F_2^c measurements from ZEUS or H1.
Figure 11.9 illustrates the $F_2^c(x, Q^2)$ data extracted with CASCADE, which are compared to the CCFM prediction using the unintegrated gluon density A0, which shows a good agreement. However, for the third and fourth Q^2 bin at high x values small jumps towards higher F_2^c are be observed. These jumps are most probably due to

the acceptance, which is in this particular bin around 18%, as shown in figure 11.2a), thus decreasing the reliability of the measurement for largest x as the extrapolation is large. This difficulty is also observed for the F_2^c values extracted with HVQDIS as

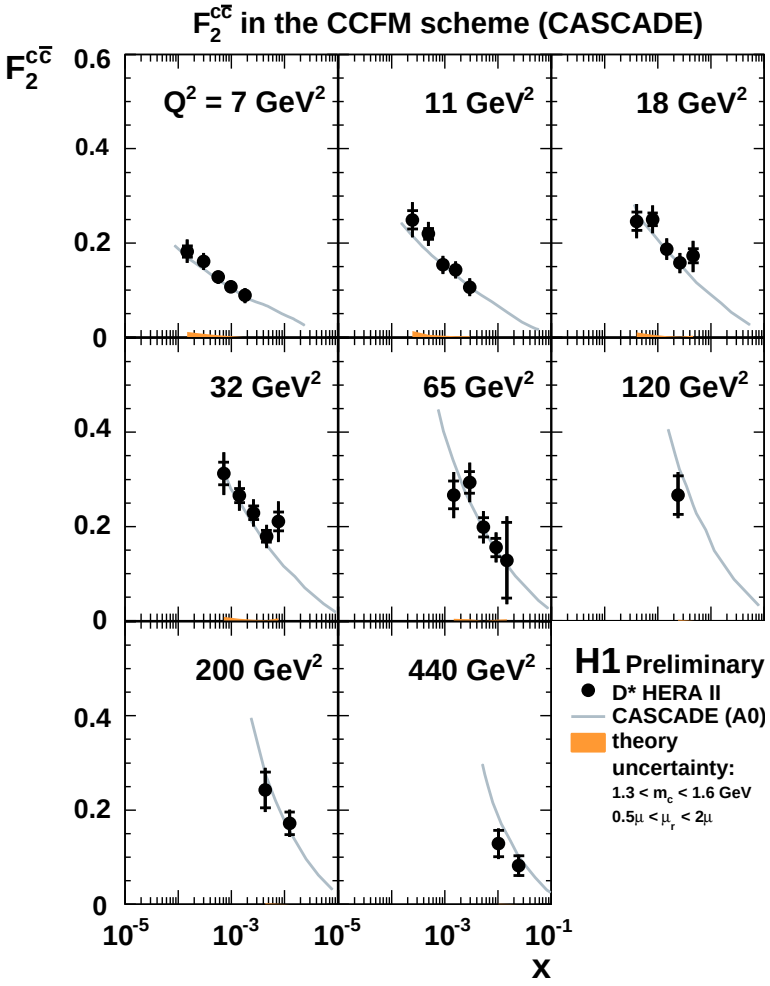

Figure 11.9.: *The extracted F_2^c in the CCFM scheme extrapolated by CASCADE with the extrapolation uncertainties (except for the fragmentation error) illustrated as shaded error bars at the bottom of a Q^2 bin. The high Q^2 cross section data utilised for the F_2^c extraction are taken from [Bri08]. The innermost error is the statistical error, while the fragmentation error is added in quadrature to the experimental systematic error. The comparison is done to the CCFM prediction provided by CASCADE utilising the A0 proton PDF.*

depicted in figure 11.10 [Dau08]. In particular for the two lowest Q^2 bins at large x the extracted F_2^c lies considerably below the theory prediction and the value extracted with CASCADE, which can also be related to the restricted phase space and the large extrapolation. However, the extracted F_2^c demonstrates nicely the scaling violations and possesses a strong rise with increasing Q^2. From previous measurements [A$^+$02] a contribution of 30% from F_2^c to the proton structure is known. Furthermore the

F_2^c extracted by HVQDIS is able to distinguish between the two different proton PDFs shown in figure 11.10. In particular at low Q^2 the description of the data is better if the CTEQ5f3 PDF is used for the calculation of the NLO QCD predictions, while at higher Q^2 both PDFs give a good description of the data.
Overall the F_2^c in the CCFM and DGLAP scheme differs significantly, which is due to

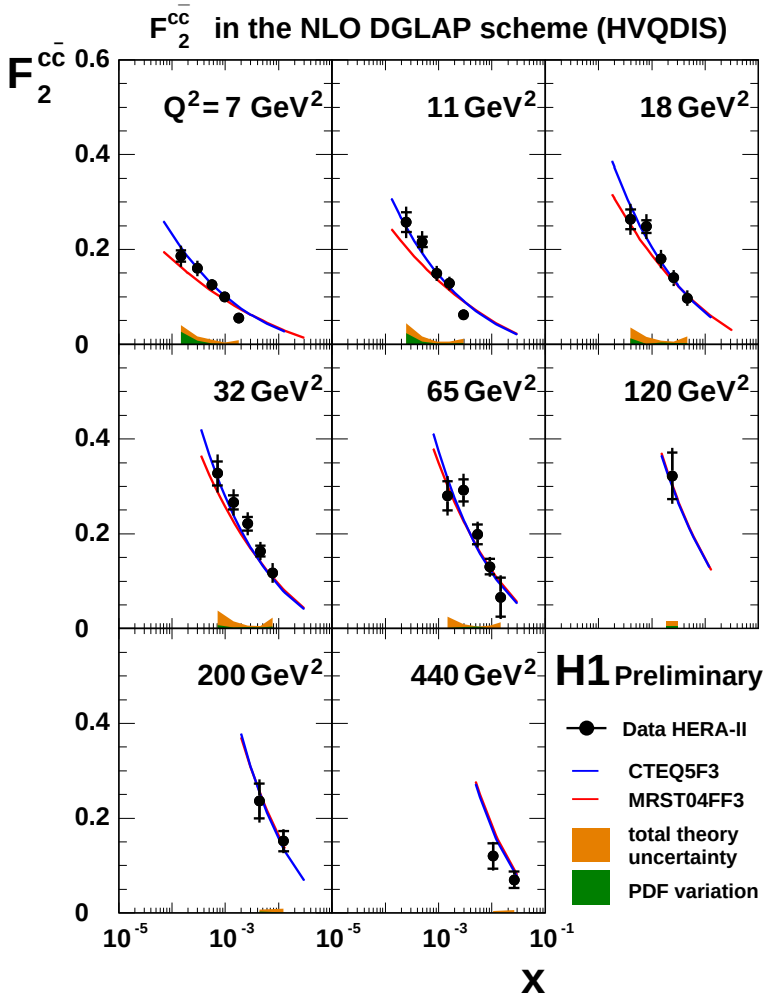

Figure 11.10.: *The extracted F_2^c in the DGLAP scheme extrapolated by HVQDIS [Dau08]. Further details are given in the caption of figure 11.10. The comparison is done to the DGLAP prediction provided by HVQDIS using the CTEQ5f3 or MRST04FF3 proton PDFs.*

the fact of different predictions of the unmeasured phase space from the two models used for the extrapolation. Moreover large differences of up to of 80% between the models remain at large x. The use of F_2^c data with such large errors in global analyses of structure function data does not make sense. To overcome this problem a phase space extension as presented in the next chapter is of use for the measurement of the charm structure function F_2^c. Thus the differences due to the model assumption are largely reduced and a more reasonable F_2^c is presented.

12. Phase Space Extension of the Measurement

A larger phase space for the D^* measurement is desirable because of new insights to heavy quark production at H1 as this is an up to now not measured region. The major benefit is the possibility of more stringent tests of pQCD in particular of the implemented heavy flavor schemes for the treatment of the heavy quark mass. Moreover the extraction of F_2^c profits significantly from a larger phase space coverage (see section 12.4). Such an extension has only recently became possible as the reconstruction version 48 implements a better track reconstruction especially at low transverse momenta [Pit07]. Furthermore the dead material description is improved [Pit08] compared to older reconstruction versions. The simulation and reconstruction version 48 is also utilised for the MC and corresponds to dst5 in data. A significant reduction of systematic errors is expected with the recent reconstruction version.
This chapter concentrates on $\eta(D^*)$ and $p_T(D^*)$ distributions to demonstrate the fea-

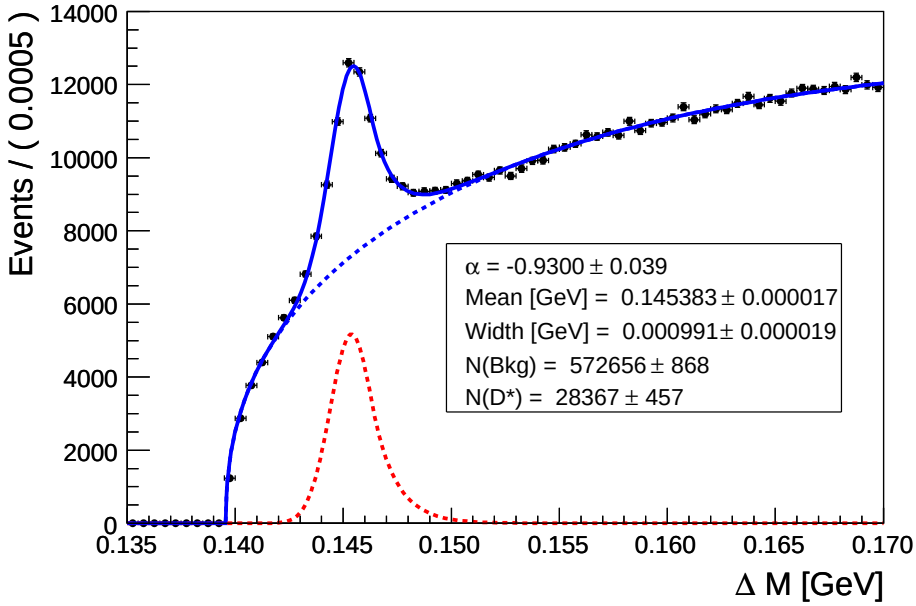

Figure 12.1.: *The ΔM distribution of the selected data sample (see table 12.1) in the extended phase space includes additional cuts for $p_T(D^*) < 1.5$ GeV (see section 12.1). The result of the asymmetric fit parametrisation is stated in the box.*

sibility of a measurement in an extended phase space. A large phase space extension in $p_T(D^*)$ and $|\eta(D^*)|$ down to values of 0.8 GeV and up to values of 1.9 in $\eta(D^*)$ is feasible and studies performed are presented here. These studies concern the shapes of the ΔM distribution and in particular the description of the D^0 mass peak position and width in data by MC, as a window cut around the nominal D^0 mass of $|M(K\pi) - M(D^0)| < 0.08$ GeV is applied. Moreover the binning of the measurement

needs an optimization as now matrix unfolding is employed, where the result of performed studies is presented in section 12.2. For a complete analysis the other cross section variables have to be studied as well, and the systematic uncertainties have to be re-calculated.
The ΔM distribution of the extended phase space within the cuts summarised in table 12.1 is displayed in figure 12.1. Additional cuts on the specific energy loss of a particle, dE/dx (for an introduction see e.g. [Weg99]) are only applied for $p_T(D^*) < 1.5$ GeV. The result of the asymmetric fit parametrisation is stated in the box. An increase of the non-resonant background of more than a factor 2 is observed, while the signal increases by 40% compared to the standard phase space (see figure 5.5). An additional reduction of the background is possible by applying dE/dx cuts additionally for the $p_T(D^*) > 1.5$ GeV region.

12.1. Selection

The selection cuts for the extended phase space are summarised in table 12.1, while the first four cuts define the visible range of the extended phase space cross section measurement. In addition to the transverse momentum, pseudo-rapidity and invariant

name	value
Virtuality	$5 < Q^2 < 100$ GeV^2
Inelasticity	$0.02 < y < 0.70$
Transverse momentum	$p_T(D^*) > 0.8$ GeV
Pseudo-rapidity	$\lvert\eta(D^*)\rvert < 1.9$
$p_T(K)$	> 0.3 GeV
$p_T(\pi)$	> 0.3 GeV
$p_T(\pi_{\text{slow}})$	> 0.08 GeV
$p_T(K) + p_T(\pi)$	> 1.5 GeV
$\lvert\eta(K, \pi, \pi_{\text{slow}})\rvert$	< 2.0
$\lvert M(K\pi) - M(D^0)\rvert$	< 0.08 GeV
ΔM	< 0.170 GeV

Table 12.1.: *Selection cuts on the transverse momenta and pseudo-rapidity of the D^* track and the tracks of its decay particles for the extended phase space region. Additional cuts for the invariant masses of the reconstructed heavy mesons are applied. The first four cuts define the visible range of the extended phase space cross section measurement.*

mass cuts, more special cuts are applied to improve the signal-to-background ratio for D^* mesons with a transverse momentum of less than 1.5 GeV. Because of the geometry of the CJCs (see section 3.3) the track efficiency at very low momenta of $p_T \lesssim 0.11$ GeV is charge dependent. Thus negatively charged tracks are reconstructed with a higher efficiency and resolution than positively charged tracks. Therefore only negatively

charged slow pion tracks are selected in the $p_T(D^*) < 1.5$ GeV region. Because of the strong increase of background towards low p_T further cuts on the energy loss of identified particles, dE/dx, are applied for the $p_T(D^*) < 1.5$ GeV region. These dE/dx cuts are 2% on the kaon likelihood for D^* mesons with a transverse momentum between 1.0 and 1.5 GeV and 5% on the likelihood of all decay particles of the D^* meson for $p_T(D^*) < 1.0$ GeV.
In order to check the resolution of the track reconstruction and the description of the MC in the extended phase space a comparison of the width and position of the D^0 mass peak in data and MC is done. The procedure utilised here is also applied for the estimation of the uncertainty of the D^0 mass window cut for the standard phase space cross section measurement (see section 9.1).
The result is displayed in figure 12.2 as a function of η for $|\eta(D^*)| < 1.9$ with four new bins indicated in the histogram. The error bar denotes the width of the D^0 mass peak estimated by a fit. The nominal D^0 mass [Y+06] is indicated by the middle dashed line together with two additional dashed lines, which indicate the mass window cut applied during the selection. For the additional η bins with $|\eta(D^*)| > 1.5$ the width

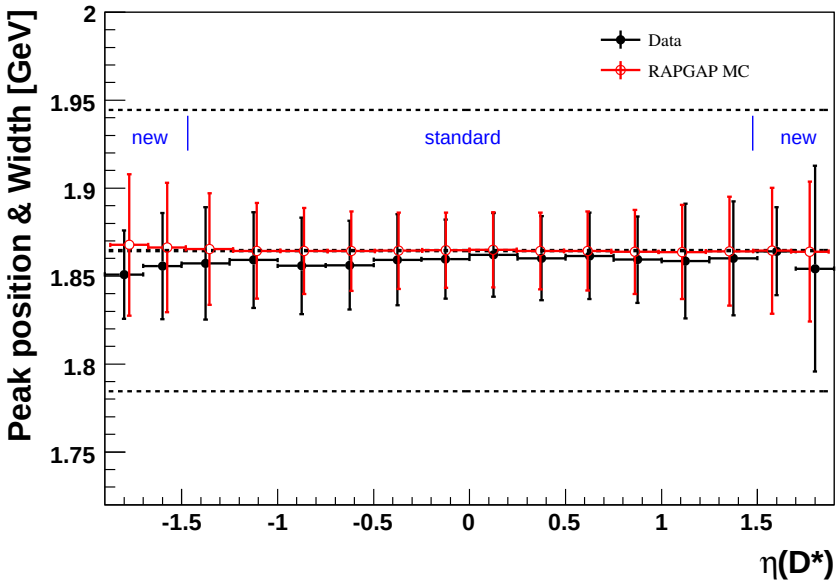

Figure 12.2.: *The width and position of the D^0 mass peak as a function of $\eta(D^*)$ for data (filled circle) and MC (open circle) in the extended phase space region of the D^* meson. The new bins are indicated in the histogram.*

of the D^0 meson in data decreases compared to the standard $\eta(D^*)$ region except for the most forward $\eta(D^*)$ bin, which is affected by the increase of the combinatorial background. The MC does not fully describe this behaviour and instead predicts the expected $\eta(D^*)$ dependence of the width of the D^0 mass peak. Overall the D^0 mass position in data is systematically below the nominal D^0 mass. However, no strong degradation compared to the standard phase space region is observed and thus remaining effects in $|\eta(D^*)| > 1.5$ can be included in systematic errors. Figure 12.3 provides a similar study as a function of $p_T(D^*)$ down to 0.8 GeV and up to 20 GeV where the new bins are indicated in the histogram. The D^0 mass position in data is

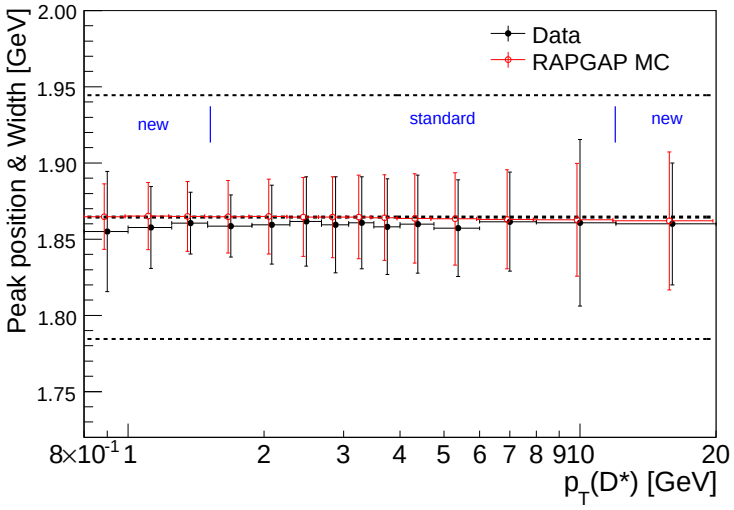

Figure 12.3.: *The width and position of the D^0 mass peak as a function of $p_T(D^*)$ for data (filled circle) and MC (open circle) in the extended phase space region of the D^* meson. The new bins are indicated in the histogram.*

systematically below the nominal D^0 mass as it was observed for the $\eta(D^*)$ distribution. The new $p_T(D^*)$ bins below 1.5 GeV are in general described, both show a increasing widths towards low momenta and additionally a decreasing D^0 peak position. The MC overestimates the D^0 mass resolution at low $p_T(D^*)$, while for $p_T(D^*) > 1.5$ GeV the resolution is only slightly overestimated.
Because of the larger $\eta(D^*)$ range the trigger efficiency of the track condition has also

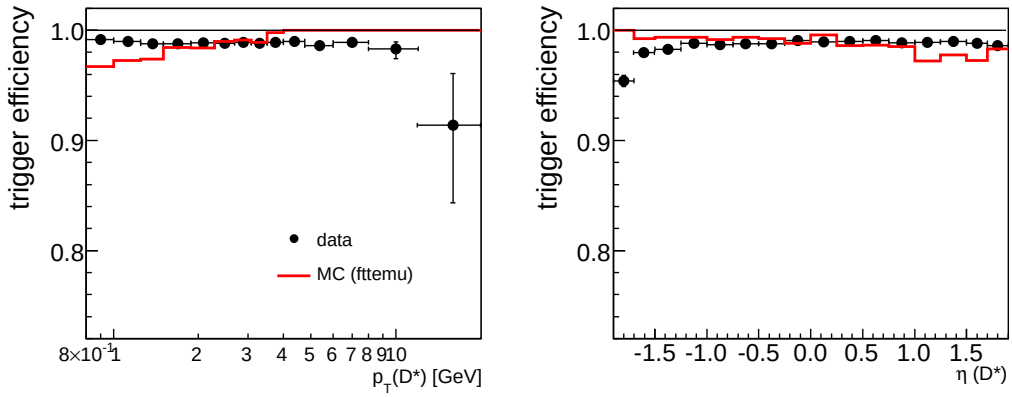

Figure 12.4.: *The trigger efficiency in data (only FTT period) for the extended phase space as a function of $p_T(D^*)$ a) and $\eta(D^*)$ b) compared to the trigger efficiency calculated from the FTT simulation fttemu. Note the zero suppressed y axis.*

been checked. The trigger efficiency is calculated from the range within which the Fast Track Trigger was active. The trigger efficiency is determined according to equation 8.3 from data (filled circles) and MC (solid line) as a function of $p_T(D^*)$ and $\eta(D^*)$ and illustrated in figure 12.4a) and 12.4b) respectively. Other distributions are checked as

well and overall high trigger efficiencies of $\sim 98\%$ are observed in data, which can be cross-checked with MC. The trigger efficiency determined from MC is depicted as solid line in the histogram and describes the data reasonably well. However, in backward directions a overshoot of the MC by 4% is oberved. A possible explanation is a not fully efficient pre-amplifier of the CJC, which is not correctly implemented in MC. The difference at low $p_T(D^*)$ is currently not fully understood and is under investigation.

The ΔM Distributions of the Extended Phase Space

The ΔM distribution of the additional bins in the pseudo-rapidity and the transverse momentum of the D^* meson as selected by the cuts summarised in section 12.1 are presented here. The ΔM distributions for the additional $\eta(D^*)$ bins are depicted in figure 12.5 with the bin borders indicated in each ΔM distribution. The top row are the two additional bins in backward direction and the bottom row the two additional ones in forward direction. Overall the combined signal and background fit for the

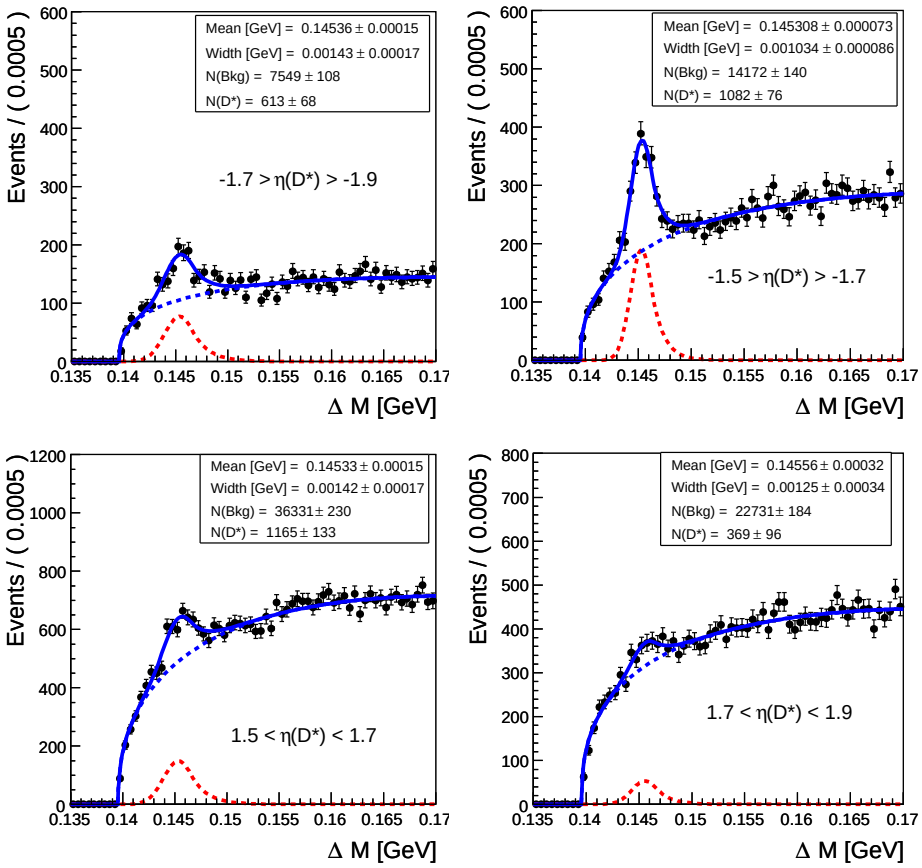

Figure 12.5.: *The ΔM distribution with the combined signal and background fit for the additional bins in $\eta(D^*)$.*

additional bins in $\eta(D^*)$ looks also reasonably. However, the most forward bin is affected by background. For a precise measurement it might be useful to restrict the $\eta(D^*)$ range slightly to 1.8 in order to exclude more background.

Figure 12.6 shows the ΔM distributions for the three additional $p_T(D^*)$ bins. The

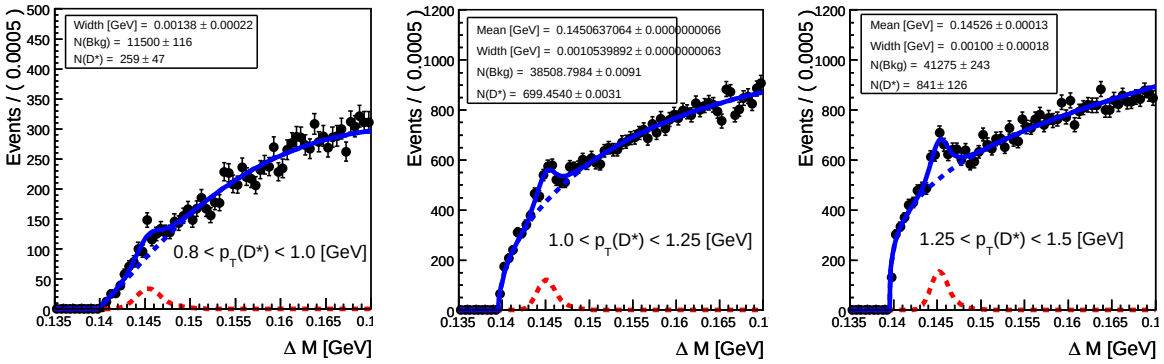

Figure 12.6.: *The ΔM distribution with the combined signal and background fit for the additional bins in $p_T(D^*)$.*

lowest $p_T(D^*)$ bin from 0.8 to 1.0 GeV is highly background dominated and clearly needs further studies. Otherwise the distributions are reasonably fitted with the sum of a Crystal Ball and Granet function and look promising.

12.2. Matrix Unfolding

Although the bin-by-bin method gives reliable results as discussed in section 8.1 the mathematically adequate way is to use the complete information of the detector response matrix and to do a matrix unfolding. This is especially true if a higher precision (finer binning) of the measurement is desirable, which is the case for the extended phase space. Furthermore matrix unfolding improves several drawbacks of the bin-by-bin method. For instance a consistent error propagation is provided by the covariance matrix for the statistical errors. Moreover the model dependencies are reduced if matrix unfolding is implemented and migrations are treated in a consistent way.
As introduced in section 5.3 a measurement in high energy physics is of the type $\mathbf{y} = \mathbf{A} \cdot \mathbf{x}$ where $\mathbf{A}$ denotes the detector response matrix, $\mathbf{y}$ the measurement vector and $\mathbf{x}$ the true vector. The true vector can be obtained if the matrix $\mathbf{A}$ is inverted such that $\mathbf{A^{-1}} \cdot \mathbf{y} = \mathbf{x}$. Furthermore the matrix $\mathbf{A}$ incorporates migrations from outside the visible region inside the measured one. Compared to direct matrix inversion a numerically more stable approach is given by the singular value decomposition (SVD, e.g. [BL98]), which a priori checks if the inverted matrix exist. The SVD method is implemented in the TDecompSVD class, which is provided by `ROOT` [BR]. The SVD of a real $m \times n$ matrix $\mathbf{A}$ is its factorisation of the form:

$$\mathbf{A} = \mathbf{USV}^T \ , \tag{12.1}$$

where $\mathbf{U}$ is a $m \times n$ orthonormal matrix, $\mathbf{V}$ is an $n \times n$ orthogonal matrix while $\mathbf{S}$ is an $n \times n$ diagonal matrix with non-negative diagonal elements. The quantities $s_i \geq 0 \equiv S_{ii}$ are called singular values of the matrix $\mathbf{A}$ and are ordered from largest to smallest values with increasing index i. The singular values provide information about

the matrix $\mathbf{A}$ itself. For instance the rank of the matrix $\mathbf{A}$ is the number of non-zero singular values. The inverse $\mathbf{A^{-1}}$ is given by:

$$\mathbf{A}^{-1} = \mathbf{V}\mathbf{S}^{-1}\mathbf{U}^T \ . \tag{12.2}$$

The true unfolded solution vector $\mathbf{x}$ is obtained from:

$$\mathbf{x} = \underbrace{(\mathbf{V}\mathbf{S}^{-1}\mathbf{U}^T)}_{\mathbf{A^{-1}}} \cdot \mathbf{y} = \sum_{j=1}^{n} \frac{1}{s_j} c_j \mathbf{v}_j \quad \text{with} \quad c_j = \mathbf{y}^T \cdot \mathbf{u}_j \ . \tag{12.3}$$

The unfolding method has a deficit which one can understand from the fact that the complete solution is a superposition of linear combinations. Thus the contribution of eigen vectors $\mathbf{v}_j$ with small singular values s_j, which are compatible with zero, dominates the whole solution because these $\mathbf{v}_j$ are multiplied by large factors $(1/s_j)$. These insignificant contributions can be suppressed by so-called regularisation methods, which implement either simple truncation methods or advanced smooth transitions[1] from significant to insignificant coefficients. The latter one is preferable because the truncation method has the disadvantage that it creates additional oscillations [BL98]. Even though advanced and complex methods to avoid such behaviour exist, it is useful to analyse the singular values and the contribution of a $\mathbf{v}_j$ to the solution of $\mathbf{x}_j$. This procedure allows to optimise (a priori) the number of significant bins of a measured quantity which improves the statistical precision of a measurement.

Optimised Binning with Matrix Unfolding

In order to determine the amount of significant bins of a distribution the following is done by using the equations 12.1 and 12.3:

1. Determine the Response matrix $\mathbf{A}$ and perform the singular value decomposition ,
2. obtain singular values s_j and coefficients c_j ,
3. check the number of significant s_j .

As an example figure 12.7a) and b) illustrate this method for the $\eta(D^*)$ and $p_T(D^*)$ distribution in the standard binning extended to cover the additional phase space. The significance[2] of the j^{th} coefficient c_j to the matrix solution (see equation 12.3) is indicated as solid line with the axis on the left-hand side, while the impact of this j^{th} solution to the complete matrix solution is indicated as dashed line with the axis on the right-hand side. The number of significant bins is estimated from the dotted line, which indicates the 95% confidence level. If a bin has a significance smaller than this level the coeffcient is compatible with zero at the given confidence level and can be removed from the solution without introducing a bias. The number of bins estimated from this kind of study is compatible to the number, which is also optained from studies of the purity in the case of the bin-by-bin unfolding. That is due to the high resolution

[1] One example of a smooth regularisation method is the so-called *Tikhonov regularisation*, which is implemented by the RooUnfold package and the RUN package from V. Blobel.

[2] Singular value s_j normalised to the statistical error of the measurement for a certain bin j.

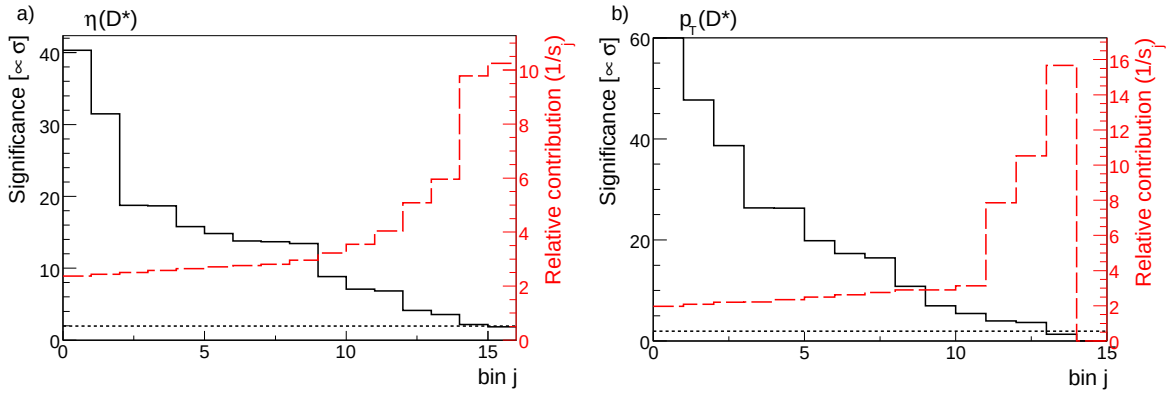

Figure 12.7.: *The significance of the coefficient c_j of the matrix solution (solid line) with the axis on the left hand-side whereas the impact of the j solution to the complete matrix solution indicated as dashed line with the axis on the right hand-side. The dotted line at the bottom indicates the 95% confidence level for the chosen binning in $\eta(D^*)$ a) and for $p_T(D^*)$ b).*

in p_T and η where the binning is also influenced by statistics. For variables that show a worse resolution, like y, larger improvements by matrix unfolding are expected.

Comparison of the Data Correction Methods

The comparison between the matrix unfolding and the bin-by-bin correction method is performed by utilising both methods for the extended phase space. The results of the bin-by-bin method are calculated according to equations 5.6 for the acceptance and 5.7 for the efficiency. For the matrix unfolding the full detector response matrix

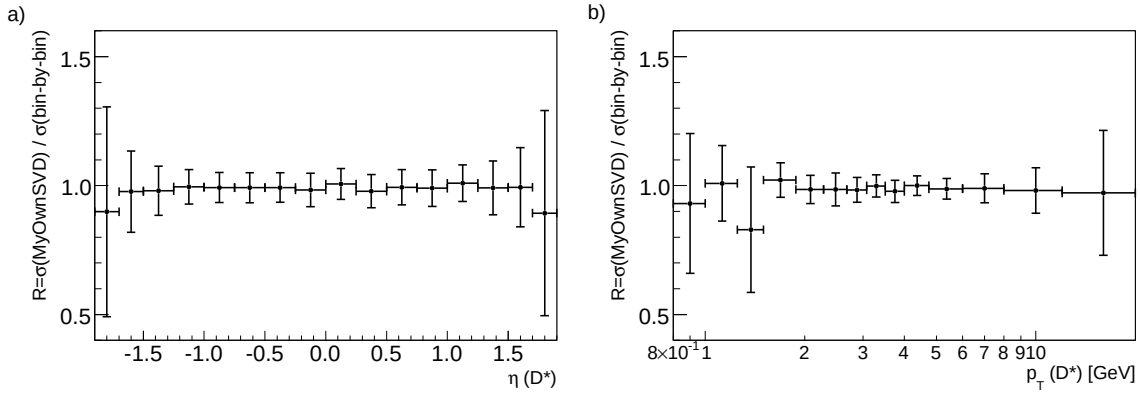

Figure 12.8.: *The ratio of the cross section calculated with the matrix unfolding method (MyOwnSVD) to the bin-by-bin method as a function of $\eta(D^*)$ a) and $p_T(D^*)$ b).*

is forwarded to the SVD based matrix unfolding according to equation 12.1. Thus the unfolded cross section treats migrations between the measured bins in a correct way with the smallest bias possible. The matrix unfolding method implemented for the

present analysis does not use regularisation.
Figure 12.8a) displays the ratio of the matrix unfolded cross section to the bin-by-bin corrected cross section as a function of $\eta(D^*)$. The statistical error of the matrix unfolded cross sections is assigned for the ratio in order to avoid double counting of errors. A nice agreement is observed, although the outermost bins are lowish within the matrix unfolding method by 10%. Here one expects some model dependencies in the bin-by-bin correction due to the unmeasured region $|\eta(D^*)| > 1.9$. For the $p_T(D^*)$ distribution also a good agreement is observed as illustrated in figure 12.8b).

12.3. Cross Sections

The D^* meson cross sections are calculated utilising the matrix unfolding method for the correction of the detector effects. Up to now a detailed study of all systematic error sources is not finished because a large fraction of the uncertainty sources requires the use of the matrix unfolding method. As this requires a major re-design of the analysis code only statistical errors are assigned for the cross sections and also for the F_2^c extraction presented in section 12.4.
The selection of the D^* is described in section 12.1. The exact bin borders and selection cuts are still subject to change. Nevertheless the determined D^* cross sections provide interesting insights, i.e. in the forward $\eta(D^*)$ direction as illustrated in figure 12.9a). The sudden decrease of the outermost bins originates from the not finally optimised matrix unfolding procedure, where a regularization method could be of help. Nonetheless, in comparison to the LO MC prediction from CASCADE the agreement

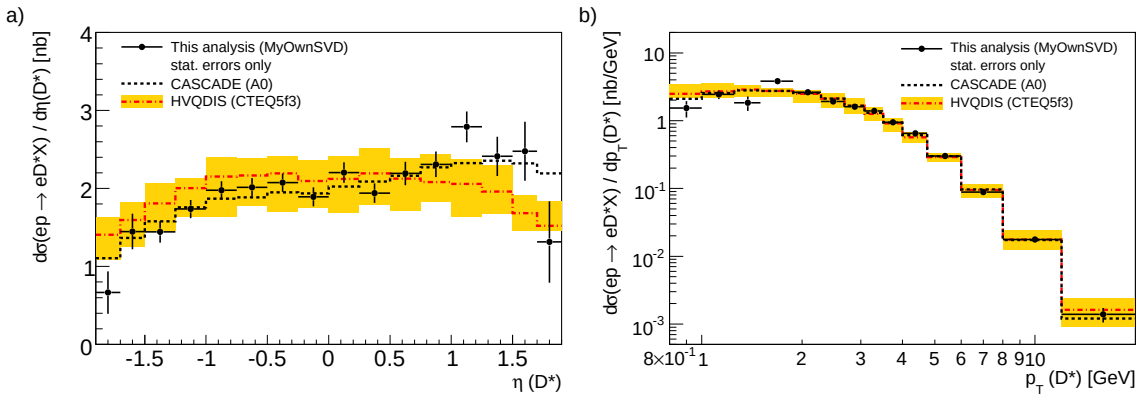

Figure 12.9.: *Differential D^* cross section data (filled circles) as a function of $\eta(D^*)$ a) and $p_T(D^*)$ b) in the visible range as defined in table 12.1. For the measurement only statistical errors are assigned. The data are compared to CASCADE and the NLO calculation HVQDIS. The bands for the expectation of HVQDIS for the CTEQ5f3 (shaded) PDF are obtained by varying parameters according to table 11.1.*

is quite nice, while the NLO QCD prediction from HVQDIS with the CTEQ5f3 proton PDF significantly undershoots the data in forward directions. The HVQDIS is utilised with the central parameters as summarised in table 11.1 and incorporates also the $\hat{s}$

fragmentation. The error (shaded bands) for the NLO prediction from HVQDIS is obtained by varying the parameters according to table 11.1. The observed discrepancy is clearly a topic that requests a double differential measurement, which can shed more light on D^* meson production in this region.
The measurement of the transverse momentum starting at $p_T(D^*) > 0.8$ GeV is also extended towards higher values of $p_T(D^*) < 20.0$ GeV as illustrated in figure 12.9b). Despite the tentative level of the measurement a good agreement of the data to CASCADE and the NLO QCD prediction by HVQDIS is observed, especially the nearly flat distribution at low $p_T(D^*)$.
With an additional cut in the photon-proton rest frame of $p_T^*(D^*) > 2$ GeV a NLO QCD prediction in the ZM-VFNS is possible. The calculations are kindly provided by C. Sandoval and G. Kramer [San08] and use the recent CTEQ66m proton PDF [N+08]. The calculation implements the fragmentation prescription as described in [AKK08]. Figure 12.10a) illustrates the NLO QCD prediction in the ZM-VFNS. Also

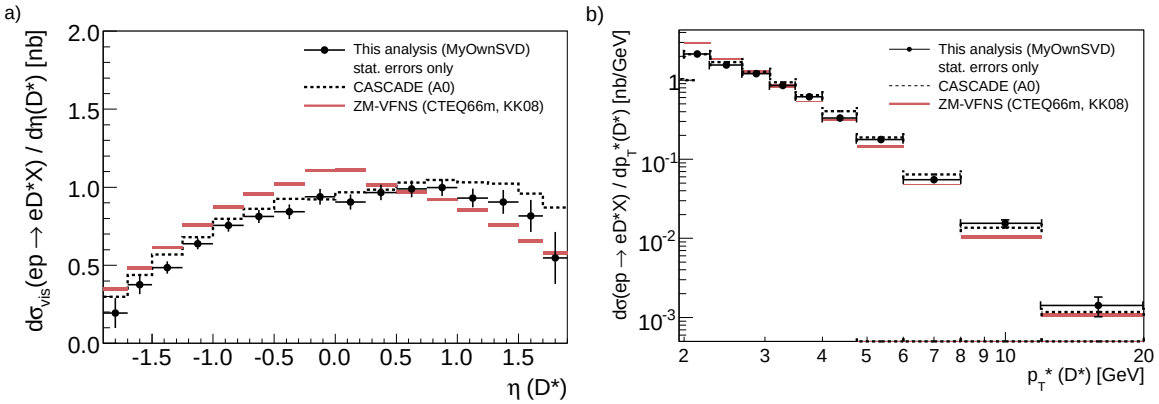

Figure 12.10.: *Differential D^* cross section data (filled circles) as a function of $\eta(D^*)$ a) and $p_T^*(D^*)$ b) in the visible range as defined in table 12.1. An additional cut of $p_T^*(D^*) > 2$ GeV in the γP rest-frame is applied. For the measurement only statistical errors are assigned. The data are compared to a NLO QCD prediction from the ZM-VFNS [San08]. The calculation uses the CTEQ66m proton PDF [N+ 08] and the fragmentation treatment as described in the KK08 scheme [AKK08].*

here a discrepancy in the forward direction is observed and in particular a completely different shape. For comparison also the CASCADE with an additional $p_T^* > 2$ GeV is displayed, which reproduces the shape of the $\eta(D^*)$ distribution reasonably well, although in forward directions CASCADE provides a more shallow slope compared to the data.
The $p_T^*(D^*)$ distribution in the γP rest-frame is depicted in figure 12.10b) and is overall reasonably well described by the NLO prediction from ZM-VFNS and CASCADE. However, the ZM-VFNS is above the data at lowest $p_T(D^*)$. In particular this region could be affected by the massless treatment of charm-quarks in the ZM-VFNS, which starts to get inappropriate at this low scales.

Double-differential Cross Sections

The double-differential measurement as a function of $y - Q^2$ is illustrated in figure 12.11 for the extended phase space of the D^* meson. The data and MC values are

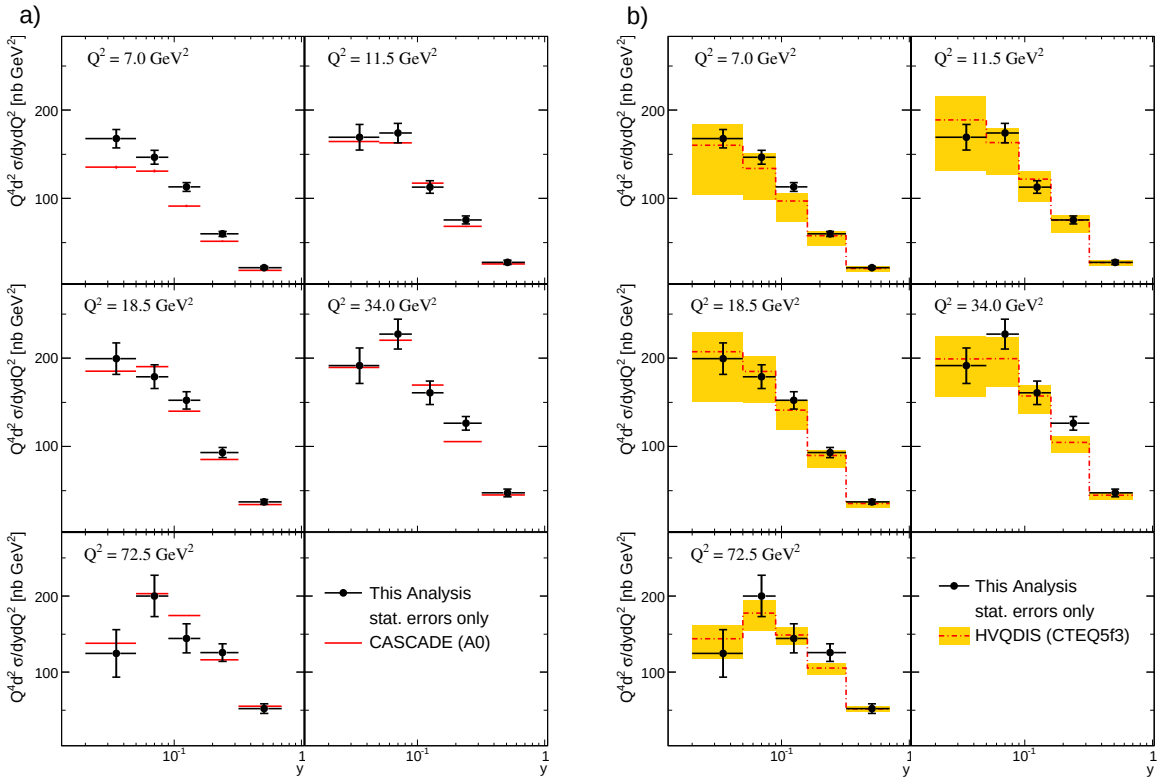

Figure 12.11.: *Double-differential cross section data as a function of y in bins of Q^2 compared to CASCADE a) and HVQDIS b). Both models use the $\hat{s}$ fragmentation model. The bands for the expectation of HVQDIS for the CTEQ5f3 (shaded) PDF are obtained by varying parameters according to table 11.1. Only statistical errors are assigned to the data. (All values are multiplied by Q^4 for better visibility.)*

multiplied by Q^4 for better visibility. Only statistical errors are assigned to the data. The cross section data are compared to the LO MC program CASCADE in 12.11a) and to the NLO QCD prediction from HVQDIS in 12.11b). For both models the $\hat{s}$ fragmentation model is utilised. Overall a nice agreement for both models with the data is observed. The error (shaded bands) for the expectation of HVQDIS for the CTEQ5f3 proton PDF is obtained by varying the parameters according to table 11.1. This theoretical uncertainty is especially large at low y and low Q^2.

12.4. The Charm Contribution to the Proton Structure

The extraction of the charm structure structure function F_2^c from the double-differential measurement in $y - Q^2$ in the extended phase space reduces the extrapolation to the full phase space significantly. In turn this larger phase space coverage reduces the extrapolation uncertainties as the differences between CCFM and DGLAP diminish.

On average the phase space coverage is now approximately 65%, which approaches the level that is achieved with the extraction of F_2^c from inclusive charmed meson displaced track measurements (around 80%) [H+08].
As previously the extrapolation factor is calculated from:

$$f^{\text{extra}} = \frac{\frac{d^2}{dydQ^2} \cdot \sigma^{\text{theo}}_{\text{full}}}{\frac{d^2}{dydQ^2} \cdot \sigma^{\text{theo}}_{\text{vis}}} \; . \tag{12.4}$$

The theoretical prediction is calculated from CASCADE, RAPGAP and HVQDIS. Fig-

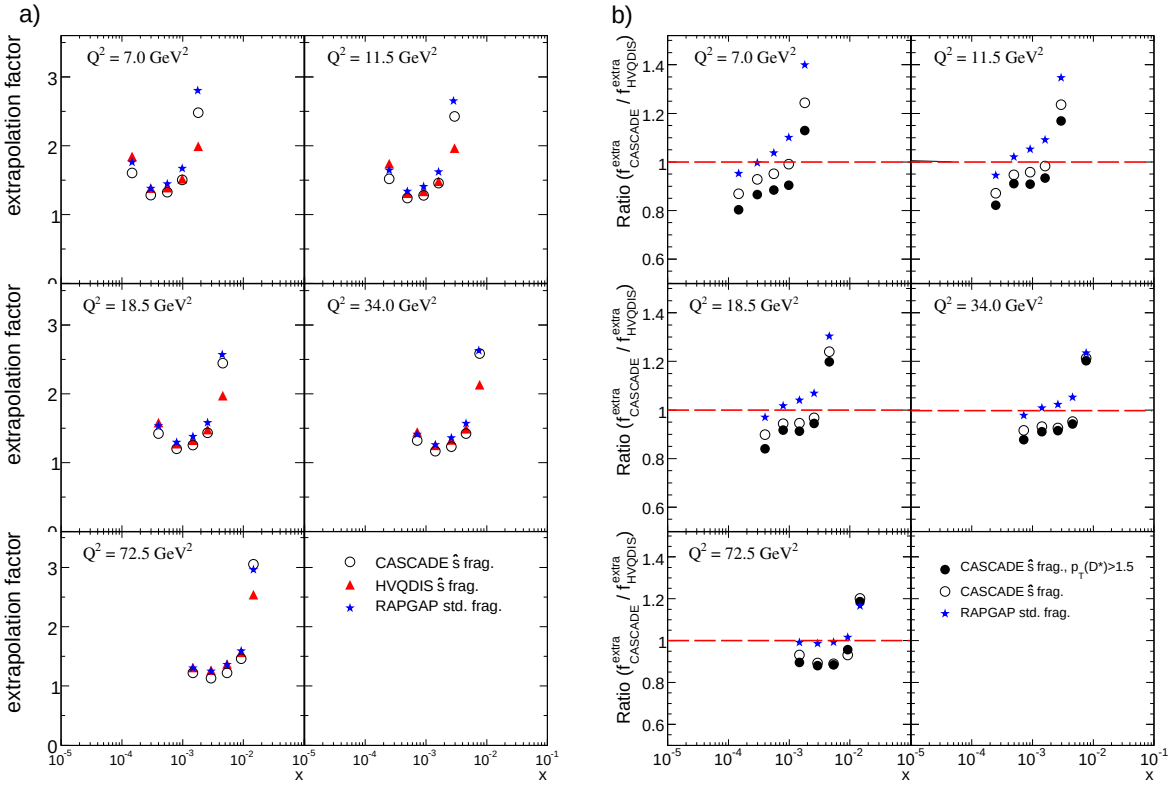

Figure 12.12.: *Extrapolation factor to the full phase space as estimated by HVQDIS compared to the ones calculated with CASCADE and RAPGAP in bins of the extracted F_2^c a). The extrapolation factors for a given phase space as predicted by CASCADE and RAPGAP are normalised to the prediction of HVQDIS as illustrated in b).*

ure 12.12a) illustrates the extrapolation from the visible to the full phase space of the D^* meson. The averaged extrapolation factor is around 1.5, i.e. a 65% phase space coverage is achieved. The largest extrapolation factors are still located at high x owed to the fact that the restriction in $\eta(D^*)$ is too harsh. Figure 12.12b) illustrates the extrapolation factors from CASCADE in two different p_T regions of $p_T(D^*) > 1.5$ (filled circles) and $p_T(D^*) > 0.8$ (open circles). For both samples $|\eta(D^*)| < 1.9$ is applied and the determined extrapolation factors from the two CASCADE samples are normalised to the extrapolation factor from HVQDIS in the same phase space. A lowered $p_T(D^*)$

cut of 0.8 GeV compared to 1.5 GeV does only reduce the difference in extrapolation between HVQDIS and CASCADE at low Q^2 and not too large x where differences at a level of $20 - 25\%$ between CASCADE and HVQDIS remain. The larger Q^2 regime

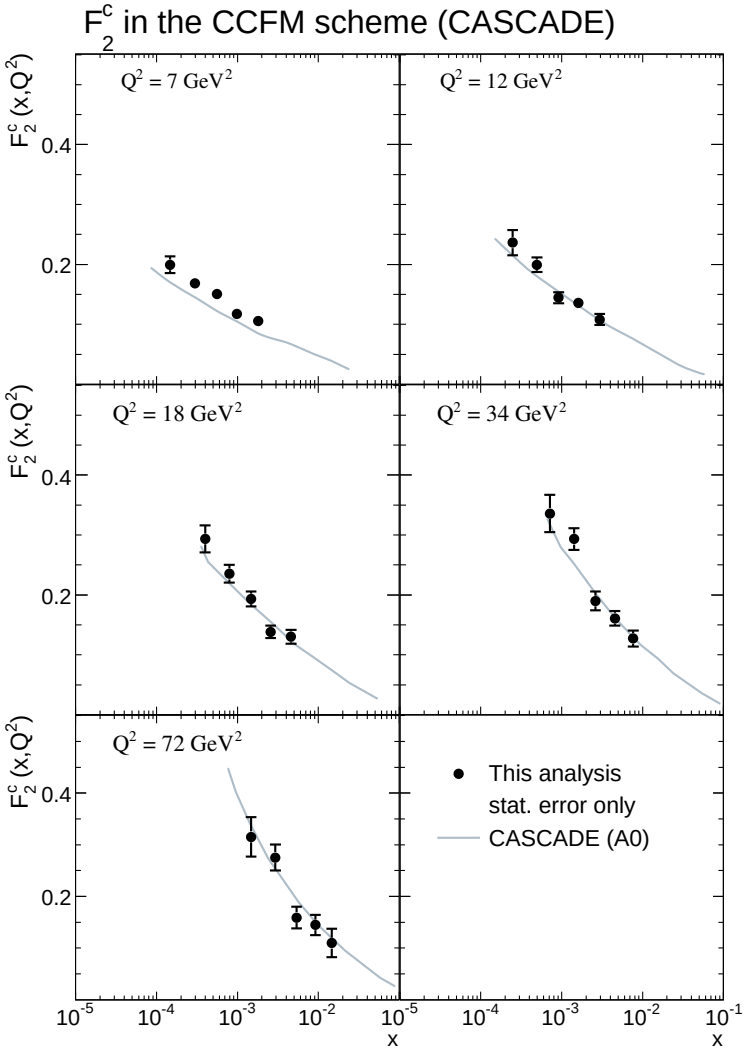

Figure 12.13.: *The extracted F_2^c with statistical errors only extrapolated by CASCADE. No experimental systematic uncertainty is assigned. The comparison is done to the CCFM prediction provided by CASCADE using the A0 proton PDF.*

does not profit that significantly from the lowered $p_T(D^*)$ cut, as higher Q^2 correspond on average to a higher transverse momentum of the D^* meson. Overall differences of approximately 10% are observed, which is an acceptable level for a model uncertainty. As for the cross sections in the extended phase space also for the extracted F_2^c only statistical errors are assigned.
F_2^c is extracted by utilising two models for the extrapolation to the full phase space. The charm structure function in the extended phase space is shown in figure 12.13 for the extrapolation by CASCADE and in figure 12.14 for the one by HVQDIS. Compared to each other the extracted F_2^c data illustrate a smoother behaviour than the

F_2^c extracted from the more restricted phase space (see figures 11.9 & 11.10) and additionally a reasonable agreement between the two extractions is observed. The data

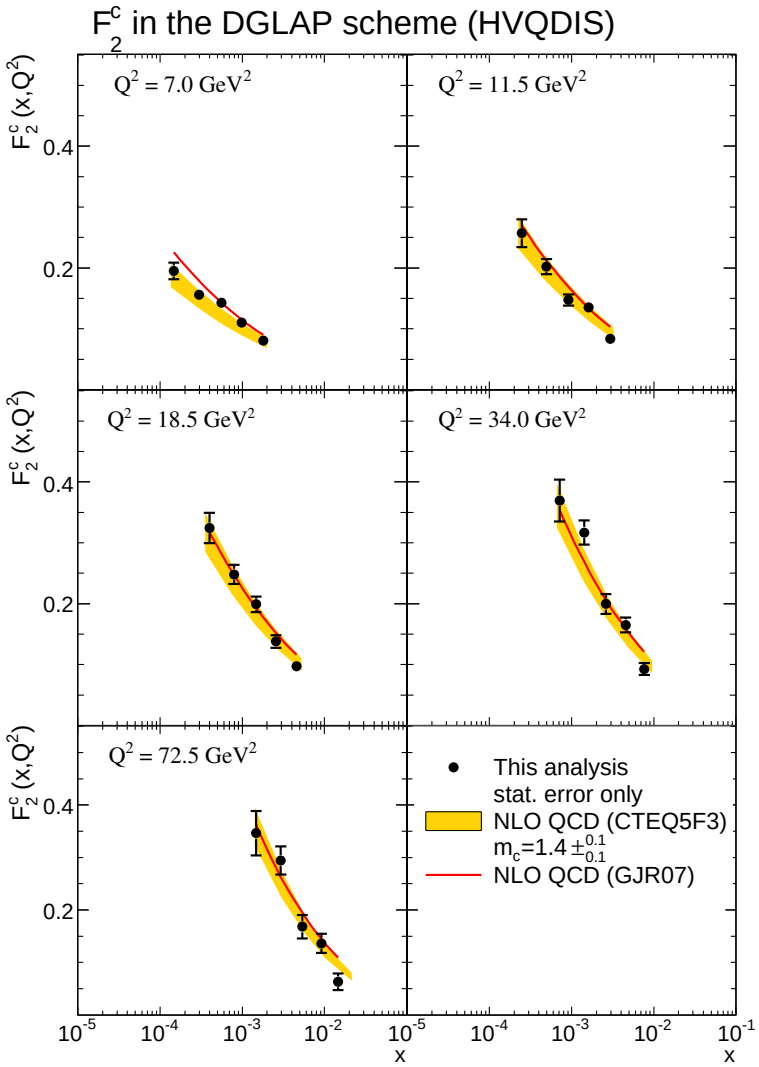

Figure 12.14.: *The extracted F_2^c with statistical errors only extrapolated by HVQDIS. No experimental systematic uncertainty is assigned. The comparison is done to the DGLAP prediction of provided by HVQDIS with the CTEQ5f3 and a more recent proton PDF from GJR [GJDR08].*

are compared to the prediction from CASCADE using the A0 proton PDF with a nice agreement even at highest Q^2 and largest x. For the extraction in the DGLAP scheme the F_2^c data are compared to the prediction utilising the CTEQ5f3 proton PDF where a variation of the charm mass $m_c = 1.4 \pm 0.1$ GeV is done. In addition a prediction from a recent global fit analysis in the FFN scheme of the GJR-group [GJDR08] is displayed. The NLO QCD prediction using the GJR07 proton PDF appears to be higher than the CTEQ5f3 prediction but both describe the data reasonably well.

13. Conclusion & Outlook

Heavy Flavor production provides an additional constraint on the gluon density at low x independent to the inclusive structure function analysis. The presented measurement of the D^* meson production cross section in deep inelastic scattering with the H1 detector employs data corresponding to an integrated luminosity of 347 pb^{-1}, covering the whole HERA II data taking period. Compared to the previous H1 publication, this analysis includes an eightfold increase in statistics and covers the region $5 < Q^2 < 100$ GeV^2 in photon virtuality and the increased region $0.02 < y < 0.70$ in the inelasticity of the scattering process. The visible range of the D^* meson is restricted in transverse momentum and pseudo-rapidity to $p_T(D^*) > 1.5$ GeV and $|\eta(D^*)| < 1.5$. The use of the $e\Sigma$-method for the reconstruction of the event kinematics provides an improved resolution, which allows the analysis of an increased phase space towards lower inelasticity. Moreover the change of the reconstruction method provides a significantly reduced systematic error, for example for D^* mesons produced in forward direction. The total D^* production cross section in the visible region is measured to

$$\sigma^{\text{tot}}_{\text{vis}}(e^{\pm}p \to e^{\pm}D^{*\pm}X) = 4.85 \pm 0.07\ (\text{stat.}) \pm 0.42\ (\text{syst.})\ \text{nb}\ .$$

The single and double-differential cross sections are reasonably well described by the MC programs RAPGAP and CASCADE, which provide leading-order pQCD predictions supplemented with parton showers. Furthermore the distributions have been compared to the next-to-leading order pQCD predictions from HVQDIS where an adequate description has been found. The pseudo-rapidity distribution of the D^* meson shows a sensitivity to the proton parton density used in RAPGAP or HVQDIS. The NLO prediction by HVQDIS lies below the data in the forward direction in particular at low transverse momenta of the D^* meson which confirms the previously seen excess by the H1 Collaboration. Moreover the cross section data shows a sensitivity to the mass treatment of the heavy quark (FFNS, ZM-VFNS, GM-VFNS) in the pQCD predictions. However, this is difficult to disentangle from other effects originating from the extraction method of the proton parton density functions and from the restrictions of the MC programs and NLO calculations.
The measured D^* cross sections have been utilised to derive the charm contribution to the proton structure, $F_2^c(x, Q^2)$, with an eighteenfold increase in data statistics compared to the previous H1 publication. Overall, F_2^c is reasonably described even though in the phase space of the cross section measurement large uncertainties arise from different models, i.e. CASCADE versus HVQDIS, used for the extrapolation to the full phase space. The F_2^c data as extracted with HVQDIS are able to distinguish between the parton density functions from the CTEQ and MRST group, especially at low Q^2. F_2^c shows a larger sensitivity to these differences than the cross section in the pseudo-rapidity of the D^* meson. In order to have a significant impact on global analyses by the fitter groups (CTEQ, MRST/MSTW, GJR) the F_2^c data requires a better under-

standing of the large extrapolation uncertainties from different models.
For more insights into the theoretical treatment of heavy flavor production and for the reduction of the extrapolation uncertainties it is desirable to extend the phase space of the measurement. Such an extension is possible due to an improved track reconstruction at H1, which in turn leads to a reduction of the experimental systematic error. Promising studies concerning a significant phase space extension of the D^* production towards lower transverse momentum of $p_T(D^*) > 0.8$ GeV and larger pseudo-rapidity of $|\eta(D^*)| < 1.9$ have been presented. A statistical gain of 40% compared to the standard phase space has been shown. In this region an even larger excess in $\eta(D^*)$ in forward direction in comparison to the more restricted phase space measurement has been observed. Further studies are clearly needed to pinpoint the origin of this excess. The extended phase space is of particular use for the extraction of F_2^c because it reduces the extrapolation to the full phase space and thus the extrapolation uncertainty. A first extraction of F_2^c taking only statistical errors into account indicates smaller model dependencies due to the larger phase space coverage.

Outlook

The measurement of the D^* cross section in an enlarged phase space provides further insights into charm production and can be utilised to test the pQCD predictions in the different heavy flavor schemes, namely ZM-VFNS, FFNS and GM-VFNS, with precise double-differential measurements in a stringent way. In addition a more precise understanding of the extrapolation uncertainties arising for the extraction of the charm contribution to the proton structure can reduce the dependencies on the underlying model. A more precise F_2^c would be of use for the global analyses of the fitter groups and could help to further constrain cross section predictions for the LHC.

Part II.

The H1 Fast Track Trigger

14. The Fast Track Trigger System

To exploit the higher luminosity provided after the HERA machine upgrade the H1 experiment [A+97a] has built a three level Fast Track Trigger FTT [B+01]. The FTT is integrated in the H1 trigger system with the characteristic that the third level of the H1 trigger system is realised as the FTT level three system. The task of the FTT system is to provide a high reduction factor to cope with the increased event rates at the upgraded HERA machine.
The FTT utilises 12 wire layers out of the 56 wire layers of the H1 Central Jet Chambers as illustrated in figure 14.1. These 12 wire layers are organised in four trigger

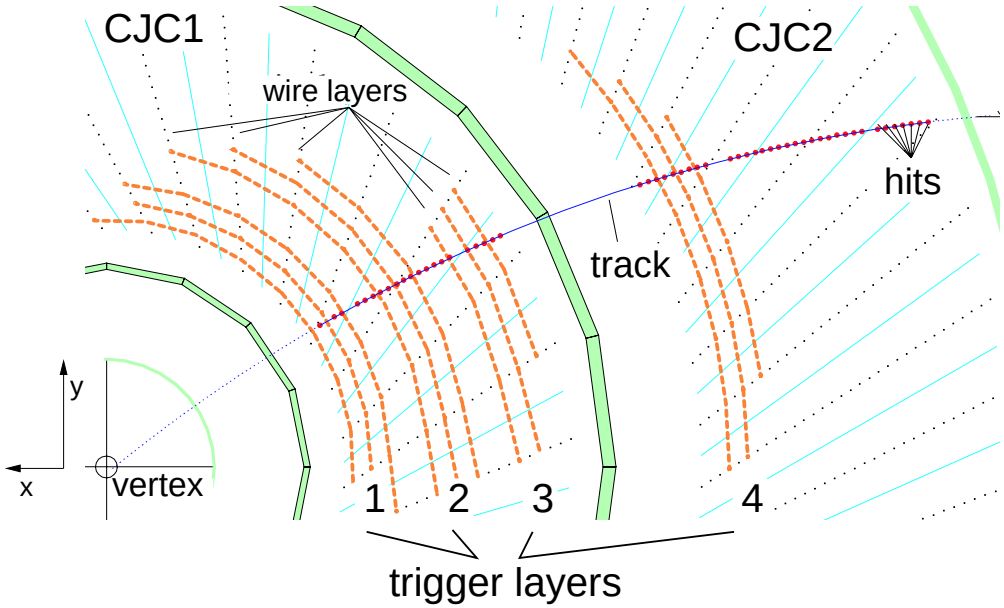

Figure 14.1.: *The xy plane of the H1 central jet chambers (CJC1 and 2) is shown. The Fast Track Trigger (FTT) utilises four groups of three wire layers out of the* 56 *wire layers of the CJCs.*

layers of three wire layers within which a search for track segments is performed. The analogue signals from both ends of the selected wires are digitised with a sampling rate of 80 MHz. Hits are identified by a fast Qt algorithm implemented in a FPGA. The z position (along the beam and chamber wire direction) is determined using charge division [Sch04].
Identified hits are filled into shift registers for further analysis and a track segment search. To reduce the bandwidth an effective sampling rate of 20 MHz is used at level one. Within a trigger group hit patterns stored in the shift registers are compared with pre-calculated, calibrated masks. This comparison is done in parallel for all trigger groups using Content Addressable Memories (CAMs) performing in total $5 \cdot 10^{12}$ mask comparisons per second. If a track segment is found, the corresponding track

curvature $\kappa = 1/p_T$ and the azimuthal angle ϕ are obtained from hard wired logic associated with the uncoded CAM output. In a next step track segments are linked to L1 tracks. For this purpose track segments from the four trigger layers are filled into four corresponding $\kappa\phi$ histograms of the size 16×60. A sliding window technique

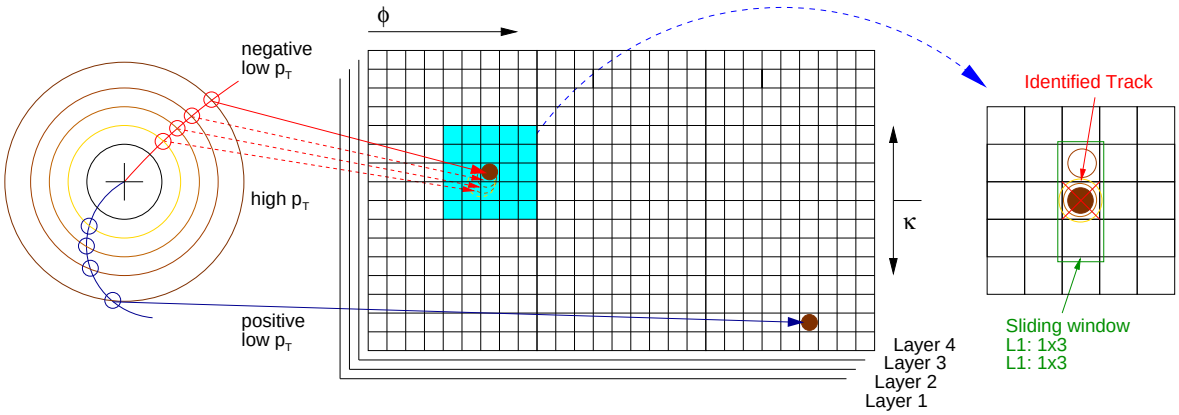

Figure 14.2.: *Schematic drawing of the segment linking of FTT L1. The track segments from the four trigger layers are filled into four corresponding $\kappa\phi$ histograms and a sliding window technique is used to link track segments to tracks by requiring a coincidence of at least 2 out of 4 trigger layers. For FTT L2 the linking is done with a higher resolution.*

is used to link track segments to tracks by requiring a coincidence of at least 2 out of 4 trigger layers as indicated in figure 14.2. Within the L1 latency of 2.3 μs trigger decisions based on the track multiplicity, the number of tracks above transverse momentum thresholds and the event topology are formed. A more detailed description of the FTT L1 system is given in [B+04; Fle03].
In the FTT L2 system [W+03], the full 80 MHz information is restored and used for validating the track segments found at L1. The linking step is repeated using histograms with 60×640 bins in the $\kappa\phi$ plane. Again a track is defined as the coincidence of at least 2 out of 4 trigger layers. In order to increase precision a track fit [Wis03] is performed on six Multi Purpose Boards (MPB [M+05; SCS]) based on the three-dimensional information of the validated track segments. For this purpose each MPB is equipped with four Floating-Point DSPs (Texas Instruments TMS320C6701).
A non-iterative helix track fit [Kar91] uses the x and y positions of the track segments to determine κ and ϕ whereas a linear fit of the z position of the track segments yields the polar angle θ. To improve the track parameter resolution a primary vertex constraint is applied. Each DSP performs up to two track fits. In total, FTT L2 can reconstruct up to 48 tracks per event which is sufficient for more than 98% of the events of interest. The fitted track parameters are sent to the *L2 decider card* (L2 decider) where trigger decisions based on track multiplicities, event topology, transverse momenta are formed. Also simple invariant mass calculations are possible for events with less than eight tracks [Ber07] are performed. The L2 trigger decisions are sent to the central trigger within the L2 latency of 23 μs.
As an overview the hardware implementation of the FTT, including FTT L3 (see chapter 15), is illustrated in figure 14.3 together with the trigger data flow.

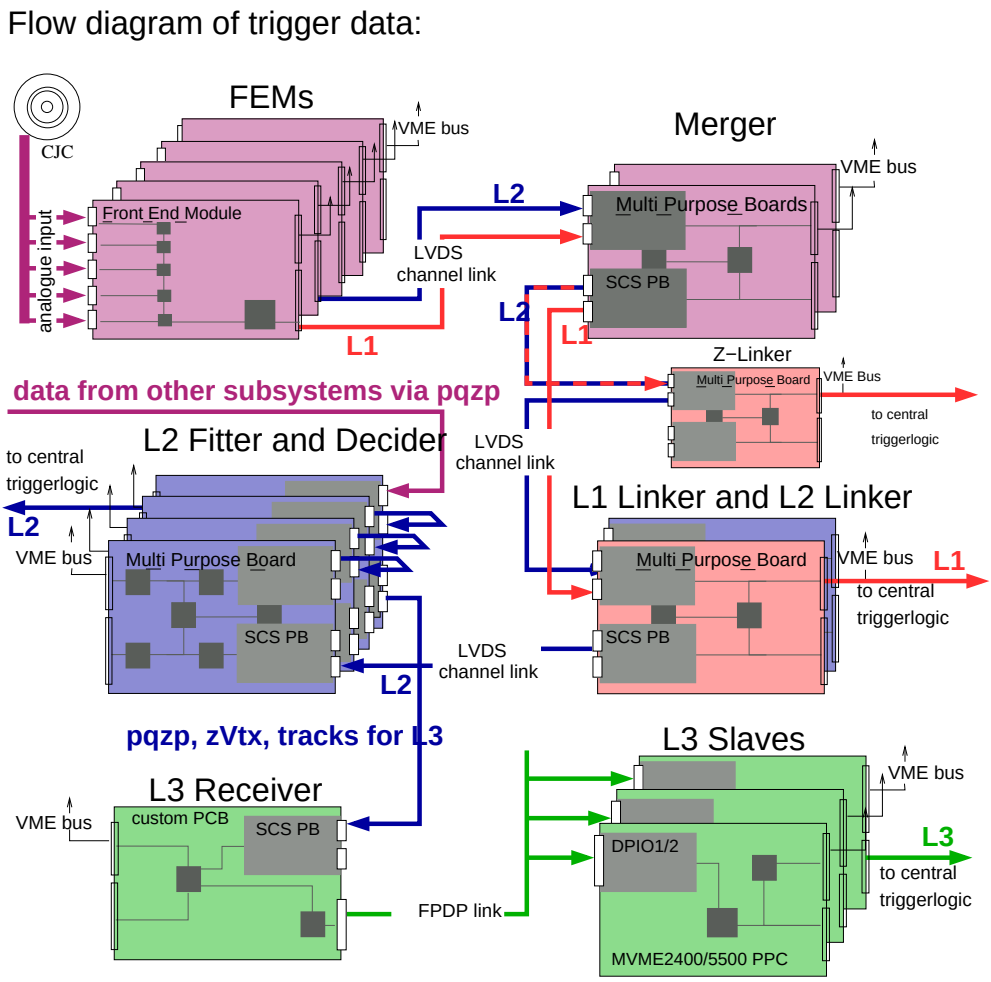

Figure 14.3.: *Sketch of the trigger data flow through the complete FTT system starting from raw hits of designated wire layers of the CJCs to track segments at level one combined to coarse L1 tracks and refined L2 tracks and finally to fitted three-dimensional L2 tracks used by the L3 system together with additional information for a partial event reconstruction.*

14.1. The FTT Simulation

In order to develop and finally commission the hardware of the FTT all levels are implemented into a hardware like simulation. The `fttemu` program was developed using `C` with respect to a modular design of the software [Wis03]. The modular structure of `fttemu` uses the BOS bank system, which allows the output of every information needed for the commissioning of the system in a formatted way, which is of similar structure as for the data taking. The simplified functional principle of the simulation is depicted in figure 14.4. The basic input to the simulation are raw data,i.e. hits on the FTT signal wires (raw hits). The raw hits are either directly used from a copy of the CJC related hit banks in the FTT format or are re-calculated from allready reconstructed CJC tracks. The processing of the hits follows strongly the hardware concept of the FTT (see previous section) therefore the whole digitisation and Qt analysis is

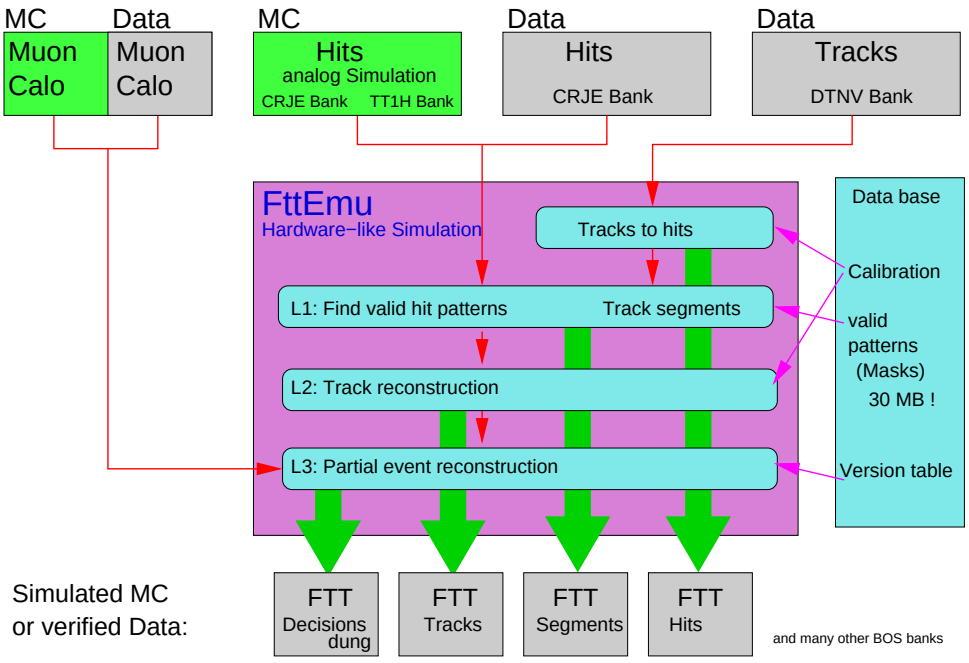

Figure 14.4.: *Simplified sketch of the functioning of the FTT simulation. Possible input data are raw hits from data or hits re-calculated from tracks and MC allowing the verification (data) or simulation (MC) of the FTT trigger decisions. The complete hardware like simulation provides all steps of the hit processing from segments to tracks to invariant masses. In addition for the simulation of L3 the other subdetector information from data or MC is available.*

performed where at the end track segments are reconstructed. Valid track segments are linked to rather coarse tracks at level one and full three-dimensional tracks at level two. For this step different calibration and mask banks are loaded from a database. Afterwards the high precision L2 track parameters together with the information from other subsystems is utilised by the L3 simulation for the calculation of invariant masses and the particle identification based on information of other subsystems as explained later (see section 15.2). The trigger decisions of all FTT trigger levels are available for comparisons to data.
The L3 simulation code is extracted with the use of preprocessor statements [Sau09] from the on-line code. The preprocessor statements filter on-line version related functions which are only provided by the commercial OS. Also the memory addressing, the readout and the communication with the central trigger are filtered. For the selection code a version number is assigned, which is increased with a change of the selection code. During the simulation the version number corresponding to the run range is looked up allowing comparisons between simulated and data events. Also the implementation of new selection algorithms and the adjustment of cut variables is possible with the simulation.

14.2. The Post-processing for H1 Monte Carlo Production

The FTT project was part of the HERA II upgrade program and thus a trigger simulation of the FTT was not part of the initially released H1 trigger software (`h1trig`), which is integrated into the H1 simulation and reconstruction software (`h1simrec`). Because of the development of the `fttemu` program as a hardware-like simulation of the FTT it uses a large memory fraction. This large memory fraction forbids to inte-

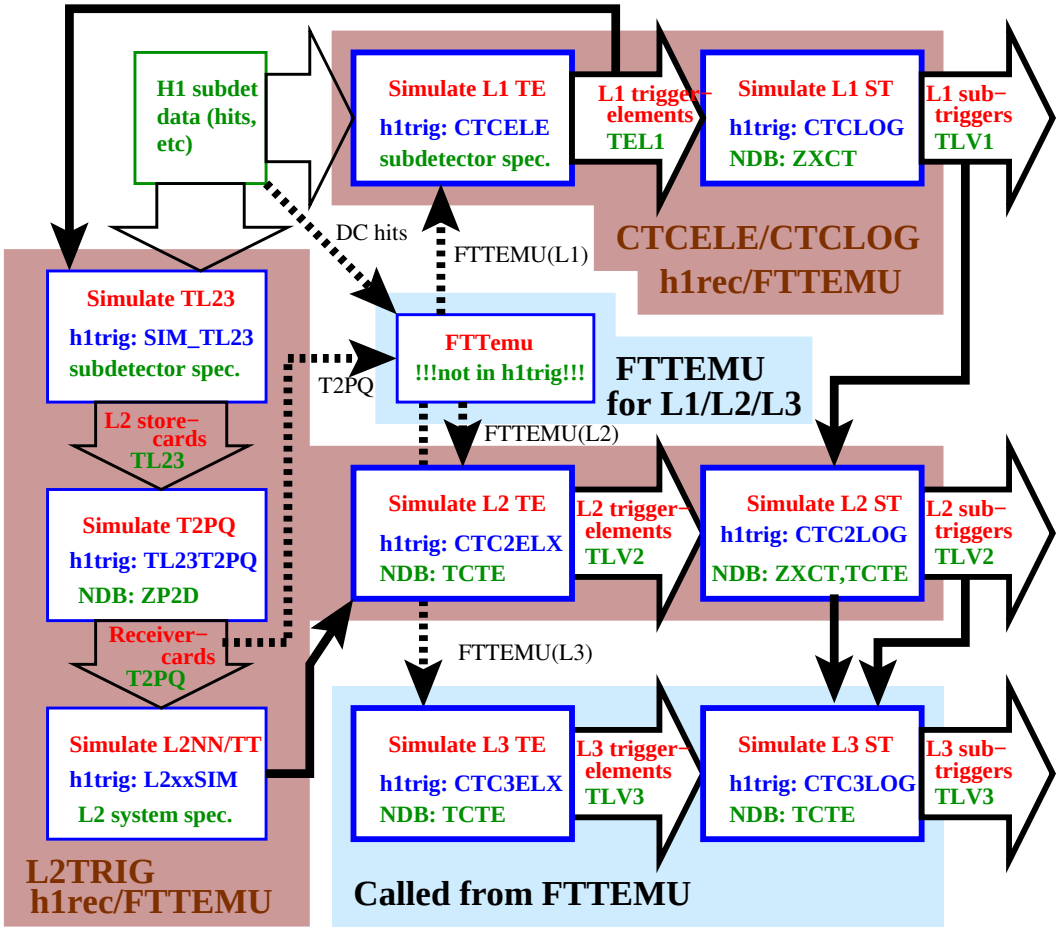

Figure 14.5.: *Sketch of the H1 trigger simulation based on input BOS banks from the H1 detector simulation and reconstruction indicated by the upper left box. The standrad data flow is indicated by the solid arrows whereas the new trigger information and its processing*

grate `fttemu` in `h1trig` at least at times when memory was still expensive and limited. Although nowadays this memory restriction is not present any more, an integration was not done because of the necessary major re-design of the `fttemu` program.
As FTT conditions are used in almost all major production triggers of H1, it is highly desirable to have a automated procedure for the integration of `fttemu`. The solution that was chosen is that every MC sample is post-processed by `fttemu`; a new program takes care of the correct re-simulation of the H1 trigger simulation in order to account for FTT trigger decisions at all three levels. The work that was completed in the scope

of the present thesis is the implementation of the necessary tools and routines for the `fttemu` post-processing as discussed in the following.
Figure 14.5 shows the data flow for the `h1trig` software (database banks are indicated by NDB). The solid lines together with the dark shaded boxes indicate the `h1trig` simulation for the standard MC processing scheme without incorporating the FTT information. The post-processing scheme involves the `fttemu` program as indicated by the light shaded boxes together with the dashed lines. Afterwards part of the `h1trig` routines (`L2trig`,`Ctcele/Ctclog`) are called in order to update all subtrigger information, which use FTT trigger conditions.
The post-processing is tested with MC samples in order to check for the correct re-

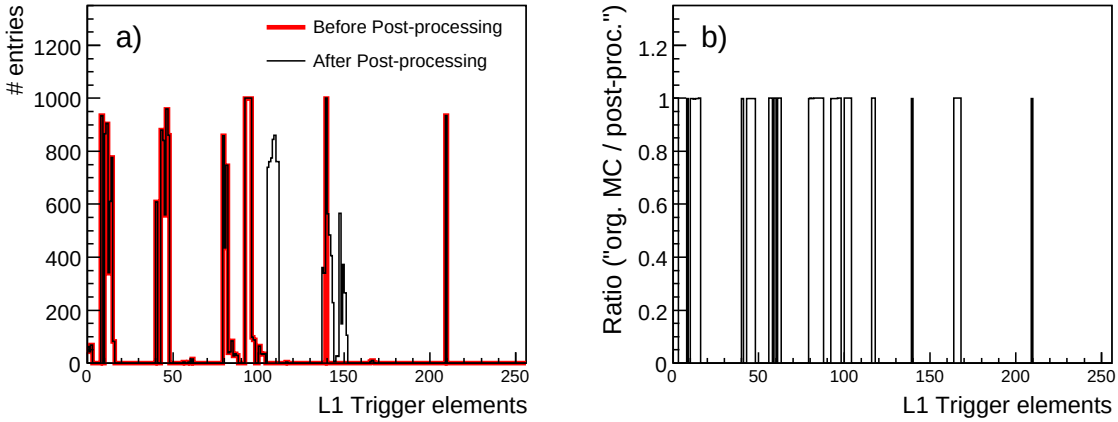

Figure 14.6.: *Shown is the distribution of the L1 triggerelements in MC before and after the post-processing a) and ratio of the two MC samples b) where non-FTT trigger elements are not allowed to change.*

simulation of the `h1trig` simulation. Figure 14.6 shows the distribution of L1 trigger elements a) for not post-processed events (thick line) and post-processed events (thin line). The level one FTT triggerelements are defined from $104 - 111$ and $136 - 151$. Trigger elements, which do not contain FTT conditions are not allowed to change, as illustrated by the ratio of not post-processed events divided by post-processed events b). For the level two system not only the FTT level two trigger elements have to be updated but also L2 trigger systems (L2NN) have to be re-simulated as L2NN uses FTT level one trigger elements as input. The correct re-simulation of the L2NN system is demonstrated elsewhere [Jun07]. For the FTT level three trigger elements the situation is rather easy as there are no other L3 systems in the H1 trigger system. Therefore FTT L3 trigger elements simply appear after the post-processing of the MC samples in the official banks. This is cross-checked with the FTT internal trigger decision that is sent to the CTL [Jun07]. The completed implementation of the post-processing within `fttemu`, by using also additional `h1trig` code, works reliable, fast and increases the output only by 20%. Thus the implementation of the presented post-processing scheme for MC is also applied for the H1 MC production within the grid.

15. The Level three system

The H1 trigger system is designed such that a L3 decision is able to abort the readout of the whole H1 detector (see section 3.5). In order to profit in terms of rate reduction the L3 decision has to be faster than the read-out time otherwise the abort of the read-out does not pay off. Because of the linear correlation with the accumulated dead time the decision time should be as short as possible. Constraints due to a fixed available rate budget originating from the tracker frontend systems require large reduction factors, whilst keeping a high efficiency for physics signals of interest. The optimal way to ensure this goal for many different processes is realised by a partial on-line track based event reconstruction that considers also information from other detector subsystems for better selectivity.

Key Technologies

Technically this was achieved by a farm of PowerPCs running in parallel where each PowerPC executes one algorithm[1] for a physics signal of interest. In order to fulfill these requirements within the latency of about 100 μs a fast distribution and processing of the data is needed. In summary the key technologies for the FTT level three system are briefly discussed as follows:

Real Time Operating System, RTOS A Real Time system ensures predictable and deterministic response times for the processing of an event together with a minimal latency. The advantage of RTOS based systems is the use of a priority based task scheduling whereas standard OS typically use a „first come first serve“ policy. Thus standard OS do not guarantee that high priority threads[2] will be executed in preference to lower priority threads, which in contrast is guaranteed by a RTOS. Moreover the chosen Tornado RTOS vxWorks [Win99] protects against task inversion, i.e. a low priority thread blocks a high priority thread from accessing the CPU.

Computing power An on-line track based invariant mass calculation demands large computing power for events with high multiplicity, for example for a three track final state more than $1 \cdot 10^5$ combinations have to be calculated. For a trigger system it is enough to identify a first interesting candidate, which is reflected in the general concept of L3 such that the calculations are terminated after the first valid candidate. In order to provide the necessary computing power within the

[1] Or two if the latency allows a second one.

[2] A Thread enables a program to split itself into two or more (pseudo-) simultaneously running tasks.

L3 latency of about 100 μs for the calculations it was decided to use PowerPCs[3] [Nau03].

Front Panel Data Port, FPDP Because of the short L3 decision time a fast data distribution within L3 is the most important design goal. The FPDP link provides the ability to transfer the data simultaneously to all connected PowerPCs realised by the FPDP point-to-multipoint protocol. Thus data transmission times via the FPDP link of approximately 10.35 μs are achieved (see section 15.1).

15.1. The Hardware Implementation

The hardware of the third trigger level [Nau03; Jun04] consists of five (extendable up to 16) finally implemented commercial standard VME PowerPCs [Mot00] operated with the real time operating system vxWorks [Win99]. Thus the key factors for the L3 software design which are a minimal interrupt latency and a short thread switching latency are fulfilled. A schematic overview of the L3 system is illustrated in figure 15.1.

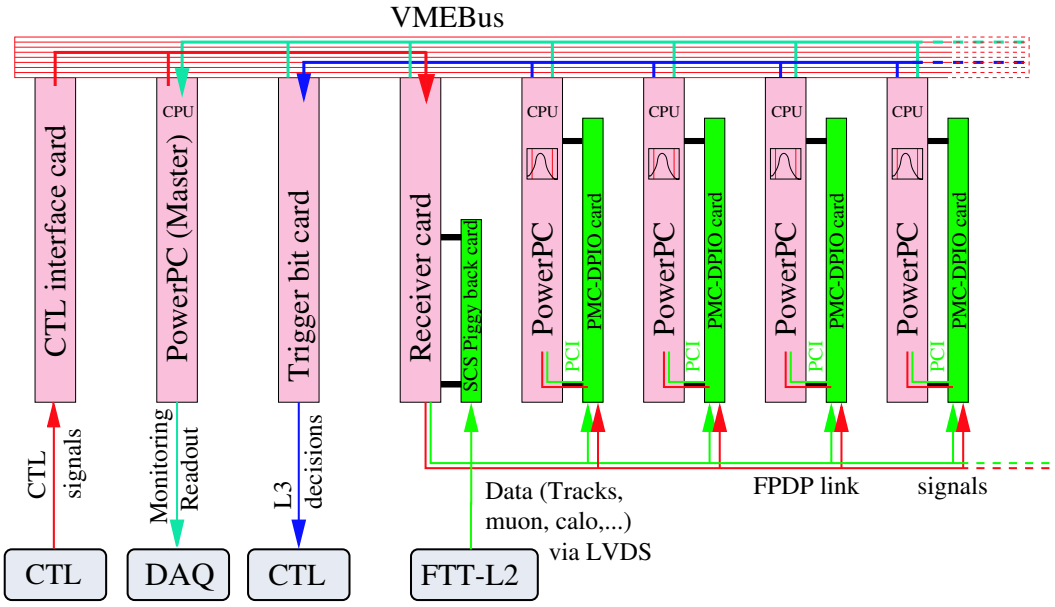

Figure 15.1.: *Schematic view of the L3 system with the data and signal lines. For a detailed description of the implemented cards see text.*

The previously described input data are received on a LVDS channel link interface card (*SCS piggy back card*, [SCS]) attached to a custom made receiver board (*receiver card*). The receiver card utilising a single FPGA (Altera EP20K400) receives and buffers the L2 data. From the L3 receiver card the data are distributed to all PowerPC cards via a 20 MHz FPDP (Front Panel Data Port [ANS98]) link (640 Mbit/s) using commercial *PMC-DPIO cards* (PCI Mezzanine Cards [IEE]) attached to the PowerPCs.

[3] Alternative concepts with utilising FPGAs have not been realised due to the size limitation at that time, such that only low multiplicity events could be computed. Nowadays one would possibly choose the processing power of graphics cards providing a better environment for such problems.

The advantage of the FPDP link is the ability to transfer the data simultaneously to all connected PMC-DPIO cards. The total amount[4] of data per event amounts to 207 words (see section 15.2) corresponding to a data transmission time via the FPDP link of approximately 10.35 μs. The shortness of this transfer time is a key parameter of the L3 system as the whole decision time is about 130 μs. The PowerPCs execute dedicated selection algorithms to derive trigger decisions. The communication with the central trigger is done with two dedicated input/output cards labelled as *CTL interface card* and *trigger bit card*. One so-called *master* VME PowerPC controls and readout the L3 system allowing off-line data consistency checks.

The PowerPCs

The L3 system uses one master and up to 16 *slave* PowerPCs, see figure 15.2, for the calculations. They are implemented as A32/D32 VME cards and possess a MPC750 (32 bit) PowerPC G3 processor with 450 MHz and 32 MB memory (Motorola MVME2400, [Mot00]). A 10/100 MBit/s ethernet interface is implemented. In order to allow fast and convenient boot procedures the PowerPCs have a FlashROM where the kernel of the operating system is deposited.
The hardware architecture [Mot97] of these PowerPCs provides the flexibility that is

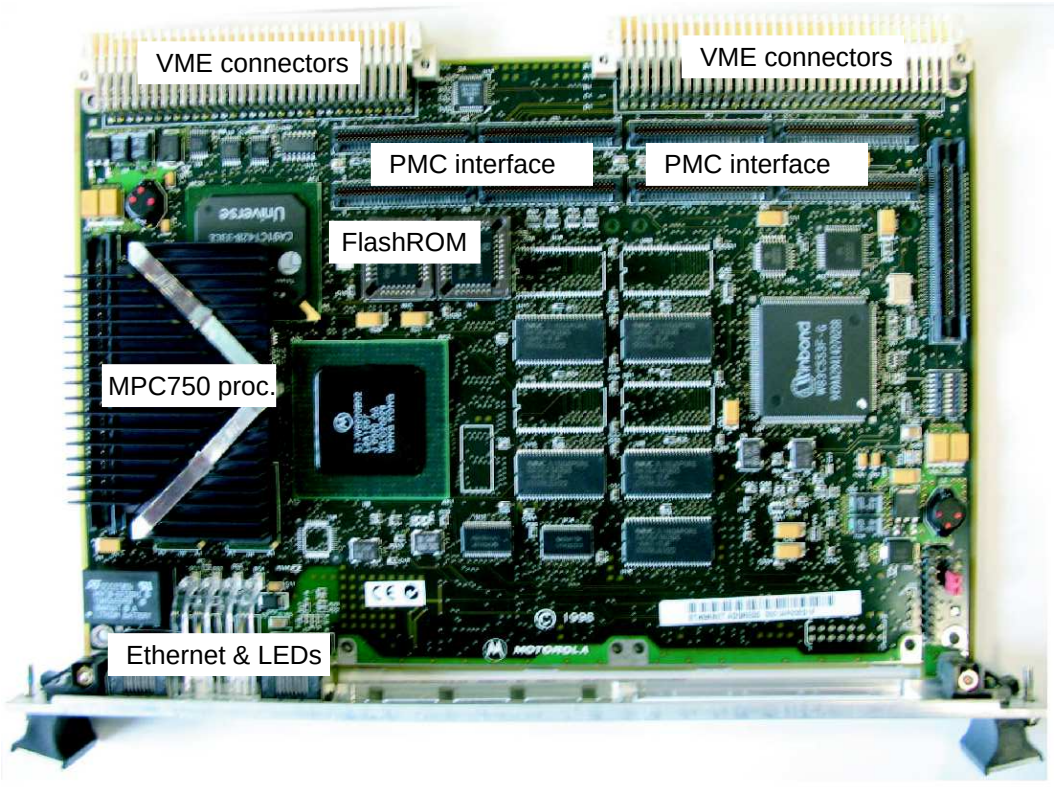

Figure 15.2.: *A picture of a PowerPC board, which can carry a PMC-DPIO card for data reception, as utilised for the L3 system. The different components are labelled and shortly described in the text.*

[4]For 48 fitted L2 tracks.

needed for the realisation of the L3 system. Namely the use of PMC-DPIO cards and the use of the FPDP link as described in section 15.2 demands free configurable transmission schemes. These schemes also imply the use of VME and PCI interrupt lines, which are also configurable as desired. For measuring program execution times the PowerPC has a counter which is incremented every fourth CPU cycle corresponding to a resolution of 40 ns.

The Receiver Card

The L3 receiver card is a standard VME mainboard utilised for the data buffering and carrying a LVDS piggy back card as L2-L3 interface (SCS piggy back card). The receiver card is implemented as a A24/D32 VME card and acts as buffer and main interface between the L2 system, which uses 100 MHz LVDS channel links for the data distribution and the L3 PowerPC farm using the 20 MHz FPDP link. The data received from the SCS piggy back card are buffered in a large FPGA (Altera 'APEX20K400'). The chosen FPGA provides enough space for embedded FIFOs, which are utilised to decouple the different transfer rates. The buffered data are transmitted via the FPDP link using the FPDP protocol, which is also implemented in the FPGA of the receiver card. The FPDP protocol is realised with different signal standards. For the L3 system TTL was chosen.
A schematic view of the custom made receiver card with its embedded chips and connectors is illustrated in figure 15.3. To ease commissioning a Joint Test Action Group (JTAG) interface and LEDs are implemented. For the reception of the incoming data the receiver card possesses a PMC interface, which is used by the SCS piggy back card is equipped with LVDS connectors and a FPGA. The FIFO of the SCS piggy back

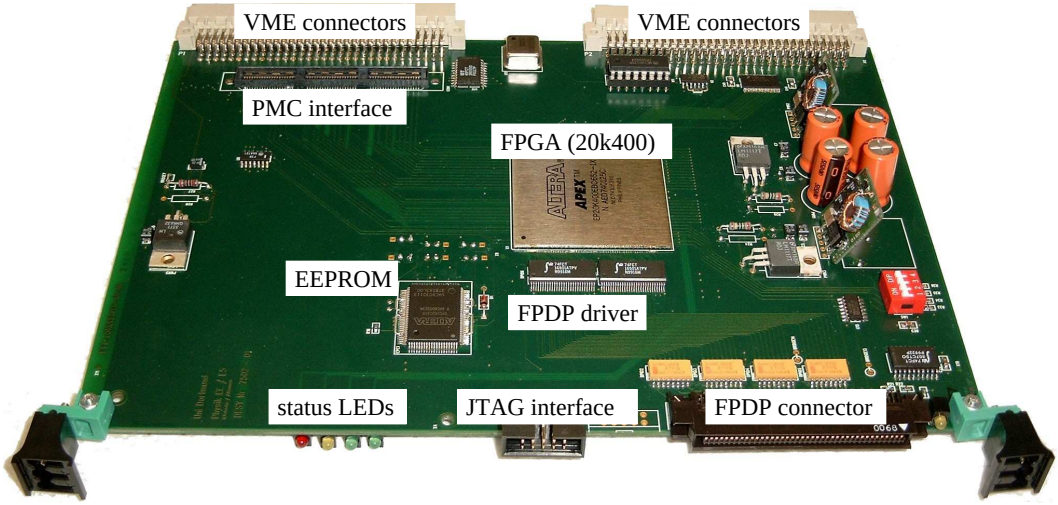

Figure 15.3.: *A picture of the L3 receiver card as developed for the L3 system. The different components are labelled and described in the text.*

card is clocked with 40 MHz and buffers the data sent at 100 MHz via the LVDS link. A SCS piggy back card to receiver card data transmission protocol using 48 data lines and up to 12 control lines is implemented.
The details of the programming for the FPGA of the receiver card is discussed in detail

elsewhere [Jun04]. Implemented are a LVDS-FIFO where the data from the SCS piggy back card is stored with a rate of 40 MHz. A second FIFO (VME-FIFO) which is readable and writable via VME is utilised for the readout of the receiver card. The 16 bit wide header (see table 15.1) of the event data provides a filter possibility before filling the FIFOs. This header is stripped off at the receiver card and only the 32 bit wide data are processed and flushed to the FPDP bus. Flushed data are compared to a predefined EOT pattern to identify the end of data transmission. Moreover the receiver card produces control signals: the EOT signal released with the last data word of the event data and two reset signals. The EOT signal uses one of two reserved lines (RES1, [ANS98]) which are synchronous to the data transfer, while the reset signals use programmable I/O lines (*PIO*) which are asynchronous to the data transfer.

The PMC-DPIO card

The PMC-DPIO card where *DPIO* stands for Digital Parallel Input/Output is connected via a PMC connector to the PCI bus of the PowerPC. For the L3 system the input configuration is utilised to receive the data transmitted by the receiver card and to buffer the data in a FIFO. During commissioning also the output configuration was used.
The PMC-DPIO card produces PCI interrupts which are seen by the CPU of the slave PowerPC. The connection to the PCI bus allows a Direct Memory Access (DMA) transfer between the FIFO of the PMC-DPIO card and the memory of the slave PowerPC. The PMC-DPIO card provides a variety of configurations for the DMA transfer and the interrupt handling. The interrupts implemented are the control signals from the receiver card and an interrupt that is generated if the first word of the event data in the FIFO is received. The data are only written to the FIFO if there is a DVALID signal synchronous to the data that is sent by the receiver card. The EOT signal is converted to an EOT interrupt. For monitoring purposes several other interrupts encoding the fill level of the PMC-DPIO card FIFO (empty, half-full, full) are implemented. The FIFO of the PMC-DPIO card has a depth of 8000 words, which has to be compared to the maximal amount of data expected from L2 of about 210 words.
Due to the DMA the CPU is not involved during the data transfer and is able to perform other tasks increasing the overall performance. The configuration is chosen such that the first word of the incoming data on the PMC-DPIO card triggers an interrupt, which signals the slave PowerPC to start the DMA transfer to its memory. The destination address for the data transfer is written to the configuration RAM of the PMC-DPIO card. The DMA transfer stops if the EOT interrupt is received or the expected maximum length of the event data is reached.

The CTL Interface Card and the Trigger Bit Card

The communication to the central trigger is done by a custom made CTL interface card and the trigger bit card [Lap06]. The trigger bit card is implemented as a standard A24/D32 VME card and provides in total 48 bits which are set individually via VME. A possible L3 decision is accompanied by a strobe signal in order to inform the CTL that the decision of the L3 system is indeed valid for the processed event. The L3 decisions are than utilised at the CTL to derive the global L3Keep or L3Reject signal

that is fanned out to all detector subsystems. In the rare cases where a decision is not fast enough a default CTL decision is made depending on the implemented trigger.
The CTL signals L3Keep and L3Reject going to the L3 system are received by the CTL interface card and translated to VME interrupts seen by the master PowerPC. These signals are distributed via the receiver card to the connected slave PowerPCs.

15.2. Input Data & Processing

The L2 decider forwards the data in a fixed data transmission scheme via an LVDS [Nat00] channel link (5 Gbit/s) operated with 100 MHz to the L3 system. The transmitted data contain the L2 fitted track parameters, the reconstructed z vertex position and L1 trigger information from other detector systems (PQZP data). The L3 system utilises information from the calorimeter and muon system. The calorimeter system delivers sorted information about the 16 highest energy depositions in the calorimeter whereas the muon systems delivers information about the 64 possible modules containing a muon candidate. The track information is utilised to reconstruct particle resonances and with the additional information from other detector systems a particle identification is performed.
For the communication between L2 and L3 a protocol was implemented considering the implications given by the L3 hardware design. The data are transmitted with 48 bit words in one block consisting of severall sub-blocks taking into account the different data types. In order to identify the sub-blocks a sub-block header word is used as described in table 15.1.
All 48 bit words contain a 32 bit data word accompanied by a 16 bit header word

header bits	data bits	comments
0xCF90	0xCF90 000N	z vertex header
0xCF9z	value	z vertex data (z=zvtx type)
0xCF8m	0xCF8m 000T	track header (m=modus)
0xC8pi	value	track data (p=track parameter)
0xCF2F	CF2F 000u	PQZP header (u=number of blocks)
0xCF2b	CF2b 000K	PQZP subheader (b=PQZP type (< 15))
0xC2bj	value	PQZP data (b=PQZP type (< 15))
0xCFFF	0xEEEEEEEE	end of transfer

Table 15.1.: *The data formation of the L3 input data implemented for the L3 protocol (48 bit wide transmission) which consists of* 16 *bit wide header words and* 32 *bit wide data words. The capital italic letters* N, T, K *denote the total amount of words of a certain data type, e.g.* T*=number of data words. Small italic letters* i, j *symbolise counters for the individual data types with the exception that* u *labels the number of transmitted PQZP blocks.*

encoding the data type and a counter. The sub-block header word itself contains also the type and the amount of data in the sub-block. The end of a sub-block is therefore given by the amount of data plus one where the next sub-block header word is placed.

The end of the whole data block is marked by a special *end of transfer* pattern (EOT). With this transmission protocol a fixed amount of 54 words of PQZP information is transmitted whereas the track information sub-block is of the length of the actual number of fitted L2 tracks per event. The FTT tracks are encoded in different modes m, where e.g. for $m = 2$ each track is represented with three 32 bit float words. Moreover a z vertex word is sent that encodes the event z vertex. Thus the total amount of data per event is given by: $N(\text{PQZP}) + N(\text{z vertex}) + 3 * N(\text{track})$ with additional 8 sub-block header words to identify the different data types (see table 15.1). In the case of the maximal 48 fitted L2 tracks the total amount of transferred data per event is 207 words.

Data Distribution

For the data transfer from the receiver card to the slave PowerPCs a L3 protocol as described in table 15.2 was defined. This L3 protocol utilises the control signals of the receiver card and the formatted data structure introduced in table 15.1. As explained

control lines	header + data bits	IR from PMC-DPIO card	answer of slave PowerPCs
DVALID	0xCF90 CF90 000n	FIFO not empty (FNE)	first word starts DMA
add. RES1	0xCFFF EEEEEEEE	end of transfer (EOT)	last word terminates DMA
PIO1	pulse	Abort	abort all routines (L3Reject)
PIO2	pulse	Prepare	prepare routines for event

Table 15.2.: *The L3 protocol as implemented for the data transmission between the receiver card and the slave PowerPCs. The formatted data structure is introduced in table 15.1.*

before the receiver card strips off the 16 bit wide header (see table 15.1) and sends only the 32 bit wide data via the FPDP link to the PMC-DPIO cards. The first word of the event data starts the data processing of the slave PowerPC. The end of the event data is marked by the EOT signal, which is issued if the pattern comparison done by the FPGA of the receiver card is true. As part of the FPDP protocol every valid data word that is flushed to the FPDP link is accompanied by a DVALID signal synchronous to the transmitted data word. Only data accompanied by a DVALID signal are written to the FIFO of the PMC-DPIO card.

Processing of Data

In the following the data processing of the PowerPCs is described including all routines that are necessary to transfer the data from the FIFO of the PMC-DPIO card to the memory of the slave PowerPC, to prepare the data and to finally derive the trigger decisions. A whole test data processing scheme was finished during the development [Nau03] but it turned out during the commissioning that this scheme was not flexible enough to account for the meanwhile modified requirements. Thus this scheme took too much time in order to initialise the system and run efficiently the data processing. For the final L3 commissioning completed in the scope of this thesis a re-design of the system initialisation and data processing scheme was done.

The data processing developed is divided into three subsequent *steps* which consist of several threads:

1. the data transmission step,
2. the preparation step,
3. the selection step.

The data transmission step contains the reception of the L2 data and the data distribution within the L3 system and uses hardware protocols for the FPDP link and the DMA transfer.
The preparation and selection steps are software based utilising severall threads. A function call takes approximately 1 μs which demands a design with a minimum number of threads involved. The inter-process communication and synchronisation between the threads is implemented by special signals called semaphores which are provided by the real time operating system. A semaphore has – to first approximation – two different states, *locked* or *unlocked*, and is able to control threads with different priorities as implemented in the three processing steps. In addition they guarantee a fast and

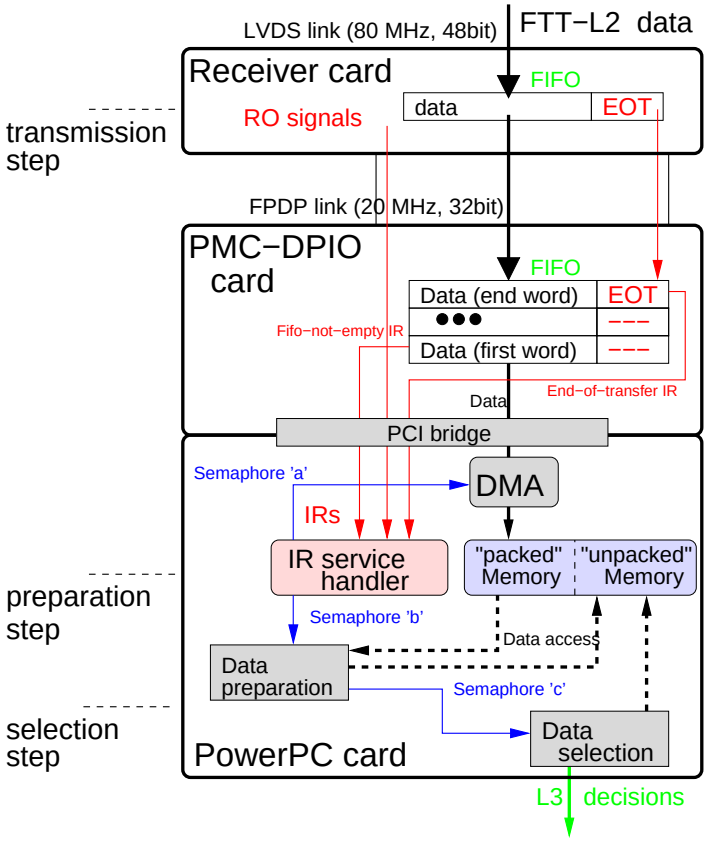

Figure 15.4.: *Schematic view of the data transmission and processing within the L3 system from the receiver card to the PMC-DPIO card and finally to the PowerPC. The semaphores are part of the inter-process communication of the threads used in the software of the PowerPCs.*

prompt answer to interrupts necessary to ensure decisions within the L3 latency.
A detailed sketch of the data processing and signal handling is illustrated in figure 15.4. The reception of the first word of the L2 event data by the FIFO on the PMC-DPIO card is indicated to the CPU of the slave PowerPC via an interrupt. If this interrupt is issued semaphore 'a' is released which starts the DMA transfer from the PMC-DPIO card to a dedicated memory address (packed memory) of the slave PowerPC.
On the reception of the EOT signal another interrupt is delivered by the PMC-DPIO card. This causes the slave PowerPC to release semaphore 'b'. As the signal marks the end of the event data the DMA data transfer is stopped and the preparation of the event data starts. First the slave PowerPC performs a block consistency check of the transmitted data. The sub-block header words are used to classify the data words according to their source, i.e. is it track data from L2 or data from other subdetectors. Data structures are allocated in an unpacked memory of the slave PowerPC and contain the different data types. These structures are filled in the preparation step and contain muon data, calorimeter data and the track parameters with derived quantities, like p_x, p_y, p_z of the tracks. In order to reduce the preparation time Taylor approximations for trigonometrical functions are implemented. As soon as the data preparation has finished the last processing step is released by semaphore 'c'. The selection step executes the different selection algorithms. The first two processing steps are identical on every PowerPC whereas the third processing step is specific and contains physics selection algorithms of which examples are discussed in section 15.4.

Optimisation of the PowerPC Configuration

One of the key technologies of the L3 system is the use of a RTOS system, which implements a priority based task scheduling. The default priorities defined for the threads

Scheme of priorities	Subject of task	Assigned priority	
		old	new
FTT_L3_SLAVE_PRIO_EXIT	shutdown	50	30
FTT_L3_SLAVE_PRIO_FAST_RESET	Event Prepare	110	32
FTT_L3_SLAVE_PRIO_SLOW_RESET	L3Reject	120	34
FTT_L3_SLAVE_PRIO_DMA_START	DMA transfer	150	40
FTT_L3_SLAVE_PRIO_BLOCK_IN	prepare data	150	45
FTT_L3_SLAVE_PRIO_PHYS	physic finders	180	48
FTT_L3_SLAVE_PRIO_RO	readout	160	100

Table 15.3.: *The values of the priorities, which are assigned to the tasks of the threads of the implemented data processing scheme as described in section 15.2, are listed before the optimisation and afterwards.*

(possibly consisting of several tasks) of the L3 data processing as described previously are summarised in table 15.3 together with the optimised ones. The optimised values were derived from the fact that e.g. a simple network check of the CPU is less important than trigger routines and thus a lower priority for not severe CPU owned tasks was assigned. In order to check the optimised values of the priorities the following was done. The CTL readout provides an additional readout of the L3 trigger decisions that

came in at $t = 400$ μs and not within the L3 latency of about 130 μs, by that these are so-called *late* trigger decisions. The amount of these late decisions is completely negligible as it is by far smaller than the total number of processed events. Nevertheless it shows up partially for the D^* finder as will be discussed in section 15.5. The amount of late trigger decisions in bins of short run ranges is illustrated in figure 15.5. One can clearly see an improvement in the amount of late decisions around run number 490000, where the optimised task priorities were implemented. However, there are many structures in the distribution, which are partially due to the vacuum and beam conditions, as they influence the average event multiplicity, which directly increases the computational effort for L3. Nonetheless, if the distribution of the late decisions is

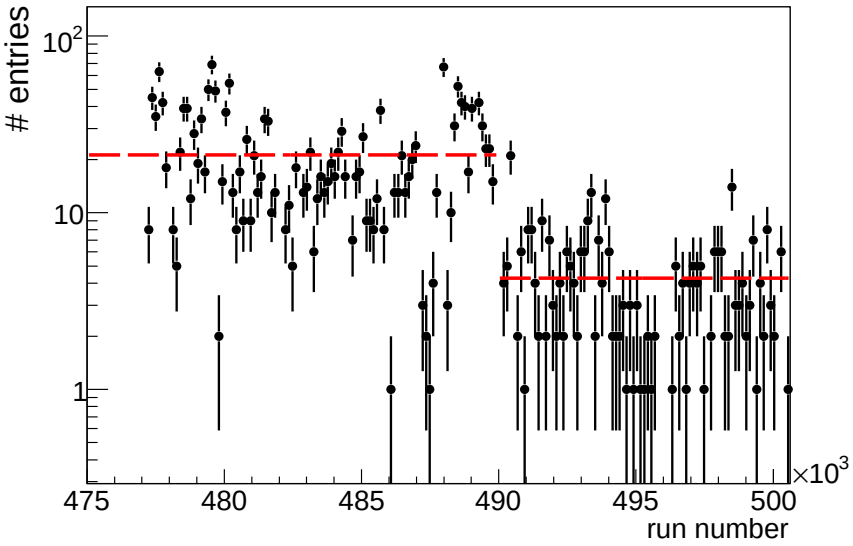

Figure 15.5.: *Distribution of so-called late L3 decisions with increasing run numbers. The clearly visible step correspond to improvements due to re-shuffling of CPU priorities assigned to the threads of the data processing.*

simply averaged before the optimisation, 21.3 ± 0.1 late decisions are observed, while after the optimisation only 4.3 ± 0.1 events are observed. This is a reduction of a factor 5 with the optimised CPU priority setting and furthermore allows the conclusion that the amount of late decisions is dominated by the priority scheduling of the PowerPCs and not by the termination behaviour of a physics algorithm.

15.3. The Readout

The readout of the L3 system splits up into three parts: there is the global H1 detector readout to which also the LAN based FTT readout belongs and there is the internal L3 readout implemented within the scope of the thesis. The implementation of the FTT readout is described in detail in [Boe07] and the readout time is illustrated in figure 15.7a) for completeness. Each of the six existing FTT crates consists of one master PowerPC, which reads out the individual cards in this special crate.

The internal readout of the L3 system is done by the L3 master PowerPC, which gathers the data from the different L3 cards by reading different VME registers (address space: A16, A24 or A32) and is itself readout by the FTT master PowerPC. A sketch of the L3 readout is depicted in figure 15.6. One basic design concept of the L3 readout was the incorporation of the slave PowerPCs. As they terminate their calculations at different points in time, the readout can only start if a slave PowerPC has terminated. In order

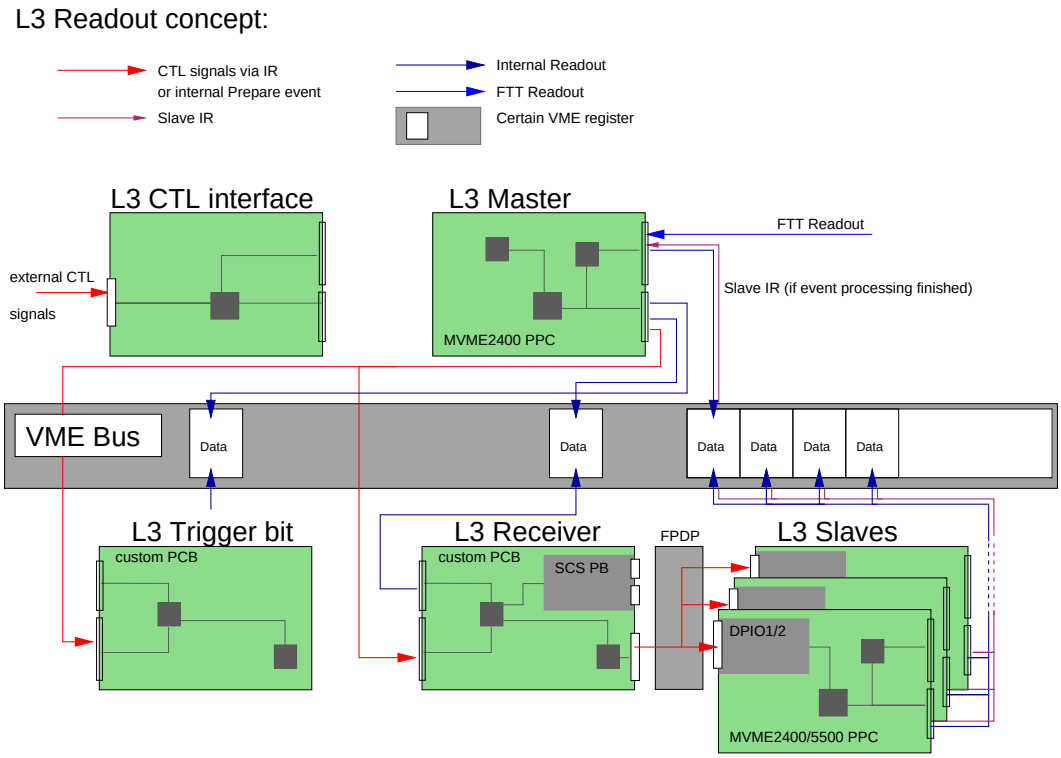

Figure 15.6.: *Sketch of the L3 readout which is part of the FTT readout. The L3 master PowerPC reads out the different cards (slave PowerPC, receiver card, etc.) via VME. Exceptional are the slave PowerPCs which are readout on the reception of an RO-IR sent by the slave PowerPCs.*

to distinguish the up to 16 slave PowerPCs a dedicated memory area that is called *user memory* and identified by the slave processor number is mapped to VME. With the end of the selection step the slave PowerPC copies all relevant data in a formatted BOS bank structure to the user memory. Afterwards the slave sends an interrupt via the VME backplane that is acknowledged by the master PowerPC where the interrupt vector comprises the slave processor number. Thus the master is informed which slave, i.e. user memory, has to be readout.
The implemented BOS banks comprise the information from the individual L3 cards as listed in the following:

TT3R Contains the raw data as receipt within the receiver card from the FTT L2 system including the information from the systems connected via the PQZP bus (Calorimeter, Muon, SPACAL, CTL L1).

TT3T Contains only the raw track parameters as received on the slave PowerPC (de

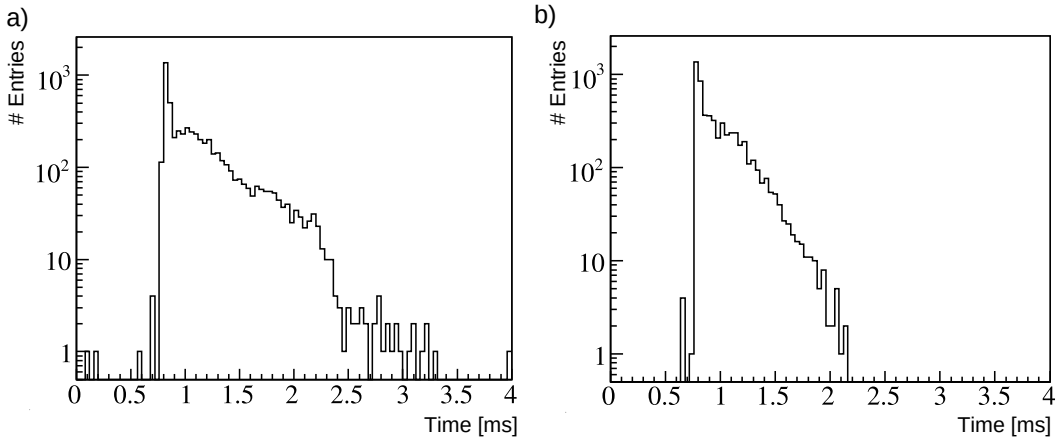

Figure 15.7.: *The total readout time a) of the FTT system done by the FTT master PowerPC and the readout time of the whole L3 system b) measured by the L3 master PowerPC.*

facto a copy of the TT2T at L2). Bank was written by one slave PPC after ensuring correct data transfer.

TT3D Contains all pre-calculated input parameters to the physics finders (largest bank) and was written during commissioning or tests for all slave PPCs.

TT3M Contains the calculated mass or particle hypothesis on which trigger decisions take place. This bank is written for every slave PPC.

TT30 Contains the up to 48 trigger bits as sent to the CTL by the trigger bit card.

The total standard[5] readout size is approximately $1,200$ words corresponding to 4.8 kB per slave PowerPC and event. Moreover a complete readout, which includes all input data (TT3D) to the physics algorithms, consists of more than $4,000$ words (16 kB) and was only done for consistency checks during commissioning. The L3 read-out time distribution is illustrated in figure 15.7b) with an average time of about 1.0 ms.
If the readout is aborted by the CTL due to the L3Reject signal, the master sends an abort signal to the receiver card which distributes it to the slave PowerPCs via the PIO lines of the FPDP bus. This puts all data processing threads of the slaves to the ready state and re-initialises the transmission scheme between the receiver card and the PMC-DPIO card. The re-initialisation process takes $12-16$ μs which is fast enough as the next event data after an aborted event comes earliest after the L2 latency of about 20 μs. A shortened initialisation process is also done after every L3Keep in order to have a defined system state before reception of the next event.

On-line Monitoring

The FTT L3 system was developed such that no further manual interaction after a reboot was needed in order to set-up the system. All routines are initialised depending

[5]The standard readout BOS banks are all banks except for the TT3D.

on the slave processor number. The report of success of the integration of L3 cards and other valuable information was transmitted to a GUI [Ber07]. As an example the logging window is depicted in figure 15.8, which contains some messages from the five implemented slave PowerPCs. The logging system was based on message queues

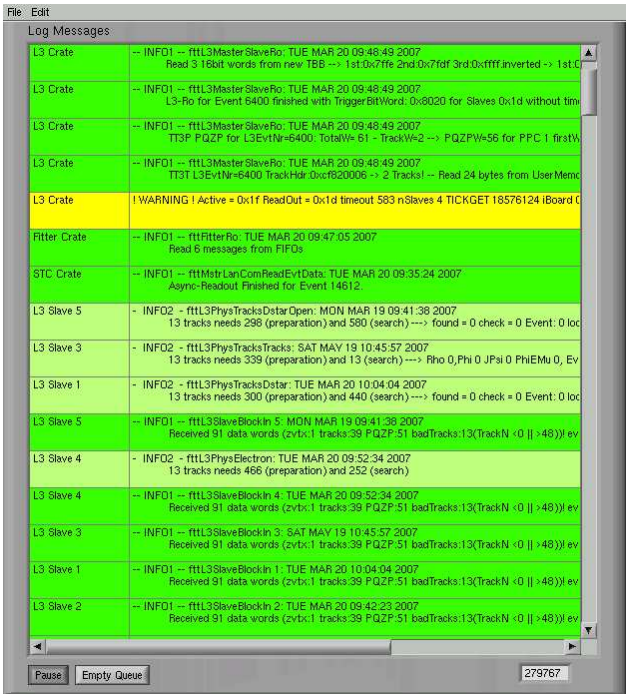

Figure 15.8.: *The on-line monitoring of the L3 system (and the whole FTT) was based on a GUI [Ber07] and a complex message system to connect all pieces of hardware to the GUI.*

in order to decouple a slave PowerPC calculating trigger decisions from the message system. Otherwise the short latency of trigger decisions would have been distorted considerably. The readout of the L3 system was steered with the GUI that allows to switch the different banks described in section 15.3 simply on or off.

15.4. Physics Algorithms

The L3 system utilises various selection algorithms[6] to identify rare processes on-line which contain c- and b-quarks. The following selection algorithms were implemented:

- D^* & inelastic J/ψ mesons with different p_T thresholds
- diffractive vector mesons
- electron & muon identification .

[6]Modifications to the executed selection algorithms and cut parameters are documented by version numbers.

The first three selections are purely track based, while the last two selections use L1 trigger informations from the calorimeter and muon systems. The selection algorithms use the prepared data (see section 15.2) and furthermore each selection algorithm use additional quantities calculated before the selection. Moreover the selection algorithms are optimised in a way that square root terms are avoided by squaring equations or Taylor approximations adopted wherever possible. All selection algorithms are implemented in `C` code and utilised as on-line (trigger) and off-line (simulation) version. Such the off-line verification of the FTT trigger decision in data as well as FTT trigger simulations (see section 14.1) are easy possible.
In the scope of this thesis different D^* and J/ψ finders were implemented[7]. However, as they both are based on invariant mass calculations the more complex one, the identification of D^* mesons, is discussed here as an example in the following. A short summary that describes the basic principles of the electron and muon identification is added.

Identification of D^* Mesons

D^* mesons are selected in the so-called golden decay channel ($D^{*\pm} \rightarrow D^0\pi^{\pm}_{\text{slow}} \rightarrow K^{\mp}\pi^{\pm}\pi^{\pm}_{\text{slow}}$, see figure 15.9), which is fully reconstructed from three charged particles. For the on-line identification of D^* mesons no particle identification is applied, thus full

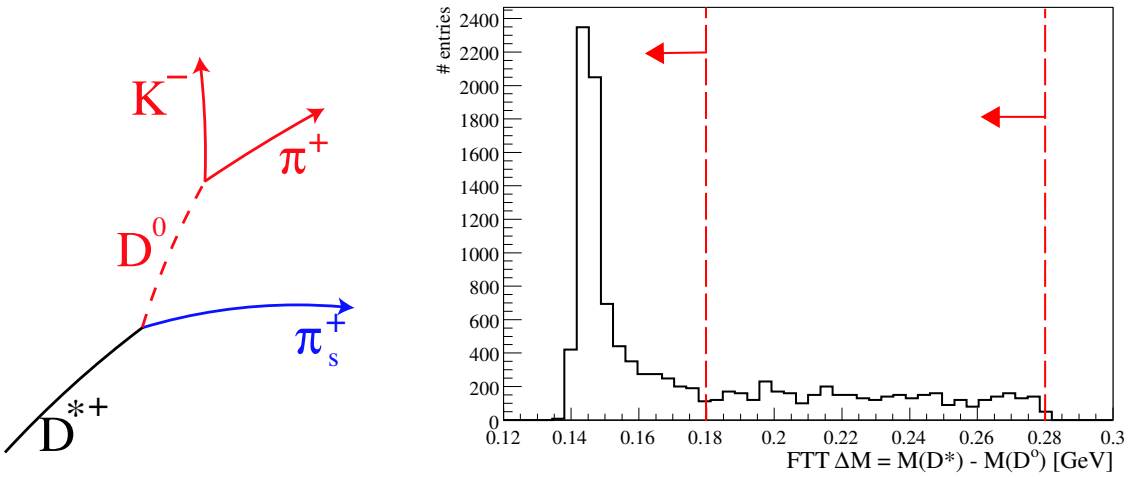

Figure 15.9.: *The so-called golden decay channel a) of the D^* meson. The FTT ΔM distribution b) for D^* candidates for a PYTHIA MC sample.*

combinatorics has to be taken into account. However, the combinatorial background is reduced by first reconstructing the D^0 candidate and afterwards the D^* candidate. The ΔM method applied here follows the same principles as done at the L4 trigger and is described in detail in chapter 5. The difference is that the cuts applied on transverse momenta and invariant mass windows at the FTT L3 level are even weaker than the ones applied in the L4 trigger system.
A simulated FTT ΔM distribution, derived from a PYTHIA signal D^* MC sample,

[7]The diffractive vector meson finder has finally not used because the rate reduction provided by FTT L2 was large enough.

is depicted in figure 15.9 together with two dashed lines indicating different ΔM cuts of $\Delta M < 0.180$ GeV and $\Delta M < 0.280$ GeV. If a candidate passes all cuts a positive trigger decision is sent to the central trigger. Otherwise the next possible track combination is tried until all possible track combinations are tested.
Three D^* triggers were setup, which use different $p_T(D^*)$ thresholds and ΔM cuts: A D^* trigger with a $p_T(D^*)$ threshold of 4.5 GeV together with a ΔM cut of $\Delta M < 0.280$ GeV (high $p_T(D^*)$ trigger) and two with a common ΔM cut of $\Delta M < 0.180$ GeV but different $p_T(D^*)$ thresholds, namely $p_T(D^*) > 2.5$ GeV (medium $p_T(D^*)$ trigger) and $p_T(D^*) > 1.5$ GeV (low $p_T(D^*)$ trigger). All three D^* conditions implement the same D^0 mass window of $|M(D^0) - 1.8645| < 0.180$ GeV and use additional p_T cuts on the transverse momentum of the three decay particles (see [Jun06] for the details).

Identification of Electrons

The L3 electron identification [Cam06] is designed to trigger electrons with energies as low as 1.2 GeV, much lower than the threshold of the standard H1 inclusive electron triggers of about 5 GeV implemented at L1. Thus the access to electrons stemming from decays of low momentum b-quarks is possible. Therefore the FTT track informa-

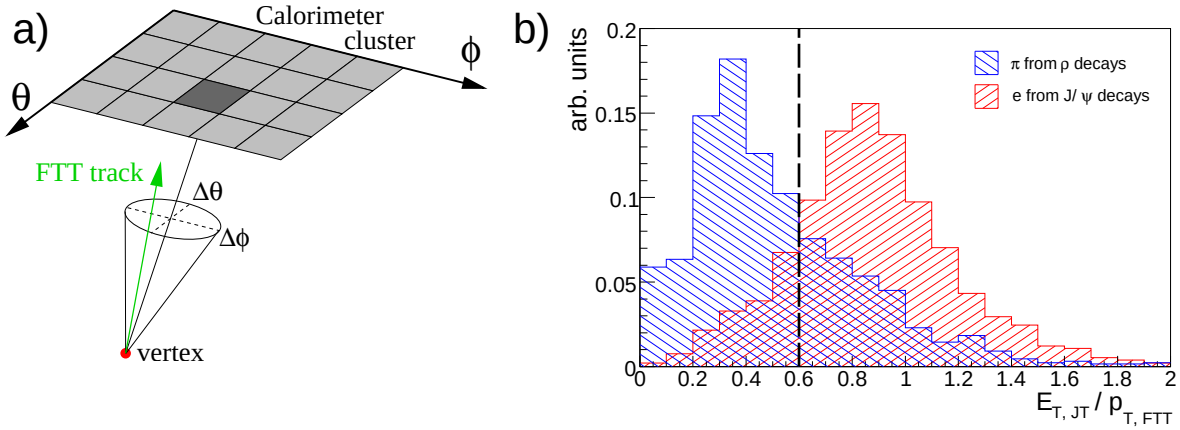

Figure 15.10.: *Matched track-cluster pairs are formed a) and their $E_{T,\,\mathrm{JT}}/p_{T,\,\mathrm{FTT}}$ ratio is calculated b), which provides an identification of electrons and pions as indicated by the vertical dashed line. Histogram provided by [Sau09].*

tion is combined with the L1 calorimeter information from the jet trigger (JT) [H+99b] within an acceptance window determined by $\Delta\theta$ and $\Delta\phi$ as indicated in figure 15.10a). The JT provides a list of energy sorted clusters (jets) and is sensitive to low energy depositions providing good topological information. For the energy measurement the electromagnetic and hadronic part of the calorimeter is combined. The main focus is on discriminating electrons from high energetic pions. In a non-compensating calorimeter (like the H1 LAr Calorimeter), the detectable energy is smaller for hadrons than for electrons of the same energy. Therefore, a lower cut on the $E_{T\ \mathrm{JT}}/p_{T\ \mathrm{FTT}}$ ratio (transverse energy measured by the jet trigger divided by the FTT measured transverse momentum of the tracks) as displayed in figure 15.10b) permits a coarse distinction of electrons and charged hadrons, although uncalibrated raw data as available at trigger

level were used.
Different triggers using the L3 electron identification were implemented: two single tag (sT) electron finders with a medium (1.5 GeV) and a high (2.0 GeV) p_T threshold and a double tag (dT) electron finder with a low (1.2 GeV) p_T threshold. Different cuts on the $E_{T,\,\mathrm{JT}}/p_{T,\,\mathrm{FTT}}$ ratio are implemented for these electron finders. The medium sT implements $E_{T,\,\mathrm{JT}}/p_{T,\,\mathrm{FTT}} > 0.5$, while for the high sT > 0.6 was used and the double tag electron finder used $E_{T,\,\mathrm{JT}}/p_{T,\,\mathrm{FTT}} > 0.3$.

Identification of Muons

The L3 muon identification [Sau09] is performed by matching FTT tracks with information received from the L1 muon trigger system, which consists of 64 modules. The main focus is to increase the discrimination between muons originating from the

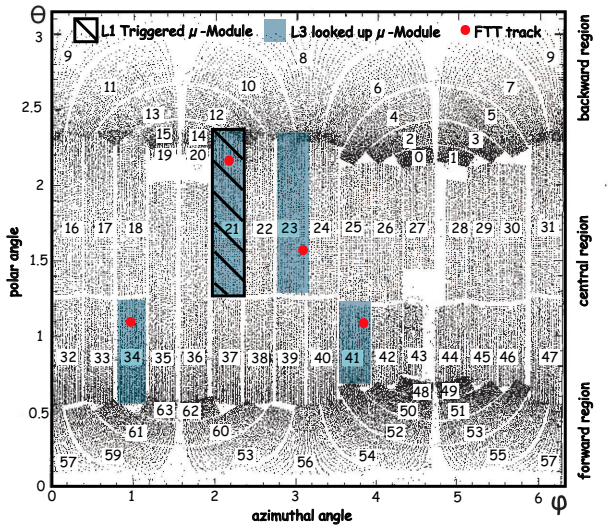

Figure 15.11.: *Hit map of the central muon system. The numbers label the 64 different modules. The basic idea of the L3 muon identification is illustrated: The thick points refer to FTT tracks extrapolated to the muon system and matched to muon modules (shaded boxes). As the L1 triggered muon module* 21 *(hatched) contains a FTT track the event is accepted.*

ep interaction vertex and cosmic muons or back scattered beam debris. Several H1 muon triggers were verified and bandwidth for additional triggers was gained (see figure 15.19).
The muon identification was performed if at least one of the L1 muon modules was fired. The track-muon assignment using look up table techniques was performed during the data preparation step. A positive bit comparison between the look up muon information and the muon trigger information leads to the identification of a muon candidate as illustrated in figure 15.11, where the hit map of the central muon system in the $\theta\phi$ plane is overlayed with the information of an event containing four tracks and one muon.

15.5. Performance

In order to give a short overview on the performance that is achieved with the FTT system four quantities are utilised. These are track and mass resolutions, time behaviour, rate reduction and efficiency. First results of the level three system of the FTT have been presented at [J+07].

Resolutions

The dominant influence on the mass resolution originates from the L2 track resolution which is dominated by the θ resolution. Detailed studies concerning the resolution of the L3 system can be found elsewhere [Ben07]. The peak resolutions are as follows:

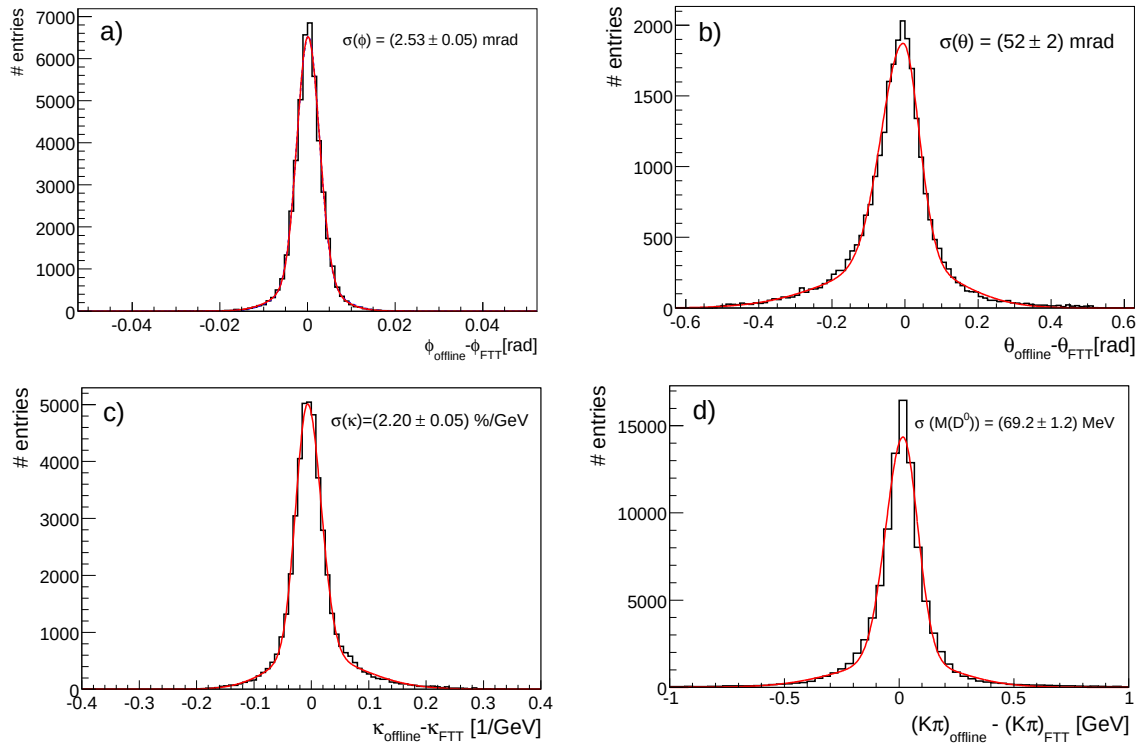

Figure 15.12.: *The resolution σ of the FTT L2 track parameters a) ϕ, b) θ and c) $1/p_T = \kappa$ determined from the comparison to the off-line reconstructed tracks. As an example the mass resolution for the D^0 mass is shown in d).*

$\sigma_{\mathrm{FTT},1/p_T} \approx 2.2\%/\mathrm{GeV}$, $\sigma_{\mathrm{FTT},\phi} \approx 2.5$ mrad and $\sigma_{\mathrm{FTT},\theta} \approx 50$ mrad. With these values the FTT system achieved the design goals for the resolutions of the track parameters. The resolution of the FTT L2 fitted tracks has the dominant impact on the mass resolution, as an example the mass resolution for the D^0 meson is shown in d).

Time Response

The time measurements of different parts of the algorithms is done by using the high resolution clock, which is provided by the PowerPC. The operating system provides

routines to make use of this clock for time measurements. The time is measured in units of 40 ns. The following time-stamps are measured:

1. start of the data transfer from the receiver card to the PMC-DPIO card
2. end of the DMA transfer to the slave memory
3. end of the preparation algorithm
4. end of the selection algorithm

The time difference between these points is the time consumption of the individual steps, which are the transmission time $T_{\text{trans}} = [2] - [1]$, the preparation time $T_{\text{prep}} = [3] - [2]$, the selection time $T_{\text{sel}} = [4] - [3]$ and the total time $T_{\text{tot}} = T_{\text{trans}} + T_{\text{prep}} + T_{\text{sel}}$. The most time consuming part of the system is the software part implemented for the data preparation and selection step. The simultaneous data transfer to the PMC-DPIO cards from the receiver card ensures data transmissions within 10.3 μs for the maximal number of data words (see section 15.2). The time needed to transfer the data from the FIFO of the PMC-DPIO card to the memory of the PowerPCs using the fast DMA access is negligible.
In the following the time behaviour for three selection algorithms is discussed for the MVME2400 type PowerPC as a measure of the achieved performace. The time con-

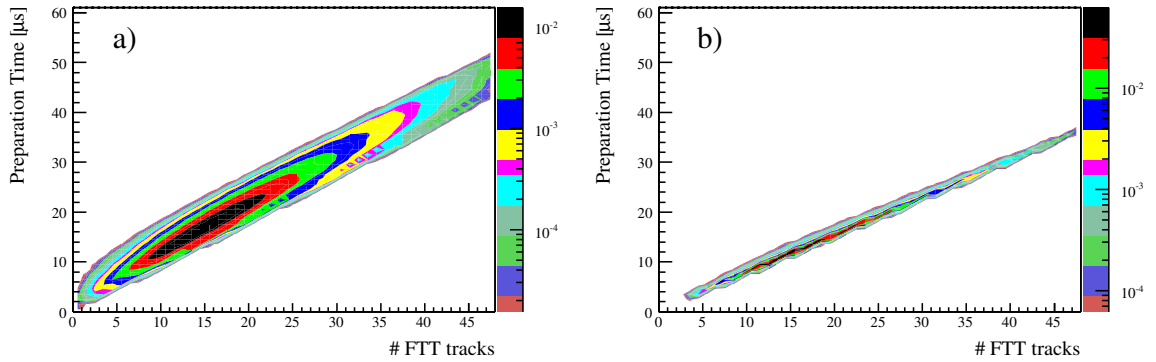

Figure 15.13.: *The data preparation time against the number of processed tracks a) for the electron selection algorithm and b) for the D^* selection algorithm. For the D^* selection a minimum track multiplicity of three tracks is required.*

sumption for the data preparation per event against the number of processed tracks is depicted in figure 15.13a) for the electron selection algorithm and in figure 15.13b) for the D^* selection algorithm. Both selection algorithms show a linear behaviour up to 48 tracks. The data preparation times of the other selection algorithms show a similar linear behaviour. The steeper slope and larger spread for the electron selection algorithm is due to the additional preparation of the calorimeter data. For the D^* data preparation a minimum track multiplicity of three tracks is required. In total the data preparation time is dominated by the calculation of the track parameters, which takes for the highest track multiplicities about 1/3 of the available time leaving about 80 μs

for the actual selection algorithms.
In figure 15.14 the total time of the D^* selection algorithm is depicted as function of

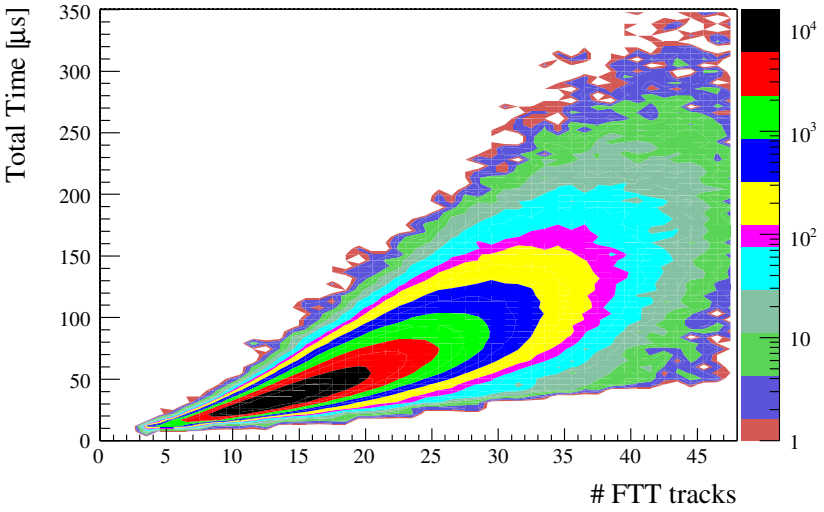

Figure 15.14.: *The total time consumption in µs for the D^* selection algorithm as function of the number of processed FTT tracks.*

the number of processed FTT tracks. The bottom linear edge of the distribution is given by the sum of the transmission and data preparation time. The expected slope for a three body decay is n^3 if n denotes the number of FTT tracks. Because of the decay via the D^0 resonance and the condition that the selection is terminated after the first D^* candidate the expected slope for the worst case scenario is $\propto (n^2 + n)$. The

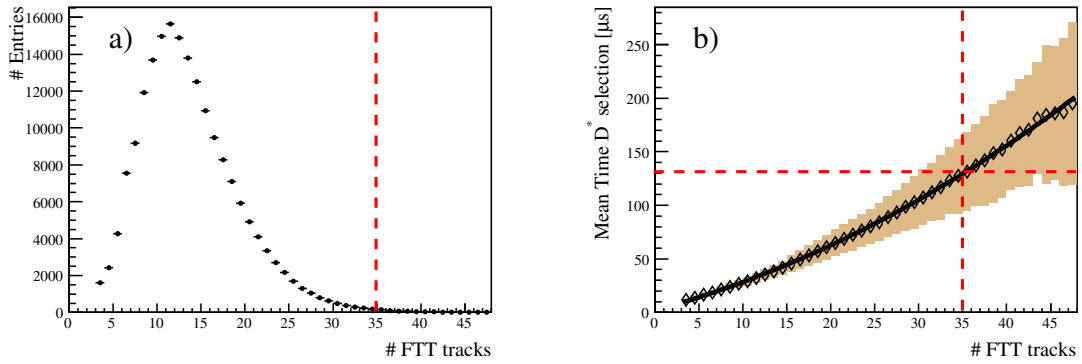

Figure 15.15.: *The amplitude of the fitted L3 time consumption is shown in a) for the D^* selection algorithm as function of the number of FTT tracks. The amplitude corresponds to the number of entries in the fitted slice of the original distribution. The fitted mean in bins of the track multiplicity is shown in b) as function of the number of FTT tracks.*

distribution shown in figure 15.14 is fitted with a Gaussian function in slices of the track multiplicity. The mean value and the RMS of the fitted track multiplicity slice

is shown in figure 15.15b). The mean time consumption is fitted with the polynomial function $f(n) = 1.74 \cdot n + 0.05 \cdot n^2$. For track multiplicities of up to 35 FTT tracks the limit of 130 μs is met as indicated by the intersection of the dashed lines. The weak quadratic term is responsible for the steeper slope that ends up with time consumptions greater 130 μs for track multiplicities above 35 as shown in figure 15.15b).
The amplitude of the fitted slice of the total time consumption distribution shown in figure 15.15a) corresponds to the number of events with the same FTT track multiplicity. The trigger losses due to selection times larger than 130 μs are estimated on the basis of figure 15.15a) as indicated by the dashed line. The fraction of events for track multiplicities above 35 is 0.3%, which is negligable as simulated D^* meson events show a track multiplicity of less than 25 tracks for 99.9% of the events. Therefore events with multiplicities larger than 35 tracks are predominantly background events.
In figure 15.16a) the total time of the electron selection algorithm is depicted as func-

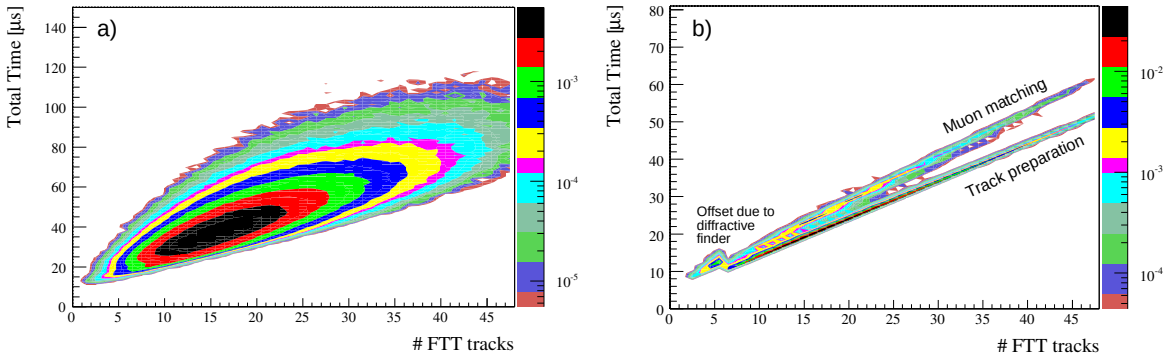

Figure 15.16.: *The total time consumption in μs for the electron a) and muon selection algorithm b) as function of the number of processed FTT tracks. An additional search for diffractive vector mesons is done on this PowerPC. This results in the offset for low track multiplicities between two and five processed tracks b).*

tion of the number of processed FTT tracks. The total time consumption shows a linear behaviour which dies out due to the low statictics at high track multiplicities.
The fast termination of the muon selection algorithms allows an additional diffractive vector meson search on the same PowerPC. In figure 15.16b) the total time consumption of the muon and diffractive selection algorithm is depicted as function of the number of processed FTT tracks. The diffractive vector meson search is done for track multiplicities between two and five tracks within $2-3$ μs, which is illustrated by figure 15.16b) where the offset at low multiplicities is due to this finder.
The time consumption for the muon selection algorithm is characterised by two different slopes as illustrated in figure 15.16b). For $N_\mu = 0$ the time consumption is the sum of the preparation and transmission time (lower band) whereas for $N_\mu > 0$ the muon selection algorithm is executed (upper band). The time that is needed for the selection of muons is given by the difference between the two bands and takes for 48 tracks approximately 10 μs.
With the use of G3 PowerPCs all selection algorithms fulfill the requirement of termi-

nating below the L3 latency of 130 μs for the physics signal of interest. The events with higher D^* selection times as the L3 latency for high multiplicity events are dominated by background. Nevertheless an upgrade to G4 PowerPCs was developed. It has been demonstrated [Jun04] that the use of MVME5500 type PowerPCs would decrease the maximal time consumption of the D^* selection algorithm by one third to approximately 140 μs for 48 tracks reducing the losses to below 0.01%. Because of the interferences with the ongoing data taking and the negligible losses of the G3 PowerPCs it was decided to not perform this upgrade.

Rate Reduction of the L3 Subtriggers

The major design criterion of the FTT system and especially L3 is to provide a high rate reduction. Most of the FTT L3 based subtriggers have large L1 raw rates as they are designed for the photoproduction regime where the rate increases drastically because of the $1/Q^4$ dependence of the cross section.
The technical commissioning of the level three system was finished during the beginning of the year 2006 (around run 449000) such that a first hardware setup was utilised for trigger purposes. An additional commissioning of the physics subtriggers had started; the anticipated rates as obtained from `fttemu` simulation studies [Ben07] clarified the picture from data, which suffered in the beginning from limited statistics due to rate limitations for the new triggers.
First a D^* and a J/ψ meson trigger (both at low p_T threshold) have been set-up in order to get more insights on the rates and the reliability of the L3 system. As the D^* decay is the benchmark process for the third trigger level, D^* subtriggers are discussed here in detail, whereas others are summarised in terms of their rate reduction at the end of this section. Figure 15.17 illustrates a rate overview of subtrigger s53, which comprises a L3 D^* condition. The prescale corrected raw rates of s53 as function of

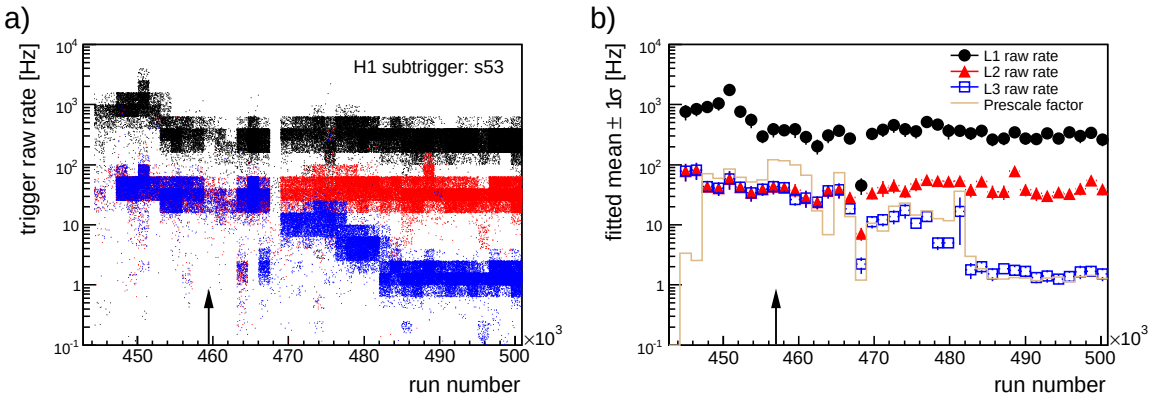

Figure 15.17.: *The prescale corrected raw rates of s53 at different trigger levels against the run number are shown in a), while b) depicts Gaussian fits of slices of the raw rates. In addition the average prescale factor is calculated for each run number slice. The arrow denotes L3Reject test runs; more details are given in the text.*

the run number at different levels of the H1 trigger scheme are illustrated in figure 15.17a). The prescale (see section 3.5) is assigned at level one to subtriggers with high

rates in order to keep the global trigger rate within the available bandwidth. Figure 15.17b) displays the mean and width of Gaussian fits to slices of short run ranges and additionally the averaged prescale for this run range is indicated as solid line. The level one rates (filled circles) reach up to 500 Hz, while the L2 rate (filled triangular) goes up to 80 Hz and the L3 rate (open boxes) coincides until run 466000 with the L2 rate because the L3Reject signal was not activated at that time. Starting with run number 466000 the L3Reject was activated, which is clearly visible as the L3 rate does not coincide any more with the L2 rate.
Before the implementation of the L3Reject in the standard H1 running, it was tested

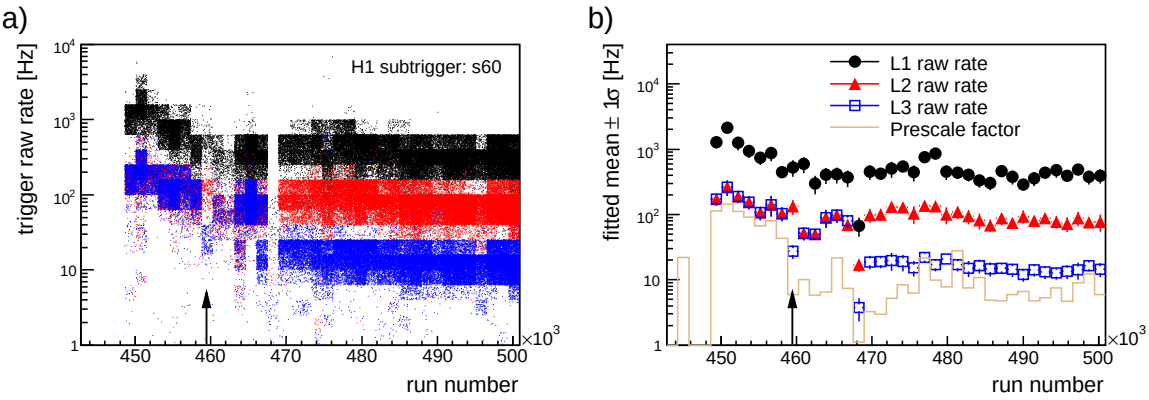

Figure 15.18.: *The prescale corrected raw rates of s60 at different trigger levels against the run number are shown in a), while b) depicts Gaussian fits of slices of the raw rates. In addition the average prescale factor is calculated for each run number slice. The arrow denotes L3Reject test runs; more details are given in the text.*

in two different configurations:

1. Two subtriggers (s67 & s76) were verified by the L3 track-muon match during cosmic data taking for runs 458466 – 458575,

2. Two subtriggers (s53 & s60) were verified by the L3 D^* and J/ψ condition during luminosity data taking for runs 458827 – 459322.

The results of the second test configuration are illustrated by figure 15.17 for the s53 and in figure 15.18 for s60 as there is a decreased L3 rate compared to the L2 rate indicated by the arrow. The L3Reject test shows up more prominent in figure 15.18 as this subtrigger was also better tuned for the physics needs, while s53 (see figure 15.17) was not finally tuned at that time. The successful L3Reject test runs, where also the ability of all other H1 subdetector systems to process this early event abort signal was demonstrated, led to the decision to fully activate the L3Reject for the time after the HERA shutdown in mid 2006.
After the L3Reject activation the final commissioning of the D^* triggers took place. Although detailed simulations were made before, the optimal tuning could only be made within a running system because the rates depend to a large extent on the beam and vacuum conditions of the HERA machine. The tuning is especially visible for

the D^* subtrigger s53 as illustrated by figure 15.17b). The continuous effort led to a reduction of the L3 output rate by a factor of 10 accompanied by a reduction of the prescale factor. A first trigger using the high $p_T(D^*)$ D^* condition from L3 was s122, followed subsequently by two other D^* subtriggers, which comprise a low and a medium $p_T(D^*)$ threshold. The implemented conditions and run ranges are summarised elsewhere [Jun06].
A measure of the performance of the implemented subtriggers is the rate reduction, which is expressed as a rate reduction factor determined from the individual rates at different trigger levels of a subtrigger. The high performance of the FTT L3 system in terms of high rate reduction factors allowed the integration of many subtriggers. An overview is given in figure 15.19 where a) illustrates the rate reduction of FTT L2 (triangles), FTT L3 (squares) and the total FTT (circles) rate reduction for a subset of subtriggers that use L3 conditions. Figure 15.19b) illustrates the FTT L3 output rate (squares) together with the average prescale (solid line), which was assigned to this subtrigger, for the same selection of subtriggers as in a). The ΔM method in

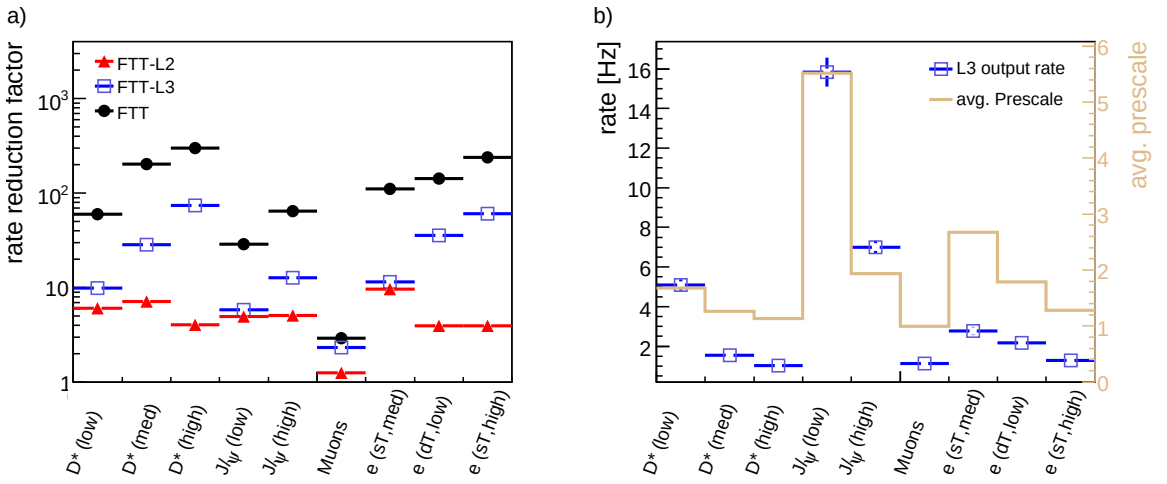

Figure 15.19.: *The rate reduction factors a) and the L3 output rates with the corresponding average prescale b) for some of the physics finders implemented in FTT L3. They are derived from the fitted rate distributions of certain subtriggers, e.g. the raw rates (see figure 15.17a)) are fitted by linear functions for stable trigger conditions. The fraction of these rates is used to derive the rate reduction factors.*

conjunction with $p_T(D^*)$ cuts is highly effective in the removal of background processes and provides high rate reduction factors. For instance the high $p_T(D^*)$ trigger gave a rate reduction factor of about 60 as illustrated in figure 15.19, while the low $p_T(D^*)$ trigger gave only a rate reduction factor of about 10. The numbers given are relative to FTT L2, which itself gave rate reduction factors for the D^* triggers of about 5 indicated by the filled triangles. In total rate reduction factors of several hundred are achieved with the D^* trigger settings.
For the high p_T single tag electron trigger a rate reduction factor of about 60 was achieved. Only with a double tag electron finder it is possible to implement a subtrigger at a very low p_T threshold of 1.2 GeV. A single tag electron finder with a p_T threshold

of 1.5 GeV has already a rate of ~ 2.5 Hz.
The rate reduction factors that were achieved for the track-muon match was between a factor of 3 in the central region by rejecting cosmic muons (see figure 15.19) and 10 in the forward and backward region mostly rejecting beam induced background. With these improvements regions of the muon trigger system which suffered from large beam background and which were excluded previously in the H1 trigger system could be included [Sau09]. In addition the global muon trigger rate could be considerably reduced, thus opening bandwidth for other triggers.

Efficiency of the L3 Algorithms

The efficiency of the L3 D^* identification as function of $p_T(D^*)$ obtained from an independently triggered D^* sample is shown in figure 15.20 for the three different $p_T(D^*)$ thresholds. The efficiency for all three D^* triggers starting at a transverse momentum as low as 1.5 GeV up to 14 GeV is about $45\% - 50\%$. The higher efficiency for the high $p_T(D^*)$ threshold is due to an increased ΔM cut of 0.28 GeV. For comparison the efficiency estimated from a PYTHIA MC sample is shown as solid line in figure 15.20b) for the high (filled circle) $p_T(D^*)$ trigger. Taken into account the complexity of the FTT D^* triggers the FTT simulation is in good agreement with the data efficiency. The presented FTT L3 D^* triggers are able to identify D^* mesons with a transverse

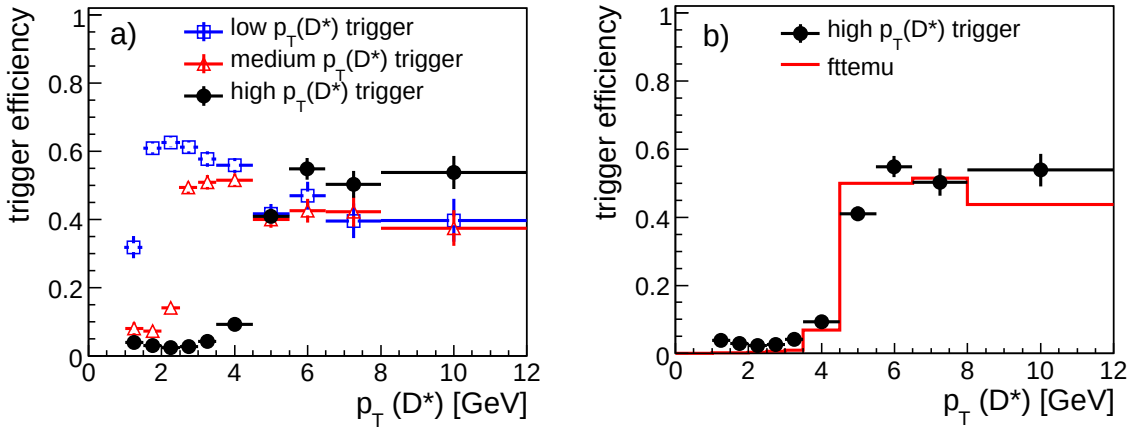

Figure 15.20.: *The L3 trigger efficiency a) determined from data as a function of $p_T(D^*)$ for the low (square), medium (triangles) and high (filled circle) $p_T(D^*)$ trigger corresponding to thresholds of $p_T(D^*) > 1.5$, 2.5 and 4.5 GeV. The L3 trigger efficiency of the high $p_T(D^*)$ trigger is compared to the one determined from a PTYHIA MC sample.*

momentum as low as 1.5 GeV with high efficiencies. More detailled studies concerning the efficiency of the L3 D^* triggers can be found elsewhere [Ben07].
The efficiency of the L3 electron trigger in data is checked with the decay $J/\psi \to e^+e^-$. The signature of these events is suitable as they contain only two isolated electrons with a transverse momentum of typically $1 - 4$ GeV, which covers the range of the implemented L3 electron triggers. Figure 15.21 shows the L3 electron identification

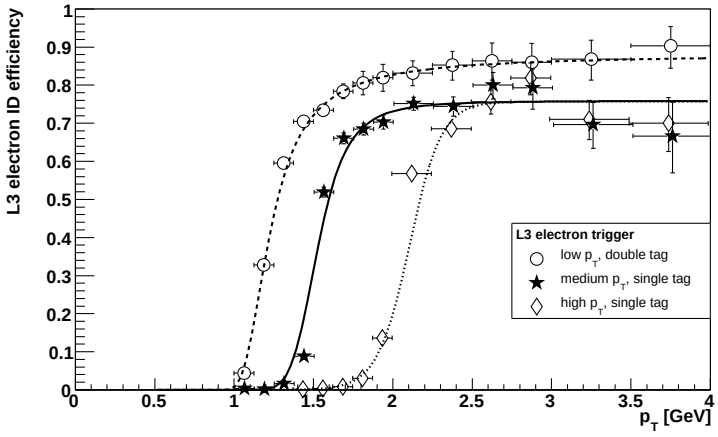

Figure 15.21.: *The L3 electron identification efficiency (taken from [Sau09]) of the single tag medium and high p_T electron finder (filled stars/open diamonds) as function of p_T. The double tag electron finder (open circles) with the lowest p_T threshold for the electron is also shown. The different p_T thresholds of* $1.2, 1.5$ *and* 2.0 GeV *are clearly visible. (For visibility reasons the horizontal bin centres are slightly shifted.)*

efficiency for two single tag electron finders with a medium and a high p_T threshold and for a double tag electron finder with a low p_T threshold. The slightly higher L3 electron identification efficiency of the double tag electron finder is due to relaxed track cuts. The efficiency of the L3 identification for isolated muons is verified with data using the decay $J/\psi \to \mu^+\mu^-$ to be above 98% ($p_T > 1.7$ GeV) [Sau09].

15.6. Conclusion

The FTT was a three level trigger system providing coarse track information at the first trigger level within 2.3 μs and precise track information at the second trigger level within 20 μs. A full event analysis and a selection of track based exclusive final states was performed at the third trigger level within 130 μs. The combination of track information with information from other H1 trigger subsystems allows to identify electrons and muons on-line. All three levels of the FTT system were fully operational since 2006 and have fulfilled the specification. Figure 15.22 illustrates the final commission-

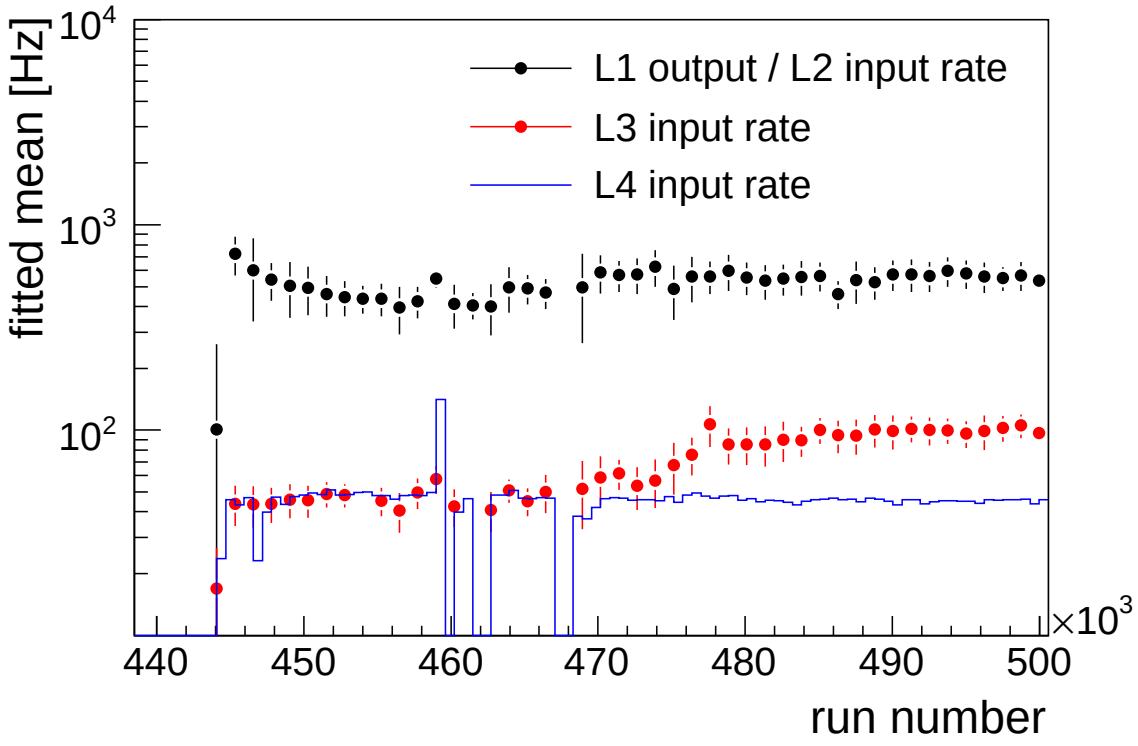

Figure 15.22.: *The global H1 trigger rates at different levels as a function of the run number are shown. The L3Reject provided by FTT L3 system allowed, from the HERA shutdown in mid 2006 onwards, the data taking with a higher L3 input rate. Previously, before mid 2006, the L3 input rate was restricted to the L4 input rate because of no further rate reduction in L3 at that time. The spike in the L4 rate (run* $\sim$ *459000) was due to the L3Reject test runs as discussed in section 15.5.*

ing of the FTT L3 system. H1 made full use of the early reject capabilities of the FTT and implemented the L3Reject starting with run numbers 466000. This activation is observed in the increase of the L3 input rate which otherwise would have been fixed to the L4 input rate as seen prior to the activation. The full use of the L3Reject allowed the implementation of several subtriggers utilising the selection and rate reduction capabilities of the FTT L3 system. In order to cope with varying beam and background conditions and in order to fully exploit the delivered luminosity under given bandwidth

limitations two exclusive J/ψ and three exclusive D^* triggers were set up within the scope of this thesis. Rate reduction factors of several hundred were achieved with the implemented trigger setup.
High performances were achieved for triggering D^* mesons identified in the golden decay channel. Moreover the particle identification algorithms collected large data samples that will permit measurements of charm and beauty production in an extended kinematic region at lowest transverse momenta. As an example results of the D^* triggers are shortly summarised here. Due to the very good final FTT performance

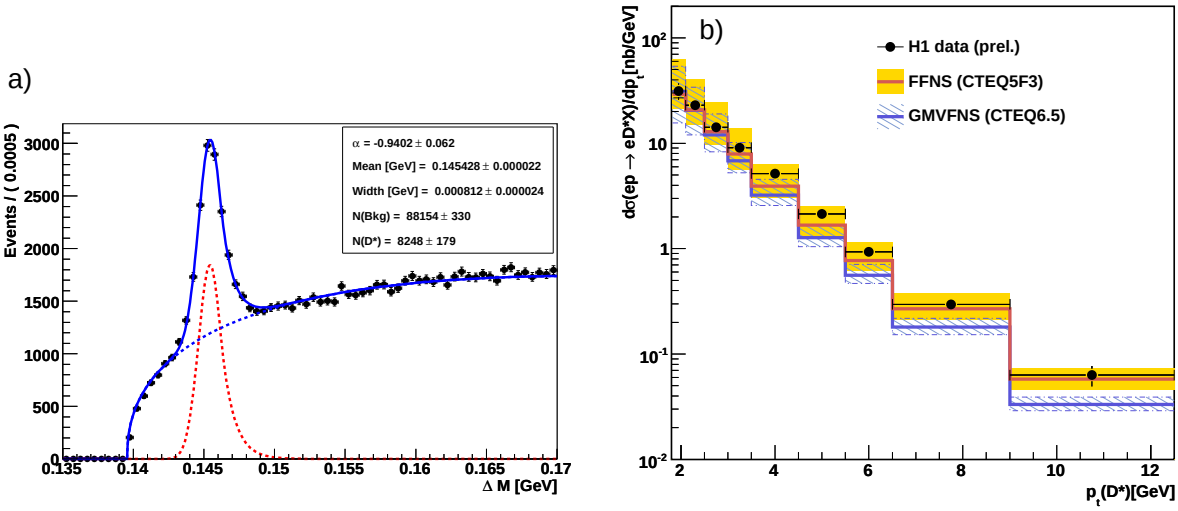

Figure 15.23.: *The untagged photoproduction D^* meson sample that is collected by the FTT (left). Inclusive $p_T(D^*)$ cross section in untagged photoproduction (right) compared to the NLO calculation FMNR (Taken from [Urb09]). The data were triggered and taken by FTT L3 during mid 2006-2007.*

a large data sample of untagged D^* meson photoproduction was taken as illustrated in figure 15.23a). The analysis [Urb09] of a D^* meson photoproduction sample covers more than $9,000$ D^* mesons, corresponding to an eightfold increased statistics in an increased phase space compared to previous measurements at H1. The comparison of NLO QCD predictions based on different heavy flavor schemes (GM-VFNS & FFNS), see figure 15.23b), can provide information on the mass treatment complementary to the DIS analysis presented in this thesis.

A. Cross Section Tables

Binning	$d\sigma/dQ^2$ [nb/GeV^2]	$\delta^{\text{stat.}}$ [%]	$\delta^{\text{sys.}}_{unc.}$ [%]	$\delta(\text{E}_{e'})$ [%]	$\delta(\theta_{e'})$ [%]	$\delta(\text{E}_{\text{had}})$ [%]	δ(model) [%]	δ(frag) [%]
5.0 - 6.0	0.49	$\pm$4.5	$\pm$8.5	$^{-0.3}_{+0.0}$	$^{+0.3}_{-0.3}$	$^{+0.0}_{-0.0}$	$^{+0.9}_{-0.9}$	$^{+2.2}_{-2.1}$
6.0 - 8.0	0.38	$\pm$3.5	$\pm$8.5	$^{+0.2}_{-0.1}$	$^{+1.0}_{-1.0}$	$^{+0.0}_{-0.0}$	$^{+0.8}_{-0.8}$	$^{+2.2}_{-2.2}$
8.0 - 10.0	0.31	$\pm$3.9	$\pm$8.5	$^{+0.0}_{-0.6}$	$^{+0.7}_{-0.7}$	$^{+0.0}_{-0.0}$	$^{+1.6}_{-1.6}$	$^{+0.3}_{-0.9}$
10.0 - 13.0	0.20	$\pm$4.1	$\pm$8.5	$^{+0.6}_{-0.4}$	$^{+1.6}_{-1.6}$	$^{+0.1}_{-0.0}$	$^{+2.3}_{-2.3}$	$^{+0.7}_{-0.5}$
13.0 - 19.0	0.13	$\pm$3.4	$\pm$8.5	$^{+0.5}_{-0.5}$	$^{+1.1}_{-1.1}$	$^{+0.0}_{-0.0}$	$^{+0.6}_{-0.6}$	$^{+2.6}_{-2.9}$
19.0 - 27.5	0.068	$\pm$4.1	$\pm$8.5	$^{+0.7}_{-0.6}$	$^{+1.0}_{-1.0}$	$^{+0.0}_{-0.0}$	$^{+1.0}_{-1.0}$	$^{+1.7}_{-1.4}$
27.5 - 40.0	0.041	$\pm$4.2	$\pm$8.5	$^{+0.6}_{-0.4}$	$^{+0.8}_{-0.8}$	$^{+0.0}_{+0.0}$	$^{+0.5}_{-0.5}$	$^{+2.4}_{-2.6}$
40.0 - 60.0	0.017	$\pm$6.0	$\pm$8.5	$^{+0.7}_{-0.8}$	$^{+0.7}_{-0.7}$	$^{+0.0}_{-0.0}$	$^{+0.7}_{-0.7}$	$^{+2.0}_{-2.0}$
60.0 - 100.0	0.0075	$\pm$6.6	$\pm$8.5	$^{+1.6}_{-1.2}$	$^{+1.0}_{-1.0}$	$^{-0.0}_{+0.0}$	$^{+0.9}_{-0.9}$	$^{+2.2}_{-2.5}$

Table A.1.: *The differential $D^{*\pm}$ meson production cross section as a function of the photon virtuality Q^2. The error breakdown is done such, that the total statistical and bin-to-bin uncorrelated systematical error is given first. Afterwards the signed bin-to-bin correlated error (see chapter 9) is given, where the superscript value corresponds to the upward variation and the other one is the downward variation. Error values less than* 0.05% *are given as* 0.0%.

Binning	$d\sigma/dy$ [nb]	$\delta^{\text{stat.}}$ [%]	$\delta^{\text{sys.}}_{unc.}$ [%]	$\delta(\text{E}_{e'})$ [%]	$\delta(\theta_{e'})$ [%]	$\delta(\text{E}_{\text{had}})$ [%]	δ(model) [%]	δ(frag) [%]
0.02 - 0.05	12.53	±4.2	±8.5	$^{-2.3}_{+2.3}$	$^{+0.6}_{-0.6}$	$^{-9.8}_{+11.1}$	$^{-0.7}_{+0.7}$	$^{+2.9}_{-3.4}$
0.05 - 0.09	19.01	±3.0	±8.5	$^{-0.8}_{+0.7}$	$^{+0.9}_{-0.9}$	$^{-2.9}_{+3.1}$	$^{-0.6}_{+0.6}$	$^{+1.9}_{-1.3}$
0.09 - 0.18	15.00	±2.4	±8.5	$^{+0.0}_{-0.1}$	$^{+1.0}_{-1.0}$	$^{+0.1}_{+0.1}$	$^{-0.2}_{+0.2}$	$^{+2.1}_{-2.0}$
0.18 - 0.26	11.17	±3.3	±8.5	$^{+0.3}_{-0.4}$	$^{+1.1}_{-1.1}$	$^{+1.6}_{-1.7}$	$^{+0.9}_{-0.9}$	$^{+1.5}_{-1.3}$
0.26 - 0.36	6.89	±3.9	±8.5	$^{+0.9}_{-0.6}$	$^{+1.0}_{-1.0}$	$^{+3.1}_{-2.5}$	$^{+2.1}_{-2.1}$	$^{+1.6}_{-1.1}$
0.36 - 0.50	3.85	±4.8	±8.5	$^{+1.4}_{-1.5}$	$^{+0.9}_{-0.9}$	$^{+3.9}_{-3.7}$	$^{+3.6}_{-3.6}$	$^{+1.3}_{-0.7}$
0.50 - 0.70	1.95	±7.8	±8.5	$^{+7.2}_{-5.9}$	$^{+0.8}_{-0.8}$	$^{+1.4}_{-0.9}$	$^{+4.6}_{-4.6}$	$^{+1.4}_{-1.1}$

Table A.2.: *The differential D^* meson production cross section as a function of the inelasticity y.*

Binning	$d\sigma/dW_{\gamma P}$ [nb/GeV]	$\delta^{\text{stat.}}$ [%]	$\delta^{\text{sys.}}_{unc.}$ [%]	$\delta(\text{E}_{e'})$ [%]	$\delta(\theta_{e'})$ [%]	$\delta(\text{E}_{\text{had}})$ [%]	δ(model) [%]	δ(frag) [%]
70.00 - 110.00	0.032	±2.3	±8.5	$^{-0.5}_{+0.5}$	$^{+0.9}_{-0.9}$	$^{-2.3}_{+2.2}$	$^{-0.5}_{+0.5}$	$^{+1.9}_{-1.4}$
110.00 - 140.00	0.034	±2.9	±8.5	$^{+0.2}_{-0.3}$	$^{+1.0}_{-1.0}$	$^{+0.7}_{-0.3}$	$^{+0.0}_{-0.0}$	$^{+2.1}_{-2.1}$
140.00 - 170.00	0.031	±3.3	±8.5	$^{+0.4}_{-0.3}$	$^{+1.1}_{-1.1}$	$^{+1.9}_{-1.8}$	$^{+0.9}_{-0.9}$	$^{+1.8}_{-1.7}$
170.00 - 200.00	0.022	±4.0	±8.5	$^{+1.1}_{-1.0}$	$^{+1.1}_{-1.1}$	$^{+3.6}_{-3.2}$	$^{+3.1}_{-3.1}$	$^{+1.1}_{-0.3}$
200.00 - 230.00	0.014	±5.6	±8.5	$^{+1.7}_{-1.6}$	$^{+0.9}_{-0.9}$	$^{+3.8}_{-3.7}$	$^{+3.5}_{-3.5}$	$^{+1.5}_{-1.1}$
230.00 - 260.00	0.0095	±9.0	±8.5	$^{+6.3}_{-4.8}$	$^{+0.8}_{-0.8}$	$^{+1.7}_{-1.1}$	$^{+5.9}_{-5.9}$	$^{+0.9}_{-0.1}$

Table A.3.: *The differential D^* meson production cross section as a function of $W_{\gamma P}$.*

Binning	$d\sigma/dx$ [nb]	$\delta^{\text{stat.}}$ [%]	$\delta^{\text{sys.}}_{unc.}$ [%]	$\delta(\text{E}_{e'})$ [%]	$\delta(\theta_{e'})$ [%]	$\delta(\text{E}_{\text{had}})$ [%]	δ(model) [%]	δ(frag) [%]
0.000028 - 0.00020	2333.8	±6.6	±8.5	$^{+3.4}_{-3.2}$	$^{+1.4}_{-1.4}$	$^{+2.8}_{-2.5}$	$^{+3.6}_{-3.6}$	$^{+1.1}_{-0.1}$
0.000200 - 0.00035	4622.1	±4.1	±8.5	$^{+1.3}_{-1.4}$	$^{+1.0}_{-1.0}$	$^{+2.7}_{-2.4}$	$^{+1.9}_{-1.9}$	$^{+2.0}_{-1.9}$
0.000350 - 0.00060	3387.9	±3.4	±8.5	$^{+0.7}_{-0.7}$	$^{+1.0}_{-1.0}$	$^{+1.7}_{-1.6}$	$^{+1.7}_{-1.7}$	$^{+1.5}_{-0.9}$
0.000600 - 0.00100	2181.2	±3.2	±8.5	$^{+0.4}_{-0.4}$	$^{+0.9}_{-0.9}$	$^{+1.0}_{-0.8}$	$^{+1.0}_{-1.0}$	$^{+1.4}_{-0.9}$
0.001000 - 0.00170	1168.3	±3.2	±8.5	$^{+0.1}_{-0.1}$	$^{+0.9}_{-0.9}$	$^{+0.0}_{-0.1}$	$^{+0.9}_{-0.9}$	$^{+1.8}_{-1.3}$
0.001700 - 0.00330	509.3	±3.2	±8.5	$^{-0.0}_{+0.0}$	$^{+0.9}_{-0.9}$	$^{-1.8}_{+1.5}$	$^{-0.5}_{+0.5}$	$^{+2.1}_{-2.4}$
0.003300 - 0.02000	32.3	±4.0	±8.5	$^{-0.6}_{+0.6}$	$^{+0.9}_{-0.9}$	$^{-4.4}_{+4.7}$	$^{-0.3}_{+0.3}$	$^{+1.0}_{-0.8}$

Table A.4.: *The differential D^* meson production cross section as a function of Bjørken x.*

Binning	$d\sigma/dx_g^{\mathrm{obs}}(D^*)$ [nb]	$\delta^{\mathrm{stat.}}$ [%]	$\delta^{\mathrm{sys.}}_{unc.}$ [%]	$\delta(\mathrm{E}_{e'})$ [%]	$\delta(\theta_{e'})$ [%]	$\delta(\mathrm{E}_{\mathrm{had}})$ [%]	δ(model) [%]	δ(frag) [%]
0.0001 - 0.0010	336.0	±8.0	±8.5	$^{+3.7}_{-3.3}$	$^{+0.6}_{-0.6}$	$^{+4.2}_{-3.8}$	$^{+1.1}_{-1.1}$	$^{+0.2}_{-0.5}$
0.0010 - 0.0017	1126.8	±4.1	±8.5	$^{+1.9}_{-1.6}$	$^{+1.0}_{-1.0}$	$^{+3.1}_{-2.7}$	$^{+0.3}_{-0.3}$	$^{+1.4}_{-0.9}$
0.0017 - 0.0033	882.2	±2.8	±8.5	$^{+0.9}_{-1.0}$	$^{+1.0}_{-1.0}$	$^{+2.1}_{-1.8}$	$^{+0.8}_{-0.8}$	$^{+1.6}_{-0.7}$
0.0033 - 0.0100	294.1	±2.1	±8.5	$^{+0.0}_{-0.0}$	$^{+1.0}_{-1.0}$	$^{-0.7}_{+0.8}$	$^{+0.2}_{-0.2}$	$^{+1.6}_{-0.8}$
0.0100 - 0.0850	5.4	±3.3	±8.5	$^{-1.7}_{+1.7}$	$^{+0.7}_{-0.7}$	$^{-7.1}_{+7.2}$	$^{+0.6}_{-0.6}$	$^{+0.2}_{-0.8}$

Table A.5.: *The differential D^* meson production cross section as a function of $x_g^{\mathrm{obs}}(D^*)$.*

Binning	$d\sigma/d\eta(D^*)$ [nb]	$\delta^{\mathrm{stat.}}$ [%]	$\delta^{\mathrm{sys.}}_{unc.}$ [%]	$\delta(\mathrm{E}_{e'})$ [%]	$\delta(\theta_{e'})$ [%]	$\delta(\mathrm{E}_{\mathrm{had}})$ [%]	δ(model) [%]	δ(frag) [%]
-1.50 - -1.25	1.10	±7.1	±8.5	$^{+1.3}_{-1.0}$	$\pm^{+1.4}_{-1.4}$	$^{+0.0}_{-0.0}$	$^{+1.6}_{-1.6}$	$^{+1.2}_{-1.9}$
-1.25 - -1.00	1.30	±5.2	±8.5	$^{+0.9}_{-0.8}$	$^{+1.2}_{-1.2}$	$^{+0.0}_{-0.0}$	$^{+0.4}_{-0.4}$	$^{+3.2}_{-3.5}$
-1.00 - -0.75	1.50	±4.3	±8.5	$^{+0.6}_{-0.6}$	$^{+1.0}_{-1.0}$	$^{-0.0}_{+0.0}$	$^{-0.7}_{+0.7}$	$^{+3.2}_{-3.9}$
-0.75 - -0.50	1.65	±4.2	±8.5	$^{+0.5}_{-0.6}$	$^{+0.9}_{-0.9}$	$^{-0.0}_{+0.0}$	$^{+1.2}_{-1.2}$	$^{+0.9}_{-0.2}$
-0.50 - -0.25	1.62	±4.2	±8.5	$^{+0.6}_{-0.5}$	$^{+1.0}_{-1.0}$	$^{+0.0}_{-0.0}$	$^{+0.4}_{-0.4}$	$^{+2.4}_{-2.7}$
-0.25 - 0.00	1.72	±4.3	±8.5	$^{+0.4}_{-0.4}$	$^{+0.9}_{-0.9}$	$^{+0.0}_{-0.0}$	$^{+0.5}_{-0.5}$	$^{+1.6}_{-1.3}$
0.00 - 0.25	1.75	±4.3	±8.5	$^{+0.4}_{-0.5}$	$^{+0.9}_{-0.9}$	$^{+0.0}_{-0.0}$	$^{+1.0}_{-1.0}$	$^{+1.2}_{-0.7}$
0.25 - 0.50	1.77	±4.6	±8.5	$^{+0.3}_{-0.4}$	$^{+0.9}_{-0.9}$	$^{+0.0}_{-0.0}$	$^{+0.5}_{-0.5}$	$^{+2.1}_{-2.5}$
0.50 - 0.75	1.78	±4.8	±8.5	$^{+0.3}_{-0.3}$	$^{+0.9}_{-0.9}$	$^{+0.0}_{-0.0}$	$^{+1.4}_{-1.4}$	$^{+1.3}_{-0.9}$
0.75 - 1.00	1.93	±4.7	±8.5	$^{+0.3}_{-0.3}$	$^{+0.8}_{-0.8}$	$^{+0.0}_{-0.0}$	$^{+1.9}_{-1.9}$	$^{+1.4}_{-1.0}$
1.00 - 1.25	1.89	±5.4	±8.5	$^{+0.3}_{-0.3}$	$^{+0.8}_{-0.8}$	$^{+0.0}_{-0.0}$	$^{+0.7}_{-0.7}$	$^{+2.3}_{-2.2}$
1.25 - 1.50	1.72	±6.2	±8.5	$^{+0.4}_{-0.4}$	$^{+0.9}_{-0.9}$	$^{+0.2}_{-0.2}$	$^{+1.8}_{-1.8}$	$^{+1.2}_{-0.6}$

Table A.6.: *The differential D^* meson production cross section as a function of the pseudo-rapidity $\eta(D^*)$.*

Binning	$d\sigma/dp_T(D^*)$ [nb/GeV]	$\delta^{\text{stat.}}$ [%]	$\delta^{\text{sys.}}_{unc.}$ [%]	$\delta(\text{E}_{e'})$ [%]	$\delta(\theta_{e'})$ [%]	$\delta(\text{E}_{\text{had}})$ [%]	δ(model) [%]	δ(frag) [%]
1.50 - 1.88	2.03	±7.7	±8.5	$^{+0.8}_{-0.8}$	$^{+1.6}_{-1.6}$	$^{+0.0}_{-0.0}$	$^{+1.1}_{-1.1}$	$^{+0.1}_{-0.1}$
1.88 - 2.28	2.10	±4.9	±8.5	$^{+0.8}_{-0.7}$	$^{+1.5}_{-1.5}$	$^{+0.0}_{-0.0}$	$^{+1.0}_{-1.0}$	$^{+0.2}_{-0.2}$
2.28 - 2.68	1.92	±3.8	±8.5	$^{+0.6}_{-0.6}$	$^{+1.2}_{-1.2}$	$^{+0.0}_{-0.0}$	$^{+0.6}_{-0.6}$	$^{+0.7}_{-1.1}$
2.68 - 3.08	1.46	±3.4	±8.5	$^{+0.5}_{-0.5}$	$^{+1.0}_{-1.0}$	$^{+0.0}_{-0.0}$	$^{+0.7}_{-0.7}$	$^{+0.7}_{-1.1}$
3.08 - 3.50	1.18	±3.4	±8.5	$^{+0.4}_{-0.5}$	$^{+0.8}_{-0.8}$	$^{+0.1}_{-0.0}$	$^{+1.2}_{-1.2}$	$^{+0.2}_{-0.2}$
3.50 - 4.00	0.86	±3.3	±8.5	$^{+0.4}_{-0.5}$	$^{+0.8}_{-0.8}$	$^{+0.0}_{-0.0}$	$^{+0.1}_{-0.1}$	$^{+0.8}_{-1.3}$
4.00 - 4.75	0.58	±3.0	±8.5	$^{+0.4}_{-0.3}$	$^{+0.6}_{-0.6}$	$^{+0.0}_{-0.0}$	$^{+0.9}_{-0.9}$	$^{+0.5}_{-0.7}$
4.75 - 6.00	0.29	±3.1	±8.5	$^{+0.2}_{-0.2}$	$^{+0.4}_{-0.4}$	$^{+0.0}_{-0.0}$	$^{+0.3}_{-0.3}$	$^{+1.0}_{-1.5}$
6.00 - 8.00	0.082	±4.9	±8.5	$^{-0.2}_{+0.0}$	$^{+0.1}_{-0.1}$	$^{+0.0}_{-0.0}$	$^{+0.8}_{-0.8}$	$^{+0.2}_{-0.1}$
8.00 - 14.00	0.012	±6.8	±8.5	$^{-0.1}_{+0.2}$	$^{+0.2}_{-0.2}$	$^{-0.0}_{+0.0}$	$^{+3.5}_{-3.5}$	$^{+1.8}_{-1.3}$

Table A.7.: *The differential D^* meson production cross section as a function of the transverse momentum $p_T(D^*)$.*

Binning	$d\sigma/dz(D^*)$ [nb]	$\delta^{\text{stat.}}$ [%]	$\delta^{\text{sys.}}_{unc.}$ [%]	$\delta(\text{E}_{e'})$ [%]	$\delta(\theta_{e'})$ [%]	$\delta(\text{E}_{\text{had}})$ [%]	δ(model) [%]	δ(frag) [%]
0.00 - 0.10	2.45	±13.9	±8.5	$^{+3.5}_{-3.2}$	$^{+1.0}_{-1.0}$	$^{+3.1}_{-2.8}$	$^{+3.8}_{-3.8}$	$^{+1.7}_{-2.5}$
0.10 - 0.20	6.61	±5.6	±8.5	$^{+2.5}_{-2.5}$	$^{+1.0}_{-1.0}$	$^{+3.6}_{-3.4}$	$^{+4.0}_{-4.0}$	$^{+1.5}_{-1.3}$
0.20 - 0.33	7.87	±3.9	±8.5	$^{+2.2}_{-2.0}$	$^{+1.2}_{-1.2}$	$^{+4.6}_{-4.3}$	$^{+3.8}_{-3.8}$	$^{+1.3}_{-0.8}$
0.33 - 0.45	8.23	±2.9	±8.5	$^{+2.0}_{-1.8}$	$^{+1.2}_{-1.2}$	$^{+4.7}_{-3.9}$	$^{+2.0}_{-2.0}$	$^{+1.6}_{-1.4}$
0.45 - 0.57	7.95	±2.3	±8.5	$^{+0.7}_{-0.8}$	$^{+1.0}_{-1.0}$	$^{+1.7}_{-1.4}$	$^{+0.6}_{-0.6}$	$^{+0.7}_{-0.1}$
0.57 - 0.70	5.55	±2.5	±8.5	$^{-1.6}_{+1.4}$	$^{+0.7}_{-0.7}$	$^{-4.1}_{+5.4}$	$^{-0.7}_{+0.7}$	$^{+0.7}_{-0.6}$
0.70 - 1.00	1.57	±2.6	±8.5	$^{-6.3}_{+7.1}$	$^{+0.1}_{-0.1}$	$^{-16.8}_{+21.0}$	$^{-1.9}_{+1.9}$	$^{+0.6}_{-0.4}$

Table A.8.: *The differential D^* meson production cross section as a function of $z(D^*)$.*

Binning	$\frac{d^2\sigma}{dydQ^2}$ [nb/GeV^2]	$\delta^{\text{stat.}}$ [%]	$\delta^{\text{sys.}}_{unc.}$ [%]	$\delta(\text{E}_{e'})$ [%]	$\delta(\theta_{e'})$ [%]	$\delta(\text{E}_{\text{had}})$ [%]	δ(model) [%]	δ(frag) [%]
Bin: 5 - 9 GeV^2:								
0.02 - 0.05	1.12	±7.2	±8.5	$^{-3.2}_{+2.9}$	$^{-1.0}_{+1.0}$	$^{-9.2}_{+10.1}$	$^{+1.4}_{-1.4}$	$^{+0.2}_{-1.0}$
0.05 - 0.09	1.62	±4.8	±8.5	$^{-1.5}_{+1.2}$	$^{+0.1}_{-0.1}$	$^{-2.7}_{+3.0}$	$^{-0.5}_{+0.5}$	$^{+0.3}_{-1.6}$
0.09 - 0.16	1.26	±4.4	±8.5	$^{-0.2}_{+0.2}$	$^{+0.8}_{-0.8}$	$^{+0.2}_{+0.3}$	$^{-0.6}_{+0.6}$	$^{+0.7}_{-3.1}$
0.16 - 0.32	0.78	±4.4	±8.5	$^{+0.4}_{-0.7}$	$^{+1.4}_{-1.4}$	$^{+2.1}_{-2.3}$	$^{+0.5}_{-0.5}$	$^{+0.8}_{-3.5}$
0.32 - 0.70	0.24	±6.6	±8.5	$^{+2.6}_{-2.2}$	$^{+1.3}_{-1.3}$	$^{+3.2}_{-2.8}$	$^{+3.8}_{-3.8}$	$^{+0.5}_{-2.5}$
Bin: 9 - 14 GeV^2:								
0.02 - 0.05	0.52	±8.1	±8.5	$^{-1.7}_{+1.8}$	$^{+1.4}_{-1.4}$	$^{-8.8}_{+9.7}$	$^{+0.2}_{-0.2}$	$^{+0.2}_{-0.9}$
0.05 - 0.09	0.89	±6.1	±8.5	$^{-0.4}_{+0.8}$	$^{+1.4}_{-1.4}$	$^{-2.1}_{+2.3}$	$^{-0.2}_{+0.2}$	$^{+0.2}_{-1.1}$
0.09 - 0.16	0.63	±6.1	±8.5	$^{-0.5}_{-0.5}$	$^{+0.9}_{-0.9}$	$^{+0.2}_{-0.4}$	$^{+0.6}_{-0.6}$	$^{+0.3}_{-1.4}$
0.16 - 0.32	0.44	±5.2	±8.5	$^{+0.3}_{-0.4}$	$^{+0.9}_{-0.9}$	$^{+1.9}_{-1.8}$	$^{+2.3}_{-2.3}$	$^{+0.2}_{-0.8}$
0.32 - 0.70	0.14	±8.0	±8.5	$^{+2.5}_{-2.5}$	$^{+0.8}_{-0.8}$	$^{+3.2}_{-2.7}$	$^{+4.2}_{-4.2}$	$^{+1.0}_{-0.2}$
Bin: 14 - 23 GeV^2:								
0.02 - 0.05	0.32	±8.8	±8.5	$^{-1.7}_{+2.6}$	$^{+1.9}_{-1.9}$	$^{-9.7}_{+11.6}$	$^{-2.0}_{+2.0}$	$^{+0.2}_{-0.8}$
0.05 - 0.09	0.41	±7.1	±8.5	$^{-0.2}_{+0.2}$	$^{+1.6}_{-1.6}$	$^{-3.1}_{+2.4}$	$^{-1.2}_{+1.2}$	$^{+0.3}_{-0.1}$
0.09 - 0.16	0.32	±5.9	±8.5	$^{-0.2}_{+0.1}$	$^{+1.1}_{-1.1}$	$^{-0.5}_{+0.5}$	$^{-1.1}_{+1.1}$	$^{+0.2}_{-1.0}$
0.16 - 0.32	0.22	±5.4	±8.5	$^{+0.4}_{-0.4}$	$^{+1.0}_{-1.0}$	$^{+2.3}_{-1.5}$	$^{+1.3}_{-1.3}$	$^{+0.1}_{-0.6}$
0.32 - 0.70	0.059	±7.7	±8.5	$^{+3.0}_{-2.5}$	$^{+0.9}_{-0.9}$	$^{+3.1}_{-2.9}$	$^{+3.3}_{-3.3}$	$^{+0.1}_{-0.5}$
Bin: 23 - 45 GeV^2:								
0.02 - 0.05	0.11	±9.3	±8.5	$^{-1.7}_{+1.4}$	$^{+1.3}_{-1.3}$	$^{-12.0}_{+12.1}$	$^{-3.1}_{+3.1}$	$^{+0.1}_{-0.4}$
0.05 - 0.09	0.15	±7.0	±8.5	$^{-0.9}_{+0.2}$	$^{+1.0}_{-1.0}$	$^{-3.0}_{+4.3}$	$^{-1.3}_{+1.3}$	$^{+0.2}_{-0.1}$
0.09 - 0.16	0.13	±6.4	±8.5	$^{+0.6}_{-0.4}$	$^{+1.2}_{-1.2}$	$^{-0.5}_{+0.1}$	$^{-0.5}_{+0.5}$	$^{+0.1}_{-0.2}$
0.16 - 0.32	0.079	±5.6	±8.5	$^{+0.5}_{-0.5}$	$^{+0.7}_{-0.7}$	$^{+1.7}_{-1.6}$	$^{+0.5}_{-0.5}$	$^{+0.1}_{-0.5}$
0.32 - 0.70	0.027	±7.7	±8.5	$^{+2.8}_{-2.5}$	$^{+0.7}_{-0.7}$	$^{+3.0}_{-2.6}$	$^{+3.5}_{-3.5}$	$^{+0.1}_{-0.4}$
Bin: 45 - 100 GeV^2:								
0.02 - 0.05	0.0088	±62.7	±8.5	$^{-2.4}_{+3.1}$	$^{+0.8}_{-0.8}$	$^{-15.7}_{+20.1}$	$^{-4.4}_{+4.4}$	$^{+0.1}_{-0.1}$
0.05 - 0.09	0.029	±12.5	±8.5	$^{-0.5}_{+0.4}$	$^{+1.0}_{-1.0}$	$^{-4.9}_{+4.6}$	$^{+2.1}_{-2.1}$	$^{+0.1}_{-0.1}$
0.09 - 0.16	0.028	±10.5	±8.5	$^{-0.2}_{+0.1}$	$^{+0.4}_{-0.4}$	$^{-1.3}_{+1.1}$	$^{+0.1}_{-0.1}$	$^{+0.1}_{-0.1}$
0.16 - 0.32	0.022	±8.0	±8.5	$^{+0.9}_{-0.3}$	$^{+1.1}_{-1.1}$	$^{+1.6}_{-1.0}$	$^{+0.3}_{-0.3}$	$^{+0.1}_{-0.1}$
0.32 - 0.70	0.0064	±11.0	±8.5	$^{+3.7}_{-3.2}$	$^{+0.8}_{-0.8}$	$^{+3.2}_{-3.0}$	$^{+1.8}_{-1.8}$	$^{+0.1}_{-0.2}$

Table A.9.: *The double-differential D^* meson production cross section as a function of $y - Q^2$.*

Binning	$p_T(D^*)$ [nb/GeV]	$\delta^{\text{stat.}}$ [%]	$\delta^{\text{sys.}}_{unc.}$ [%]	$\delta(\text{E}_{e'})$ [%]	$\delta(\theta_{e'})$ [%]	$\delta(\text{E}_{\text{had}})$ [%]	δ(model) [%]	δ(frag) [%]
Bin: 1.5 - 2.5 GeV:								
-1.50 - -0.75	0.60	±6.1	±8.5	$^{+1.0}_{-0.7}$	$^{+1.7}_{-1.7}$	$^{+0.0}_{-0.0}$	$^{+1.3}_{-1.3}$	$^{+2.3}_{-0.1}$
-0.75 - 0.00	0.61	±6.5	±8.5	$^{+0.8}_{-0.7}$	$^{+1.5}_{-1.5}$	$^{+0.0}_{-0.0}$	$^{+1.1}_{-1.1}$	$^{+0.5}_{-4.6}$
0.00 - 0.75	0.70	±6.5	±8.5	$^{+0.7}_{-0.6}$	$^{+1.5}_{-1.5}$	$^{+0.0}_{-0.0}$	$^{+0.9}_{-0.9}$	$^{+1.2}_{-7.3}$
0.75 - 1.50	0.90	±7.4	±8.5	$^{+0.6}_{-0.7}$	$^{+1.4}_{-1.4}$	$^{+0.1}_{-0.1}$	$^{+1.4}_{-1.4}$	$^{+1.1}_{-6.4}$
Bin: 2.5 - 3.5 GeV:								
-1.50 - -0.75	0.39	±4.6	±8.5	$^{+0.7}_{-0.7}$	$^{+1.0}_{-1.0}$	$^{+0.0}_{-0.0}$	$^{+0.9}_{-0.9}$	$^{+0.2}_{-2.2}$
-0.75 - 0.00	0.48	±3.9	±8.5	$^{+0.4}_{-0.6}$	$^{+0.9}_{-0.9}$	$^{+0.0}_{-0.0}$	$^{+1.2}_{-1.2}$	$^{+0.1}_{-0.9}$
0.00 - 0.75	0.49	±0.2	±8.5	$^{+0.4}_{-0.5}$	$^{+1.0}_{-1.0}$	$^{+0.0}_{-0.0}$	$^{+0.6}_{-0.6}$	$^{+0.2}_{-2.2}$
0.75 - 1.50	0.56	±6.6	±8.5	$^{+0.4}_{-0.4}$	$^{+0.9}_{-0.9}$	$^{+0.1}_{-0.0}$	$^{+0.3}_{-0.3}$	$^{+0.6}_{-3.9}$
Bin: 3.5 - 5.5 GeV:								
-1.50 - -0.75	0.13	±4.4	±8.5	$^{+0.9}_{-0.8}$	$^{+0.8}_{-0.8}$	$^{-0.0}_{+0.0}$	$^{-0.2}_{+0.2}$	$^{+0.3}_{-2.3}$
-0.75 - 0.00	0.21	±3.3	±8.5	$^{+0.4}_{-0.4}$	$^{+0.8}_{-0.8}$	$^{-0.0}_{+0.0}$	$^{+0.8}_{-0.8}$	$^{+0.2}_{-1.8}$
0.00 - 0.75	0.20	±3.6	±8.5	$^{+0.2}_{-0.2}$	$^{+0.5}_{-0.5}$	$^{-0.0}_{-0.0}$	$^{+0.7}_{-0.7}$	$^{+0.1}_{-1.1}$
0.75 - 1.50	0.18	±4.5	±8.5	$^{+0.2}_{-0.1}$	$^{+0.6}_{-0.6}$	$^{+0.0}_{-0.0}$	$^{-0.1}_{+0.1}$	$^{+0.5}_{-0.1}$
Bin: 5.5 - 14.0 GeV:								
-1.50 - -0.75	0.0049	±11.4	±8.5	$^{+1.1}_{-1.6}$	$^{+0.7}_{-0.7}$	$^{+0.0}_{-0.0}$	$^{-1.0}_{+1.0}$	$^{+0.1}_{-0.9}$
-0.75 - 0.00	0.014	±5.8	±8.5	$^{+0.2}_{-0.2}$	$^{+0.2}_{-0.2}$	$^{+0.0}_{-0.0}$	$^{-0.6}_{+0.6}$	$^{+0.1}_{-0.8}$
0.00 - 0.75	0.019	±5.2	±8.5	$^{-0.3}_{+0.2}$	$^{+0.1}_{-0.1}$	$^{-0.0}_{+0.0}$	$^{+1.6}_{-1.6}$	$^{+0.1}_{-0.7}$
0.75 - 1.50	0.016	±6.0	±8.5	$^{-0.4}_{+0.4}$	$^{-0.0}_{+0.0}$	$^{-0.0}_{+0.0}$	$^{+1.1}_{-1.1}$	$^{+0.5}_{-0.1}$

Table A.10.: *The double-differential D^* meson production cross section as a function of $p_T - \eta$.*

B. List of Abbreviations

BOS *Bank Object System*
Data storage format used by H1. Data are organised in banks or tables.

BPC *Backward Proportional Chamber*
Proportional chamber in the backward region of the H1 Detector.

BST *Backward Silicon Tracker*
Silicon detector close to the beam pipe in backward direction.

CAM *Content Addressable Memory*
Memory that provides the inverse operation compared to RAM. The input is the value and the output is the address of this value.

CIP *Central Inner Proportional Chamber*
Proportional chamber in the central region of the H1 detector. For the HERA II data taking replaced by the improved CIP2000.

CJC *Central Jet Chamber*
Two large wire chambers of the central tracking system of the H1 Detector.

COP *Central Outer Proportional Chamber*
Proportional chamber between the two CJCs. Deactivated for the H1 data taking incorporating L3Rejects.

COZ *Central Outer Z Chamber*
Wire chambers in the H1 central tracking system that improves the resolution in z.

CPU *Central Prozessing Unit*
Core of the modern computer architecture.

CST *Central Silicon Tracker*
Silicon device in the central region close to the beam pipe.

CTL *Central Trigger Logic*
Combines all trigger decisions from the different trigger subsystems.

$\mathbf{d_{ca}}$ *Distance of Closest Approach*
Smallest distance between a particle track and the origin.

DCRφ *Drift Chamber Rφ*
Uses CJC hit information to derive trigger decisions based on tracks in the r-φ plane.

DESY *Deutsches Elektronen-Synchrotron*
Large research institue of the Helmholtz alliance in Hamburg.

DIS *Deep Inelastic Scattering*
At HERA deep inelastic scattering processes are observed from $Q^2 \geq 1\ \mathrm{GeV}^2$.

DMA *Direct Memory Access*
Direct data transfer without using the CPU needs certain memory adresses where data should be stored.

DPIO *Digital Parallel Input Output*
Labels a PCB from the VMetro company that allows the parallel transfer of data with a certain signal standard.

DSP *Digital Signal Processor*
Optimised chip for the processing of special algorithms.

EOT *End of Transfer*
Signals that determines the end of a data transfer.

EEPROM ***E**lectrically **E**rasable **P**rogrammable **R**ead-**O**nly **M**emory*
Programmable chip that is used to store the programming of a FPGA.

FADC ***F**lash **A**nalog **D**igital **C**onverter*
Converts analogue signals to digital ones. The resolution achieved is determined by the number of bits used for the conversion.

FEM ***F**ront **E**nd **M**odul*
Specialised PCB that digitises the CJC analogue information used by the FTT system.

FIFO ***F**irst **I**n **F**irst **O**ut*
Chip that allows the access to stored data only in a certain order.

FNE ***F**IFO **n**ot **e**mpty*
Signal of the DPIO card released if one word is received in the on-board FIFO.

FFNS ***F**ixed **F**lavor **N**unber **S**cheme*
Concept for the massive treatment of heavy quark mass effects in pQCD.

FPDP ***F**ront **P**anel **D**ata **P**ort*
Specialised bus for parallel data transfer simulataneously to all connected receivers.

FPGA ***F**ield **P**rogrammable **G**ate **A**rray*
Chip with re-programmable logic cells. Executes specialised algorithms with high performance.

FSR ***F**inal **S**tate **R**adiation*
Next-to-leading order effect in QED from the outgoing lepton line.

FST ***F**orward **S**ilicon **T**racker*
Silicon detector close to the beam pipe in the forward region of the H1 detector.

FTD ***F**orward **T**racking **D**etector*
Enhances the forward tracking capabilities of the H1 detector.

FTT ***F**ast **T**rack **T**rigger*
Three level trigger system that provides trigger decisions based on three-dimensional high resolution tracks and a partial event reconstruction at trigger level.

FTTEMU ***F**ast **T**rack **T**rigger **Emu**lation*
Hardware like simulation of the FTT for the comissioning and optimisation of the FTT. Used for physics analyses to check the trigger decision in data.

GM-VFNS ***G**eneral-**M**ass **V**ariable **F**lavor **N**unber **S**cheme*
Concept for a combined massive and massless treatment of heavy quark mass effects in pQCD, which depends on the scale.

GUI ***G**raphical **U**ser **I**nterface*
Provides in general easy access to a complex program. Here used for the FTT running.

HERA ***H**adron-**E**lektron-**R**ing **A**nlage*
Large electron proton storage located at DESY in Hamburg.

ISR ***I**nterrupt **S**ervice **R**outine*
Connected to a hardware interrupt. Does a fast acknowledge and initialises the interrupt action.

ISR ***I**nitial **S**tate **R**adiation*
Next-to-leading order effect in QED from the incoming lepton state.

JTAG ***J**oint **T**est **A**ction **G**roup*
Standardised bus for the programming of chips, like FPGAs.

L2KEEP
CTL decision to keep an event at level two.

L2NN ***L**evel 2 **N**euronal **N**etwork*
Level two trigger subsystem which implements neuronal networks.

L2TT ***L**evel 2 **T**opological **T**rigger*
Level two trigger system based on topological information.

L3KEEP
CTL decision to keep an event at level three.

L3REJECT
CTL decision to reject an event at level three.

LAR ***L**iquid **Ar**gon Calorimeter*
Main calorimeter of the H1 Detector divided in an electromagnetic and hadronic part.

LVDS ***L**ow **V**oltage **D**ifferential **S**ignal*
Differential fast signal transfer standard.

MPB ***M**ulti **P**urpose **B**oard*
Special PCB for the FTT developped by SCS with three large FPGAs and four DSPs. Is used for different purposes and provides connectors for four piggy-back cards.

MVME ***M**otorola **VME***
Special VME proccessor cards developped by Motorola.

PCI ***P**eripheral **C**omponent **I**nterconnect*
Specialised bus system that allows for the connection of cards to the CPU.

PIO ***P**arallel **I**nput **O**utput*
Signal line of the FPDP bus for special purposes. In FTT used as clear lines.

PCB ***P**rinted **C**urcuit **B**oard*
Realises complex electronical curcuits, basically all electronic cards are PCBs.

PMC ***P**CI **M**ezzanine **C**ard*
Standard for piggy back cards, which are mounted on other PCBs.

Power-PC ***P**erformance **O**ptimised **W**ith **E**nhanced **R**ISC microprocessor architecture for **P**ersonal **C**omputers*
Special processor architecture from Apple/IBM/Motorola.

PPC ***P**ower-**PC***
see Power-PC.

PQZP ***P**arallel **Q**uickbus **Z**ero-Suppression **P**rocessor*
16 bit wide Bus for the transmission of data in the H1 detector (L2L3Bus).

QCD ***Q**uantum **c**hromo**d**ynamics*
Gauge theory that describes the strong interaction of colored objects.

QED ***Q**uantum **e**lectro**d**ynamics*
Gauge theory that describes the electromagnetic interaction of charged objects.

RAM ***R**andom **A**ccess **M**emory*
memory that can be read from and written to in arbitrary sequence.

RES ***Re**served **S**ignal*
Special signal line of the FPDP bus. Here used as EOT signal.

RISC ***R**educed **I**nstruction **S**et **C**omputer*
Makes use of a restricted instructions set that can be executed faster than the standard ones.

ROM ***R**ead **O**nly **M**emory*
Memory that can only be read from.

RTOS ***R**eal **T**ime **O**erating **S**ystem*
Ensures preditiable and deterministic response times during the processing. Free and non-free RTOS exist.

S ***S**ubtrigger*
Logical combination of triggerelements by the CTL, usually the the number is added, e.g. s122.

SCS ***S**uper **C**omputing **S**ystems*
Swiss company (Zürich) that develoopped parts of the FTT (MPB).

SPACAL ***Spa**ghetti **Cal**orimeter*
Calorimeter in the backward region of the H1 Detector based on a Lead scintillating-fibre sandwich structure.

STC ***S**ubsystem **T**rigger **C**ontroller*
Interface between the H1 detector and the individual subsystem.

TCP/IP ***T**ransmission **C**ontrol **P**rotocol / **I**nternet **P**rotocol*
The protocoll is used for data transmission within LANs.

TE ***T**rigger **E**lement*
Information decoded bit wise that provides information on a trigger condition.

TTL ***T**ransistor **T**ransistor **L**ogic*
Class of digital circuits where logical and amplifying functions are realised by transistors. In addition the differential TTL exists which is similar to LVDS.

VME ***V**ERSA **m**odule **E**urocard*
Standard bus system with a normalised backplane.

ZM-VFNS ***Z**ero-**M**ass **V**ariable **F**lavor **N**umber **S**cheme*
Concept for the massless trfeatment of heavy quark mass effects in pQCD.

Bibliography

[A+82] Aubert, J. et al. Phys. Lett. B, **114**, (1982), p. 373.

[A+93] Andrieu, B. et al. Nucl. Instr. and Meth., **336**, (1993), p. 460.

[A+97a] Abt, I. et al. (H1). Nucl. Instr. and Meth., **A386**, (1997), p. 310 & 348.

[A+97b] Appuhn, R.-D. et al. Nucl. Instr. and Meth., **386**, (1997), p. 397.

[A+99] Adloff, C. et al. (H1). Nucl. Phys., **B545**, (1999), pp. 21–44. http://arxiv.org/abs/hep-ex/9812023.

[A+02] Adloff, C. et al. (H1). Phys. Lett., **B528**, (2002), pp. 199–214. http://arxiv.org/abs/hep-ex/0108039.

[A+03] Adloff, C. et al. (H1). Eur. Phys. J., **C30**, (2003), pp. 1–32. http://arxiv.org/abs/hep-ex/0304003.

[A+07] Aktas, A. et al. (H1). Eur. Phys. J., **C51**, (2007), pp. 271–287. http://arxiv.org/abs/hep-ex/0701023.

[A+08a] Aaron, F. D. et al. (H1). Phys. Lett., **B665**, (2008), pp. 139–146. http://arxiv.org/abs/hep-ex/0805.2809.

[A+08b] Aaron, F. D. et al. (H1). Submitted to Eur.Phys.J.C. http://arxiv.org/abs/hep-ex/0808.1003.

[A+08c] Aaron, F. D. et al. (H1). Eur. Phys. J., **C54**, (2008), pp. 389–409. http://arxiv.org/abs/hep-ex/0711.2606.

[ACOT94] Aivazis, M. A. G., Collins, J. C., Olness, F. I. and Tung, W.-K. Phys. Rev., **D50**, (1994), pp. 3102–3118. http://arxiv.org/abs/hep-ph/9312319.

[AGIS83] Andersson, B., Gustafson, G., Ingelman, G. and Sjostrand, T. Phys. Rept., **97**, (1983), pp. 31–145. http://dx.doi.org/10.1016/0370-1573(83)90080-7.

[AGLP89] Andersson, B., Gustafson, G., Lonnblad, L. and Pettersson, U. Z. Phys., **C43**, (1989), p. 625. http://dx.doi.org/10.1007/BF01550942.

[AKK08] Albino, S., Kniehl, B. A. and Kramer, G. Nucl. Phys., **B803**, (2008), pp. 42–104. http://arxiv.org/abs/hep-ph/0803.2768.

[AM74] Artru, X. and Mennessier, G. Nucl. Phys., **B70**, (1974), pp. 93–115.

[ANS98] ANSI/VITA 17-1998. **17**.

[AOT94] Aivazis, M. A. G., Olness, F. I. and Tung, W.-K. Phys. Rev., **D50**, (1994), pp. 3085–3101. http://arxiv.org/abs/hep-ph/9312318.

[AP77] Altarelli, G. and Parisi, G. Nucl. Phys., **B126**, (1977), p. 298. http://dx.doi.org/10.1016/0550-3213(77)90384-4.

[B+87] Brun, R. et al. Technical Report CERN-DD/EE-81-1.

[B+97] Bizot, J. C. et al. *Strategy studies for the H1 topological L2 trigger (L2TT)* (1997).

[B+01] Baird, A. et al. IEEE Trans. Nucl. Sci., **48**, (2001), pp. 1276–1285. http://arxiv.org/abs/hep-ex/0104010.

[B+04] Berger, N. et al. Proc. of the 2004 NSS Symposium, **A518**, (Oct. 2004), pp. 542–543.

[BB95] Bassler, U. and Bernardi, G. Nucl. Instrum. Meth., **A361**, (1995), pp. 197–208. http://arxiv.org/abs/hep-ex/9412004.

[Ben07] Beneckenstein, D. *Effiziensstudie und Optimierung der dritten Stufe des schnellen Spurtriggers*. https://www-h1.desy.de/psfiles/theses/h1th-471.pdf (2007). Diploma thesis.

[Ber07] Berger, N. *Measurement of Diffractive* Φ *Meson Photoproduction at HERA with the H1 Fast Track Trigger*. Ph.D. thesis, ETH Zürich, Switzerland (2007). ETH No. 17169, https://www-h1.desy.de/psfiles/theses/h1th-459.ps.

[BH34] Bethe, H. and Heitler, W. Proc. Roy. Soc. Lond., **A146**, (1934), pp. 83–112.

[BHPS80] Brodsky, S. J., Hoyer, P., Peterson, C. and Sakai, N. Phys. Lett., **B93**, (1980), pp. 451–455.

[Bjo66] Bjorken, J. D. Phys. Rev., **148**, no. 4, (1966), pp. 1467–1478. http://dx.doi.org/10.1103/PhysRev.148.1467.

[Bjo69] Bjorken, J. D. Phys. Rev., **179**, no. 5, (1969), pp. 1547–1553. http://dx.doi.org/10.1103/PhysRev.179.1547.

[BKK98] Binnewies, J., Kniehl, B. A. and Kramer, G. Phys. Rev. D, **58**, no. 1, (1998), p. 014,014. http://dx.doi.org/10.1103/PhysRevD.58.014014.

[BL78] Balitsky, I. I. and Lipatov, L. N. Sov. J. Nucl. Phys., **28**, (1978), pp. 822–829.

[BL98] Blobel, V. and Lohrmann, E. *Statistische und numerische Methoden der Datenanalyse* (1998).

[Blo84] Blobel, V. (DESY). DESY, **84**, (1984), p. 118.

[Blo05] Blobel, V. *New developments in track finding and fitting.* https://www-h1.desy.de/idet/itracker/TrackingGroup/AgnMin/Meet050824/blobel050824.pdf (2005).

[Boe07] Boenig, M.-O. *Messung des D^*-Meson-Produktionsquerschnitts in tiefinelastischer Streuung mit dem H1-Experiment.* Ph.D. thesis, Universität Dortmund, Germany (2007). https://www-h1.desy.de/psfiles/theses/h1th-457.ps.

[Bow81] Bowler, M. G. Zeit. Phys., **C11**, (1981), p. 169.

[BP69] Bjorken, J. D. and Paschos, E. A. Phys. Rev., **185**, no. 5, (1969), pp. 1975–1982. http://dx.doi.org/10.1103/PhysRev.185.1975.

[BR] Brun, R. and Rademakers, F. *ROOT - An Object Oriented Data Analysis Framework, Proceedings AIHENP'96 Workshop, Lausanne, Sep. 1996, Nucl. Inst. & Meth. in Phys. Res.* **A** *389 (1997) 81-86.* http://root.cern.ch/.

[Bri08] Brinkmann, M. *D^* production at high Q^2 with the H1 detector.* Ph.D. thesis, Universität Hamburg, Germany (2008). In preparation.

[C+98] Cuje, M. et al. *H1 High Luminosity Upgrade 2000 - CIP and Level 1 Vertex Trigger* (1998).

[Cal70] Callan Gross. Nucl. Phys. B, **392**, (1970), p. 162.

[Cam06] Caminada, L. *Implementation of a Trigger for the Decay $b \to eX$ on the Third Trigger Level at the H1 Experiment.* https://www-h1.desy.de/psfiles/theses/h1th-458.pdf (2006). Diploma thesis.

[CFM90a] Catani, S., Fiorani, F. and Marchesini, G. Phys. Lett., **B234**, (1990), p. 339.

[CFM90b] Catani, S., Fiorani, F. and Marchesini, G. Nucl. Phys., **B336**, (1990), p. 18.

[CG94] Cacciari, M. and Greco, M. Phys. Rev. Lett., **73**, no. 12, (1994), pp. 1586–1589. http://dx.doi.org/10.1103/PhysRevLett.73.1586.

[Cia88] Ciafaloni, M. Nucl. Phys., **B296**, (1988), p. 49.

[Col98] Collins, J. C. Phys. Rev. D, **58**, no. 9, (1998), p. 094,002. http://dx.doi.org/10.1103/PhysRevD.58.094002.

[CS87] Collins, J. C. and Soper, D. E. Ann. Rev. Nucl. Part. Sci., **37**, (1987), pp. 383–409.

[CSvN00] Chuvakin, A., Smith, J. and van Neerven, W. L. Phys. Rev., **D62**, (2000), p. 036,004. http://arxiv.org/abs/hep-ph/0002011.

[Dau08] Daum, K. and Jung, A. W. and Krüger, K. and Lipka, K. *Extraction of the Charm Contribution to the Proton Structure Function F_2^c from $D^{*\pm}$ Measurements in Deep Inelastic Scattering at HERA*. https://www-h1.desy.de/psfiles/confpap/ICHEP08/H1prelim-08-172.ps (2008).

[Dok77] Dokshitzer, Y. L. Sov. Phys. JETP, **46**, (1977), pp. 641–653.

[Dur] Durham university (MRST group). *On-line Plotting and Calculation of PDF's*. http://durpdg.dur.ac.uk/hepdata/pdf3.html.

[Els92] Elsen, E. 2nd Annual Conference on Electronics for Future Colliders (1992).

[Fer04] Ferencei, J. *HyperNews: SPACAL trigger thresholds for HERAII*. https://www-h1.desy.de/icgi-hypernews/get/Detector/Spacal/92/1/1.html (2004).

[Fey69] Feynman, R. P. Phys. Rev. Lett., **23**, no. 24, (1969), pp. 1415–1417. http://dx.doi.org/10.1103/PhysRevLett.23.1415.

[FGML73] Fritzsch, H., Gell-Mann, M. and Leutwyler, H. Phys. Lett., **B47**, (1973), pp. 365–368. http://dx.doi.org/10.1016/0370-2693(73)90625-4.

[FK72] Friedman, J. I. and Kendall, H. W. Ann. Rev. Nucl. Part. Sci., **22**, (1972), pp. 203–254.

[Fle03] Fleming, Y.H. *The H1 First Level Fast Track Trigger*. Ph.D. thesis, Univ. of Birmingham, UK (2003). DESY-THESIS-2003-045, https://www-h1.desy.de/psfiles/theses/h1th-324.ps.

[G+78] Granet, P. et al. (French-Soviet). Nucl. Phys., **B140**, (1978), p. 389.

[Gai82] Gaiser, J. E. *Charmonium Spectroscopy from readiative Decays of the J/Ψ and $\Psi'^{\star}$*. Ph.D. thesis, Stanford University (1982).

[GJDR08] Gluck, M., Jimenez-Delgado, P. and Reya, E. Eur. Phys. J., **C53**, (2008), pp. 355–366. http://arxiv.org/abs/hep-ph/0709.0614.

[GL72] Gribov, V. N. and Lipatov, L. N. Sov. J. Nucl. Phys., **15**, (1972), pp. 438–450.

[GW73] Gross, D. J. and Wilczek, F. Phys. Rev. D, **8**, no. 10, (1973), pp. 3633–3652. http://dx.doi.org/10.1103/PhysRevD.8.3633.

[H+98] H1 et al. (H1). *Proposal for an Upgrade of the H1 Forward Track Detector for HERA 2000* (1998).

[H+99a] H1 et al. (H1). *A forward silicon Tracker for H1* (1999).

[H+99b] H1 et al. (H1). *Proposal to Upgrade the LAr Calorimeter Trigger: The Jet Trigger* (1999).

[H+04] H1 et al. (H1). *H1 Fast Navigator*. http://www-h1.desy.de/general/home/intra_home.html (2004).

[H+08] H1 et al. (H1). *Measurement of F_2^{cc} and F_2^{bb} using the H1 vertex Detector at HERA*. https://www-h1.desy.de/psfiles/confpap/ICHEP08/H1prelim-08-173.ps (2008).

[Hen00] Henschel, H. and Lahmann, R. Nucl. Instr. and Meth., **A453**, (2000), p. 93.

[HJ03] Hansson, M. and Jung, H. http://arxiv.org/abs/hep-ph/0309009.

[HS95] Harris, B. W. and Smith, J. Nucl. Phys., **B452**, (1995), pp. 109–160. http://arxiv.org/abs/hep-ph/9503484.

[HS98] Harris, B. W. and Smith, J. Phys. Rev., **D57**, (1998), pp. 2806–2812. http://arxiv.org/abs/hep-ph/9706334.

[IEE] IEEE. IEEE Trans. Nucl. Sci., **1386.1**, , p. 1386.

[J+07] Jung, A. W. et al. Proc. of the 2007 IEEE NPSS RealTime Conference, **ISBN 1-4244-0867-9**, (Oct. 2007), p. IEEE Catalog Number: 07EX1643C. http://ieeexplore.ieee.org/Xplore/login.jsp?url=/stamp/stamp.jsp?arnumber=4382858&isnumber=4382726.

[Jam] James, F. *MINUIT, Function Minimization and Error Analysis*. Computing and Networks Division, CERN Geneva, Switzerland.

[Jun95] Jung, H. Comput. Phys. Commun., **86**, (1995), p. 147.

[Jun02] Jung, H. Comput. Phys. Commun., **143**, (2002), p. 100.

[Jun04] Jung, A. W. *Inbetriebnahme der dritten Stufe des schnellen Spurtriggers für das H1-Experiment*. https://www-h1.desy.de/psfiles/theses/h1th-367.pdf (2004). Diploma thesis.

[Jun06] Jung, A. W. *FTT L3 Website encoding L3 Trigger Changes*. http://www-h1.desy.de/idet/upgrade/trigger/ftt/level3/l3te_definition.html (2006).

[Jun07] Jung, A. W. *Present status of the FTT trigger simulation*. https://www-h1.desy.de/icgi-h1wiki/moin.cgi/AnalysisTools/Meeting2007-11-14 (2007).

[Jun08a] Jung, A. W. *D^* Production in DIS and Photoproduction at H1*. http://indico.cern.ch/getFile.py/access?contribId=238&sessionId=14&resId=2&materialId=slides&confId=24657 (2008). XVI. International Workshop on Deep-Inelastic Scattering and Related Subjects.

[Jun08b] Jung, A. W. *D^* Production in DIS and Photoproduction at H1.* http://indico.cern.ch/getFile.py/access?contribId=74&sessionId=2&resId=0&materialId=slides&confId=27458 (2008). 4th HERA and the LHC workshop.

[Jun08c] Jung, H. *Factorization Scale Variation.* "Private Communication" (2008).

[K+97] Köhne, J. K. et al. Nucl. Instrum. Meth., **A389**, (1997), pp. 128–133.

[Kar91] Karimäki, V. Nucl. Instr. and Meth., **A305**, (1991), p. 187.

[KLF77] Kuraev, E. A., Lipatov, L. N. and Fadin, V. S. Sov. Phys. JETP, **45**, (1977), pp. 199–204.

[KLP78] Kartvelishvili, V., Likhoded, A. and Petrov, V. Phys. Rev. Lett., **78B**, (1978), p. 615.

[Kni08] Kniehl, B. A. http://arxiv.org/abs/hep-ph/0807.2215.

[Kno96] Knowles, I.G and Sjöstrand, T. *CERN yellow report: QCD event generators.* http://doc.cern.ch/yellowrep/1996/96-01_v2/p103.ps.Z (1996).

[KOS00] Kramer, M., Olness, F. I. and Soper, D. E. Phys. Rev., **D62**, (2000), p. 096,007. http://arxiv.org/abs/hep-ph/0003035.

[Kru08] Krueger, K. *Convenor of Calo Calibration Group: Calibration Uncertainties.* "Private Communication" (2008).

[KSD03] Knowles, I., Schmelling, M. and Dissertori, G. Oxford Science Publications.

[KSM92] Kwiatkowski, A., Spiesberger, H. and Mohring, H. Comput. Phys. Commun., **69**, (1992), p. 731 155.

[L+00] Lai, H. L. et al. (CTEQ). Eur. Phys. J., **C12**, (2000), pp. 375–392. http://arxiv.org/abs/hep-ph/9903282.

[Lae93] Laenen, E. and Riemersma, S. and Smith, J. and van Neerven, W. L. Nucl. Phys. B, **392**, (1993), p. 162 & 229.

[Lap06] Laptin, L. *CTL Interface and Trigger bit card - Design & Programming.* "Private Communication" (2006).

[Lip08] Lipka, K. and Daum, K. *F2cc from H1 data - Implementation of $\hat{s}$ fragmentation.* https://www-h1.desy.de/icgi-h1wiki/moin.cgi/HeavyFlavourWorkingGroup/F2cc_from_D*?action=AttachFile&do=get&target=lipka-080701.pdf (July 2008).

[Loh06] Lohwasser, K. *Performance studies of the Fast Track Trigger at the H1-experiment.* https://www-h1.desy.de/psfiles/theses/h1th-435.ps (June 2006). Diploma thesis.

[Lon92] Lonnblad, L. Comput. Phys. Commun., **71**, (1992), pp. 15–31. http://dx.doi.org/10.1016/0010-4655(92)90068-A.

[Lon95] Lonnblad, L. Z. Phys., **C65**, (1995), pp. 285–292. http://dx.doi.org/10.1007/BF01571885.

[M+05] Meer, D. et al. IEEE Trans. Nucl. Sci., **49**, (2005), pp. 357–361.

[Mar95] Marchesini, G. Nucl. Phys., **B445**, (1995), pp. 49–80. http://arxiv.org/abs/hep-ph/9412327.

[Mot97] Motorola Literature Distribution Center. Data sheet MPC750/D.

[Mot00] Motorola. http://www.freescale.com.

[MST06] Martin, A. D., Stirling, W. J. and Thorne, R. S. Phys. Lett., **B636**, (2006), pp. 259–264. http://arxiv.org/abs/hep-ph/0603143.

[N+08] Nadolsky, P. M. et al. Phys. Rev., **D78**, (2008), p. 013,004. http://arxiv.org/abs/hep-ph/0802.0007.

[Nad08] Nadolsky, P. *Implications of PDF analysis for collider observables.* http://indico.cern.ch/getFile.py/access?contribId=1&sessionId=0&resId=0&materialId=slides&confId=27439 (2008).

[Nat00] National Semiconductor. http://www.national.com.

[Nau03] Naumann, J. *Entwicklung und Test der dritten H1-Triggerstufe.* Ph.D. thesis, Universität Dortmund, Germany (2003). https://www-h1.desy.de/psfiles/theses/h1th-305.ps.

[NS+08] Niebuhr, C., Schmitt, S. et al. *Lumi-TF: Luminosity status report* (June 2008).

[P+00] Pitzl, D. et al. Nucl. Instr. and Meth., **A454**, (2000), p. 334.

[P+02] Pumplin, J. et al. JHEP, **07**, (2002), p. 012. http://arxiv.org/abs/hep-ph/0201195.

[Pet83] Peterson, C. and Schlatter D. and Schmitt, I. and Zerwas, P.M. Phys. Rev. D, **27**, (1983), p. 105.

[Pit07] Pitzl, D. *CJC Studies on MC.* https://www-h1.desy.de/idet/itracker/TrackingGroup/AgnMin/Meet0712/cjcmc.pdf (2007).

[Pit08] Pitzl, D. *Tracking on DST5: Physics Opportunities.* https://www-h1.desy.de/h1/iww/iminutes/talks.20080207/Pitzl.pdf (2008).

[San08] Sandoval, C. *Calculation in the ZM-VFNS.* "Private Communication" (2008).

[Sau09] Sauter, M. *Measurement of the b cross section at production threshold from semi-leptonic b-quark decays*. Ph.D. thesis, ETH Zürich, Switzerland (2009). In preparation.

[SCEN+99] Schultz-Coulon, H. C., Elsen, E., Nicholls, T., Coughlan, J. and Rick, H. IEEE Trans. Nucl. Sci., **46**, (1999), pp. 915–919.

[Sch03] Schmidt, S. *Messung charminduzierter Zweijetereignisse in tiefinelastischer ep-Streuung mit dem H1-Detektor bei HERA*. Ph.D. thesis, Universität Hamburg, Germany (2003). DESY-THESIS-2004/043, https://www-h1.desy.de/psfiles/theses/h1th-363.ps.

[Sch04] Schöning, A. Nucl. Instr. and Meth., **A518**, (2004), pp. 542–543.

[Sch08] Schienbein, I. *Status GM-VFNS: Theory & Experimental review of HQ Production in ep Scattering*. "Private Communication" (2008).

[SCS] SCS Supercomputing Systems. company, Zurich, Switzerland.

[T+07] Tung, W.-K. et al. JHEP, **02**, (2007), p. 053. http://arxiv.org/abs/hep-ph/0611254.

[TKS02] Tung, W.-K., Kretzer, S. and Schmidt, C. J. Phys., **G28**, (2002), pp. 983–996. http://arxiv.org/abs/hep-ph/0110247.

[Tlu99] Tluczykont, M. *Z-Kalibration der zentralen Spurenkammer des H1-Detektors bei HERA*. https://www-h1.desy.de/psfiles/theses/h1th-147.ps (1999). Diploma thesis.

[Tol08] Toll, T. *MC@NLO for photoproduction*. http://indico.cern.ch/materialDisplay.py?contribId=230&sessionId=14&materialId=slides&confId=24657 (2008).

[TR98a] Thorne, R. S. and Roberts, R. G. Phys. Lett., **B421**, (1998), pp. 303–311. http://arxiv.org/abs/hep-ph/9711223.

[TR98b] Thorne, R. S. and Roberts, R. G. Phys. Rev., **D57**, (1998), pp. 6871–6898. http://arxiv.org/abs/hep-ph/9709442.

[Urb09] Urban, K. *Measurement of inclusive and Di-jet D^* meson photoproduction at HERA*. Ph.D. thesis, Universität Heidelberg, Germany (2009). In preparation.

[VK05] Verkerke, W. and Kirkby, D. *The RooFit toolkit for data modeling* (2005).

[W+92] Wolff, T. et al. Nucl. Instr. and Meth., **A323**, (1992), p. 357.

[W+03] Wissing, C. et al. Proc. of the 14th IEEE - NPSS Real time Conference 2005, pp. 233–236.

[Weg99] Wegener, D. *Einführung in die Kern- und Elementarteilchenphysik - Vorlesungsskript*. http://www.physik.tu-dortmund.de/E5/?content=25&lang=de (3. Auflage 1998/99).

[Wei73] Weinberg, S. Phys. Rev. D, **8**, no. 12, (1973), pp. 4482–4498. http://dx.doi.org/10.1103/PhysRevD.8.4482.

[Win99] Wind River System Inc. *vxworks programmers guide, 5.4* (1999).

[Wis03] Wissing, C. *Entwicklung eines Simulationsprogrammes und Implementierung schneller Spuralgorithmen für den neuen H1-Driftkammertrigger*. Ph.D. thesis, Universität Dortmund, Germany (2003). https://www-h1.desy.de/psfiles/theses/h1th-300.ps.

[Y+06] Yao, W. M. et al. (Particle Data Group). J. Phys., **G33**, (2006), pp. 1–1232. http://pdg.lbl.gov.

[Z+07] ZEUS et al. *D^* in DIS and Measurement of F_2^c*. http://www-zeus.desy.de/physics/hfla/public/abstracts07/ (2007).

Danksagung

Geschafft, die Arbeit ist tatsächlich fertig geworden. Ich danke allen meinen Freunden und Kollegen bei H1 ohne die mir diese Arbeit nicht möglich gewesen wäre. Mein besonderer Dank gilt Herrn Professor Dr. H.-C. Schultz-Coulon, der es mir ermöglicht hat, diese Doktorarbeit in einer internationalen Kollaboration und in einer sehr angenehmen Arbeitsatmosphäre anzufertigen. Besonders danke ich meinem Doktorvater für das Verständnis in schwierigen persönlichen Zeiten. Seine Motivationsfähigkeit und sein Interesse auch über grosse Entfernung hat zum Erfolg dieser Arbeit maßgeblich beigetragen. Herrn Prof. Dr. N. Herrmann danke ich für das Interesse an meiner Arbeit und die spontane Bereitschaft die Aufgabe des Zweitgutachters wahrzunehmen, sowie für die gute und entspannte Atmosphäre im IRTG Graduiertenkolleg.
Bei zwei Kollegen bedanke ich mich ganz besonders herzlich: Bei Katja Krüger für ihre stete Bereitschaft jeden verwirrenden und manchmal auch falschen Plot zu diskutieren und des Pudels Kern aufzudecken; ohne Ihre Diskussionsbereitschaft hätte meine Doktorarbeit in der vorliegenden Form nicht entstehen können und bei Andre Schöning von dem ich den Enthusiasmus für den FTT abbekommen habe und der immer ein offenes Ohr und eine Lösung für ein neues Hardware Feature hat und das zu fast jeder Uhrzeit.
Die Arbeit innnerhalb der FTT Gruppe hat mir besonders viel Spass gemacht und ich werde die vielen Stunden in der Halle, während derer wir den FTT und L3 in Betrieb genommen haben, nicht vergessen. Erwähnt seien hier Christoph, Marc-Oliver, Michel, Nik und auch Claus Kleinwort dessen trockener Humor jedes FTT Meeting bereichert hat.
Die besondere Arbeitsatmosphäre in der H1 Halle werde ich ebenfalls in sehr guter Erinnerung behalten. Ich empfand es als eine grosse verständnisvolle Familie in der es immer darum ging das Experiment effizient in Betrieb zu halten. Diese Arbeit in der Halle hat mir sehr viel Spass gemacht, auch wenn es mal wieder spät oder früh geworden ist. Ich danke allen “Hallenbwohnern“ (Eberhard, Thorsten, Leonid, Martin, und allen anderen) für die stete Hilfsbereitschaft, wenn mal wieder irgendwas nicht so wollte wie es sollte und für das Verständnis wenn der FTT und L3 mal wieder den ganzen Laden lahmgelegt hatte. Mein besonderer Dank gilt hier Stefan Schmitt der immer mal schnell geguckt hat, ob wir denn jetzt wirklich ein L3Reject gesehen haben.
Allen Kollegen, die die sprachliche und logische Qualität der Arbeit verbessert haben, gilt hier mein grosser Dank. Erwähnt seien hier allen voran Katja Krüger, die sich auch durch den dunkelsten sprachlichen Dschungel meiner Arbeit geschlagen hat. Außerdem danke ich Herrn Prof. D. Wegener für seine hilfreichen Kommentare zu meiner Arbeit und viele wertvolle Diskussionen. Dave South danke ich für seine sehr spontane Bereitschaft in letzter Minute mein Englisch zu verbessern. Auch Carsten Niebuhr danke ich für seine Bemühungen meinem Detektorkapitel ein wenig mehr Logik und Konsistenz einzuhauchen. Das Theoriekapitel profitierte von der gewissenhaften Korrekturlesung durch Hannes Jung und seine klärenden Anmerkungen.
Einen besonderen Dank gilt es der ehemaligen (Christoph, Daniel, Dirk, Fatih, Jörg,

Kristin, Marc-Oliver, Michael, Mo) und momentanen (Eva, Klaus, Michi) Besatzung des Büros 1a604 (die "Kapitänskajüte") auszusprechen: insbesondere Klaus, der beizeiten (unter Mitnahme hervorragender Büroausstattung) in die Kapitänskajüte umgezogen ist, sei für seine Ermahnungen auch mal zu schreiben und nicht nur neue Plots zu machen gedankt. Viele Siege (OK, auch einige Niederlagen) am Kickertisch auf dem Berg oder sonstwo bleiben unvergessen. Ich danke auch für die ständige Bereitschaft mal wieder über die Irrungen und Wirrungen der Physik & Analyse und der Welt im besonderen zu schnacken. Michi danke ich für seine unkomplizierte Art und die herzliche Wärme die er bereitwillig teilt. Marc-Oliver, von dem ich den Analysecode übernommen habe, danke ich für tiefere Einblicke in `ROOT`, gute Zusammenarbeit und viele gemütliche Stunden im Vogel. Den vielen Freunden des gepflegten Kaffeetrinkens und Diskutierens (Benno, Eberhard, etc.) in der Kapitänskajüte sei für Rat und Tat gedankt. Oftmals sind auch die Admiräle Wegener und Schultz-Coulon mit an Deck und sorgten für die Sicherheit und den Rückhalt, wenn es mal wieder durch unsicheres Fahrwasser gegangen ist, auch dafür danke ich Ihnen. Meinen Kollegen und Freunden (Alex, Alex, Felix, Frederik, Michael, Rainer, Victor, etc.) aus meinem zweiten Heimathafen Heidelberg danke ich ebenfalls für die herzliche Aufnahme und viele nette Grillabende und Kickerturniere. Für viele interessante Gespräche über Medizin und anderes danke ich Daniel, der immer spontan Zeit hat für einen gemütlichen Abend in der Heidelberger Altstadt.
Besonders herzlich danke ich auch meinen mittlerweile weiter verstreuten Freunden (Aco, Daniel, Dirk, Jens, Jesko, Johannes, Jörg, Stefan und Sven) die immer für mich da sind. Auf die vielen traditionellen Zusammenkünfte beim kickern (Reeperbahnfestival), segeln (Flachgewässer oder Mittelmeer) oder brunchen (Weihnachten) freue ich mich immer ganz besonders. Auch bei Kai, Markus und Jörg bedanke ich mich herzlich für die vielen gemütlichen Abende & Gespräche in den letzten Jahren und die Versorgung mit Schlafsäcken und Wurst.
Meinen Eltern und meiner Familie danke ich ebenfalls herzlich, der Rückhalt und die Unterstützung waren für mich immer eine große Hilfe. Ganz herzlich danke ich meiner Freundin Silke, die dafür gesorgt hat, dass ich auch in der Endphase der Arbeit an grundlegende Dinge wie Essen und Erholung gedacht habe. Für das Verständnis meiner gelegentlichen Arbeitsexzesse danke ich Dir ganz besonders und freue mich auf die gemeinsame Zukunft mit Dir.

Diese Arbeit wurde mit Mitteln des Bundesministeriums für Bildung und Forschung unter der Projektnummer 05H16VHB und mit Mitteln des IRTG Graduiertenkollegs der Universitäten Heidelberg, Mannheim, Oslo und Bergen gefördert.